Western Australian
Geothermal
CENTRE OF EXCELLENCE

Perth Basin Assessment Program

Project 2: GEOMODEL

Authors:

N. E. Timms, S. Corbel, H. Olierook, P. G. Wilkes, C. Delle Piane, H. A. Sheldon, R. Alix, F. G. Horowitz, M. E. J. Wilson, K. A. Evans, C. Griffiths, L. Stütenbecker, S. Israni, P. J. Hamilton, L. Esteban, P. Cope, C. Evans, L. Pimienta, C. Dyt, X. Huang, J. Hopkins, and D. Champion

October 2012

CSIRO

Curtin University

The University of Western Australia
Achieving International Excellence

Government of Western Australia

Enquiries should be addressed to:

Nick Timms
Curtin University

Kent Street
Bentley WA 6102
n.timms@curtin.edu.au

ISBN 978-0-643-10905-6

Report 3

Project 2: Perth Basin Geomodel
N. E. Timms, S. Corbel, H. Olierook, P. G. Wilkes, C. Delle Piane, H. A. Sheldon, R. Alix, F. G. Horowitz, M. E. J. Wilson, K. A. Evans, C. Griffiths, L. Stütenbecker, S. Israni, P. J. Hamilton, L. Esteban, P. Cope, C. Evans, L. Pimienta, C. Dyt, X. Huang, J. Hopkins, and D. Champion. - PRINT

Copyright and Disclaimer

© 2012 WAGCoE To the extent permitted by law, all rights are reserved and no part of this publication covered by copyright may be reproduced or copied in any form or by any means except with the written permission of WAGCoE.

Important Disclaimer

WAGCoE advises that the information contained in this publication comprises general statements based on scientific research. The reader is advised and needs to be aware that such information may be incomplete or unable to be used in any specific situation. No reliance or actions must therefore be made on that information without seeking prior expert professional, scientific and technical advice. To the extent permitted by law, WAGCoE (including its partners, employees and consultants) excludes all liability to any person for any consequences, including but not limited to all losses, damages, costs, expenses and any other compensation, arising directly or indirectly from using this publication (in part or in whole) and any information or material contained in it.

CSIRO

Curtin University

The University of Western Australia
Achieving International Excellence

Government of Western Australia

AUTHOR AFFILIATIONS AND CONTRIBUTIONS

*Section contribution in parentheses

Nicholas Timms[A] (1, 2, 3, 4, 5, 7), Soazig Corbel[B] (1, 2, 5, 6), Hugo Olierook[A] (3, 4, 7), Paul Wilkes[B] (1, 2), Claudio Delle Piane[B] (4, 5), Heather Sheldon[B] (5), Remi Alix[B, C] (5), Frank Horowitz[B, D] (1, 2), Moyra Wilson[A] (3, 4), Katy A. Evans[A] (8), Cedric Griffiths[B] (6), Laura Stütenbecker[A, E] (3, 4, 8), Shankar Israni[A, B, F] (4, 5), Joseph Hamilton[G] (4, 7), Lionel Esteban[B] (4), Patricia Cope[G] (4), Cody Evans[B] (4), Lucas Pimienta[B] (4), Chris Dyt[B] (6), Xiu Huang[B] (6), Jacob Hopkins[A] (8), and David Champion[H] (8).

[A] Department of Applied Geology, Curtin University, GPO Box U1987, Perth, WA 6845

[B] CSIRO Earth Sciences and Resource Engineering, PO Box 1130, Bentley WA 6102, Australia

[C] Université Montpelier 2 Sciences et Techniques - Place Eugène Bataillon - 34095 Montpellier

[D] Now a Visiting Professor at Cornell University, USA

[E] Institut für Geologische Wissenschaften, Freie Universität Berlin, Malteserstraße 74-100, 12249 Berlin, Germany

[F] Now at: Global Ore Discoveries, 15a Tate Street, Albion, QLD, 4010, Australia

[G] ALS Ammtec Mineralogy Division, 6 Macadam Place, Balcatta, WA 6021

[H] Geoscience Australia, ACT, Australia

CONTENTS

EXECUTIVE SUMMARY XI

PREFACE XIII

ACKNOWLEDGEMENTS XIV

1. RE-ASSESSMENT OF THE 3D STRUCTURAL AND STRATIGRAPHIC ARCHITECTURE OF THE PERTH BASIN 1

1.1 Introduction 1

1.2 Geological background 1

1.2.1 Regional potential fields data for the Perth Basin 2

1.2.2 Previous structural models of the Perth Basin 4

1.3 Approach / Analytical Technique 5

1.4 Results 10

1.4.1 New regional gravity and aeromagnetic images of the Perth Basin 10

1.4.2 A new structural interpretation of the Perth Basin 10

1.5 Discussion 21

1.5.1 The geological significance of the new 3D model of the Perth Basin 21

1.5.2 Implications of the new structural interpretation for geothermal exploration 22

1.5.3 Implications of the new 3D model for geothermal exploration 22

1.5.4 Limitations of the new 3D model 22

1.5.5 Goals for future research / Recommendations for further work 23

1.6 Summary 23

2. RESOLVING THE SUBSURFACE GEOLOGY OF THE PERTH METROPOLITAN AREA IN 3D **25**

2.1 Introduction 25

2.2 Geological Background 26

2.3 Approach / Analytical Technique 31

2.3.1 Using land surface topography, drainage network and geological maps to interpret faults in the Perth Metropolitan Area 32

2.3.2 A new detailed gravity survey for Perth Metropolitan Area 32

2.3.3 A wavelet technique ('worming') applied to the new Perth Metropolitan Area gravity dataset 33

2.3.4 2D gravity forward modelling 34

2.3.5 Vertical Seismic Profiling (VSP) in the Perth Metropolitan Area 34

2.3.6 Development of a 3D model of the Perth Metropolitan Area 34

2.4 Results 37

2.4.1 A new interpretation of the fault network in the Perth Metropolitan Area from topography, drainage network and geology 37

2.4.2 New gravity maps and worms for Perth Metropolitan Area 40

2.4.3 2D gravity forward models 44

2.4.4 A new 3D geological model of the Perth Metropolitan Area 45

2.5 Discussion 50

2.5.1 A new structural model of the Perth Metropolitan Area 50

2.5.2 Controls on the geometry of Jurassic to the Cretaceous stratigraphic formations in the central Perth Basin 52

2.5.3 Implications of the new 3D model for geothermal exploration 53

2.5.4 Limitations of the new 3D model 54

2.5.5 Goals for future research / Recommendations for further work 54

2.6 Summary 55

3. CHARACTERISATION OF THE SEDIMENTARY/LITHOLOGICAL HETEROGENEITY OF POTENTIAL GEOTHERMAL TARGET ROCKS IN THE PERTH METROPOLITAN AREA 56

3.1 Introduction 56

3.2 Summary of the stratigraphy of Pinjarra-1, Cockburn-1, Gingin-1 and Gingin-2 58

3.3 Approach 60

3.4 Results 61

3.4.1 Description of the lithofacies scheme for the Mesozoic strata of the central Perth Basin 61

3.4.2 Spatial and temporal distribution of lithofacies in drill core 64

3.4.3 Bedform thickness analysis of Cockburn-1 core 65

3.5 Discussion 72

3.5.1 Evaluation of spatial and temporal variations in lithofacies 72

3.5.2 Implications for the evolution of depositional environment during the early Mesozoic 72

3.5.3 Identification of sedimentologically-favourable potential geothermal targets 73

3.5.4 Sedimentary structures as potential flow baffles, barriers and causes of permeability anisotropy in coarse-grained lithofacies 73

3.5.5 Goals for future research 73

3.6 Summary 74

4. MINERALOGY, DIAGENESIS AND PETROPHYSICAL PROPERTIES OF POTENTIAL GEOTHERMAL TARGET ROCKS IN THE CENTRAL PERTH BASIN 75

4.1 Introduction 75

4.2 Geological background 76

4.3 Approach 77

4.3.1 Mineralogy 77

4.3.2 Logging of diagenetic structures / fabrics 79

4.3.3 Porosity characterisation by image analysis 79

4.3.4 Porosity imaging by scanning electron microscopy 80

4.3.5 Laboratory measurements of porosity and permeability 80

4.3.6 Thermal conductivity 81

4.4 Results 82

4.4.1 Petrography and mineralogy 82

4.4.2 Diagenesis 91

4.4.3 Porosity and permeability data 95

4.4.4 Thermal conductivity data 98

4.5 Discussion 100

4.5.1 Detrital mineralogy 100

4.5.2 Diagenesis 101

4.5.3 Controls on porosity and permeability 102

4.5.4 Controls on thermal conductivity 103

4.5.5 Goals for future research 103

4.6 Summary 103

5. CALIBRATING POROSITY AND PERMEABILITY FROM WIRELINE LOGS: A CASE STUDY OF COCKBURN-1 WELL 105

5.1 Introduction 105

5.2 Approach 105

5.3 Analysis of porosity-permeability profiles in Cockburn-1 107

5.4 Discussion 110

5.4.1 Limitations 110

5.4.2 Goals for future research 111

5.5 Summary 111

6. HOT SEDIMENTARY AQUIFER CHARACTERIZATION USING STRATIGRAPHIC FORWARD MODELLING, PERTH BASIN, AUSTRALIA 112

6.1 Introduction 112

6.2 Stratigraphic Forward Modelling 112

6.3.1 Basic principles of Sedsim operation 113

6.4 Method 117

6.5 Application to the Yarragadee Formation, Perth Basin 118

6.5.1 Conceptual model presentation 120

6.5.2 Review of input parameters 120

6.5.3 Stratigraphic Forward Modelling Results 122

6.5.4 Testing and calibration of simulations 122

6.6 Results 124

6.7 Discussion and Conclusion 126

6.8 Summary 127

7. FAULT-RELATED DAMAGE AND DIAGENESIS AND IMPLICATIONS FOR FAULT PERMEABILITY IN THE NORTH PERTH BASIN 128

7.1 Introduction 128

7.2 Approach 130

7.3 Results 133

7.3.1 Sedimentary Logging and Petrography 133

7.3.2 Diagenetic minerals and fabrics 133

7.3.3 Meso-scale structural analysis 134

7.3.4 Microstructural analysis of fractures and stylolites in Apium-1 138

7.3.5 Porosity and Permeability characterisation 140

7.4 Discussion 142

7.4.1 Facies and environment 142

7.4.2 Relative structural and diagenetic history 143

7.4.3 Mass transfer associated with stylolitization 145

7.4.4 Porosity and permeability evolution 145

7.4.5 Hydrological properties of faults/fault zone structures in the present day Perth Basin 147

7.4.6 Goals for future research 148

7.5 Summary 148

8. QUANTIFICATION OF MAGNITUDE AND LENGTH SCALE VARIATION OF HEAT PRODUCTION FROM THE BASEMENT ROCKS OF THE PERTH BASIN 150

8.1 Introduction 150

8.2 Geological Background 150

8.3 Methods 154

8.4 Results 155

8.4.1 Leeuwin Complex: Comparison of laboratory analyses with GRS results 155

8.4.2 All samples: heat production 156

8.4.3 Mineral Hosts 160

8.5 Discussion 161

8.5.1 Comparability of GRS and ICP data 161

8.5.2 An analogue for the Perth Basin Basement? 161

8.5.3 Typical Length Scale of Variation 162

8.5.4 Stochastic models for heat distribution 163

8.5.5 Contribution of basement heat flow to the overall heat flow budget 165

8.6 Goals for future research 165

8.7 Summary 166

9. REFERENCES 167

APPENDIX A LISTING OF STUDENTS 181

APPENDIX B CONFERENCE AND WORKSHOP CONTRIBUTIONS 181

APPENDIX C SCIENTIFIC PUBLICATIONS 181

EXECUTIVE SUMMARY

The Western Australian Geothermal Centre of Excellence (WAGCoE) conducted scientific and engineering research into WA's geothermal resources, principally Hot Sedimentary Aquifer (HSA) resources in the Perth Basin. Project 2 of the Perth Basin Assessment Program focused on the development of a geological model of the Perth Basin. Knowledge of the structural architecture and stratigraphic geometry of the Perth Basin is a vital prerequisite for understanding subsurface fluid and heat flow. This understanding is fundamental to the identification of geothermal prospects and to effective aquifer management in the Perth Basin. The present report provides new approaches, data sets and analyses for characterising the structural and sedimentary geology of the Perth Basin. Results are presented in eight sections:

Section 1. The most up-to-date publically available aeromagnetic, gravity, bathymetry and digital terrain data are reprocessed to develop the first three-dimensional model of the entire Perth Basin. This model incorporates newly identified faults and fault segment extensions.

Section 2. A new high-resolution, three-dimensional model of the Perth Metropolitan Area (PMA) is presented. The PMA model incorporates a dense network of faults of several orientations which account for depth and thickness changes in subsurface geology, and horizontal compartmentalisation of the subsurface geology is indicated on a scale of 1.5-2 km.

Section 3. A new sedimentological model is developed for key geothermal target formations in the central Perth Basin via a lithofacies analysis of core from existing deep petroleum exploration wells. Complex stacking arrangement of lithofacies on the order of 10 cm to approximately 2 m vertical scale is observed in all formations and wells, which indicates complex switching of different sedimentary depositional environments in time and space.

Section 4. New data is presented on petrography, detrital and diagenetic mineralogy, and laboratory-measured petrophysical data (porosity, permeability, thermal conductivity) from core from key geothermal target formations in the central Perth Basin. These data provide vital new fundamental parameters for geothermal exploration of the Perth Basin.

Section 5. Wireline logs from Cockburn-1 well were used to estimate porosity and permeability traces, providing insight into the variation of these parameters with depth for a continuous vertical profile.

Section 6. A stratigraphic forward model of the Yarragadee aquifer (using Sedsim) provides an insight into the three-dimensional stratigraphic architecture of a key geothermal target of the Perth Basin.

Section 7. The effects of faulting on fluid flow properties are assessed via a multi-scale analysis of core of a potential geothermal target formation from the damage zone of a regional fault in the North Perth Basin. Subvertical fault-related fractures have been sealed by brecciation, quartz and siderite cementation; sub-horizontal stylolites are common and contain halos of quartz cementation. These studies indicate that most, if not all of the faults in the northern Perth Basin would be sealing at depths relevant to geothermal exploration.

Section 8. The contribution of radiogenic heat from the basement to the Perth Basin is characterised using existing and newly acquired data from the Leeuwin complex, SW Australia, and existing data from proposed analogues to the Perth Basin basement in Antarctica. Estimates of the total heat flow due to radioactive decay in the basement are of the order of 25 to 56 mW m^{-2}, and geothermal gradients calculated for plausible thermal conductivity values are 17 to 35 °C km^{-1}.

The data in this report provides new fundamental constraints from which geothermal potential can be assessed and geothermal resources can be defined in the Perth Basin.

PREFACE

The Western Australian Geothermal Centre of Excellence (WAGCoE) was established in 2009 for an initial three year term with a $2.3M grant from the Western Australian Department of Commerce. WAGCoE operated as an unincorporated joint venture between CSIRO, University of Western Australia, and Curtin University, with CSIRO as the Centre agent. The remit of WAGCoE was to assist the Western Australian Government to provide a foundation for a sustainable geothermal industry by conducting advanced scientific and engineering research into WA's geothermal resources, principally HSA resources in the Perth Basin, and to develop and transfer to industry innovative new technologies for direct heat use.

In order to deliver on this task, WAGCoE was structured into three mutually supportive research Programs:

- Perth Basin Assessments (Program 1)
- Above-Ground Engineering (Program 2)
- Deep Heat and Future Resources (Program 3)

The Perth Basin Assessments Program contained the following four research Projects:

- WAGCoE Data Catalog (Project 1)
- Perth Basin Geomodel (Project 2)
- Hydrothermal Simulations (Project 3)
- Reservoir Productivity and Sustainability (Project 4)

This document is the final research report of Project 2 within Program 1 of WAGCoE. The format of the document is that of a summary report; detailed tabulations of technical data and results are to be found in the supporting research reports, papers and theses cited herein.

ACKNOWLEDGEMENTS

WAGCoE was funded by the Western Australian government and the partners of CSIRO, the University of Western Australia, and Curtin University. We also received financial support from our industry associates, Green Rock Energy Ltd and GT Power Pty Ltd. We acknowledge the use of regional geophysical datasets from Geoscience Australia and Geological Survey of Western Australia in Section 1. We gratefully acknowledge the guidance and assistance provided by GT Power Pty Ltd and Green Rock Energy Ltd for financial support and help with securing permissions from Councils and Department of Mines and Petroleum, and for various exploration activities in their geothermal lease holdings. We particularly thank Atlas Geophysics for their professionalism and collaboration in acquiring new high resolution gravity data in the Perth metropolitan area in 2009 and 2010, presented in Section 2. Two University of Western Australia students - Thomas Hoskin and John Mitchell – are also thanked for their assistance with gravity data acquisition. We thank Curtin Department of Exploration Geophysics staff for collaboration in the Vertical Seismic Profiling (VSP) surveys carried out at St Hilda's School, Mosman Park and in Kensington. Rockwater Pty Ltd kindly provided assistance in accessing the new geothermal borehole at St Hilda's School. Maxam Australia Pty Ltd is acknowledged for the provision of explosives and expertise in the conduct of the VSP surveys. Dariush Nadri of CSIRO provided processing expertise in reprocessing the VSP data. We thank the Western Australia Core Library facility for their assistance with access to the core and sampling. C. Delle Piane, L. Esteban and S. Israni acknowledge receipt of funding through a CSIRO ISF project "Rock Physics for geothermal applications". Sandra McLaren (University of Melbourne) is thanked for assistance during acquisition of thermal conductivity data. The Institute of Geoscience Research (TIGeR) at Curtin University is thanked for provision of some of the equipment used in this study. Susanne Schmidt (CSIRO) is thanked for her assistance with the Zeiss Axio Imager II system. H. Olierook thanks ARC Energy Ltd for use of their porosity and permeability data from Apium-1 (Section 7). We thank Elaine Miller and Rob Hart (Curtin University) for support with electron microscopy. Cameron Huddlestone-Holmes, Susanne Schmidt, June Hill, Domenik Wolf-Boenisch and Mike Trefry are acknowledged for their careful reviews of earlier versions. We thank Angelo Vartesi for his draftsmanship and assistance with compilation of the report. We acknowledge support from the Western Australian Geothermal Centre of Excellence.

1. RE-ASSESSMENT OF THE 3D STRUCTURAL AND STRATIGRAPHIC ARCHITECTURE OF THE PERTH BASIN

1.1 Introduction

Knowledge of the 3D structural architecture and stratigraphic geometry are vital prerequisites for understanding subsurface fluid flow in the Perth Basin. This understanding is fundamental to the identification of geothermal prospects and the effective management of Hot Sedimentary Aquifers (HSA) and Engineered Geothermal Systems (EGS). Gravity and aeromagnetic data can provide a wealth of information about the subsurface in poorly exposed terrain, such as the onshore and offshore Perth Basin. In this study, publically available aeromagnetic, gravity, bathymetry and digital terrain data are reprocessed to re-evaluate the structural architecture of the onshore and offshore Perth Basin. These data are then integrated with existing stratigraphic data from petroleum wells and water bores to develop a new 3D model of the whole Perth Basin. The quality of the publically available 2D seismic data for the onshore Perth Basin is poor and was considered to be unreliable and not used in this study.

1.2 Geological background

Geological mapping of the Perth Basin by the Geological Survey of Western Australia (GSWA) began in 1962 and results of this work were summarised by Playford et al. (1976) and Cockbain (1990). The Perth Basin has a broad graben structure and extends from the Northampton Block in the north to the south coast of WA. It formed through Permo-Cretaceous rifting of Greater India and Australia (Harris, 1994; Song and Cawood, 2000). The eastern boundary of the Basin is formed by the Darling Fault. The western boundary is approximately 150 km offshore, significantly west of the 200 m isobath. Three inliers of Precambrian igneous and metamorphic rocks are present in the Perth Basin in the Northampton Block, the Leeuwin Block and the Mullingarra inlier (Cockbain, 1990).

Extensive (and faulted) sheets of Permian and Triassic stratigraphy are present in the deepest parts of the basin, deposited after an initial rift phase (Rift I of Song and Cawood, 2000). This was followed by deposition of the fluvio-deltaic Cattamarra Coal Measures, deposited in an intra-cratonic NNW-ESE to E-W rifting during the Early Jurassic, (Rift II-1 of Song and Cawood, 2000) (Willmott, 1964; Playford et al., 1976; Harris, 1994; FrogTech, 2005). These were overlain by the marine-influenced Cadda Formation during the middle Jurassic, which becomes thicker to the northwest (Playford et al., 1976). The fluvial-dominated Yarragadee Formation was deposited across the entire onshore Perth Basin during a middle Jurassic syn-rift phase (Rift II-2 of Song and Cawood, 2000), resulting in E-W extension (Fairbridge, 1953; Playford et al., 1976; Harris, 1994). Continental break-up is marked by a regional Neocomian unconformity, formation of the Bunbury Basalt in the southern Perth Basin, followed by progradation of the restricted marine(?) Gage Sandstone, and onlapping of the marine South Perth Shale of the Early Cretaceous Warnbro Group (Fairbridge, 1953; Bozanic, 1969; Playford et al., 1976). Elsewhere in the Perth Basin, conjugate strike slip faulting developed and dextral-normal oblique slip occurred on NNW-striking faults during this N-S dextral transtension break-up phase (Harris, 1994).

Sedimentation continued in the central Perth Basin during a thermal sag phase (middle Cretaceous to present), and minor reverse movement is interpreted to have occurred along faults during the Mid Cretaceous, possibly indicating inversion from SSE-NNW compression (Harris, 1994; FrogTech, 2005). Rifting along the southern margin of Australia via NE-SW then N-S directed extension also occurred during the Cretaceous to Early Tertiary, with minor influence in the southernmost Perth Basin (FrogTech, 2005). Minor fault reactivation is shown to occur in some parts the Perth Basin and Yilgarn Craton from Miocene to recent as a response to collision of SE Asian microcontinental fragments (FrogTech, 2005).

The Yilgarn Craton, directly to the east of the onshore Perth Basin, consists of many greenstone belts intruded extensively by multiple pulses of granitoids with different geochemical characteristics (Wilde and Nelson, 2001; Myers and Hocking, 1998). Three geologically, geophysically, and geochronologically distinct crustal components make up the southwest Yilgarn Craton, from west to east these are the Balingup, Boddington and Lake Grace Terranes (Wilde et al., 1996; Wilde, 1999). The Balingup Terrane is made up of belts of turbiditic metasediments and intensely deformed orthogneisses, such as the Chittering, Balingup and Jimperding Metamorphic Belts, intruded by younger granites such as the Logue Brook Granite (~2.690 to ~2.616 Ga; Nemchin and Pidgeon, 1997). Multiple sets of mafic dyke swarms intruded the assembled craton during Proterozoic times (i.e., post ~2.4 Ga) (Wingate and Giddings, 2000). Rocks of the Albany-Fraser Orogen occur to the south of the Yilgarn Craton and outcrop along the southern margin of Western Australia. In the southwest, an inlier known as the Leeuwin complex consists of Late Mesoproterozoic to Neoproterozoic (1100-500 Ma) orthogneiss and granite (Jansen et al., 2003). To the South of the Yilgarn Craton lies the Albany Fraser Belt, juxtaposed by the Manjimup fault. A set of NW-SE trending faults have been identified in the SW corner of the Yilgarn (Myers, 1990). These faults are proposed to have a dextral component of displacement and extend into the Albany Fraser Belt without deflection across the Manjimup fault. Two of these faults bound the Collie Basin and define its NW-SE trend. However, none of the faults are interpreted to extend into the Perth Basin.

1.2.1 Regional potential fields data for the Perth Basin

Aeromagnetic data available for the Perth Basin are mainly from a survey flown by the Bureau of Mineral Resources, a predecessor agency to Geoscience Australia (GA), in 1957 with east-west flight lines flown approximately 2 km apart and at 460 m above sea level (Newman, 1959). This data set was interpreted by Quilty (1963). Various studies by GSWA have used gravity and/or magnetic images and models to help define the main sub-basins and structural elements within the Perth Basin (Crostella and Backhouse, 2000; Iasky et al., 1991; Iasky, 1993; Lockwood and Iasky, 2004; Iasky and Shevchenko, 1995; Mory and Iasky, 1996; Myers and Hocking, 1998) (Fig. 1.1). New aeromagnetic surveys of the Perth Basin, with 400 m spacing and 60 m flying height, were flown during 2011 for GSWA and these new datasets will be very helpful in future studies of the Perth Basin. Unfortunately, the 2011 data were not available for this study.

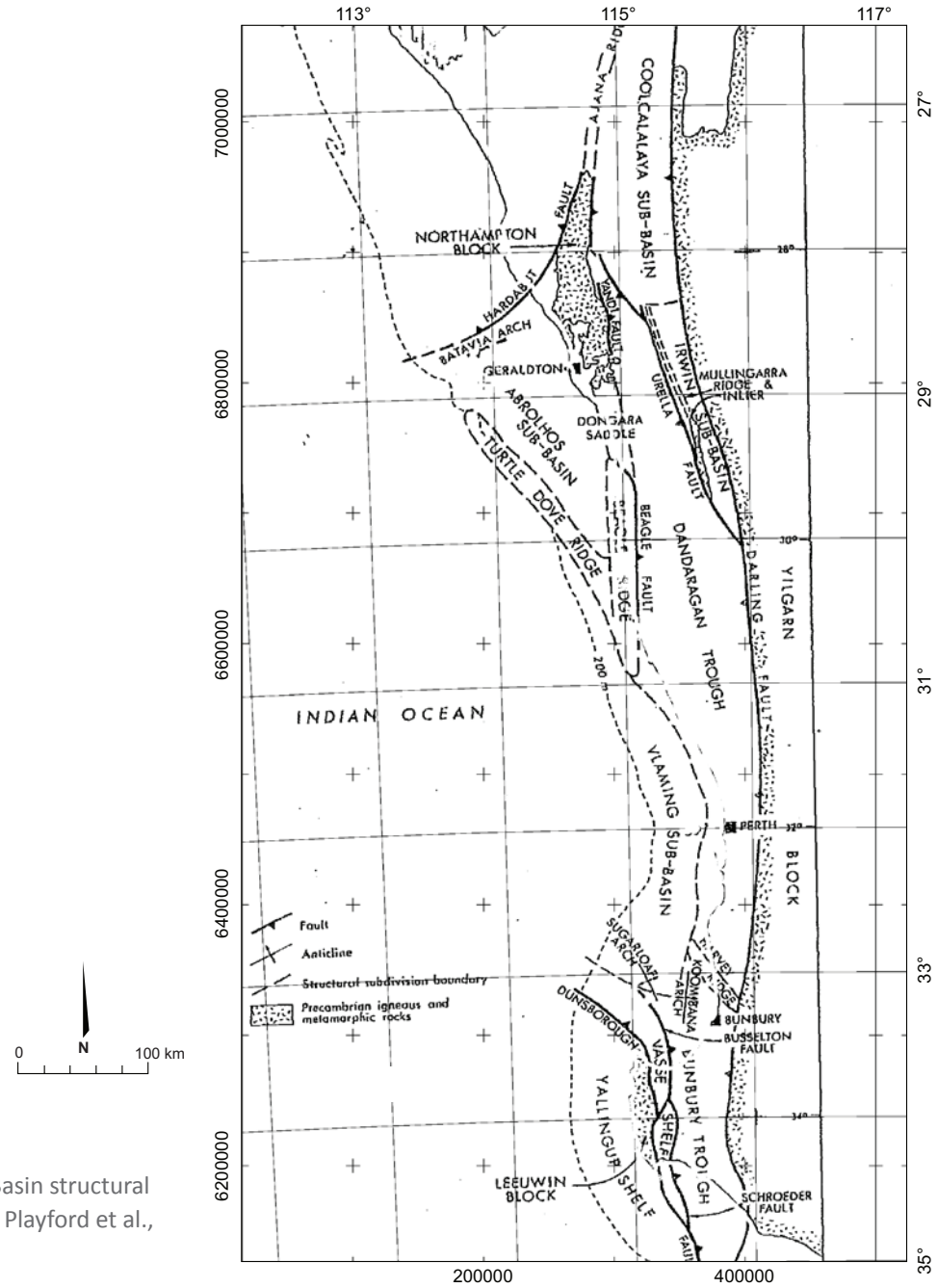

Figure 1.1: Perth Basin structural subdivisions (after Playford et al., 1976).

Gravity forward models were developed by Mory and Iasky (1996) along two approximately E-W traverses in the onshore North Perth Basin. These models show that the Dandaragan Trough is broadly asymmetric with the deepest part in the east filled with sediments up to 12 km thick, and significant topography of the basin-basement interface resulting from displacement across major faults systems such as the Serpentine, Eneabba and Beagle Faults (Fig. 1.2). Mory and Iasky (1996) identified gravity highs close to the modern day coastline known as the Turtle Dove and Beagle Ridges from West to East, respectively. Forward modelling along a traverse close to the latitude of Cervantes indicates that the basement is shallower than 2 km and 4 km for the Turtle Dove and Beagle Ridges,

respectively. Lockwood and Iasky (2004) interpreted the South Turtle Dove Ridge in the Isostatic Residual Gravity data in the offshore data for south west WA, extending northward from Bunbury to just south of Rottnest Island. They also interpret shallow basement continuing northwards from offshore Perth in the Turtle Dove Ridge. This has been intersected at the Jurien 1 well at a depth of approximately 1200 m. Maps and a gridded dataset of sediment thickness (and thus 'depth to basement') for all of the Phanerozoic basins of Australia calculated using potential field data are available as Oz Seebase via www.frogtech.com.au (Frog Tech, 2005).

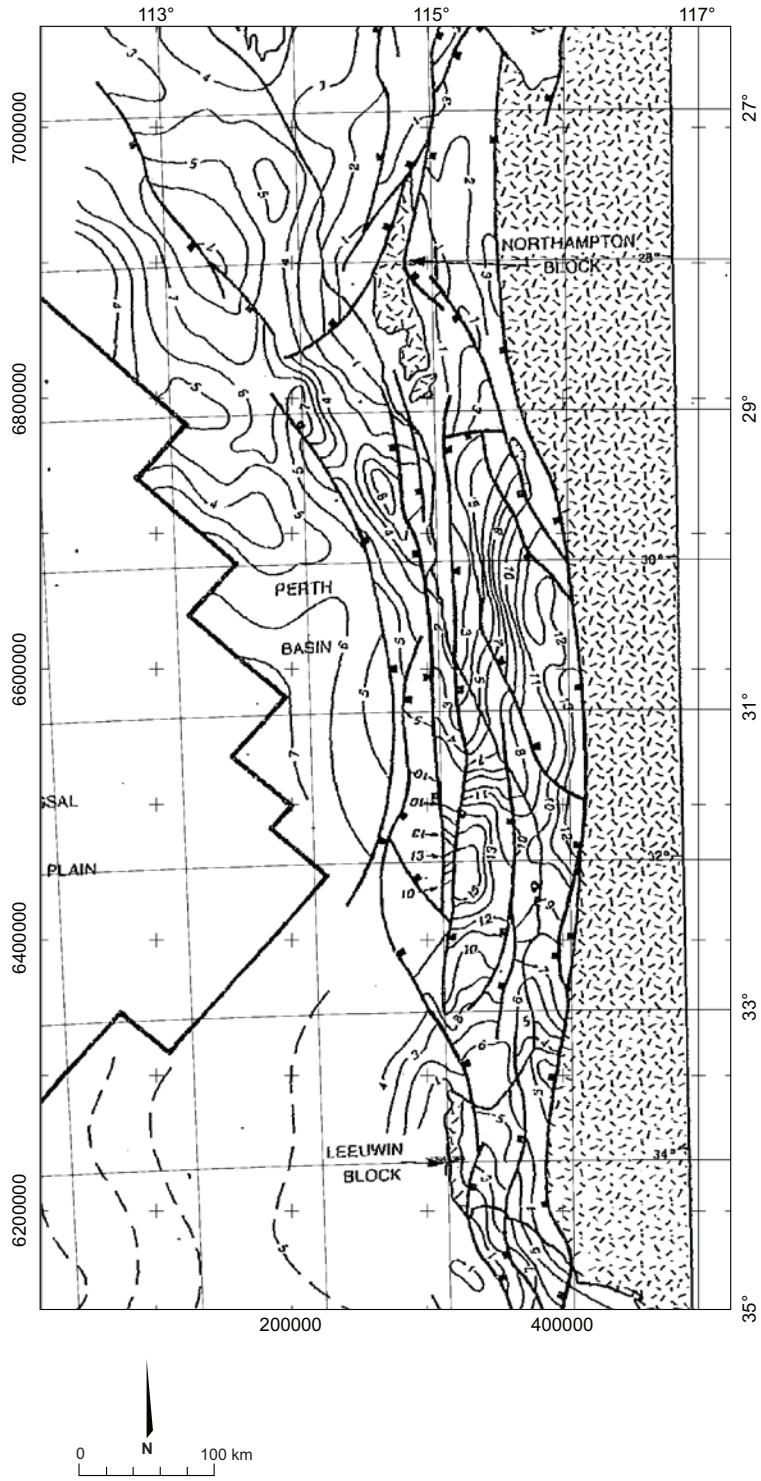

Figure 1.2: Distribution of major faults and depth to basement in the Perth Basin (after Cockbain, 1990).

1.2.2 Previous structural models of the Perth Basin

The western margin of the Australian Craton is shown by Cockbain (1990) and Myers and Hocking (1998) to comprise NW-SW and NW-SE trending jogs, where the NW-SE trending lineaments are transfer systems (Fig. 1.2). This general structural architecture was interpreted from 2D seismic data by Song and Cawood (2000). However, there are very few structures (n = 4 including the Harvey Ridge) in this orientation shown by Cockbain (1990). Other workers recognise several NW-SE trending transfer zones, such as the Cervantes and Abrolhos transfer zones. However, they are typically spaced at about 100 km, only ever inferred with no apparent fault traces to mark their existence, and do not have faults shown parallel with this orientation (with the exception of very few minor fault segments).

Several geological models have been constructed for parts of the Perth Basin in previous studies. Playford et al. (1976) compiled structural maps of the basement, Cattamarra Coal Measures, Yarragadee Formation, and Warnbro Group for the whole Perth Basin. Isopach maps for various Permian to Jurassic stratigraphic units in the north Perth Basin were developed by Playford et al. (1976) and subsequently refined by Mory and Iasky (1996). In the south Perth Basin, Iasky (1993) provided formation geometries of the base of the Warnbro Group, top of the Cattamarra Coal Measures (formerly called the Cockleshell Gully Formation), top of the Lesueur Sandstone, top of the Sue Coal Measures and the basement, all of which were interpreted from 2D seismic sections. In the north Perth Basin, isopach maps of the top Cattamarra Coal Measures, top Permian and top basement developed by Mory and Iasky (1996) were used to create a 3D geological model of the north Perth Basin (Geological Survey of Western Australia, 2011). Causebrook et al. (2006) provide formation geometries of the top of the Yarragadee Formation, the Neocomian Unconformity, top of Gage Formation, top of South Perth Shale and top of the Leederville Formation for the offshore part of the central Perth Basin. However, until this study, no 3D geological model for the entire stratigraphy of the whole Perth Basin has been published.

1.3 Approach / Analytical Technique

This study utilises digitised version of the 1957 aeromagnetic dataset released in 2010 by GA with 86 m x 86 m grid node spacing, which has been processed to as 'reduced to pole' and 'vertical gradient of reduced to pole' maps. A lower resolution (258 m x 258 m) dataset available from GA has also been incorporated because it extends further offshore and is useful for regional interpretation. Onshore and offshore gridded gravity data for the Perth Basin are available from the Geoscience Australia Geophysical Database using the Geophysical Archive Data Delivery System (GADDS) facility via www.ga.gov.au. The national onshore gravity coverage is on a grid with nominal 11 km x 11 km node spacing and has been supplemented in key areas by higher resolution surveys commissioned by the State Geological Surveys and the Northern Territory Geological Survey (NTGS). This infilling is an ongoing process with new surveys being commissioned. For further details on the National Gravity database, see Geoscience Australia website (www.ga.gov.au) and Wynn and Bachin (2009). Offshore gravity data have been computed from satellite altimetry data and are generally available at 1.5 km x 1.5 km spacing. (Sandwell and Smith, 2009). For Australia these data are available from GA as free-air gravity grids. Free-air gravity data are not corrected for bathymetry. In this study, Bouguer gravity has been computed from free-air gravity where accurate bathymetry data are available.

Digital elevation information was taken from Shuttle Radar Topographic Mission (SRTM) data from the US Space Shuttle program. These data are available at 90 m x 90 m spacing. The Isostatic Residual Gravity data for the offshore areas are produced by subtracting the predicted response for the varying seawater depth and the effects of mantle topography from the Free-air gravity data (e.g., Lockwood, 2004). Onshore the isostatic Residual Gravity data are produced by subtracting the effects of crust-mantle boundary topography from the Bouguer gravity. The two residual grids have been joined to form a composite offshore and onshore grid. The benefit of this composite dataset is that it can be used for computing depth to basement without production of artefacts generated from the

different corrections associated with onshore versus offshore datasets. A map of the first vertical gradient of the isostatic residual gravity has been computed to aid the identification of areas of shallower basement.

3D geological model of the Perth Basin

A 3D geological model was developed that covers the Perth Basin, with an extent of 680 km by 150 kilometres from approximately 28.5 to 34.5 ° South, and 113 to 116 ° East. Input data consisted of a range of publically available data, which includes previous interpretations of geological structure, geophysical datasets of the entire basin, and petroleum well data. The 3D geological modelling was done using the 3D modelling packages 3D Geomodeller (Calcagno et al., 2008) and SKUA (Jayr et al., 2008). These modelling packages use implicit definitions of the geological interfaces, which are defined as the iso-surfaces of one or several scalar fields in three-dimensional space. The scalar fields are obtained by interpolation, but several geological interfaces can be modelled at the same time, with data associated with a scalar field. This differs from 'explicit modelling', in which each object has an explicit definition.

Several datasets were used to construct the 3D geological model of the Perth Basin (Fig. 1.3). During the creation of a 3D geological model for the entire Perth Basin, several technical challenges were identified and overcome:

1. Due to the size of the domain and large quantity of input data, the model was built in three overlapping sections: South, Central and North Perth Basin. Each model overlaps by approximately one quarter of the adjacent domain because 3D Geomodeller utilises potential functions to interpolate all input data. This approach provides consistency between each model section, and reduces computation time.
2. The Perth Basin is highly faulted, and different degrees of complexity reflect the inherent variability in the quality/resolution of input data to some extent. While capturing such structural complexity in a 3D geological model is important, it was necessary to simplify the model to generate consistency across the basin and to make the model computationally feasible. Therefore, a simplified fault network was developed for the whole Perth Basin which identified only the major faults that contribute to the architecture of the basin. These faults were identified from previous studies, significant anomalies and gradients in regional gravity and aeromagnetic data, and offsets in basement structure contours.
3. Formation names differ across the latitude range of the Perth Basin, which has resulted in different stratigraphic columns for the North Perth Basin (Mory and Iasky 1996) and Central/South Perth Basin (Crostella and Backhouse 2000). These two stratigraphic columns have not been reconciled because of the lack of adequate data in the Central Perth Basin. For this study, the correlation suggested by Crostella and Backhouse (2000) was adapted for the whole Perth Basin.
4. Variations in the spatial density of stratigraphic input data across the basin represents a significant issue. In the North Perth Basin, where petroleum exploration and exploitation is important, petroleum wells, seismic data and geological studies are available (e.g., Mory and

Iasky 1996). Although the South Perth Basin also has petroleum wells and geological studies (e.g., Iasky 1993, Crostella and Backhouse 2000), the density of data is less than for the North Perth Basin. Data is comparatively scarce In the Central Perth Basin, especially onshore. Models for the Southern and Northern Perth Basin were developed first, and then the overlapping domains were used as extra constraints for the Central Perth Basin model.

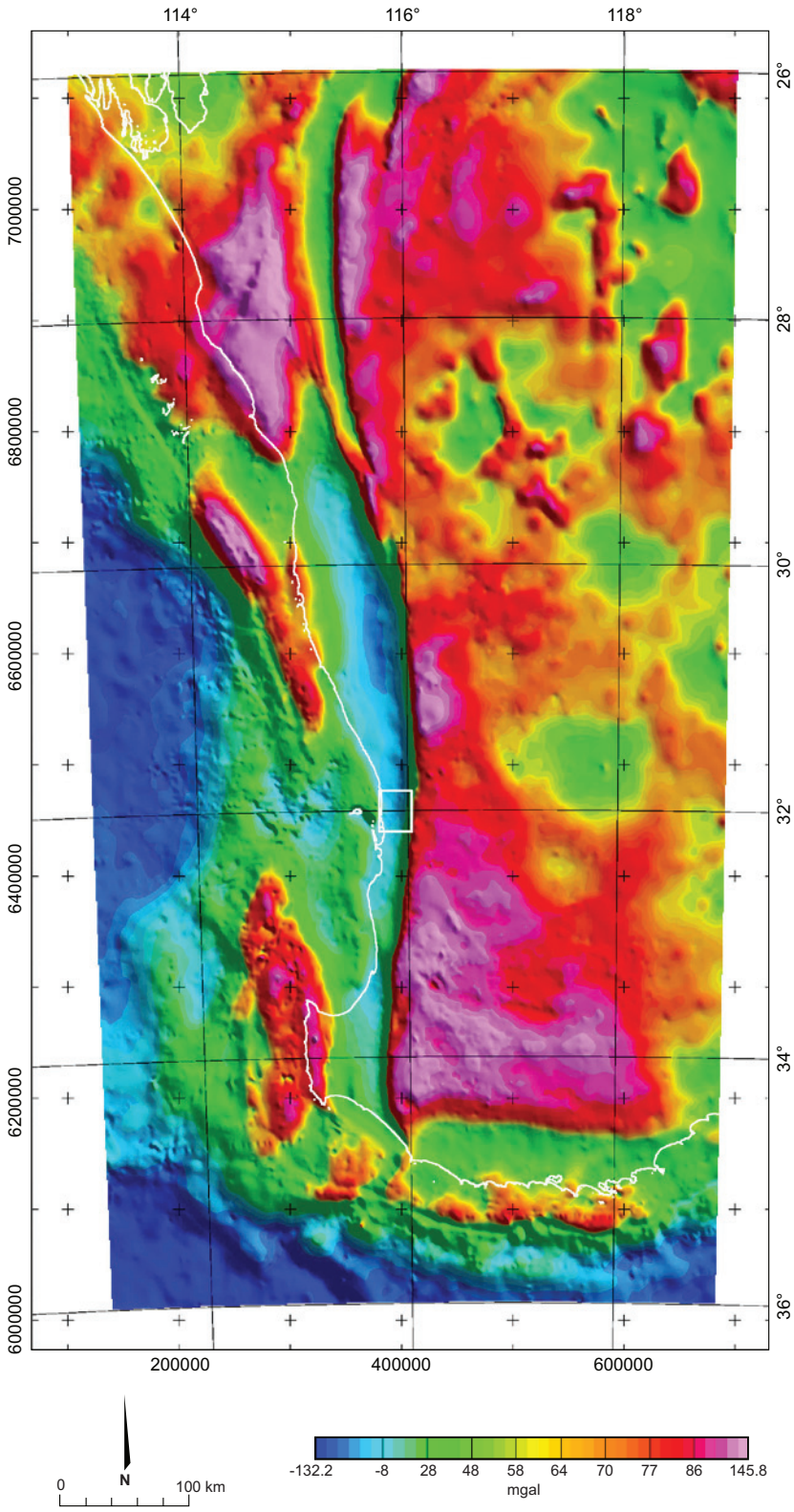

Figure 1.3: An Isostatic Residual gravity anomaly map for the Perth Basin (after Lockwood, 2004). The gridded data for this image has been windowed and converted from geographical coordinates to GDA 94 metric coordinates from the WA State grid produced by Lockwood (2004). Data units are mgals. The position of the present day coastline is indicated by the white line. Location of the Perth metropolitan area is shown by a white box.

The simplified fault network was developed using existing structural studies done with seismic data (Iasky 1993, Mory and Iasky 1996, Bale 2004, DMP 1995). It was then further simplified by selecting faults that show the greatest response in regional geophysical datasets available for the entire basin, and modelled in SKUA. During the modelling stage, the fault network also had to be modified to fit the well data. Three sub-domains in the model were developed from structure contour maps of stratigraphic surfaces interpolated from seismic sections and well data from three detailed reports (i.e., Iasky 1993, Mory and Iasky 1996, Bale 2004). All of these studies involved interpretation of multiple and interconnecting 2D seismic lines and resulted in internally consistent stratigraphic and structural architecture. Incorporation of these data involved simplification of the geometry by the removal of small-scale faults and manual smoothing of the stratigraphic surfaces in the vicinity of these faults. The model involves some simplification of the geometry of some of the large-displacement faults and/or fault systems into simple surfaces. Faults were assigned dips based on seismic interpretations where possible. Where no dip constraints exist, faults were given an arbitrary constant dip of 70° in the downthrown direction assuming normal net displacement.

Stratigraphic data from petroleum wells were extracted from the Department of Mines and Petroleum (DMP) well analysis data spreadsheet of the Perth Basin, available on their online system WAPIMS (https://wapims.doir.wa.gov.au). Only data from petroleum wells for which DMP had double-checked formation picks were incorporated in the models. Other wells were discarded, except in areas with really sparse data. In these cases, stratigraphic picks were re-assessed by WAGCoE researchers and treated with less confidence than DMP-checked wells. Formation picks from hydrogeological wells were used, where relevant. In areas of very sparse coverage like the southern and central Perth Basin, and offshore, almost all well data were utilised. Interpolation of stratigraphic boundary data between seismic report data relied on the well data.

The stratigraphic column was simplified to 15 subdivisions, and time-equivalent formations from across the Perth Basin with similar petrophysical characteristics were amalgamated (Fig. 1.4). The stratigraphic assignments of the well constraints were updated prior to incorporation into SKUA and Geomodeller. The 'depth to basement' map of DMP (1995) was used, and modified at the incorporation of the simplified fault network. Several detailed models of parts of the Perth Basin were used to constrain depths to stratigraphic surfaces in sub-domains of the model. In the northern Perth Basin model, additional constraints from GSWA (2011) were utilised to better constrain the architecture of the Dandaragan Trough. In the southern Perth Basin model, seismic interpretation of Iasky (1993) was modified to fit the well data and our fault network. In the central Perth Basin, data and interpretations from Causebrook et al. (2006) were used to better constrain the offshore part of the basin. The DMP 'depth to basement' maps are consistent with the detailed sub-models used. Finally, after residual misfit between the model surfaces and well data was assessed as satisfactory using SKUA, the three sections were merged into one single model. Little attention was given to the offshore part of the Perth Basin, which is poorly constrained in the final 3D model, because the primary focus of this study was for geothermal exploration in the onshore Perth Basin.

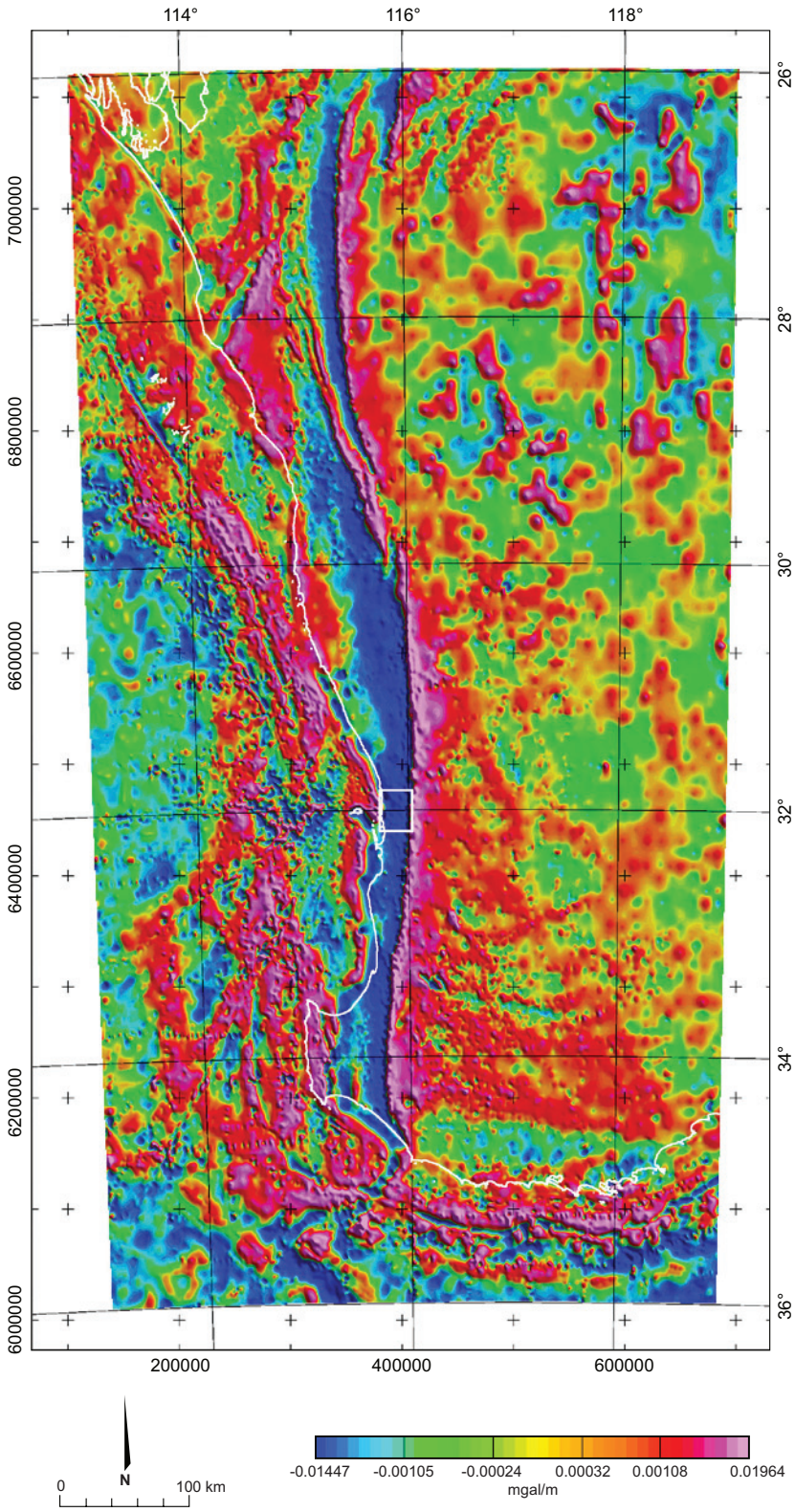

Figure 1.4: Vertical gradient of the isostatic residual gravity anomaly for the Perth Basin shown in Fig. 9. Data units are mgals / m. The position of the present day coastline is indicated by the white line. Location of the Perth metropolitan area is shown by a white box.

1.4 Results

1.4.1 New regional gravity and aeromagnetic images of the Perth Basin

Reprocessed gravity and aeromagnetic maps of the whole Perth Basin are shown in Figs 1.5 to 1.9. For the onshore Perth Basin, the most prominent features in the combined Bouguer/Free Air gravity image are the gravity low domains of the Bunbury Trough and Dandaragan Trough, separated by the Harvey Ridge. The Vasse Shelf, Beagle Ridge, Dongara Saddle, and Irwin and Coolcalalaya Sub-Basins are domains of relatively high gravity. The Perth Canyon forms a gravity low domain that meanders offshore westwards from west of Rottnest Island. The isostatic residual gravity image shows similar prominent features (Fig. 1.5). However, several features become more apparent. The NW-SE trending Turtle Dove and Mullingarra Ridges are clearly defined and bound by steep gravity gradients with strongly linear trends. The isostatic residual gravity image shows an approximately north-south trending gravity-high ridge extending from Bunbury latitudes to Rottnest Island that separates the Dandaragan and Bunbury Troughs in the East from the Vlaming Sub-basin to the West. South of Bunbury, this ridge swings in trend to NE-SW (Fig. 1.6). This ridge is best seen on the first vertical gradient of isostatic residual gravity image (Fig. 1.6). There are two domains with very low isostatic residual gravity response in the Dandaragan Trough (Fig. 1.6). The Harvey Ridge and Vasse Shelf are both visible in Figure 1.6.

The regional Perth Basin aeromagnetic map shows a broad, linear positive anomaly in the position of the Bunbury Trough, extending northwards and offshore into the Vlaming Sub-basin (Fig. 1.7). Another broad, positive anomaly occurs south of Perth along strike with the Dandaragan Trough, and seems to be associated with a positive anomaly in the adjacent basement rocks (Archaean Logue Brook and Pinjarra Granites) of the Yilgarn Craton (Fig. 1.7). The outcrop trace of the Bunbury Basalt can be seen clearly on the aeromagnetic image and runs from Bunbury to the south coast.

1.4.2 A new structural interpretation of the Perth Basin

Most basin subdivisions and basin-hosted faults interpreted by Playford et al. (1976) and Cockbain (1990) are coincident with high gradients in the gravity images (Figs 1.1, 1.2, 1.5, 1.6). Exceptions to this are the northern continuation of the Dunsborough Fault north from about 34° S and an unnamed fault that defines the eastern margin of the Vlaming Sub-Basin. Several new linear features have been interpreted from the vertical gradient of isostatic residual gravity image (Fig. 1.8). These are in similar range of orientations to faults identified in previous studies (Playford et al., 1976; Cockbain, 1990). They commonly define the margins of gravity highs, and in some cases are strike extensions of known faults (e.g., the Urella Fault). A set of NW-SE trending faults in the southwest corner of the Yilgarn craton shown by Myers (1990) are expressed in the gravity and aeromagnetic data, and, if extended to the Yilgarn margin, would explain the truncations, jogs and offsets in the boundaries of geological units (e.g., the Logue Brook Granite) of Wilde (1990). If the NW-SE-trending Boyup Brook and Tenterden Faults extend into the Perth Basin, as is highly likely, then they would form the bounding faults of the Harvey Ridge (Fig. 1.8). It is highly probable that other faults previously identified on the Yilgarn Craton in outcrop or via gravity and/or aeromagnetic anomalies also extend into the Perth Basin and visa versa, although this has not been previously recognised.

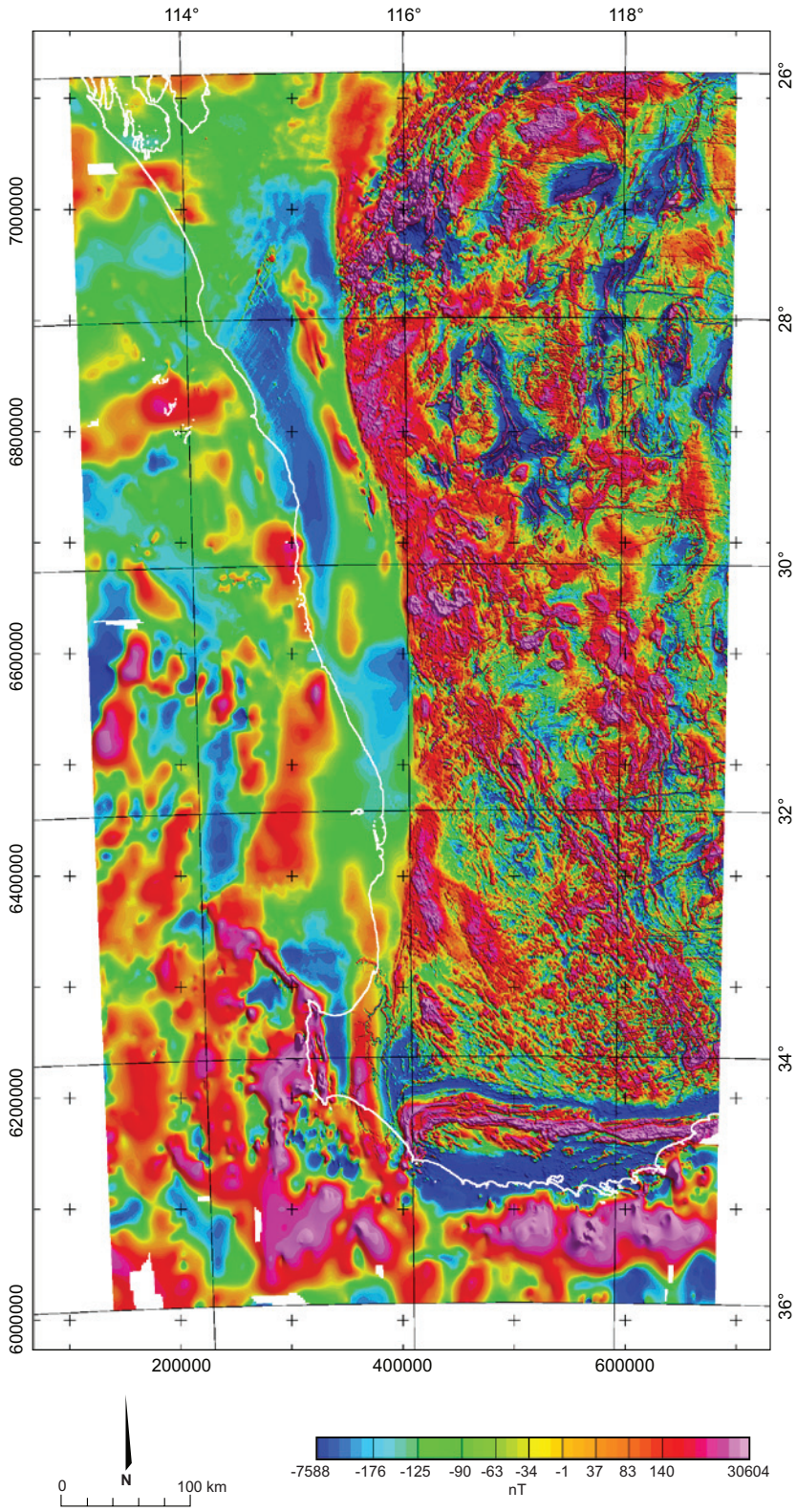

Figure 1.5: Reduced to pole aeromagnetic anomaly map for the Perth Basin. 258 m gridded data sourced from Geoscience Australia. Grid datum is GDA 94. The position of the present day coastline is indicated by the white line.

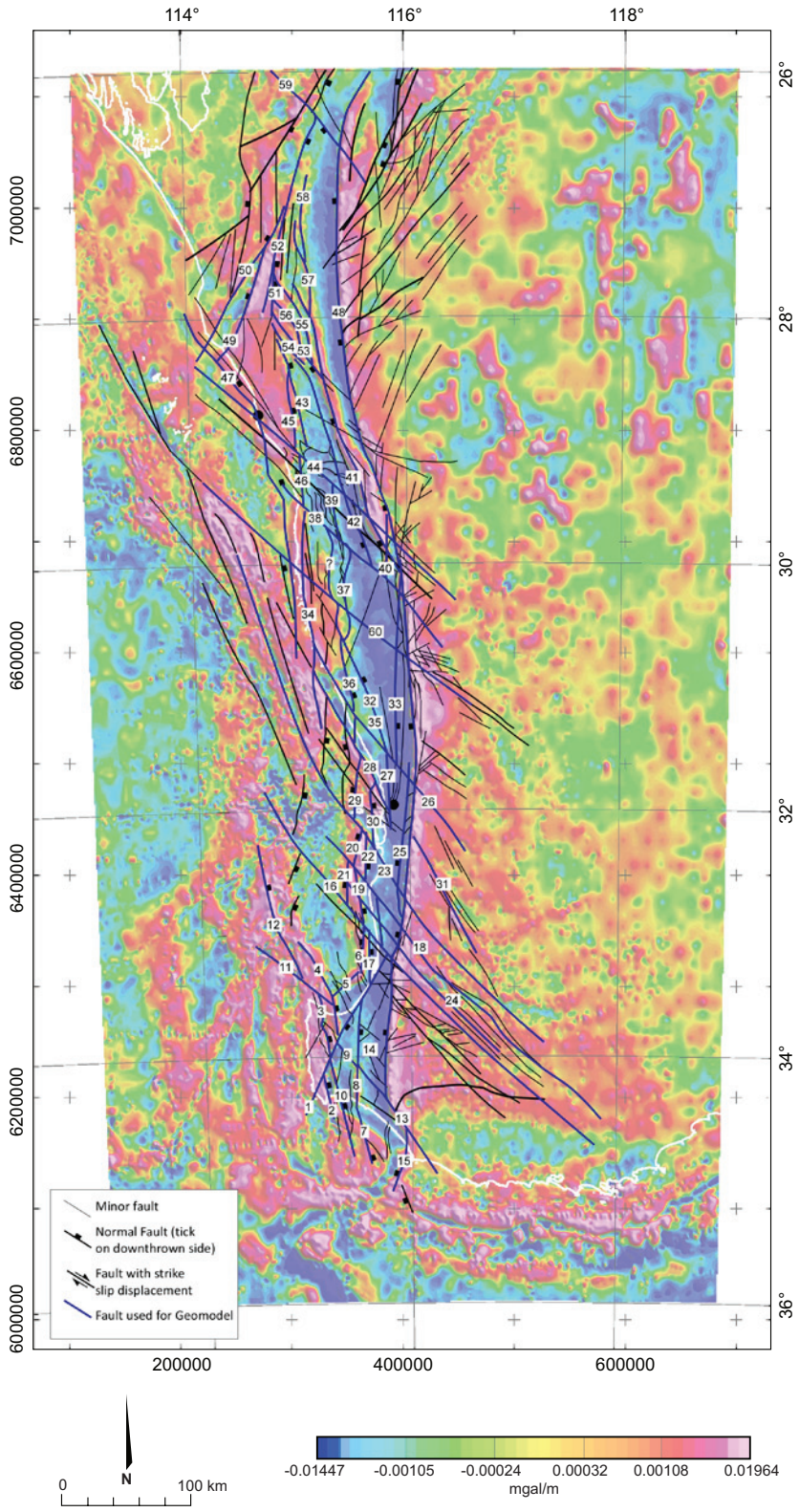

Figure 1.6: Isostatic residual gravity anomaly map for the Perth Basin showing a new interpretation of faults. See Wilkes et al. (2011) for a description of the criteria used to identify the numbered faults.

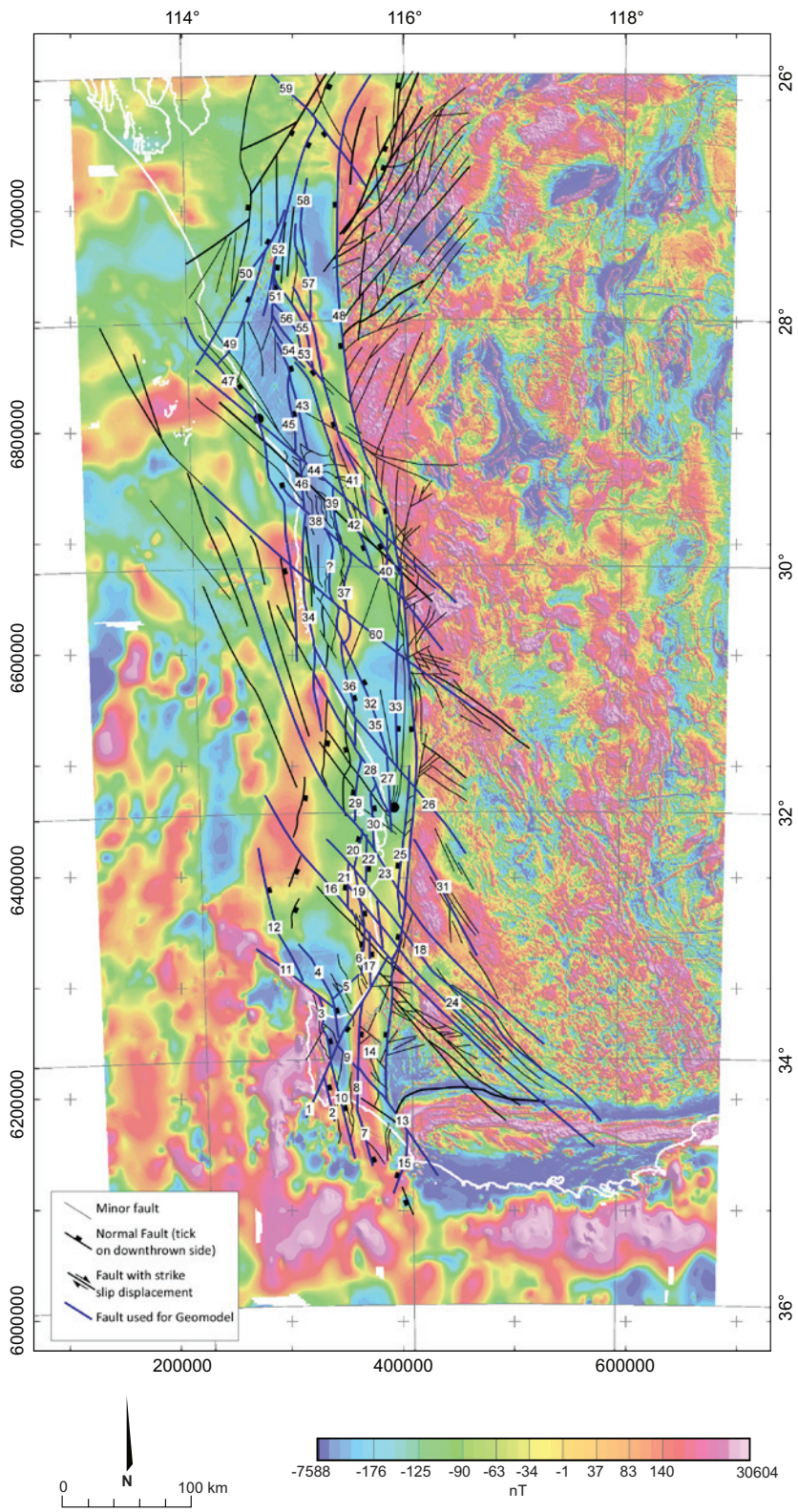

Figure 1.7: Reduced to pole aeromagnetic image for the Perth Basin showing a new interpretation of faults. See Wilkes et al. (2011) for a description of the criteria used to identify the numbered faults.

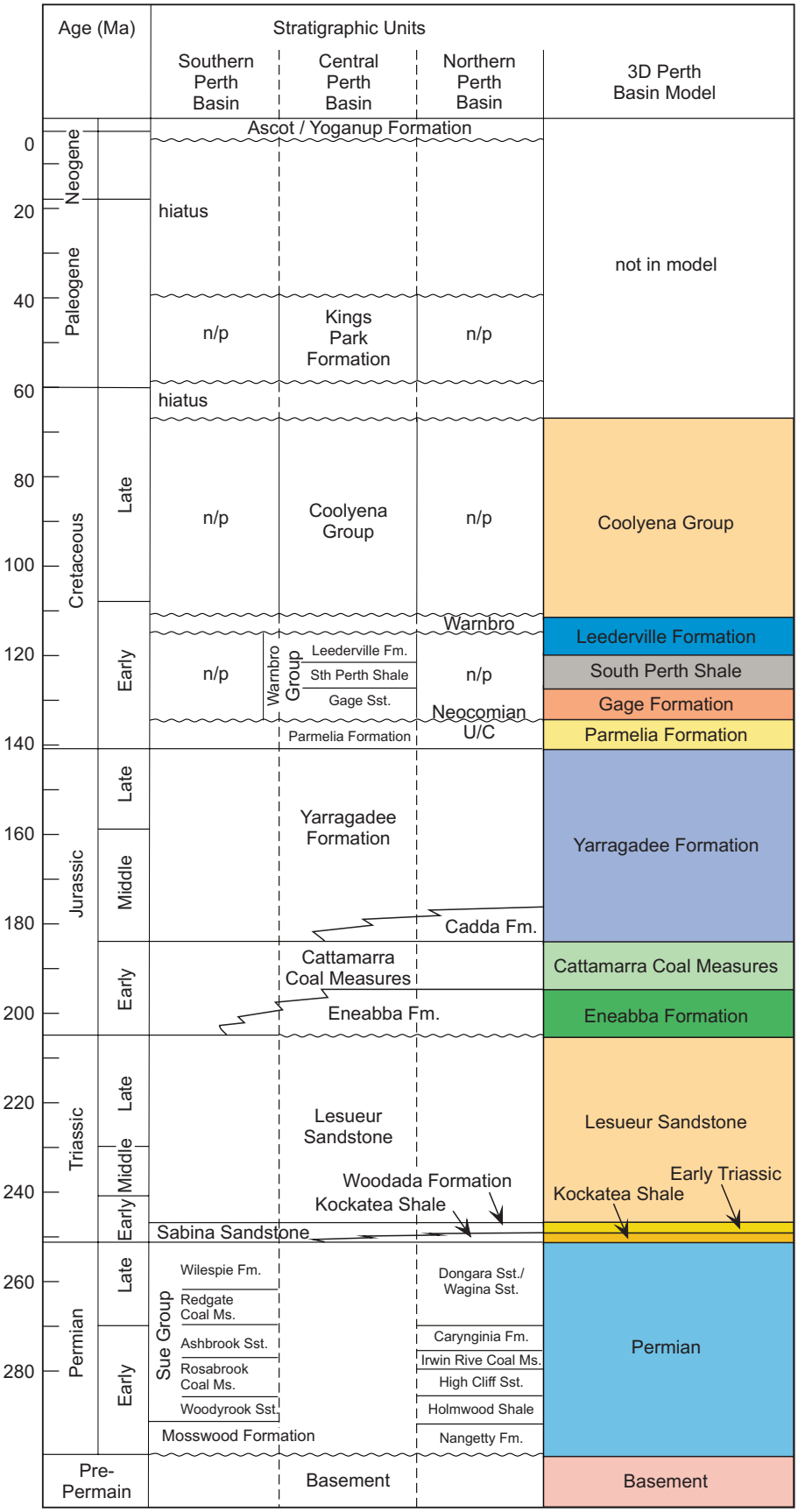

Figure 1.8: Stratigraphic column of the Perth Basin showing how units in different parts of the Perth Basin correlate with the simplified stratigraphic succession used for the 3D model.

Faults in the Perth Basin have variable magnetic signatures. Faults that coincide with locally elevated magnetic response include segments of the Urella and Beagle Faults, the intersection of unnamed faults in the Dandaragan Trough at about 30.5° S, The Serpentine Fault and a fault along the axis of the Dunsborough Trough (Fig. 1.9). These positive anomalies could be due to either relatively shallow, highly magnetic basement rocks (e.g., the Serpentine Fault), or localised Fe-rich alteration associated with fluid flow along faults. The aeromagnetic data in other areas yields little extra information about the subsurface architecture of the onshore Perth Basin.

A new interpretation of the faults of the Perth Basin consistent with linear strong gradients in gravity and aeromagnetic data is presented (Figs 1.8 to 1.9). Key faults within the Perth basin have been numbered, and criteria used for their identification are given in Wilkes et al. (2011). This new interpretation builds on previous interpretations. The main differences between the new fault network and previous interpretations are:

- Identification of NW-SE trending fault systems that link faults in the Yilgarn craton with 'transfer zones' inferred by previous workers. These displace other fault sets in the Perth Basin;
- New faults identified in areas previously with sparse faults (e.g., from Cervantes to Bunbury);
- New faults identified as part of the Urella Fault system;
- Key cross-cutting faults in the Bunbury Trough;
- New faults systems identified on the Yilgarn craton.

Results from the 3D model of the whole Perth Basin are shown in Figures 1.10 to 1.14

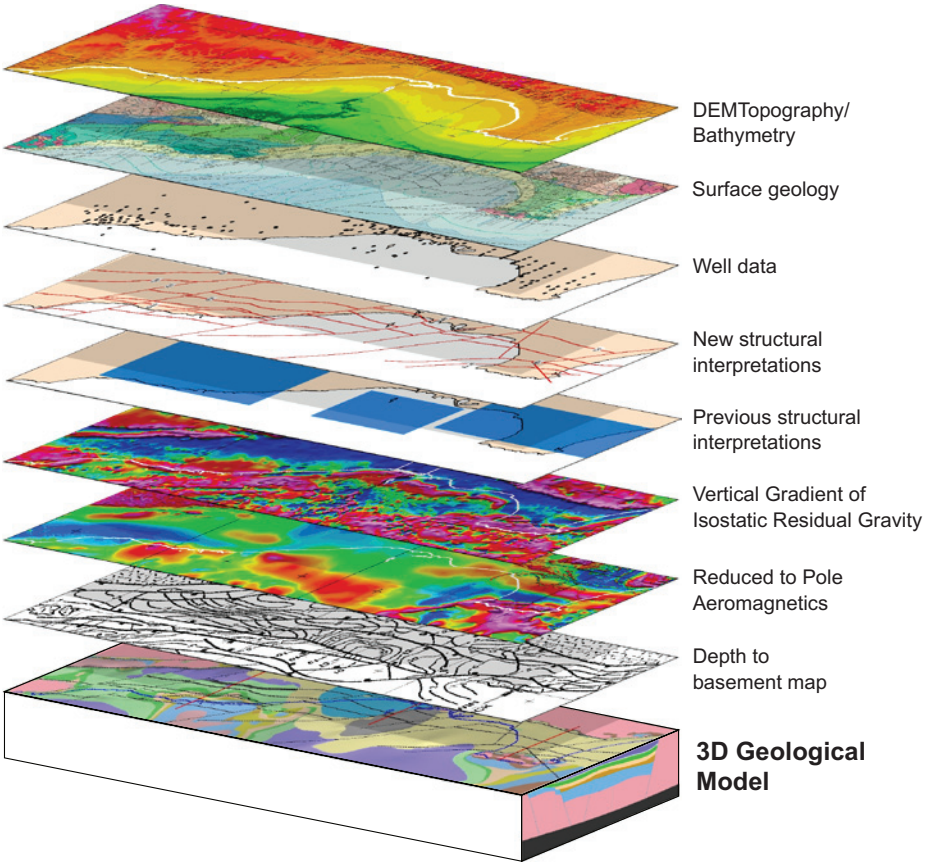

Figure 1.9: A diagram to show the variety of datasets used to construct the 3D model of the Perth Basin.

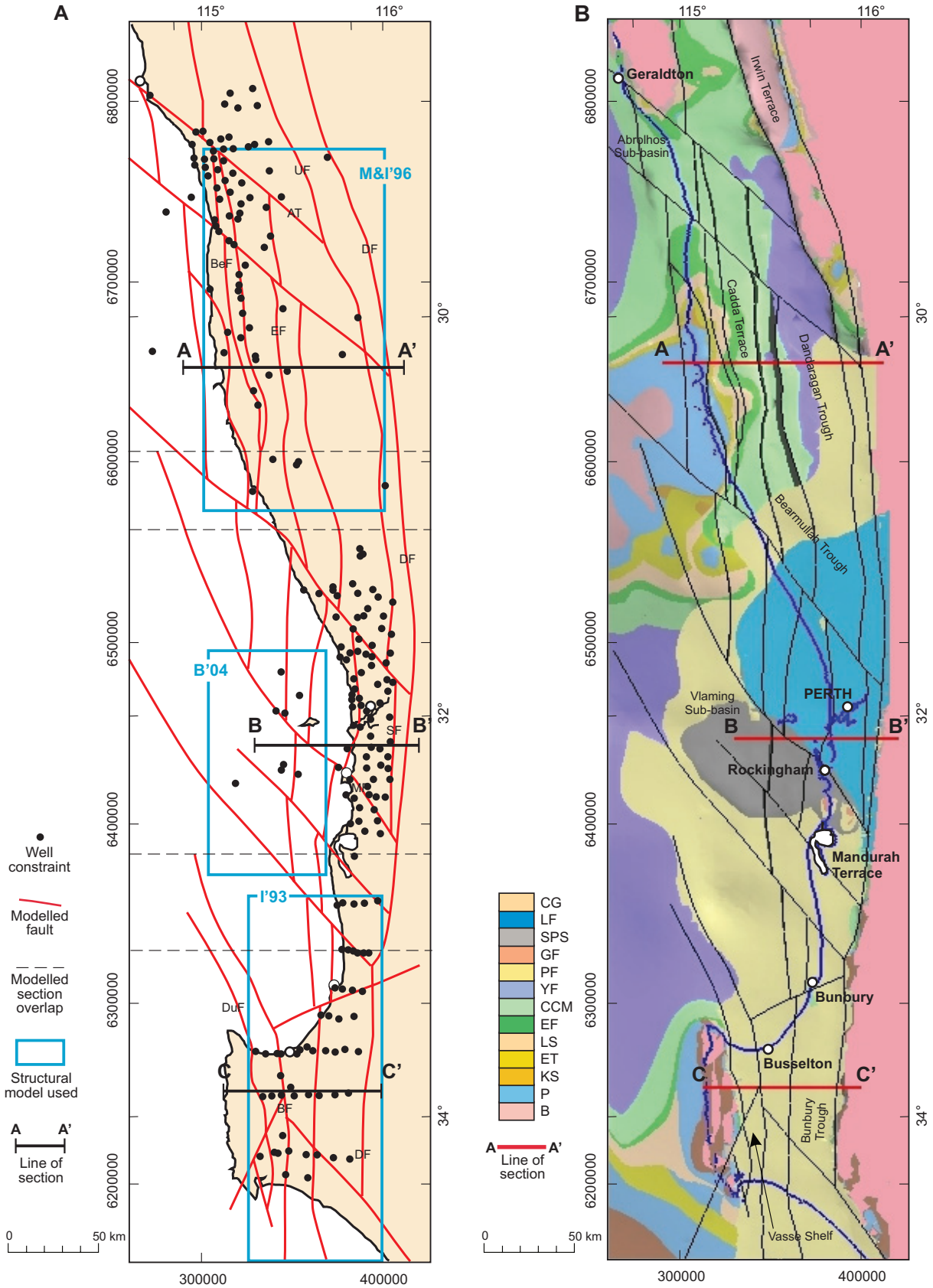
A
115°
116°
6800000
6700000
6600000
6500000
6400000
6300000
6200000
30°
32°
34°
M&I'96
B'04
I'93
UF
AT
BeF
EF
DF
SF
DuF
BF
A
A'
B
B'
C
C'
Well constraint
Modelled fault
Modelled section overlap
Structural model used
Line of section
0
50 km
300000
400000
B
Geraldton
Irwin Terrace
Abrolhos Sub-basin
Cadda Terrace
Dandaragan Trough
Bearmullah Trough
Vlaming Sub-basin
PERTH
Rockingham
Mandurah Terrace
Bunbury
Busselton
Bunbury Trough
Vasse Shelf
CG
LF
SPS
GF
PF
YF
CCM
EF
LS
ET
KS
P
B

Figure 1.10: Previous page,
(a) Map to show the extent of the 3D model of the Perth Basin, various data constraints and the simplified fault network. The boundaries of the three sub-models are shown. The northern Perth Basin model overlaps the central Perth Basin model by 43 km and the southern Perth Basin model overlaps the central Perth Basin model by 53 km. Structural models used(blue rectangles) are M&I'96 = Mory and Isaky (1996); B'04 = Bale (2004); and I'93 = Iasky (1993). The locations of all wells used to constrain the model are shown. Fault traces have been projected to present day surface. AT = Abrolhos Transfer; BF = Busselton Fault; BeF = Beagle Fault; DF = Darling Fault; DuF = Dunsborough Fault; EF = Eneabba Fault; MF = Mandurah Fault; SF = Serpentine Fault; UF = Urella Fault.
(b) A map of the top of the 3D model showing the sub-crop immediately beneath the Cenozoic stratigraphy. CG = Coolyena Group; LF = Leederville Formation; SPS = South Perth Shale; GF = Gage Formation; PF = Parmelia Formation; YF = Yarragadee Formation; CCM = Cattamarra Coal Measures; EF = Eneabba Formation; LS = Lesueur Sandstone; ET = Early Triassic; KS = Kockatea Shale; P = Permian (undifferentiated); B = basement.

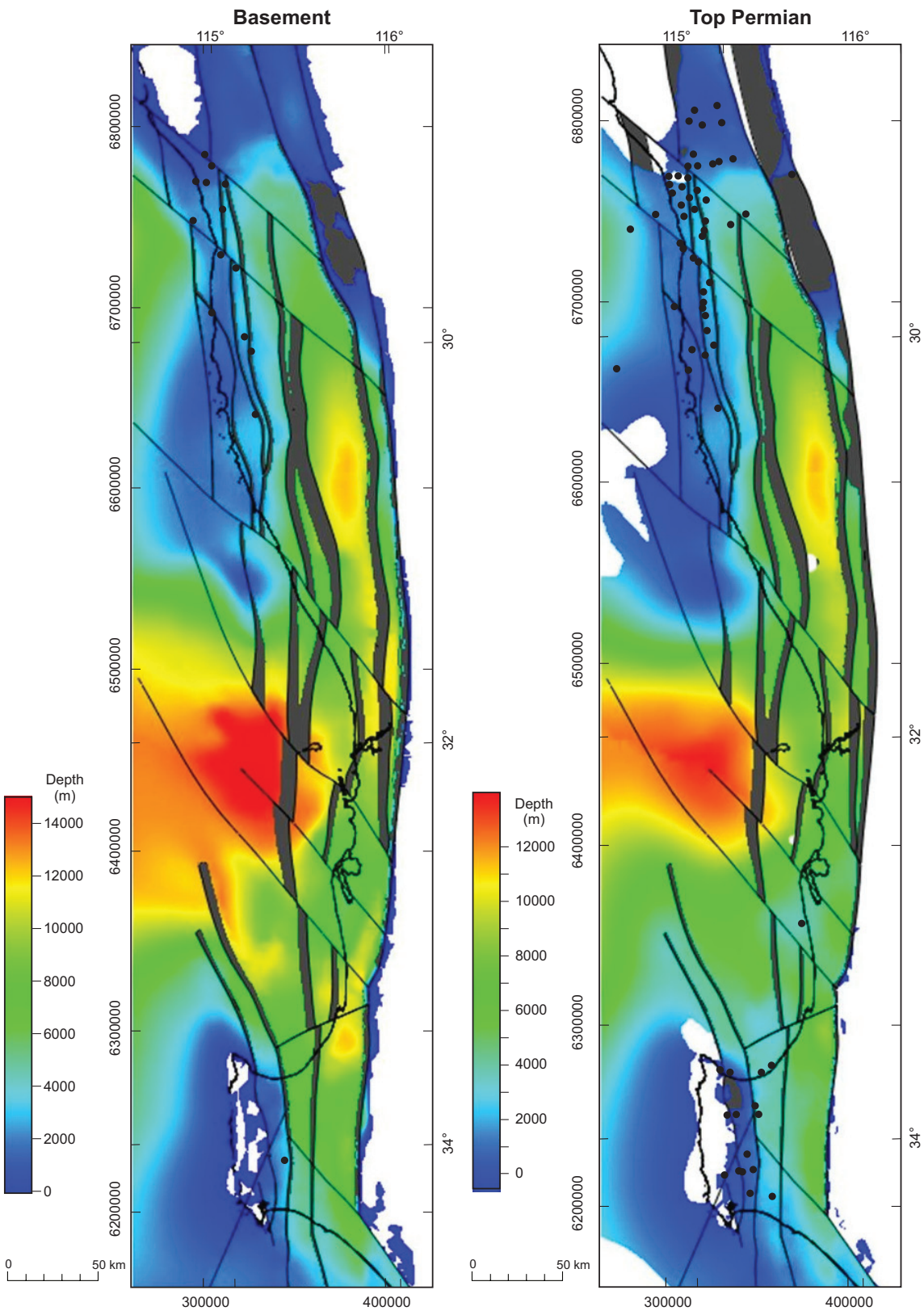

Figure 1.11: Structure maps generated from the 3D model, contoured for the depth to basement (left) and top Permian (right). The locations of wells that help constrain the surfaces are shown.

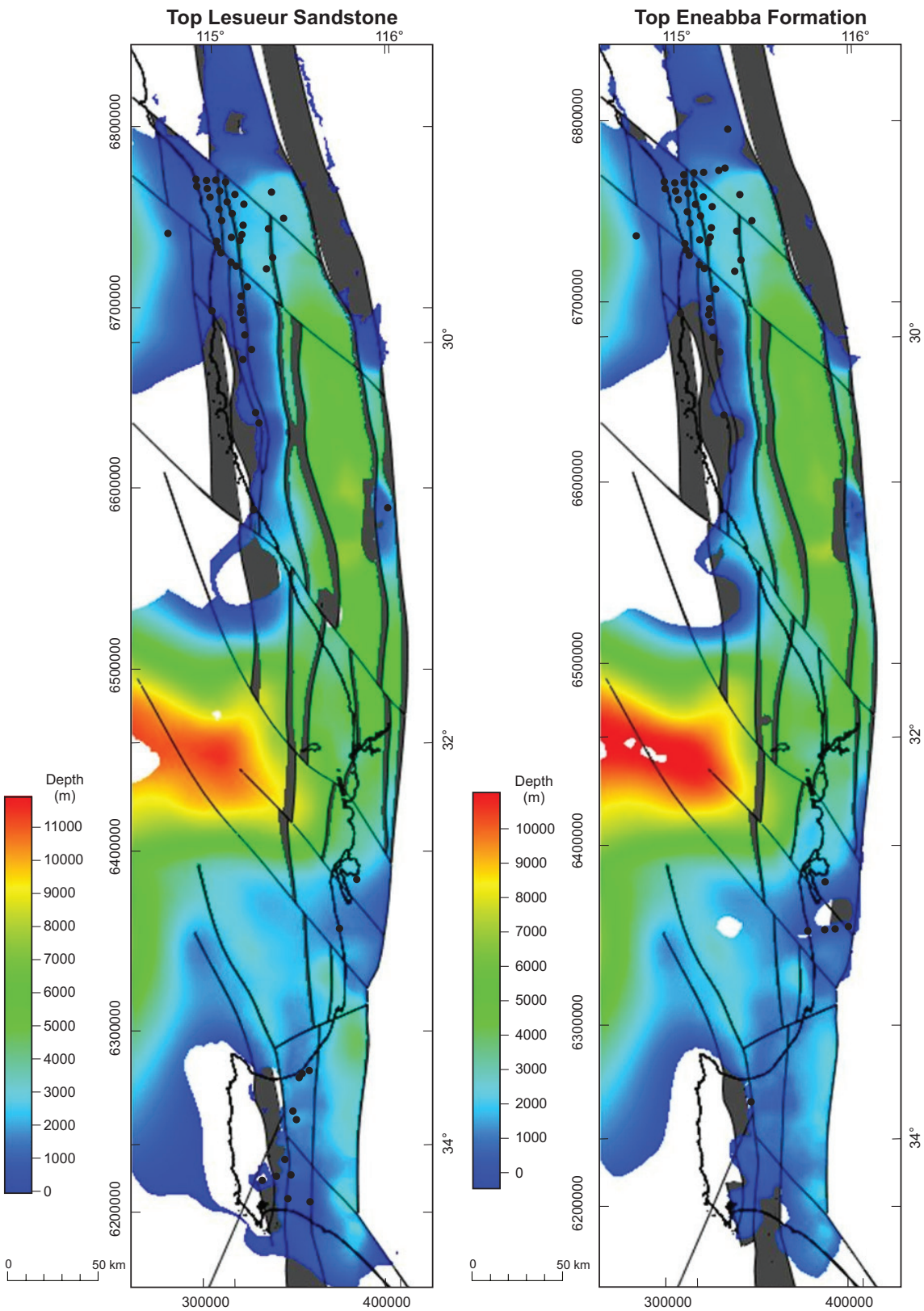

Figure 1.12: Structure maps generated from the 3D model, contoured for the depth to the top of the Lesueur Sandstone (left) and top of the Eneabba Formation (right). The locations of wells that help constrain the surfaces are shown.

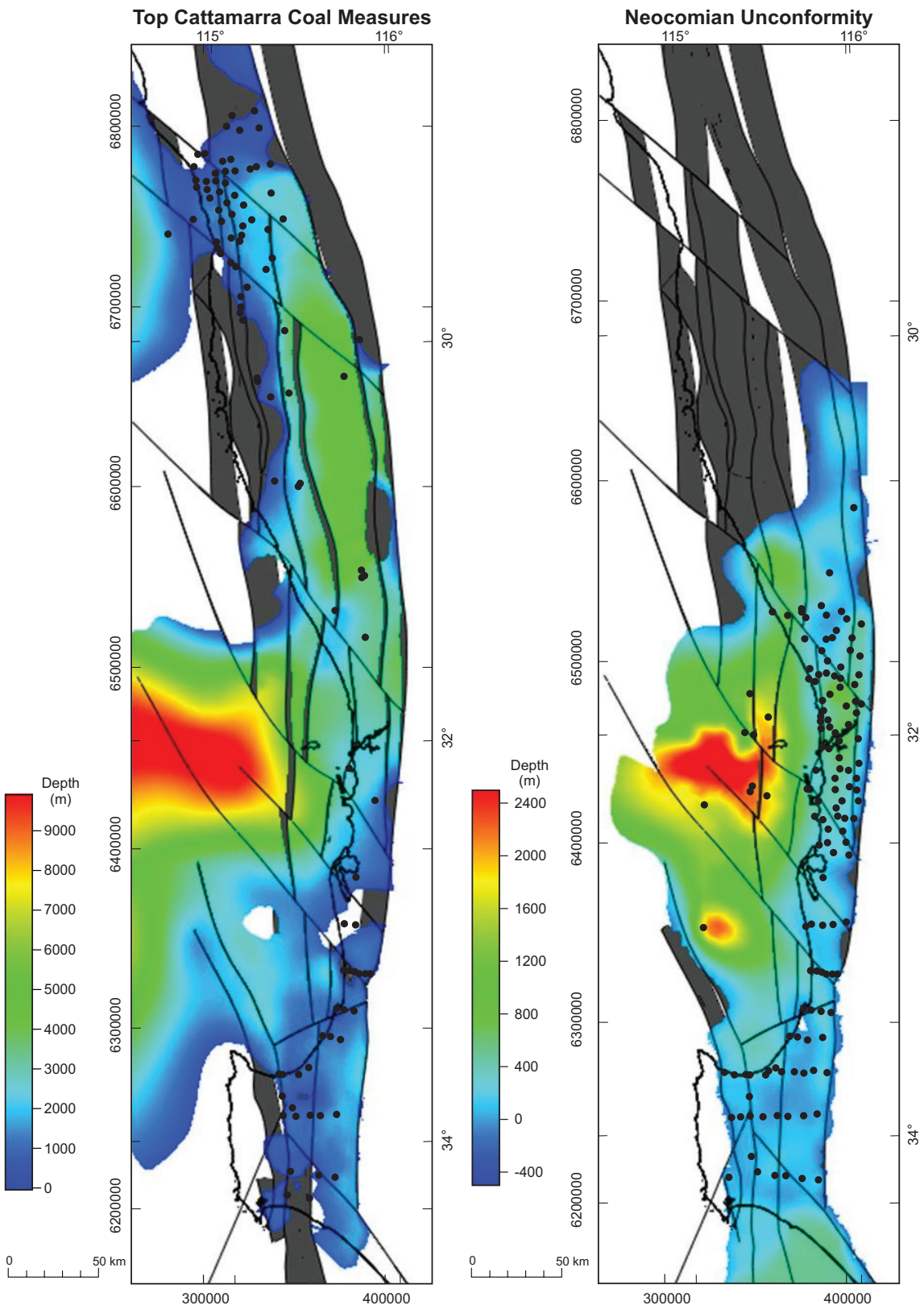

Figure 1.13: Structure maps generated from the 3D model, contoured for the depth to the top of the Cattamarra Coal Measures(left) and the Neocomian Unconformity (right). The locations of wells that help constrain the surfaces are shown.

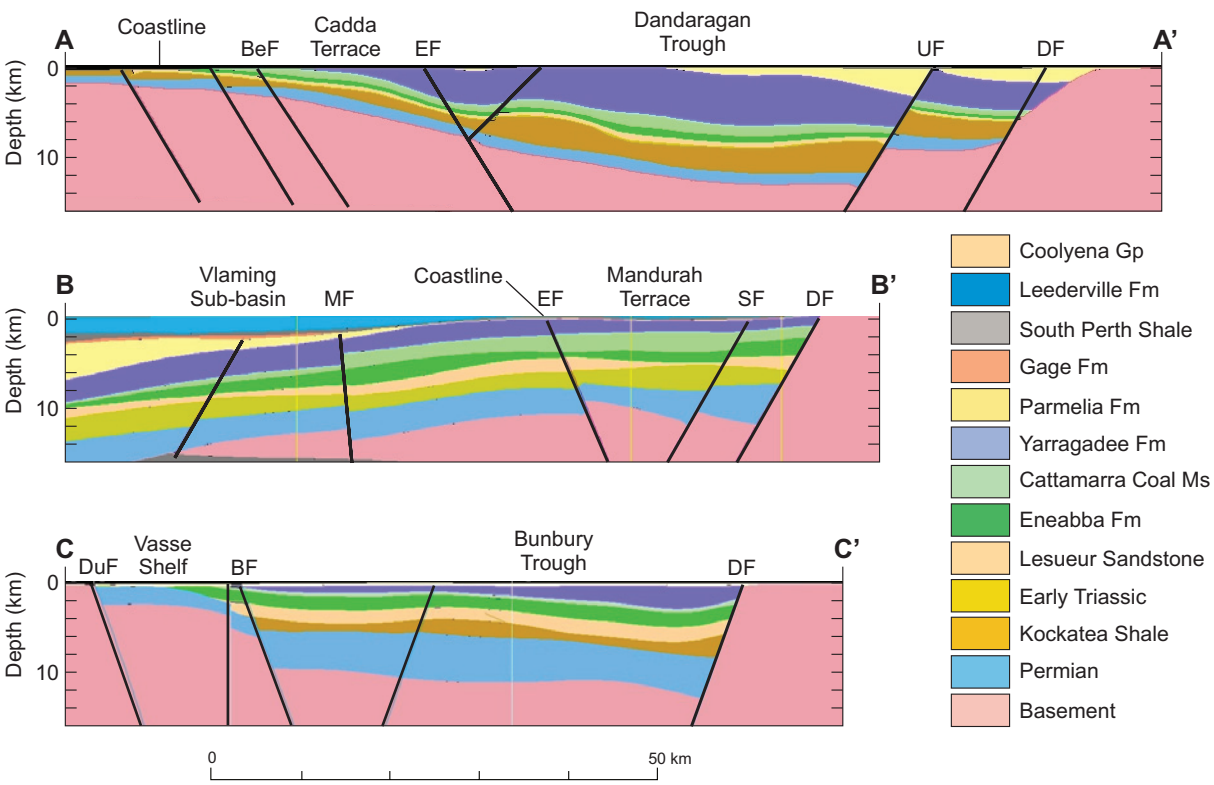

Figure 1.14: Cross sections generated from the 3D model of the Perth Basin. Sections are oriented E-W, viewing direction is northwards. The location of section lines are shown on Fig. 1.10. A-A' = northern Perth Basin; B-B' = central Perth Basin; C-C' = southern Perth Basin. BF = Busselton Fault; BeF = Beagle Fault; DF = Darling Fault; DuF = Dunsborough Fault; EF = Eneabba Fault; MF = Mandurah Fault; SF = Serpentine Fault; UF = Urella Fault.

1.5 Discussion

1.5.1 The geological significance of the new 3D model of the Perth Basin

The new 3D geological model reveals the following key points

- Dandaragan Trough is the most significant structure in the northern Perth Basin, affecting all stratigraphy to the basement. In the southern Perth Basin, the Bunbury Trough is much more asymmetric with deepest part adjacent to the Darling Fault.
- NW-SE trending faults have a significant effect on all stratigraphic units, including the basement and Neocomian unconformity. Major deflections in the stratigraphic surfaces indicate that several more NW-SE faults exist but are not modelled, especially between Perth and Geraldton.
- There is significant topography on the Neocomian unconformity, which must be affected by locally differential syn to post-Neocomian subsidence, most probably accommodated by faults.
- In the onshore central Perth Basin near Harvey/Pinjarra area, Neocomian erosion incised through the Yarragadee Formation, Cattamarra Coal Measures and even the top Eneabba Formation.
- The deepest part of the Neocomian unconformity is in the domain west of Rottnest Island. This is potentially a deeply incised palaeochannel, possibly bound/influenced by faults. It is south

of the present day Perth Canyon. Well constraints below the Neocomian unconformity in this region are absent, and so it is not clear whether the downward warping of deeper stratigraphic layers is an artefact of model interpolation or real. The thick succession in this part of the model is not consistent with the results of gravity inversions, which indicates the presence of a basement high (so-called South Turtle Dove Ridge of Lockwood (2004) and Wilkes et al. (2011)).

- Post-Neocomian stratigraphy is confined to the southern and central Perth Basin, probably due to uplift/erosion in the northern Perth Basin.
- Leeuwin, Mullingarra and Northampton blocks are surrounded by concentric zones of outwardly younging stratigraphy, indicative of progressive erosion of uplifted domains.

1.5.2 Implications of the new structural interpretation for geothermal exploration

Improved processing of the gravity and aeromagnetic data has led to refinement of the interpretation of major structures in the Perth Basin that primarily involves the identification of new faults and fault segment extensions. Some of these faults link with faults recognised in the Pilbara and Yilgarn. The implications for geothermal exploration depend entirely on the modern day permeability properties of the stratigraphic units and faults. This is covered in more detail in Sections 4 to 7 of this report and in Reid et al. (2012).

1.5.3 Implications of the new 3D model for geothermal exploration

This study represents the first 3D model of the entire Perth Basin. Currently, the only other publically available 3D model is of the North Perth Basin model (GSWA 2011). Our model uses a range of the most up-to-date, publically available data. The model builds on previous published work, e.g., Playford et al (1976), Song and Cawood (2000), Crostella and Backhouse (2000), Mory and Iasky (1996) and Iasky (1993). The principal advantages of our 3D model are that it incorporates the most up-to-date well data, particularly in the vicinity of Perth, and that it integrates onshore and offshore geophysical data to encompass the entire Perth Basin, which permits basin-wide numerical simulations. This 3D geological model was used by Reid et al. (2012) to model conductive temperatures of the entire Perth Basin. The simulated temperature field provides a picture of large-scale temperature variations in the Perth Basin, which may be used to identify potentially attractive locations of geothermal resources.

1.5.4 Limitations of the new 3D model

The new 3D geological was designed to perform basin-scale hydrothermal modelling (see Reid et al. 2012). Therefore, it is important to keep in mind that the intention of the modelling is that it captures the broad geometry of the Perth Basin, inherently involves structural and stratigraphic simplifications and as such is not suitable for smaller scale simulations / investigations. The main limitations of the model are as follows:

1. In areas where faults have been interpreted but there are no seismic surveys or petroleum wells to constrain their displacement, an interpretation of small fault throws and dipping strata has been assigned instead of large fault throws to maintain horizontal stratigraphy.

It is acknowledged that the converse is also feasible. Nevertheless, the particular choice of interpretation does not change bulk, basin-scale geometry of the stratigraphic units significantly. However, the implications of the choice of interpretation must be understood. The geothermal transport properties of any structural model (e.g., geofluid flow) greatly depend on the physical properties and sealing capacity of faults of all scales.

2. Geometric uncertainties were not explicitly quantified for the 3D geological model. The quantity and quality of data constraints vary significantly in three dimensions across the modelled area. The positions of well constraints for each stratigraphic surface (Figs 1.11 to 1.13) provide a qualitative assessment of geometric uncertainty. Furthermore, the parts of the model developed from three previous studies could be considered internally consistent. However, there are significant domains in the model where well and/or seismic constraints are scarce or absent. In these domains, the quality of the model is highly reliant on the structural interpretation from potential fields data and the surface interpolation algorithm of the modelling software. Geometric uncertainty could be quantified by using an information entropy approach developed by WAGCoE researchers (Wellmann and Regenauer-Lieb, 2011; Reid et al., 2012).

1.5.5 Goals for future research / Recommendations for further work

- Verify new regional fault network via a 3D model that incorporates available seismic sections and well data.
- Processing and interpretation of worms of the regional gravity and aeromagnetic data. A similar approach could be used as for the Perth metropolitan area (see Section 3 of this report).
- Incorporate new WA aeromagnetic data, when available. New, more detailed aeromagnetic data were acquired by GSWA during 2011 for the whole Perth Basin, with release due during 2012. New features could be apparent in higher resolution datasets, especially small-scale faults.
- The new 3D model could be used as a basis for a refinement, primarily by the addition of fault complexity.

1.6 Summary

Knowledge of the structural architecture and stratigraphic geometry of the Perth Basin is a vital prerequisite for understanding subsurface fluid flow. This understanding is fundamental to the identification of geothermal prospects and to effective aquifer management in the Perth Basin. Previous interpretations of the onshore Perth Basin have been limited to 2D maps and cross sections that have not been updated since 2004 (Lockwood and Iasky, 2004). This study integrates existing geological and potential field data to develop a new, refined regional structural interpretation of the onshore and offshore Perth Basin. Re-processing of regional geophysical data has permitted a much higher density of faults to be identified in the Perth Basin, particularly within the area from Bunbury to Lancelin. Analysis of the regional data shows that sets of NW-SE trending faults are much more prevalent across the whole Perth Basin than previously recognised, and that these faults significantly influence the structural architecture of the Perth Basin and the adjacent Yilgarn Craton. A new gravity survey of the Perth Metropolitan Area has been acquired in 2009 and 2010 with 1.5 x 1.5 km spacing and some detailed traverses. A completely new fault network has been identified in the

Perth Metropolitan Area. Modelling of the new gravity data in the Perth area shows that bedrock is shallower near the coast than it is inland and this is consistent with previous offshore gravity studies. A range of geological and geophysical data, including the vertical gradient of the isostatic residual gravity, reduced to pole aeromagnetic data, shuttle radar topographic mission digital terrain data, bathymetry data and existing geological maps, and data from existing onshore petroleum wells were utilised to generate a new 3D geological model of the Perth Basin. The benefits of the 3D model are that the integration of multiple, independent datasets provides a robust and self-consistent model of the subsurface geology. The new 3D model of the Perth Basin forms the framework for numerical simulations of fluid flow and heat transport for geothermal exploration (Reid et al., 2012).

2. RESOLVING THE SUBSURFACE GEOLOGY OF THE PERTH METROPOLITAN AREA IN 3D

2.1 Introduction

The Western Australian Geothermal Centre of Excellence (WAGCoE) focuses on hot sedimentary aquifer prospectivity in the state of Western Australia, and particularly in the Perth Basin. The Perth Metropolitan Area (PMA) lies on the onshore part of the central Perth Basin. This area is of particular interest for geothermal exploration due to the occurrence of deep aquifers and proximity to a range of potential end-users of geothermal energy. In the Perth Basin, the major deep aquifers are part of the Permian–Early Cretaceous sedimentary succession, which is known to be highly faulted elsewhere throughout the basin (Playford et al. 1976; Cockbain, 1990; Iasky, 1993; Mory and Iasky, 1996; Crostella and Backhouse, 2000; Song and Cawood, 2000). However, the 3D stratigraphic architecture and the faults that affect these deep aquifers have been barely studied in the Perth Metropolitan Area.

The most comprehensive study of the PMA to date was completed for the Perth regional aquifer modelling system (PRAMS), which is primarily constrained by stratigraphic data from boreholes (Davidson and Yu, 2006) (Fig.2.1). In the PRAMS model, depths to shallow stratigraphic units are defined with high degrees of certainty at borehole locations. However, structure contours for the base of the Yarragadee Formation are poorly defined and can only be regarded as approximate (Davidson and Yu, 2006). Furthermore, only seven faults, including the basin-bounding Darling fault, have previously been identified in the PMA, which is anomalous to the high density of faulting interpreted elsewhere in the Perth Basin (Allen, 1981; Cockbain, 1990; Davidson and Yu, 2006). Faults are important for understanding geothermal systems due to their influence on the stratigraphic geometry (potentially, both during and after deposition), and how that structure subsequently influences fluid flow. Knowledge of the subsurface structure, and knowing the likelihood and location of faults, is crucial for understanding the movement of fluids and heat.

One of the main issues in identifying faults in the PMA is that pre-Neocomian sedimentary rocks are covered by younger and commonly unlithified sediments that appear to be comparatively undeformed. Variability in the distribution and thickness of post-Neocomian sediments has been interpreted to result from draping over pre-existing fault blocks and differential compaction. Subcrop and isopach patterns of these sediments are complex and commonly have strongly linear segments with sharp kinks. However, evidence of post-Neocomian faulting is 'inconclusive' (PRAMS), because these formations are too shallowly buried to resolve structures by seismic surveys. Furthermore, outcrops have been covered and/or disrupted by anthropogenic infrastructure. Therefore, any faults that potentially could affect the deep Mesozoic aquifers, including the Yarragadee Aquifer, have not been previously mapped from surface geology.

Standard geophysical techniques that are commonly used to resolve faults in sedimentary basins are also not easy to implement in Metropolitan Areas. Seismic reflection and refraction surveys are difficult to shoot in residential areas due to various restrictive factors, such as opposition from local

residents and businesses, and potential environmental impacts. Electromagnetic and aeromagnetic methods can be useful for fault identification, but noise sources in urban areas limit their application. Regional gravity surveys can be used to detect large faults that influence basin geometry, but these datasets are usually too coarse to resolve small scale faults in areas like the Perth Metropolitan Area.

Another commonly used way to identify faults, or test existing fault interpretations, is via stratigraphic interpolation between geophysical logs and/or core from borehole arrays. In the Perth Metropolitan Area, petroleum exploration (and, therefore, deep wells) is scarce, with only one petroleum exploration well drilled within 25 km of the city centre. In contrast, shallow wells for monitoring water supply are common and are distributed throughout the area of interest. Wireline logs (e.g., Gamma ray and resistivity logs) are not always available for bores in the Perth Metropolitan Area, and are usually in analogue format.

These factors necessitate alternative and often innovative, multi-disciplinary approaches to characterize subsurface geology in the Perth Metropolitan Area. This study aims to develop such an approach to answer the following key questions:

1. Does the Perth Metropolitan area contain more faults than have been identified previously?
2. If so, then what are their orientations and distribution?
3. When were faults active and how do they affect the stratigraphic architecture?
4. If the PMA is 'fault-free', then how can this be reconciled with other areas of the Perth Basin?

The results of this study form the essential framework for models of fluid and heat flow in the Perth Metropolitan Area, presented by Reid et al. (2012).

2.2 Geological Background

The PMA is located on the Mandurah Terrace, onshore central Perth Basin. For more details on the geological setting of the Perth Basin, please refer to Section 1 of this report. For our purpose, we defined the PMA extent as shown on Fig 2.1. The PMA is approximately bounded by the Darling Fault to the east and the offshore Badaminna Fault System to the west. The present day topography in the PMA forms a coastal plain that generally lies between 0 and 200 m above sea level (Fig. 2.2). However, in detail the geomorphology is complex, and has numerous linear ridges, scarps, terraces, and valleys with angular boundaries and lateral offset patterns. Chains of lakes and wetlands have linear margins and commonly have an en echelon arrangement (Fig. 2.2). The fluvial systems make their way across the coastal plain in complex ways, and most have sharply geometric meander patterns with linear segments with a range of trends (Fig. 2.2). The surface geology comprises Pleistocene to recent sediments that have similarly complex outcrop patterns that cannot be explained simply by erosion of 'layer-cake' stratigraphy (Fig. 2.1). For example, geological boundaries are highly kinked with strongly linear segments, and boundaries cross a range of elevations such that stratigraphic units of different ages are locally juxtaposed at the same elevation (Figs 2.1 and 2.2).

The subsurface geology of the Perth Metropolitan Area has been interpreted from numerous aquifer monitoring bores, sparse deep petroleum exploration wells, and by inference from 2D seismic sections outside the PMA. A summary of the stratigraphy is shown on Figure 2.3. It is assumed that

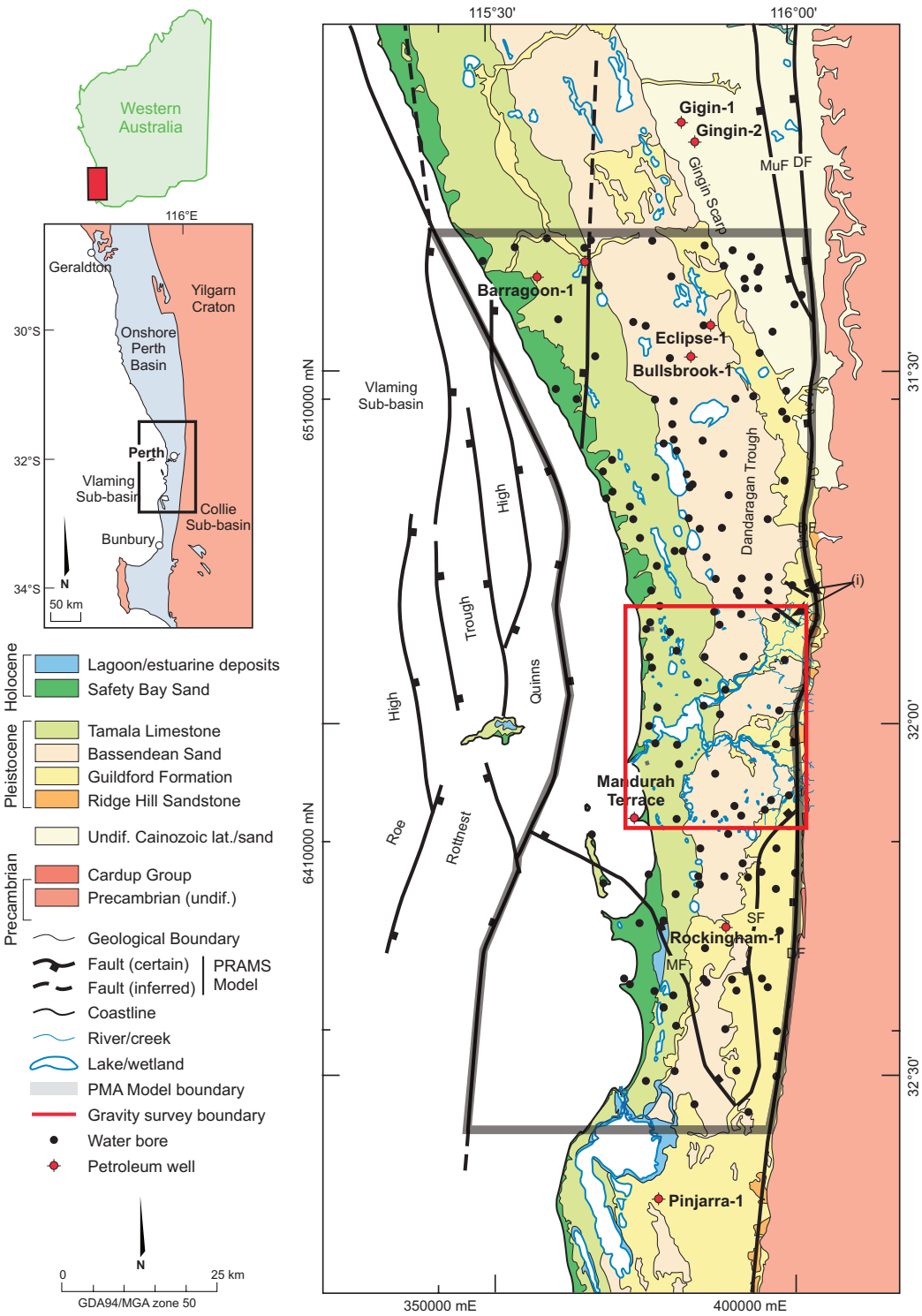

Figure 2.1: Geological map of the Perth Metropolitan Area and its surroundings after Playford et al. (1976). The positions of inferred faults and names of basin structures are after Davidson and Yu (2006). The boundaries of the Perth Metropolitan Area (PMA) 3D model and new gravity survey are shown by grey and red polygons, respectively. The location of petroleum wells and water bores used in this study are also shown (red and black circles, respectively). MuF = Muchea Fault; DF = Darling Fault; SF = Serpentine Fault; MF = Mandurah Fault. (i) Faults identified by Allen (1981).

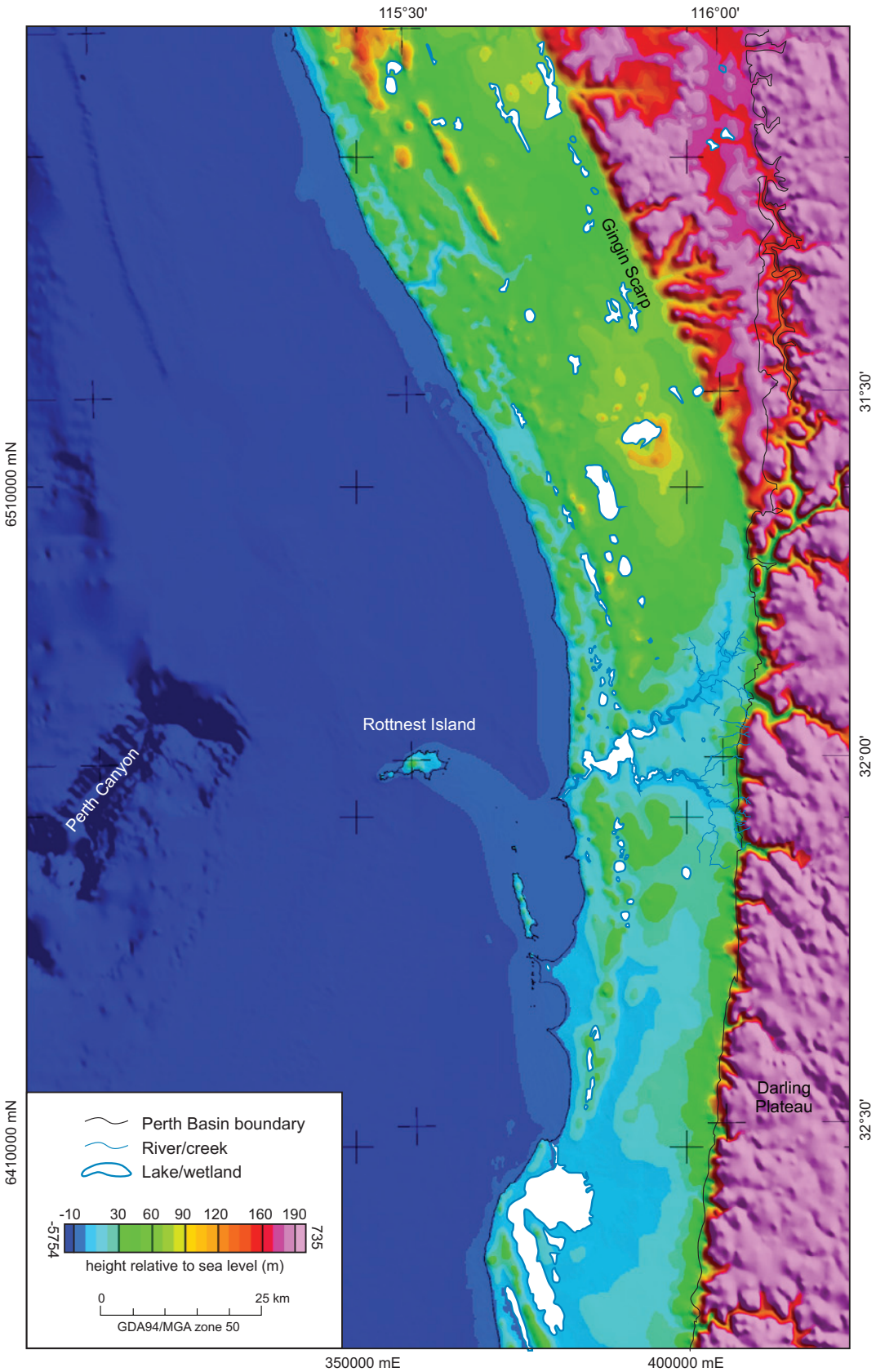

Figure 2.2: Topography of the Perth Metropolitan Area.

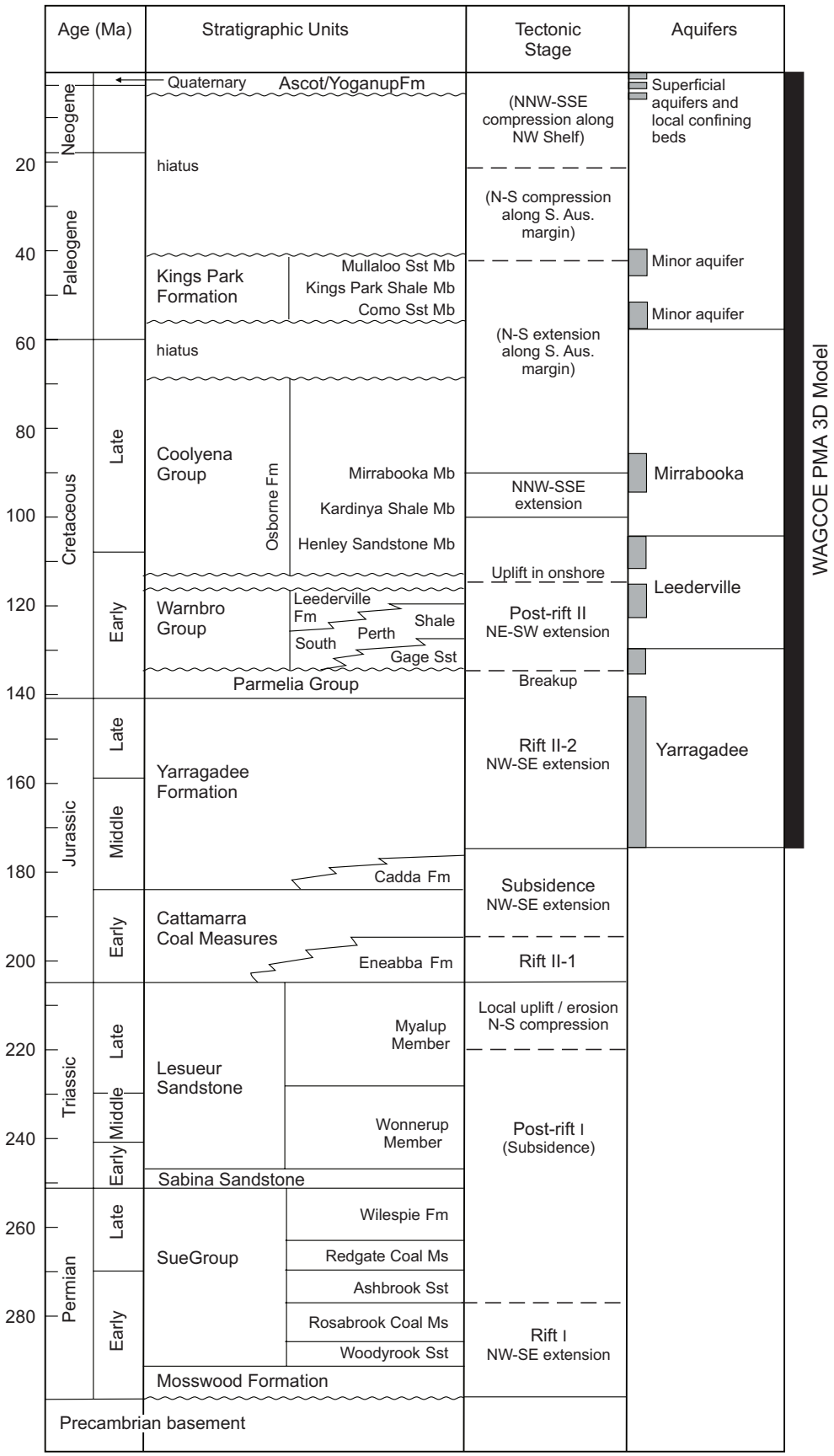

Figure 2.3: Stratigraphy of the central and southern Perth Basin, modified after Davidson (1995) and Crostella and Backhouse (2000). Tectonic stages after Song and Cawood (2000), and regional extension/ compression directions after FrogTech (2005). Aquifers modified from Davidson (1995) and Ghory (2008). Grey bars show transmissive units. Black bar shows the extent of the Perth Metropolitan Area 3D model.

extensive (and faulted) sheets of Permian and Triassic stratigraphy are present in the deepest parts of the basin in the PMA, deposited after an initial rift phase (Rift I of Song and Cawood, 2000). However, no wells intersect this stratigraphy in the PMA. The nearest well intersection of Triassic Lesueur Sandstone to the PMA is at Pinjarra-1 to the south where this unit resides at relatively shallow depths (Willmott, 1964; Playford et al., 1976). In the central and northern parts of the PMA, the deepest wells intersect the Early Jurassic, fluvio-deltaic Cattamarra Coal Measures, deposited in an intra-cratonic NNW-ESE to E-W rifting (Rift II-1 of Song and Cawood, 2000) (Willmott, 1964; Playford et al., 1976; Harris, 1994; FrogTech, 2005). These were overlain by the marine-influenced Cadda Formation during the middle Jurassic, which becomes thicker to the northwest (Playford et al., 1976). The fluvial-dominated Yarragadee Formation was deposited across the entire onshore Perth Basin during a middle Jurassic syn-rift phase (Rift II-2 of Song and Cawood, 2000), that resulted in E-W extension (Fairbridge, 1953; Playford et al., 1976; Harris, 1994). Continental break-up is marked by a regional Neocomian unconformity, formation of the Bunbury Basalt in the southern Perth Basin, followed by progradation of the restricted marine(?) Gage Sandstone, and onlapping of the marine South Perth Shale of the Early Cretaceous Warnbro Group (Fairbridge, 1953; Bozanic, 1969; Playford et al., 1976). Elsewhere in the Perth Basin, conjugate strike slip faulting developed and dextral-normal oblique slip occurred on NNW-striking faults during this N-S dextral transtension break-up phase (Harris, 1994). Sedimentation continued in the central Perth Basin during a thermal sag phase (middle Cretaceous to present), and minor reverse movement is interpreted to have occurred along faults during the Mid Cretaceous, possibly indicating inversion from SSE-NNW compression (Harris, 1994; FrogTech, 2005). Rifting along the southern margin of Australia via NE-SW then N-S directed extension also occurred during the Cretaceous to Early Tertiary, with minor influence in the southernmost Perth Basin (FrogTech, 2005). Minor fault reactivation is shown to occur in some parts the Perth Basin and Yilgarn Craton from Miocene to recent as a response to collision of SE Asian microcontinental fragments (FrogTech, 2005).

The surface geology of the Perth Metropolitan Area was mapped by Gray et al. (1952a, 1952b), and later in less detail by Playford et al. (1976) (Figs 2.1, 2.4). Outcrops of lithified rock are sparse in the metropolitan area, and are limited to patches of (predominantly) aeolian Pleistocene Tamala Limestone along a coast-parallel ridge and cliff sections adjacent to the Swan River (Gray et al., 1952a). This issue combined with the paucity of seismic data due to urban restrictions on exploration appears to have inhibited the development of a thorough structural interpretation of the Perth Metropolitan Area. Very few faults have been identified for the region from Bunbury to Lancelin in comparison to other areas in the Perth Basin (e.g., Iasky, 1993; Mory and Iasky, 1996). In fact, the only faults to be identified in the Perth Metropolitan Area in previous studies are the Darling Fault, the Muchea Fault, the Mandurah Fault, the Serpentine Fault and two unnamed NW-SE trending faults in the Swan Valley (Fig. 2.1, and also see Section 1 of this report) (Allen, 1981; Cockbain, 1990; Davidson and Yu, 2006). This study investigates whether the apparent lack of faults in the Perth Metropolitan Area is a real phenomenon, or an artefact of sparse exploration.

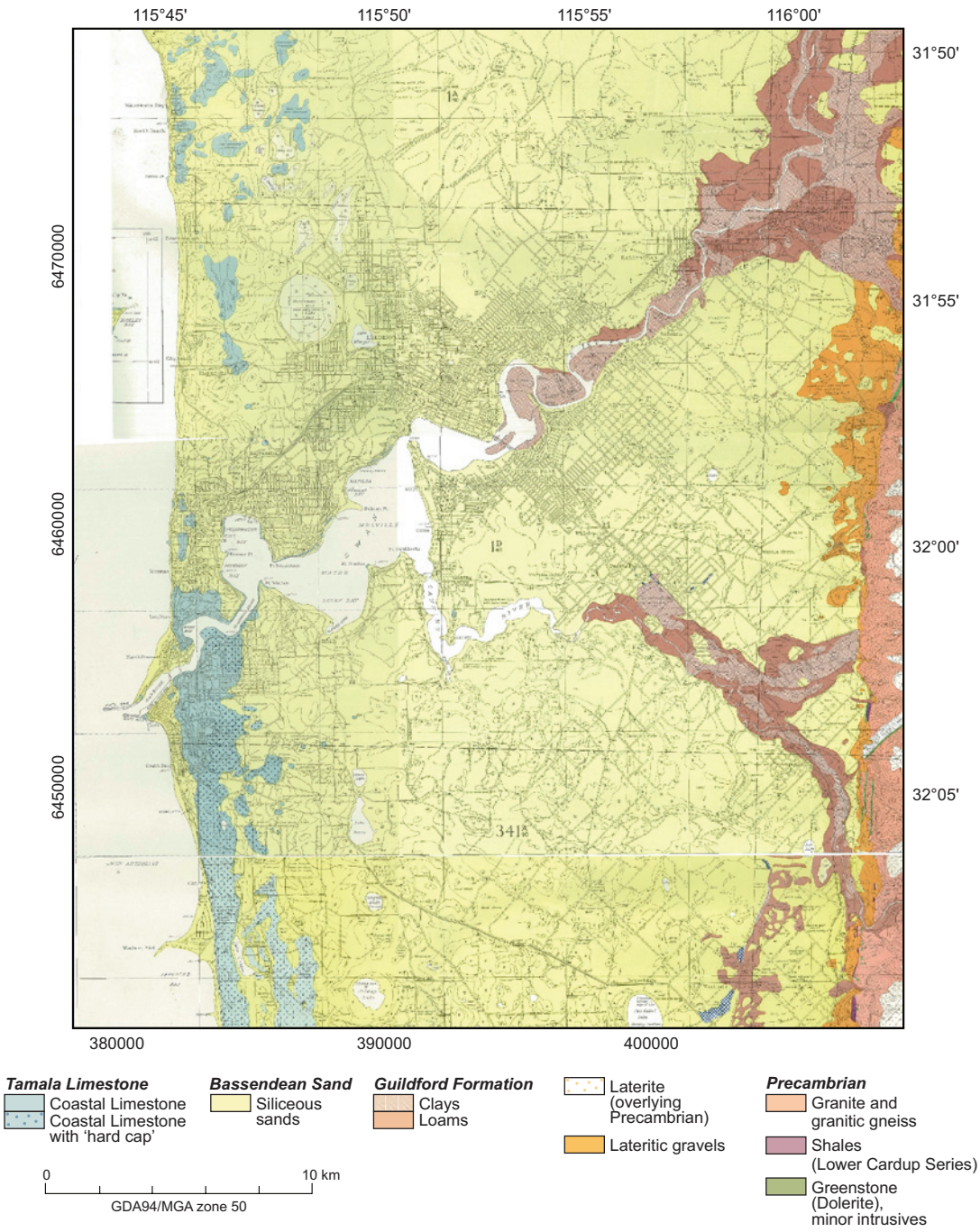

Figure 2.4: Surface geology of the central Perth Metropolitan Area, after Gray et al. (1952a, 1952b). Stratigraphy modified after Playford et al. (1976).

2.3 Approach / Analytical Technique

Although metropolitan areas rarely allow for conventional fault assessment techniques, there are usually some data available to constrain the subsurface geology. Those data commonly have different scales, different extents and different original purposes, but this diversity makes them complementary. It is essential that any inferred stratigraphy and/or faults are consistent with all of the available datasets and compatible with existing geological knowledge.

2.3.1 Using land surface topography, drainage network and geological maps to interpret faults in the Perth Metropolitan Area

A digital elevation model was developed from gridded 'ausbath 250 m' 2008 dataset, available from Geoscience Australia, to show the topography and bathymetry of the Perth Metropolitan Area. Shuttle Radar Topographic Mission (SRTM) topographic data were used to produce a DEM for the Perth Metropolitan area. These SRTM data are available at 3 second intervals – approximately 90 m x 90 m. The outline of the modern day coastline, lakes and wetlands, and fluvial drainage system were developed from Google Maps and superimposed on the DEM. These data were used to identify linear topographic scarps and linear river sections. These were inferred to represent landscape features that have been controlled by surface-penetrating faults or fractures. Faults were identified using stratigraphic offsets shown by Gray et al. (1952a; 1952b) and Playford et al. (1976). Where there is insufficient outcrop to constrain stratigraphic/geological variations associated with the scarps and fluvial jogs we assumed the following criteria to identify the sense of relative displacement across faults based on surface topography :

- Dip slip displacement is assumed to be normal sense.
- The side with lower elevation is assumed to be the downthrown side.

The resultant fault network was then compared with features seen in geophysical datasets.

2.3.2 A new detailed gravity survey for Perth Metropolitan Area

New ground gravity data with a spacing of 1.5 km x 1.5 km and also some detailed road traverses with 50 m and 100 m spacing have been acquired for WAGCoE by Atlas Geophysics, for the Perth Metropolitan Area in 2009 and 2010. These surveys used Scintrex CG3 and CG5 digital gravity meters and real time kinematic GPS positioning. These surveys have provided gravity data to 0.01 mgal accuracy and x, y and z data to better than 5 cm accuracy – enabling the usual gravity corrections to be performed to a level commensurate with the precision of the measurements.

A GPS base station with radio links to the mobile GPS receivers was positioned on various high buildings as convenient for different parts of the survey area: top of Fremantle Port Authority Building; top of Physics Building at UWA; and top of Australian Resources Research Centre Building in Kensington, Perth. Absolute positions and heights of these GPS base station positions were established using the online GPS Processing Service AUSPOS facility provided by Geoscience Australia (GA). Data for up to 24 hour periods were collected for each GPS base station position and sent to Canberra for processing using the AUSPOS facility. This returns high accuracy (within a few cm) x, y and z data for the base station positions, which in turn are used to provide accurate survey data for all the gravity stations. Gravity data have been tied in to the GA absolute network and processing has been done using the same approach as GA with a further step of the application of terrain corrections using SRTM topographic data.

2.3.3 A wavelet technique ('worming') applied to the new Perth Metropolitan Area gravity dataset

'Worming' is a multi-scale edge detection technique involving the analysis of potential fields data using wavelet functions (e.g. Hornby et al., 1999; Boschetti et al. 2000; Holden et al., 2000; Boschetti et al., 2001). Output from this technique is visualised as linear features, so-called worms, which resolve gradients in the data of different wavelengths. For gravity data, they are commonly caused by horizontally juxtaposed rock bodies with contrasting density (Fig.2.5). Short wavelength gradients are characteristic of horizontal density contrast near the surface, and only longer wavelength features that survive upward continuation progressively further above the measurement plane are commonly interpreted as deeply buried domains of horizontal density contrast.

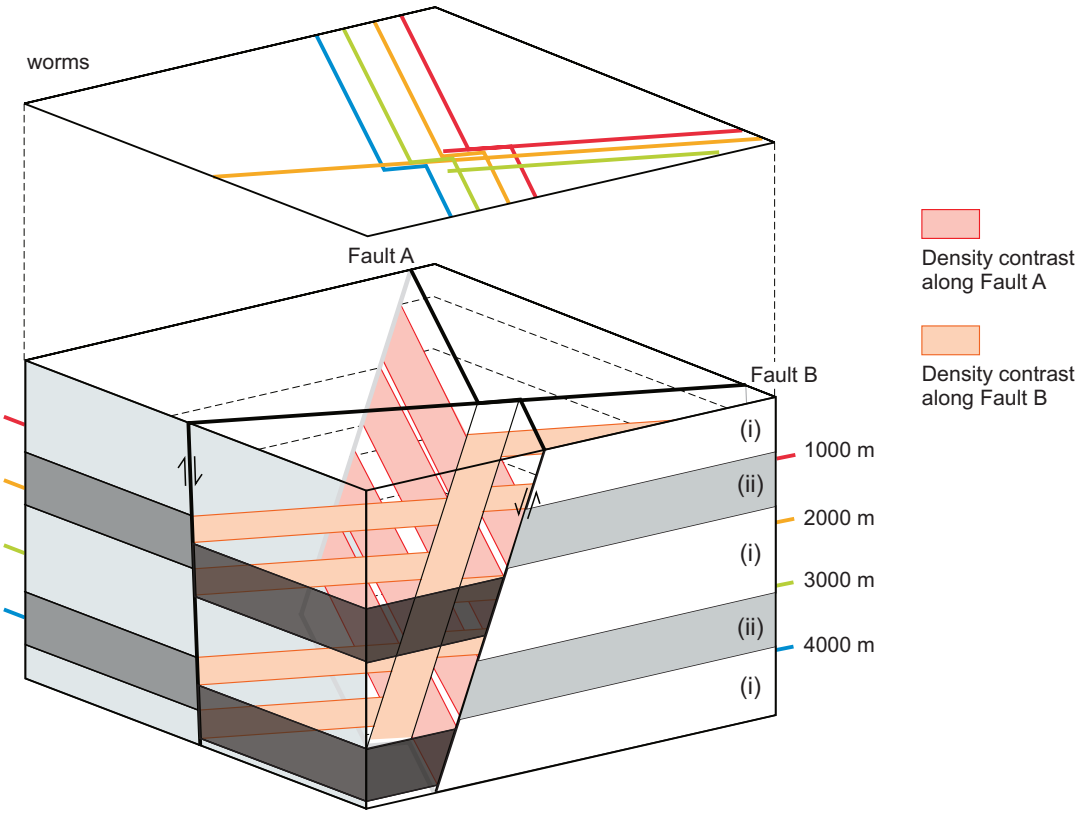

Figure 2.5: A block diagram showing the effects of faults on gravity worms. The pre-faulting geometry comprises of horizontal alternating rock layers (i) and (ii) with different density. Fault A is a large displacement fault that juxtaposes (i) with (ii) such that density contrast occurs at most places along the fault plane. Fault B is a lower displacement structure that cuts Fault A. Density contrasts are less well developed along the fault plane, except along the intersection of the two faults. Density contrasts along the fault planes result in gravity worms. Worms upward projected from different depths (colour coded as per the depths on the block diagram) show the position of the fault planes at a given depth. Parallel, spaced worm sets from different depths indicate that Fault A is a dipping plane. Fault B causes a deflection in the Fault A worms. Fault B is not expressed by all worm depths because of the heterogeneously developed density contrast along the fault plane.

Strong worm features that survive large upward continuations – because of the decay properties discussed in Hornby et al. (1999), are typically the signature of major 2D tectonic boundaries, and the worm signature of the Darling Fault system is a good example of this. Note that, since the fault surface is 2D, we can speak simultaneously both of upward continuation height and of underground locations in depth for these features, with the latter interpretation resulting from the work of Hornby et al. (2002). In this Perth study, gravity data have been upward continued in 100 m steps from 100 m to 2900 m above ground level. Dipping faults are seen from lateral offsets in the worm data derived from different depths.

2.3.4 2D gravity forward modelling

Several detailed 2D gravity forward models have been made of different E-W segments of the Perth Basin at different latitudes using Encom ModelVision software.

The sediment / basement interface has been modelled along the lines of section and takes into account the variations in density associated with the known geology. The interface has been iteratively adjusted manually and by computer inversion to provide a fit to the observed gravity data. The forward modelling utilises densities obtained from Cockburn 1 borehole geophysical data (Wilkes et al., 2011). Direct measurements of density in the Cockburn 1 borehole are only available for the depth range of 313 to 917 m. Therefore, P wave velocities (V_p) were calculated from delta t slowness borehole data and used to compute densities via Gardner's equation (Gardner et al, 1974).

$$\rho = 0.23 * \left(V_p * 3.28\right)^{0.25}$$

where V_p is in m/s and density ρ is in g/cm^3.

2.3.5 Vertical Seismic Profiling (VSP) in the Perth Metropolitan Area

Two VSP surveys were conducted in the Perth metro area in 2010, with the aim of resolving subsurface stratigraphy in the PMA. These were done in collaboration with GT Power Pty Ltd., Curtin University Department of Exploration Geophysics and Maxam Australia. The first VSP used the SHG-1 borehole at St Hilda's School in Mosman Park, recently drilled to 1008 m subsurface to access hot water to heat a new swimming pool and provide space heating. The second VSP survey was conducted in Kensington using the Department of Water monitoring bore AM 40 adjacent to the WA Department of Food and Agriculture building in Baron Hay Court Road. The VSP results unfortunately showed significant tube wave contamination and local velocity profiles were unable to be estimated with appropriate confidence (Nadri, 2011a and 2011b). Consequently, depth migrations for the SHG-1 and AM40 VSP data sets carried significant uncertainty, and are not reported here.

2.3.6 Development of a 3D model of the Perth Metropolitan Area

A multi-disciplinary and iterative approach was used to develop the 3D model of the Perth Metropolitan Area (Fig. 2.6). The modelling was done using the 3D modelling packages 3D Geomodeller (Calcagno et al., 2008) and SKUA (Jayr et al., 2008). In these two packages, implicit

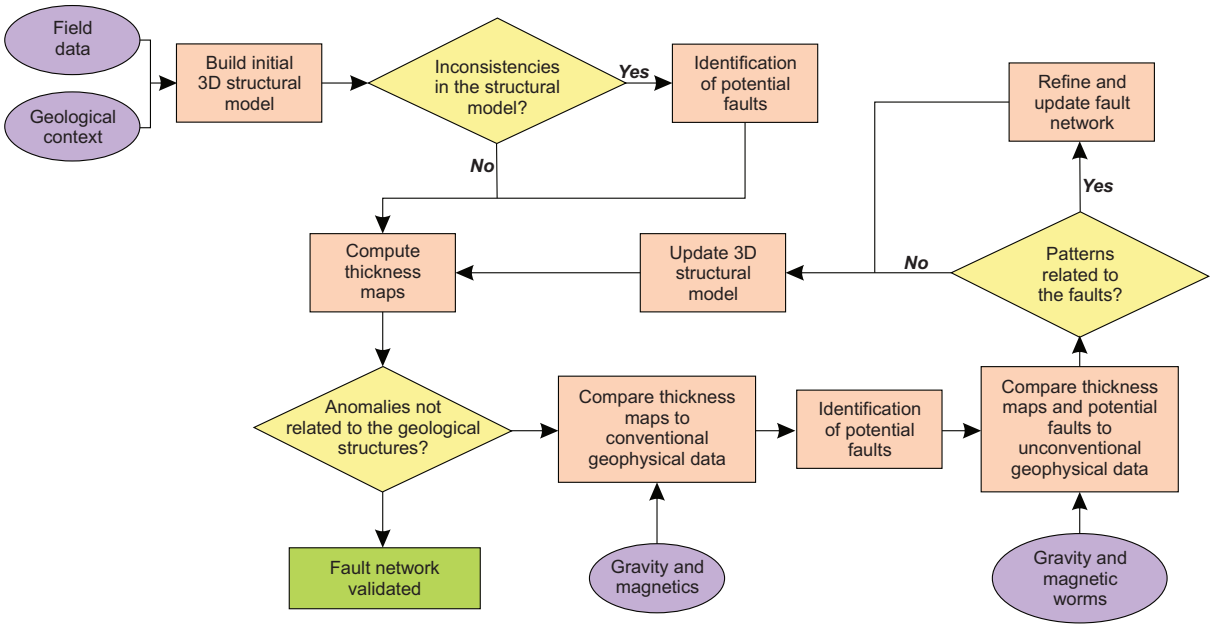

Figure 2.6: Iterative workflow to assess fault networks for the development of the Perth Metropolitan Area 3D model, depending on data available.

definitions are given to geological interfaces, which are defined as the iso-surfaces of one or several scalar fields in three-dimensional space. The scalar fields are obtained by interpolation, but several geological interfaces can be modelled at the same time, with data associated to a scalar field, not an object. 3D Geomodeller was used to generate the surfaces and SKUA was used to check the misfit between well data and surfaces by generating maps and cross sections that intersect with the wells. SKUA was also used as a database for all input data.

2.3.6.1 Initial 3D mapping of stratigraphic surfaces:

An initial 3D model of stratigraphic surfaces was modelled from 'depth to formation top' data from over 180 shallow water bores (Davidson and Yu, 2006) and 6 petroleum wells (Crostella and Backhouse, 2000) (Fig. 2.1). The modelled formations are summarized in Figure 2.3. These features were chosen because they constrain key aquifers (Fig. 2.3) at depths of interest for geothermal exploration, and have been unambiguously identified in many wells with good spatial coverage across the Perth Metropolitan Area. Some of the aquifer monitoring wells are deep enough to intersect the top of the Yarragadee Formation, but for no more than a few hundred metres. Borehole data for deeper formation boundaries are too sparse to constrain 3D surfaces. The absence of stratigraphic surfaces from boreholes that penetrate sufficient depths also provide key constraints on 3D geometry. In Geomodeller, the model is calculated using an implicit 3D potential function as the interpolator for each surface. In some cases, the interpolated surface does not honour the well data precisely. This could be due to (a) the presence of additional structural complexity that is not incorporated into the model, or (b) uncertainties associated with the stratigraphic picks in the well data.

2.3.6.2 Assessment of stratigraphic depth and thickness variations:

The 3D model is then used as a means to assess morphological variations of stratigraphic surfaces and isopachs. Where significant variations in depth and/or thickness exist, the geological context was considered to assess whether they could be explained entirely by sedimentary processes of basin fill and/or erosion, entirely by faulting, or a combination of both (i.e., syn-depositional faulting).

2.3.6.3 Resolution and modelling of subsurface faults in the Perth Metropolitan Area:

The main issue in identifying faults in the Perth Metropolitan Area, is the fact that water bores, which are the most extensive data, at best intersect the Neocomian Unconformity at the top of the Yarragadee Formation. Therefore, several datasets were utilised to develop a 3D fault network in the Perth Metropolitan area. These included: stratigraphic thickness maps from the initial 3D model, regional gravity anomaly maps, high resolution gravity data and worm maps from the new survey of the central Perth Metropolitan Area, a legacy 2D seismic line off the northern edge of the area, results of 2D gravity forward modelling, and faults identified in previous studies (Fig. 2.1, Playford et al., 1976; Davidson and Yu, 2006).

Faults identified via several independent sources were assigned a higher degree of confidence. The dip sense of fault planes was determined from gravity worms, and extrapolated from 2D seismic sections, where possible. All other faults were assigned dip values of 70°, with dip directions based on the relative displacement of stratigraphy and assuming normal displacement. Faults were modelled as discrete surfaces with consistent dips, across which stratigraphic boundaries from initial model iterations were cut and displaced. The stratigraphic surfaces were then re-calculated to minimize surface curvature. However, several stratigraphic data points were required in each fault block to permit stratigraphic surfaces to be modeled, which prohibits modelling the entire population of faults identified from land surface features. Therefore, only major faults were modelled because: (1) they were spaced far enough apart for fault blocks to contain adequate borehole data to constrain stratigraphic surfaces; (2) We had a high degree of confidence because they were commonly identified via multiple data sources, and; (3) it was assumed that they were likely to have the most significant effect on model geometry, and hence fluid flow properties.

The 3D geological model was used to assess geometric consistency and, therefore, interpretation reliability. This ensures consistency between all datasets and allows the testing of different yet plausible geological scenarios, within model constraints. For example, vertical stratigraphic offsets between distant wells could indicate either the presence of a fault, folded strata, or both. Cross checking the inferred fault location and orientation against gravity results or seismic data gives credence to interpretations, such that the inference of faults via independent criteria from several different data sources increases confidence in interpretation. The identification and addition of faults into the 3D model was an iterative process.

2.4 Results

2.4.1 A new interpretation of the fault network in the Perth Metropolitan Area from topography, drainage network and geology

There are many linear scarps with different strike lengths and orientations in the western area of the Perth Metropolitan Area where the Tamala Limestone extends along a belt broadly parallel to the coast. These scarps intersect kinks and jogs in the modern day coastline (Fig. 2.2). Lakes and wetlands in the Perth Metropolitan Area occur on the lower side (hangingwall?) of the scarps. They also define the sharply geometric nature of the Swan and Canning River systems. The lineaments identified from topography and fluvial sections coincide with truncations and jogs in the boundaries of the surface geology, which gives credence to the interpretation that they are surface traces of faults (Figs 2.7 and 2.8). Similar truncations and jogs in the geology have been used to identify additional faults in areas where topography and fluvial criteria are lacking (Figs 2.7 and 2.8). However, these areas are spatially limited to where geological variation has been mapped - along the coastal ridge, the Swan and Canning River systems and adjacent to the Darling scarp (e.g., Fig. 2.7).

Four different dominant trends (sets) of faults have been identified from topography. There appears to be a consistent overprinting relationship between the fault sets that define the following relative timing succession:

1. NNW-SSE trend
2. NNE-SSW trend
3. NE-SW trend
4. NW-SE trend

The relative displacement for individual faults is consistent across cross cutting faults. An early formed graben is bounded by NNE-SSW trending faults and is responsible for the low lying ground that contains lakes and wetlands such as Thomsons Lake, South Lake, Bibra Lake, Lake Monger, Herdsman Lake, and Lake Karrinyup. It also causes the dog-leg in the Swan River between Peppermint Grove and Dalkeith. West-dipping faults of this orientation cause the scarps along the coastline of the Perth Metropolitan Area.

Two main graben systems have been identified that control the main orientation of the present day Swan and Canning River systems. A NE-SW graben, here called the 'Kings Park Canyon' contains the Swan River. Topography associated with displacement on faults of this affinity cause the major coastal protrusions at Fremantle and Woodman Point. The Kings Park Graben is cross cut by a NW-SW trending graben, here called the 'Ardross Graben', which deflects the Swan River to the NW at Attadale. Other faults of this late NW-SE set cause minor jogs and bends in the coastline. Very few topographic features can be seen along the central part of the Perth Metropolitan Area, probably because the rocks in this position are poorly lithified and do not form scarps, rather than a lack of faults in the area. In the east, the Darling Fault is the only significant topographic feature. The Serpentine Fault is not expressed in the surface topography. However, Forrestdale Lake is positioned immediately to the east of the Serpentine Fault trace.

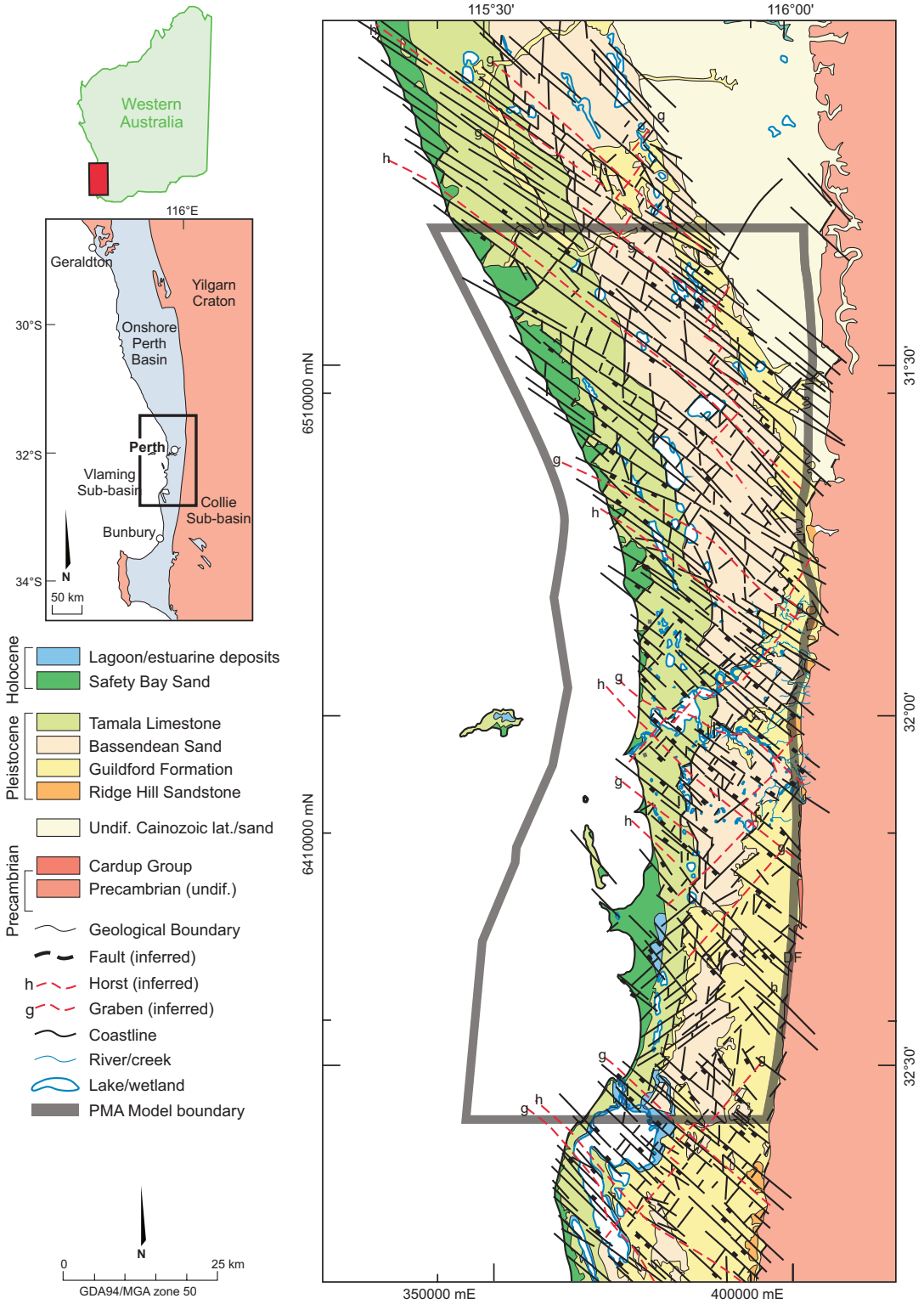

Figure 2.7: A map of the Perth Metropolitan Area showing faults inferred from surface topography and coastal plain landforms, fluvial drainage network, and geological boundaries. Note that the paucity of faults inferred northeast of the Gingin scarp reflects difficulty in interpretation in this area rather than a real fault distribution. Geological stratigraphy and boundaries after Playford et al. (1976). DF = Darling Fault.

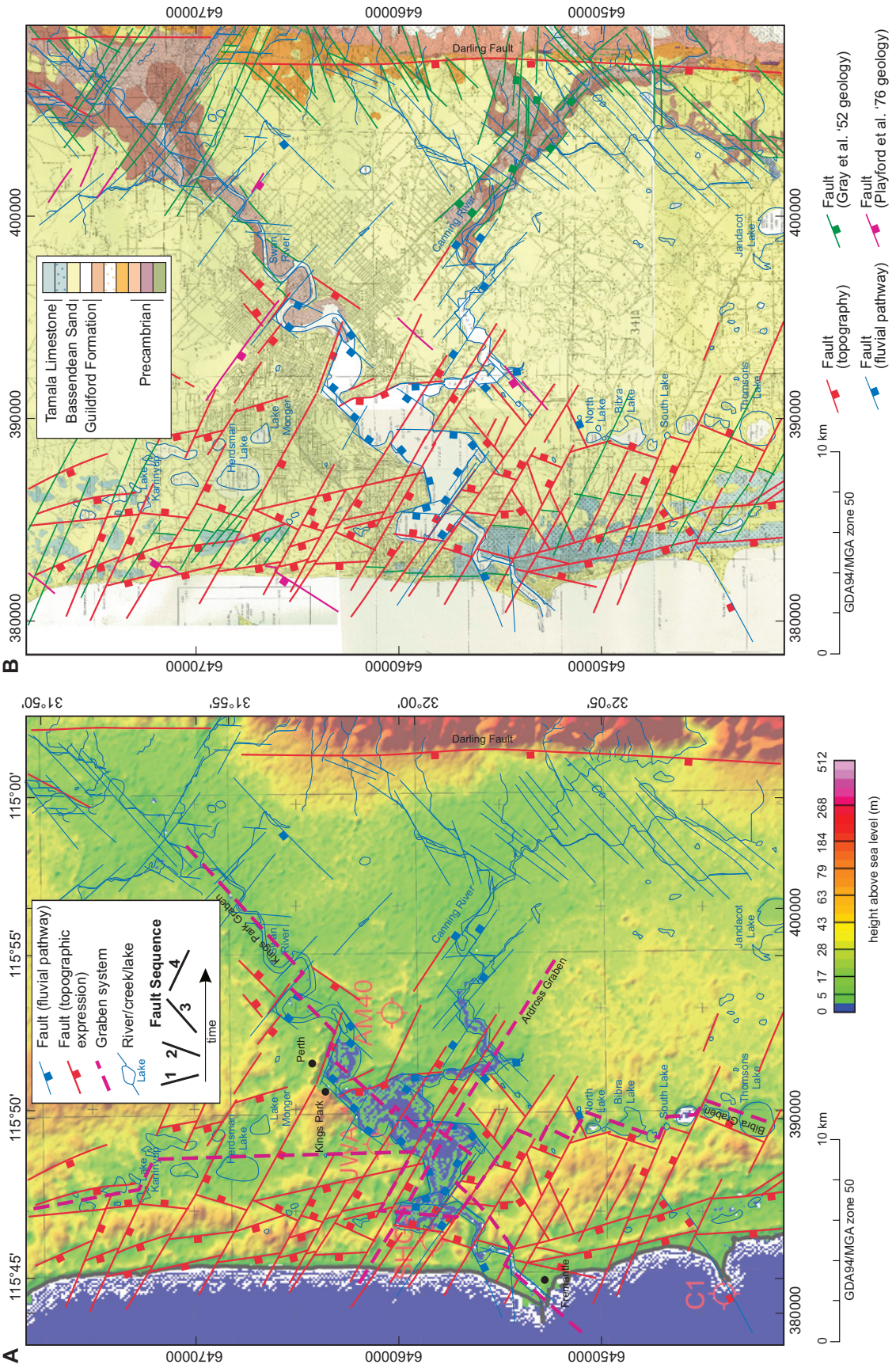

Figure 2.8: Maps of the central Perth Metropolitan Area showing faults inferred from (a) the land surface topography and fluvial drainage network; (b) Geology after Gray et al. (1952a; 1952b); (c) Geology after Playford et al. (1976). Digital elevation model in (a) has been computed from SRTM data.

Strongly linear features are also seen in the whole fluvial drainage system in the Perth Metropolitan Area, with the exception of meanders of the Swan River along the flood plain East of Perth (Fig. 2.8). Linear trends have been extrapolated short distances beyond linear fluvial sections for clarity (Fig. 2.8). They show the same set of orientations as the topographic scarps in the western and central areas, and, in most cases, are aligned with them. To the east of the Serpentine Fault, where the drainage network becomes more densely distributed, a NE-SW trending set dominates the fluvial sections. A NW-SE set that occurs near Guildford coincides with eastward displacement of the Darling and Serpentine Faults. Therefore, it is interpreted that all strongly linear fluvial sections are caused by fluvial systems that have locally exploited faults and/or fractures. However, in most cases it is difficult to interpret the sense of displacement across these structures in the east of the Perth Metropolitan Area.

2.4.2 New gravity maps and worms for Perth Metropolitan Area

Figure 2.9 shows a broadly symmetrical negative anomaly in the position of the Dandaragan Trough seen in the regional gravity data (Fig. 1.4). The anomaly increases along the axis of the trough from -100 mgal in the south to -115 mgal at the northern edge of the map. As expected, the highest values correspond to the rocks of the Yilgarn Craton to the east of the Darling Fault. Contours of the data are not always even, and show many deflections, especially in the NW of the image. The nature of these features is further revealed by the process of 'worming' of the Bouguer gravity data (Figs 2.10 and 2.11).

The lateral offsets from worms different at depths indicate that the Darling Fault dips steeply to the west (Fig. 2.10). The deflections in the worms indicate that a segment of the fault plane is deflected NNE and has a shallower dip in the deep subsurface between Wattle Grove and Midland. The other prominent set of 'deep worms' runs sub-parallel to the current coastline, inland by approximately 1.5 km. These worms are expressed in a wide range of depths, indicating that they possibly relate to a deeply penetrating structure in the same manner as the worms from the Darling Fault. This structure coincides with a linear escarpment and meander segment in the Swan River at Peppermint Grove and other natural linear escarpments to the south through Beaconsfield and Spearwood. Kinks and deflections are seen in all deep worms, and are more severe at shallower depths – an artefact of the decay of short wavelengths with upward continuation. The lateral offset of worms from different depths changes such that the structure is sub-vertical and shows both dip senses locally along its length. Two discontinuous, sub-linear sets can be seen in the deep (>1000 m) worms: another N-S trending worm runs the length of the area approximately between eastings 400 000 and 402 000, and a NW-SE trending set beneath Floreat to Kings Park (Fig. 2.10). All of the deep worm structures are seen in <1000 m worms (Fig. 2.11). The dip sense is not clear from the worm data. Several other linear shallow worms include NW-SE, NNW-SSE, N-S, and NE-SW trending sets of worms (Fig. 2.11). With the exception of NNW-SSE worms, these orientations commonly align with faults identified by other means (Fig. 2.11). The 100-500 m upward continued worms were treated with caution because of the strong possibility of artefacts resulting from the 1.5 km node spacing in parts of the gravity survey. Such artefacts can be seen in the 100 m worm data as isolated equant worms that are

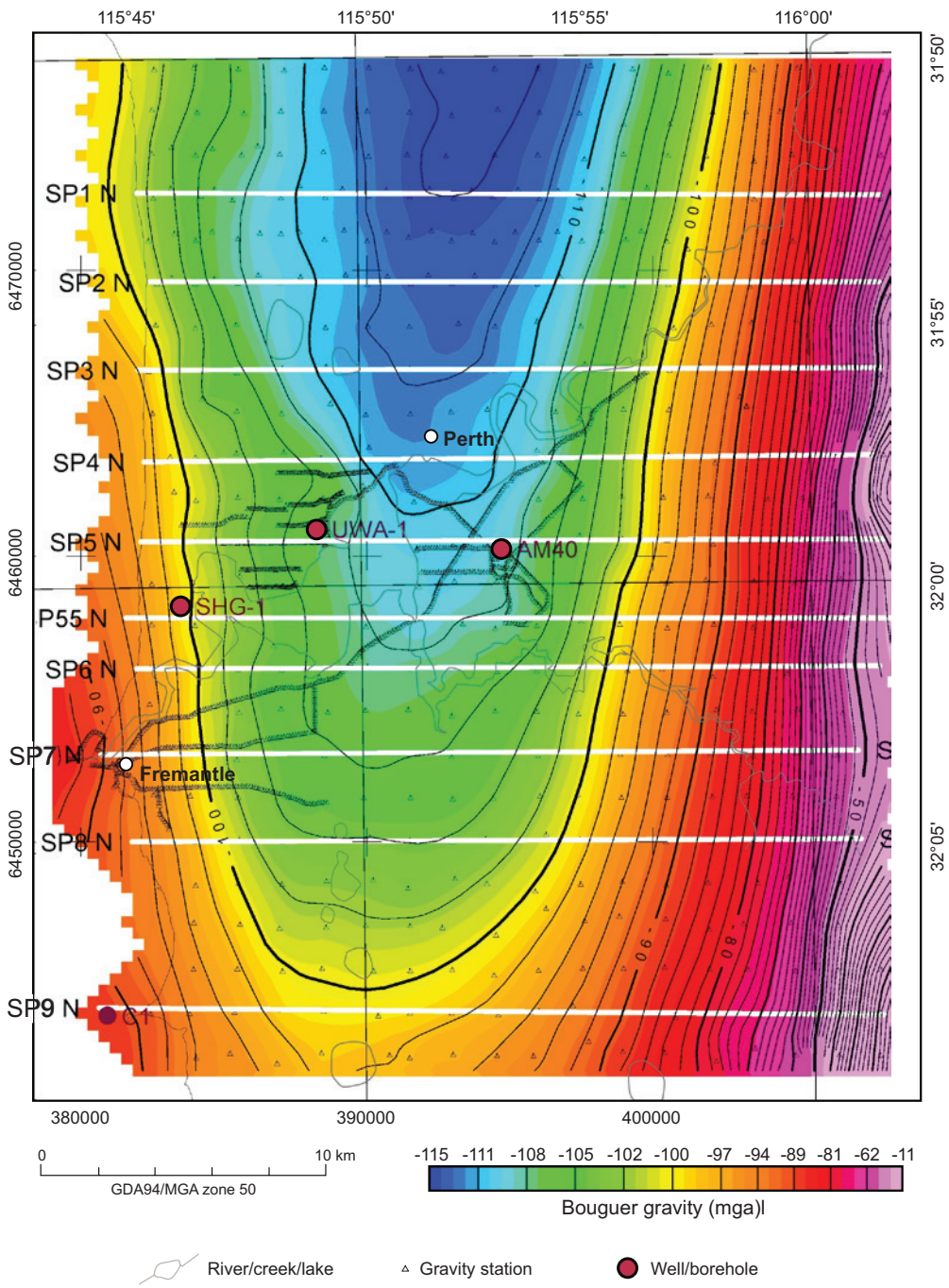

Figure 2.9: Bouguer gravity anomaly map of the central Perth Metropolitan Area showing the locations of 2009 and 2010 gravity stations (red triangles). The grid is of Bouguer gravity for a density of 2.3 g/cc, units are mgals. 2D forward modelling traverses are shown as white lines SP1 N to SP9 N.

concentric to the data collection stations (Fig. 2.11). Nevertheless, 100 and 500 m worms in areas with high data density show consistent trends to the >500 m worms. Furthermore, a discontinuous string of elongate N-S, 100-500 m worms are coincident with the northern strike extension of the Serpentine Fault at approximately 40,000 mE (Fig. 2.11). There are no strong asymmetric offsets to these worms, and so worms cannot be used to determine the dip sense of this structure.

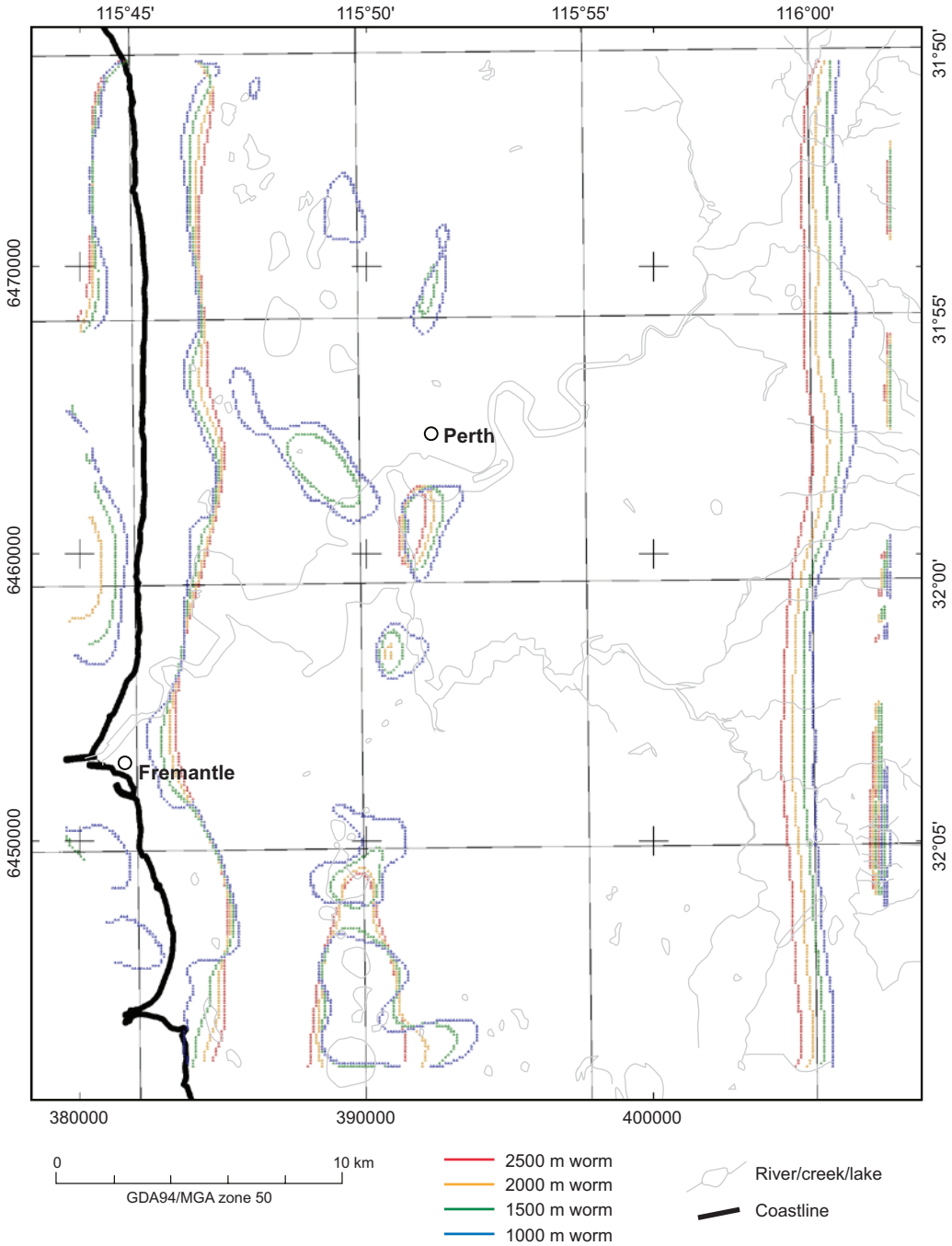

Figure 2.10: A map of selected gravity 'worms' for the central Perth Metropolitan Area gravity dataset shown in Figure 2.9. Gravity data are continued upward from 1000 to 2500 m above sea level as part of the worm computation.

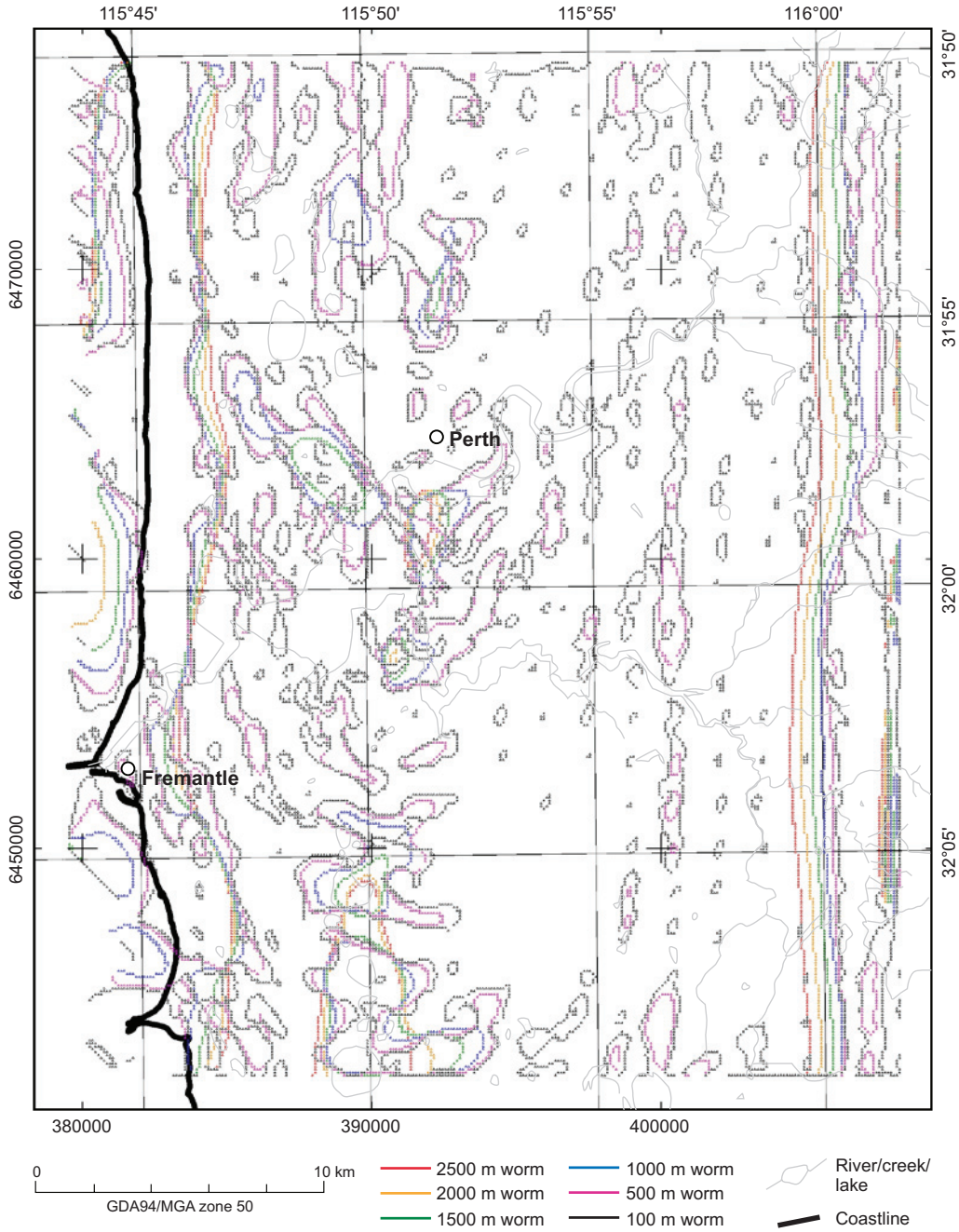

Figure 2.11: A map of gravity worms continued upward from 100 to 2500 m in the Perth Metropolitan Area.

2.4.3 2D gravity forward models

Results of 2D forward modelling along traverses shown in Figure 2.9 are shown in Figure 2.12. The models have an strike direction of 3 degrees and a plunge to the north of 1.5 degrees. The model has a strike length of 140 km and is centred on profile line SP1. The data used have been Bouguer corrected with the spherical cap method which allows for curvature of the Earth out to 167 km from each gravity station. This is consistent with the latest Geoscience Australia processing. The modelled depths to basement are very dependent on assumed density contrasts, and selection of regional levels. This modelling has used an average density of 2.39 g/cc for the sediments based on seismic velocities measured in the Cockburn 1 well, and 2.67 g/cc for the underlying basement rocks.

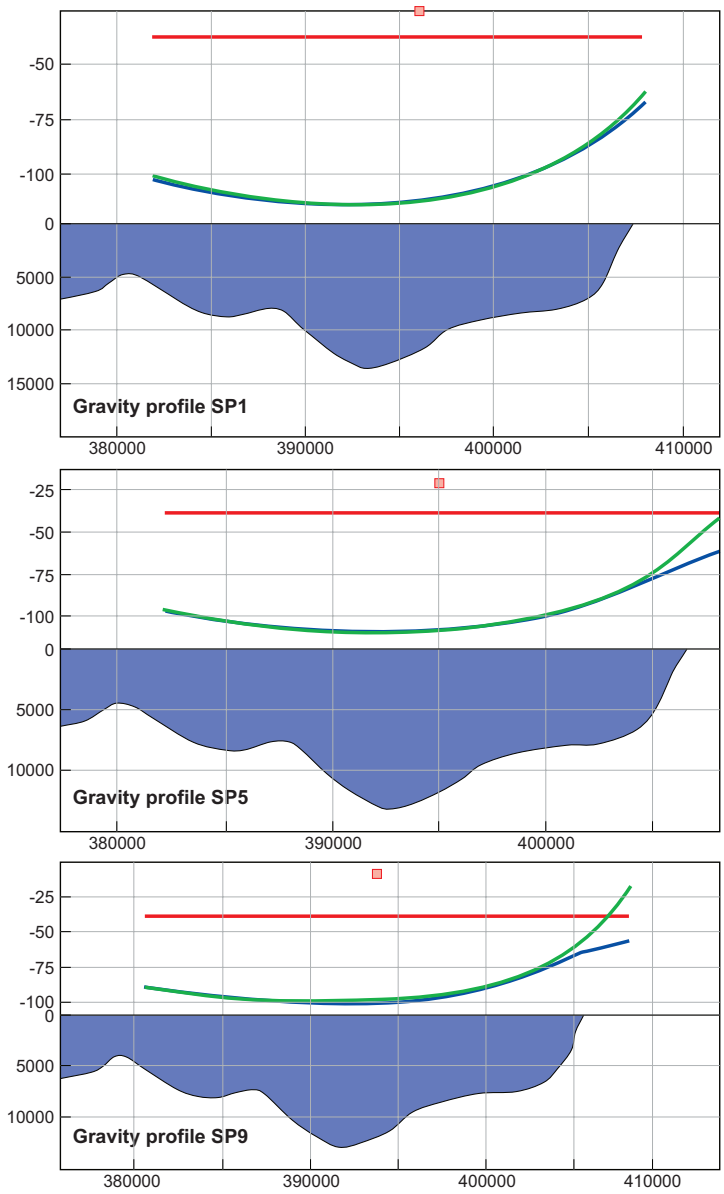

Figure 2.12: 2D gravity model profiles. (a) SP1 N. (b) SP5 N. (c) SP9 N. In each model, the top panel shows the gravity profile in black with grid sample points interpolated every 500 m. The blue curve is the modelled gravity from the depth cross section shown in blue in the lower panel. Vertical axes are in mgal for top panel and in metres below ground level in the lower panel. The pink line in the top panel is the assumed regional gravity gradient. The horizontal axis is GDA94 MGA zone 50 easting

In SP5, the coastline is close to the western end of this grid profile. Each modelled section clearly shows an increase in basin thickness associated with the Darling and Serpentine Faults (Fig. 2.12). The overall shape of the basin-basement interface is similar across all sections, indicating that the basin is broadly symmetrical in the Perth Metropolitan Area. The deepest basement is at approximately 12 km depth close to DOW borehole AM40 in profile SP5 (Fig. 2.12). Basement is shallower from approximately the location of AM40 westwards in all sections, and includes significant topography of the basin-basement interface with two basement highs occurring at approximately 380 000 E and 387 500 E (Fig. 2.12).

2.4.4 A new 3D geological model of the Perth Metropolitan Area

The new geological model covers geological formations down to the base of the Yarragadee Formation. The final fault network is shown in Figure 2.13. A total of 16 new faults were incorporated into the Perth Metropolitan Area model, and improvements were made to the location and extent of the Serpentine and Mandurah Faults previously identified by Davidson and Yu (2006). A 3D display of the model has been colour coded to illustrate the data sources used to assess the reliability of our new fault network (Fig. 2.13c).

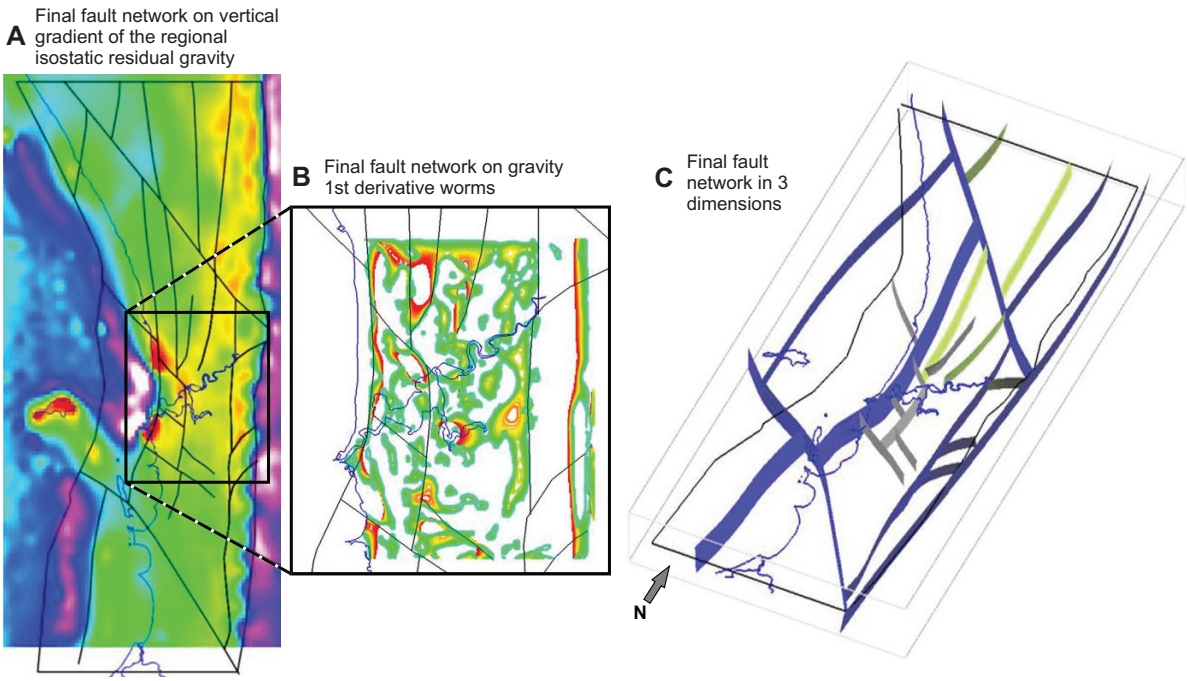

Figure 2.13: (a) The final Fault network in the PMA 3D model. Our new fault network is consistent with pre-existing work at basin scale (Crostella and Backhouse 2000, Bale 2004). (b) Gravity worm map from the central area. (c) A 3D display of the PMA model showing constraints on the new fault network. Faults in blue were inferred from more than two datasets and are the most reliable in terms of location, strike, dip and displacement sense. Faults in green were inferred from two concordant datasets. Faults in grey were only inferred from one dataset, i.e., gravity worms in the central Perth Metropolitan Area.

The final PMA 3D model resulted from over ten data integration iterations. One example of this iterative process is given in Figure 2.14. This illustrates the detection of the northern extension of the Serpentine Fault into the PMA model area from a combination of formation boundary depths, formation thickness variations and gravity worms. These features clearly show that the Serpentine Fault locally controlled sedimentation patterns, resulting in lateral stratigraphic juxtaposition detected by the gravity worms. The rationale for iterative model construction is described below:

- Yarragadee Formation – At the very beginning of the workflow, an initial 3D geological model was created using petroleum wells and water bores. At that step, it was already possible to identify potential faults (red dotted line in Fig. 2.14A) by comparison of tops and bases of

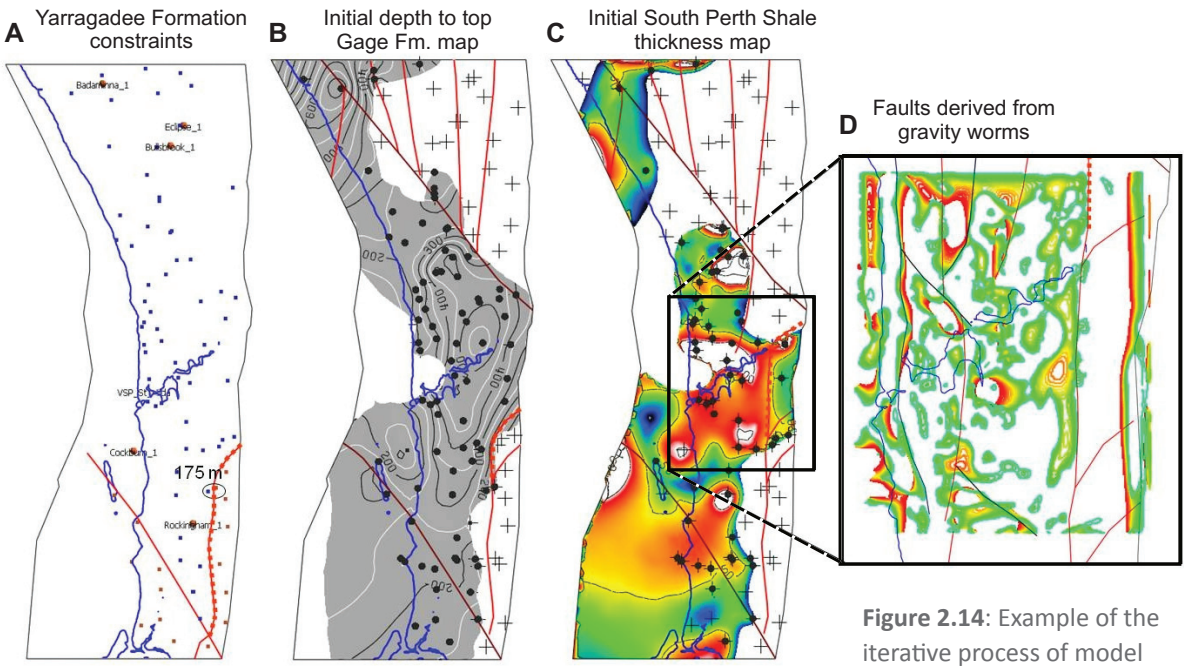

Figure 2.14: Example of the iterative process of model development. See text for details.

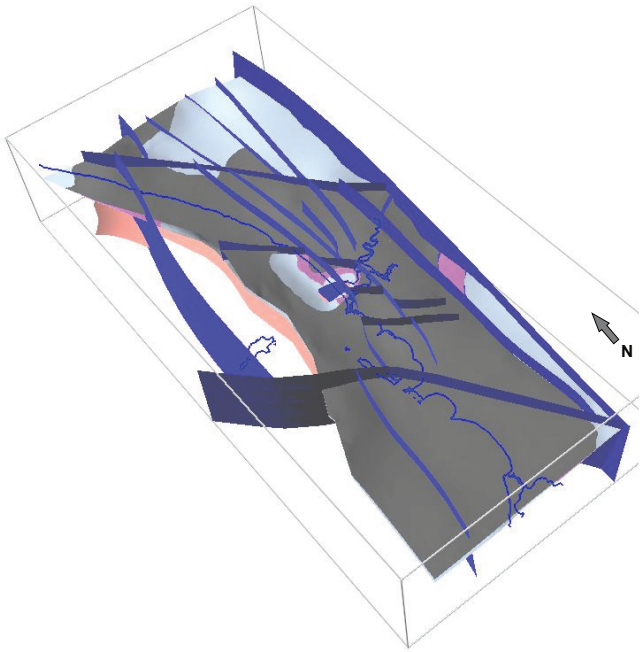

Figure 2.15: A 3D view of the final PMA model.

the Yarragadee Formation in the well data (blue and red dots, respectively). The Yarragadee Formation is significantly offset in the south east corner of the area of interest.

- Gage Formation – While the formation shown in Fig. 2.14B has no sediment in the central east area, an older formation showed sediments on the same block. This might indicate differential block movements in that area, and therefore the Serpentine Fault was extended with the new red dotted line.

- Thickness of the South Perth Shale – anomalies in formation thickness were identified on maps computed from the 3D model (Fig. 2.14C). In this example, a northern strike extension of the Serpentine Fault was interpreted from a condensed section of South Perth Shale, which caused less accommodation space over the footwall block. East of the Serpentine Fault, the formation thickness is approximately 25 m, whereas the formation is 80 m on the western, downthrown side, indicating differential block movements at the time of sedimentation.
- Gravity worms – Once some potential faults were identified, it was possible to compare the fault network to the gravity worms (Fig. 2.14D). Interpreting worms can be challenging, therefore using already interpreted faults enables the identification of patterns in the worms that are related to the faults: deep strong lines and breaks in the worms in our case. In this example, the newly defined Serpentine Fault extension fits perfectly with the worms, it even shows that the fault is quite likely to extend further north across a major NW-trending fault.

Maps of the stratigraphic formations generated from the 3D model are shown in Figures 2.16 and 2.17. The final model shows that the Yarragadee Formation is present across the PMA northeast of the Mandurah Fault and west of the Darling Fault, and ranges from 580 m to 2800 m thick in some places (Fig. 2.17). Thickness variations of the Yarragadee Formation are controlled in part by the topography of the palaeoerosion surface of the Neocomian unconformity, which shows approximately 900 m or relief. However, the isopach pattern for the Yarragadee Formation is dominated by its stratigraphic basal surface which shows up to 4000 m of relief over the PMA. The well constraints for the base of the Yarragadee Formation are poor, resulting in a high degree of uncertainty of the geometry of this surface (Fig. 2.17a,b). The depth to the Neocomian Unconformity and overlying Gage Formation and South Perth Shale are comparatively well constrained, and vary significantly across the area of interest (Fig. 2.16). The deposition of the Gage Formation appears to be aerially restricted to a N-S striking trough in the central and southern parts of the area, and a thin, NE-trending corridor to the north, isolated from the main deposition centre (Fig. 2.16C). The formation thickness pattern corresponds to the deepest parts of the Neocomian Unconformity (up to 800 m thick in the central area), indicating either passive infill of an original topographic low in the unconformity surface, and/or reflecting syn-depositional fault-related accommodation space generation (Figs 2.16, 2.17). The South Perth Shale is more regionally extensive than Gage Formation, with a similar pattern of thickening in the central axis of the Dandaragan Trough and the NE-trending corridor (Figs 2.16D, 2.17). The South Perth Shale was deposited across the South Turtle Dove Ridge to the west. However, deposition of Gage Formation and South Perth Shale was absent on fault-bounded blocks in the east and northeast of the area (Fig. 2.16). The South Perth Shale thickness is not reliable offshore due to sparse data constraints. Variation in the thickness of the Gage Formation and South Perth Shale and the depth to the Neocomian Unconformity in the vicinity of the Serpentine Fault suggests differential displacement occurred along the length of the Serpentine fault during the Cretaceous (Fig. 2.17). The same argument can be applied to all other faults in the PMA model, which must have been active during the Cretaceous. Cretaceous fault activity has been demonstrated in the offshore part of the sub-basin (Bale, 2004).

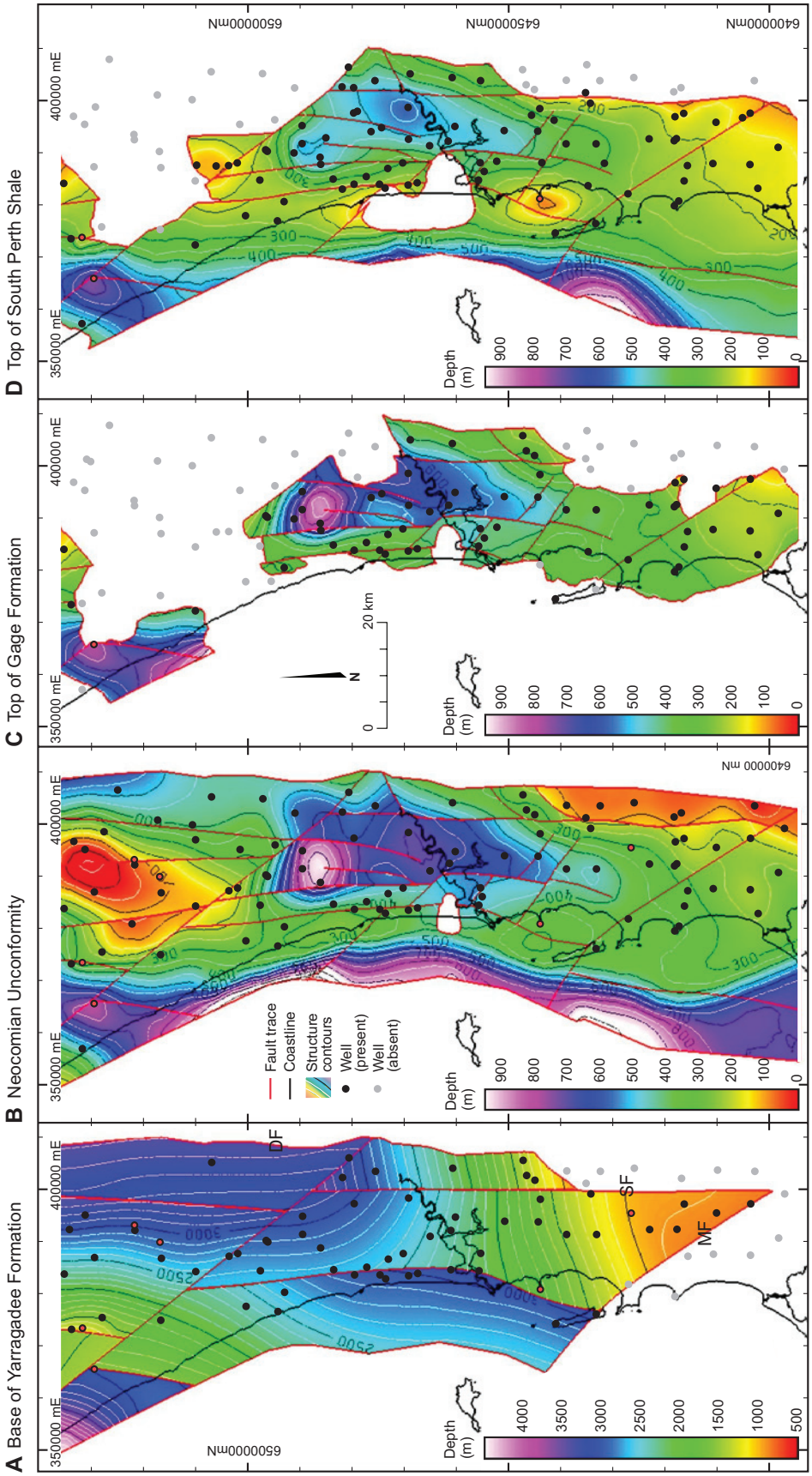

Figure 2.16: Maps showing depths in meters below sea level to geological surfaces in the PMA model. (a) Base of Yarragadee Formation. (b) Neocomian Unconformity. (c) Top of Gage Formation. (d) Top of South Perth Shale. Well constraints are shown by circles. MF = Mandurah Fault; SF = Serpentine Fault; DF = Darling Fault.

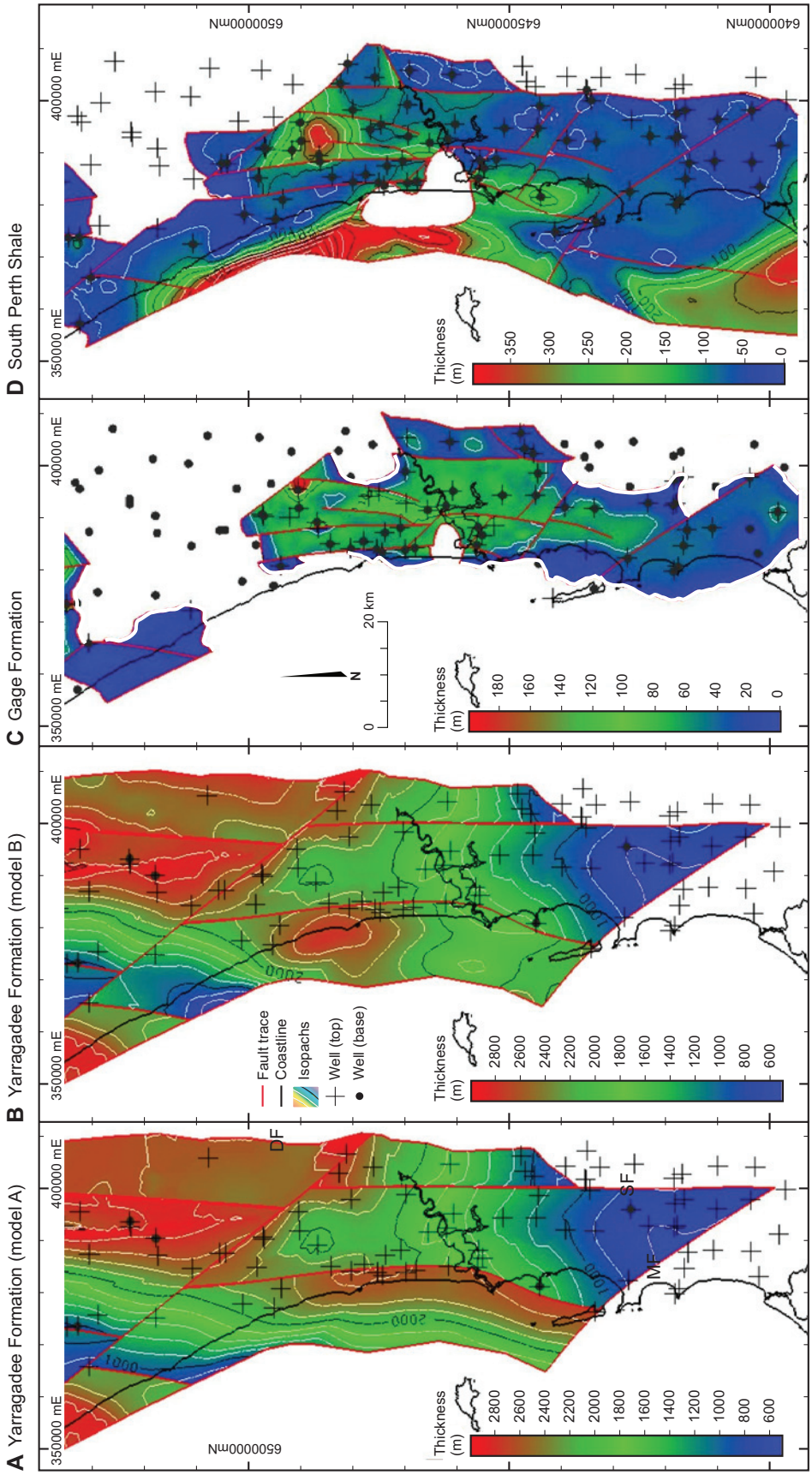

Figure 2.17: Isopach maps showing the stratigraphic thickness variations of (a) and (b) the Yarragadee Formation, (c) Gage Formation, and (c) South Perth Shale. (a) and (b) show the results of two equally likely models to illustrate uncertainty associated with scarce data points. Each model utilises the same data constraints but slightly different interpolation settings. Formation base and top constraints from well data are shown as circles and crosses, respectively. MF = Mandurah Fault; SF = Serpentine Fault; DF = Darling Fault. Only the most 'reliable' faults are shown on (a) and (b) (blue in Fig. 2.13). However, it is likely that the other faults in the PMA model also cut the Yarragadee Formation.

2.5 Discussion

2.5.1 A new structural model of the Perth Metropolitan Area

We identify a network of faults in the Perth Metropolitan Area that has not been previously recognised (Fig. 2.18). There is strong consistency between the position and orientation of faults identified via land surface topography, fluvial drainage network, geology and gravity worms from high wavelength density contrasts (Figs 2.7 and 2.18). These faults displace Pleistocene stratigraphy of the Perth Basin and extend into the basement to the east of the Darling Fault (Figs 2.7 and 2.18). They exert clear controls on the position of the Swan and Canning Rivers, wetlands, lakes and other geomorphological features of the area. It is interpreted that most of the faults in the network have displacements of tens of metres based on displacement of geological units and scarp heights. Most of the faults are not seen in gravity worms from >500 m depth. This is because either (a) anomalies associated with low displacement faults are not resolved at depth, or (b) that the faults are localised in the upper stratigraphic levels, perhaps truncating against larger faults or accommodated by distributed strain at depth. However, the trends of faults resolved by deep (>500 m) gravity worms are oblique to most common trends of surface-penetrating faults. Kinks in the deep worms align with surface faults, indicating that the larger, deep faults are displaced by faults that are not expressed in the worms. Indeed, many of the shallow worms are displaced and/or truncated by faults only seen in the geomorphology, geology and fluvial drainage network. Therefore, (a) is more likely. Furthermore, there are clearly many places where contours and subcrop patterns of most of the post-Neocomian formations in the PRAMS model coincide with faults identified in this study. However, the relationship with the faults is complex in space and time such that it is difficult to reconcile previous interpretations that the post-Neocomian stratigraphy is merely a result of passive draping over pre-existing fault blocks. A better explanation might be that fault activity continued throughout and after the Neocomian depositional hiatus, locally controlling subsidence and uplift, and thus sites of sedimentation and erosion right through the Cretaceous and Tertiary.

The trend of all fault sets identified in the Perth Metropolitan Area can be seen in regional gravity and magnetic anomaly maps in the vicinity of the Perth Metropolitan Area (Figs 1.6 and 1.7), and are, therefore, part of key fault sets that define the Perth Basin architecture. However, the approximate N-S trend of the Dandaragan Trough beneath the Perth Metropolitan Area is most likely controlled by deeply penetrating, large displacement approximately N-S trending faults, such as is seen in the deep worm data. Our study highlights an apparent disconnect between large (high displacement), deep (early?), basin-defining faults and smaller (lower displacement), ground surface-penetrating faults that control the geomorphology and drainage in the Perth Metropolitan Area. Furthermore, the position of the Darling Fault indicated by gravity worms should intersect the land surface several kilometres to the west of the present day scarp and associated geological boundary of Perth Basin sediments with Archaean rocks (Fig. 1.7). This could be due to either (a) landward erosion of an 'inactive' Darling Fault scarp and associated recent sedimentation, such that the trace of the principal displacement surface does not outcrop, and/or (b) accommodation of displacement along a series of stacked, synthetic fault surfaces, such that the principal displacement surface is blind, and slip at

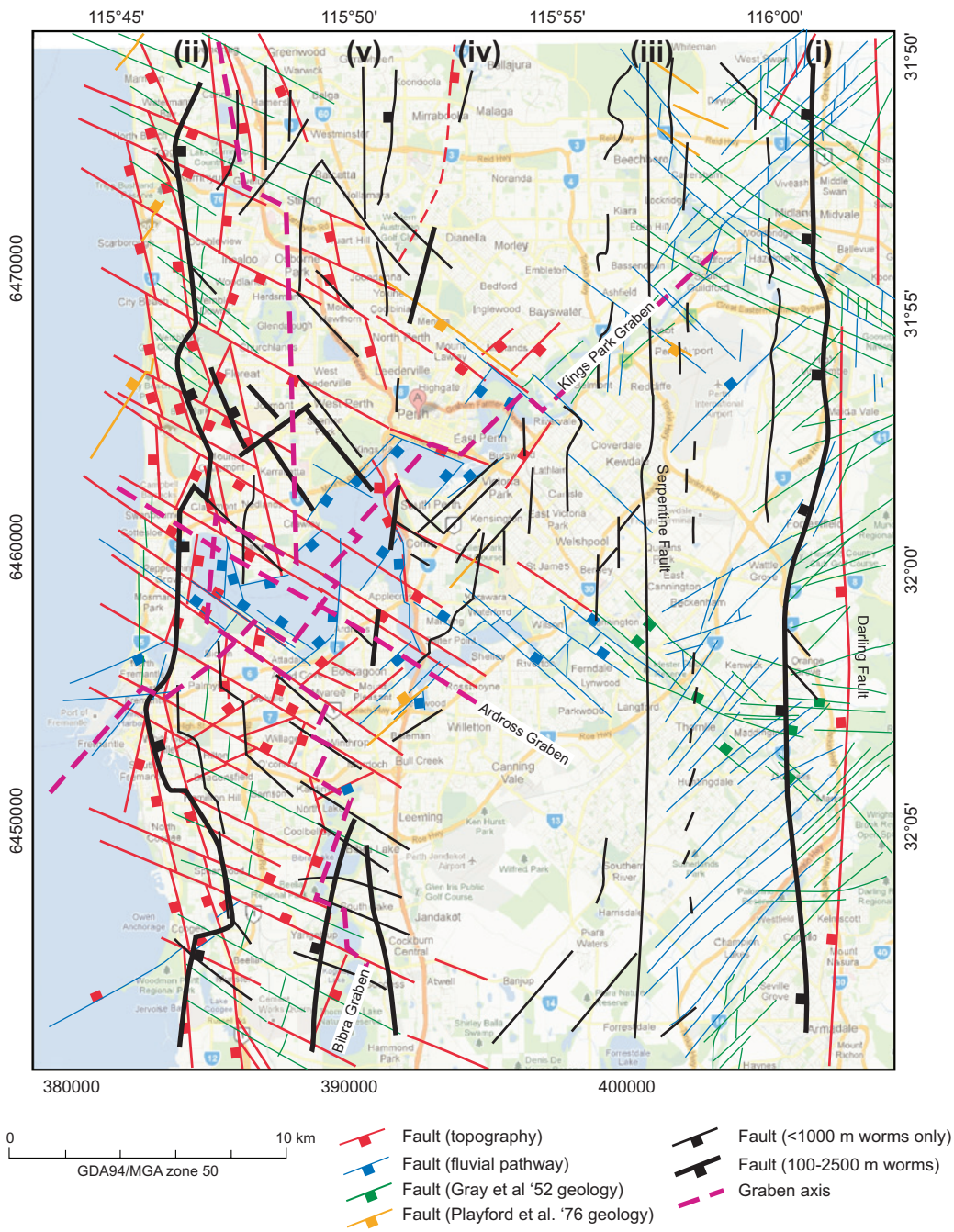

Figure 2.18: A map of the central Perth Metropolitan Area summarizing the faults identified by surface topography, fluvial drainage networks, geology and gravity worms.

the surface is accommodated by a series of faults structurally below and to the east of the main Darling Fault. Further investigation via 3D modelling of the stratigraphy of the Perth Metropolitan Area would provide a more robust understanding of these issues.

The newly identified fault network is spatially heterogeneous. We emphasise that this is largely because of the lack of constraints in some areas of the map. Therefore, the network in the PMA 3D model represents a conservative interpretation, and many more faults are likely to exist in similar orientations.

2.5.2 Controls on the geometry of Jurassic to the Cretaceous stratigraphic formations in the central Perth Basin

The depth to base of the Yarragadee varies considerably in the Perth Metropolitan Area (Fig. 2.16). In the north, the base of the Yarragadee slopes toward the Darling Fault. The base of the Yarragadee shallows to the west and south in the Perth Metropolitan Area. The general form of the deepest (>2.5 km) parts of this surface forms a broad basin with a NNE-SSW axis. This geometry is consistent with a differential subsidence associated with development of an asymmetric graben (or half graben) bound by N-S and NE-SW faults formed during NW-SE extension, either predating the deposition of the Yarragadee Formation associated with Rift phase I, or during Rift Phase II synchronous with deposition of the Yarragadee Formation (Fig. 2.3). However, structures at these depths are not resolved by the gravity worms (only upward continued to 2.5 km). Given that the Yarragadee Formation comprises fluvial, floodplain and lagoon lithofacies, which would have been deposited close to sea level, the southward and westward shallowing of the base of the Yarragadee in the case of syn-depositional faulting represents south and westward progradation of the Yarragadee fluvial system over Cattamarra Coal Measures which implies a proximal, NE source of Yarragadee sediments from the Yilgarn Craton in the PMA. Alternatively, the geometry of the base of the Yarragadee Formation could be caused by post-sedimentation differential subsidence and/or uplift along the Darling fault. The absence of the Yarragadee Formation southwest of the Mandurah Fault indicates that this fault was active during or shortly after the time of deposition of the Yarragadee Formation elsewhere, which resulted in either no deposition locally, or erosion of the Yarragadee Formation to the southwest. Cattamarra Coal Measures are the lowermost stratigraphic units intersected by wells in this location.

The Neocomian Unconformity has over 600 m of relief in the Perth Metropolitan Area, which strongly influences isopach map pattern of the Yarragadee Formation (Figs 2.16a, 2.17a,b). Some of the topography on the Neocomian Unconformity coincides with the position of faults. However, it is not completely clear whether the topography of the unconformity is the result of differential erosion controlled by pre-existing faults, or whether depth variations are a consequence of syn- to post-Neocomian faulting of a relatively planar unconformity surface. The sedimentology and isopach patterns of the overlying strata suggest that faulting continued through to at least the time South Perth Shale deposition. In any case, the deepest buried parts of the unconformity are consistent with the axis of a N-S trending graben aligned with the Dandaragan Trough. In the Perth Basin, the major deep aquifers are part of the Permian–Early Cretaceous sedimentary succession, which is highly faulted throughout the basin. Although the Warnbro Group sediments are less faulted than older sediments, we postulated that those sediments are also faulted to a lesser extent, following work done in the offshore part of that sub-basin (Bale, 2004).

The subsequent deposition of the Gage Formation during the early Cretaceous was restricted in aerial extent. Even in the initial ‘fault-free’ stratigraphic mode, its boundary aligns with NW and N-S fault systems, which indicates that the Gage Formation was either a consequence of deposition controlled by concurrent faulting, and/or the initial ‘passive’ fill of bathymetric lows on the Neocomian

unconformity palaeosurface during marine transgression. The activity of NW-SE and N-S trending faults is consistent with post-breakup NE-SW extension during the early Cretaceous (Fig. 2.3). The strong links between faults and stratigraphic geometry suggests that syn-deposition faulting is the most likely explanation. The influence of NW-SE and N-S trending faults can also be seen in the depositional extent and isopachs of the South Perth Shale, where the thickest deposition occurred along NNE-SSW trending domains. The Darling Fault, Serpentine Fault and a NW-trending fault must have formed prominent, emergent scarps during deposition of the Gage Formation and South Perth Shale. The Leederville Formation is thickest along a N-S trending, fault-bounded asymmetric trough in the west and a NNW-SSE trough in the east of the PMA, consistent with activity of N-S and NW-SE trending faults, including the Darling Fault. This pattern of sedimentation persisted during deposition of the Coolyena Group. However, faults shown on seismic lines offshore in Vlaming sub-basin are older than the Warnbro Unconformity (i.e., they do not affect formations younger than the Leederville Formation). Therefore, it is unlikely that faults in the PMA have accumulated significant slip since the Warnbro unconformity.

The well constraints for the base of the Yarragadee Formation in the 3D Perth Metropolitan Area model are not adequate to test how some of the low-displacement faults present in post-Neocomian stratigraphy affect the Jurassic stratigraphy. However, it is geologically reasonable to assume that these faults can be extrapolated to below the Neocomian Unconformity.

2.5.3 Implications of the new 3D model for geothermal exploration

Improving the geological knowledge of the Perth Metropolitan Area leads to better estimates of depth for geothermal exploration targets. Even though there are inherent structural simplifications, the new 3D model provides the most robust current interpretation of stratigraphic formation top surfaces, down to the top of the Cadda Formation in some places. Although the top of formations younger than Neocomian are well defined on the onshore basin, the geometry of the surfaces for the top and base of the Yarragadee Formation are much less certain. This should be an important consideration where the Yarragadee Formation is targeted for geothermal exploration.

The new geological model also enables checks to be made on the three dimensional connectivity between the different stratigraphic formations, either via unconformity- or fault-related juxtaposition. The 3D formation juxtaposition can significantly influence heat and fluid behaviours. For example, anomalies in fluid and heat distributions have been observed in the Perth Metropolitan Area that map precisely to the 3D architecture constrained by the new PMA model (Davidson and Yu, 2006) (Reid et al., 2011). Investigation of the effects of newly identified fault network on these anomalies has been done via hydrothermal modelling within WAGCoE (see associated report by Reid et al., 2012).

The straightforward, multidisciplinary approach presented here for identifying faults can be utilized in many locations with sparse data constraints. The iterative methodology provides increasingly complicated structural scenarios which can be tested with future data collection, and encourages well-informed exploration.

2.5.4 Limitations of the new 3D model

Some of the limitations of the 3D geological model are discussed below:

- Only formations down to the Yarragadee Formation are present in this model. Deeper formations have not been modelled due to the lack of data constraints.
- The inferred fault network is more detailed under Perth city, only because this area corresponds to the extent of the gravity worms. Additional gravity surveys would be necessary to get the same resolution of the gravity worms in the central part of the model. It is anticipated from comparisons with the north Perth Basin, which is better exposed and studied, that numerous small-scale faults exist in the modelled area. However, the lack of currently available data constraints prohibits their identification. Variability in the resolution of the fault network is of paramount consideration in the assessment of geothermal resources.
- Fault throws are difficult to quantify in sediments younger than Neocomian due to lack of data. Therefore, to get the geometry of the base of the Yarragadee Formation, we used a larger scale model that includes the whole Central Perth Basin and modelled the entire sediment succession from the basement to the Neocomian Unconformity. This provides loose constraints on the base of the Yarragadee Formation.
- In our model, the fault dips are uniform and were determined from gravity worms, 2D gravity modelling and extrapolated from outside the area of interest. However, it is likely that fault plane dips change with depth as shown in the North Perth Basin (Mory and Iasky, 1996) and the South Perth Basin (Crostella and Backhouse, 2000). It is anticipated that this uncertainty would have only secondary effects on the overall model geometry (Fig. 2.19).
- The offshore part of the model is poorly constrained, even for the Warnbro Group sediments, because of the lack of data.

2.5.5 Goals for future research / Recommendations for further work

- Acquisition and analysis of high resolution LIDAR topographic data for the Perth Metropolitan Area. A higher spatial resolution dataset (to approximately 3x3x2 m) could help improve the location of faults identified in this report and could lead to the identification of more faults.
- The 3D geological model could be improved by modification of the fault geometry at depth to match 2D gravity forward models (Fig. 2.19).
- An expansion of the high-resolution gravity survey to cover the full modelled PMA area would lead to a significant improvement in resolution of sub-surface faults.
- The geometric uncertainty of the 3D model could be quantified via the information entropy approach developed by WAGCoE (Wellmann et al., 2010; Reid et al., 2012).
- Pursue seismic characterization of the subsurface to provide extra constraints on structural controls.

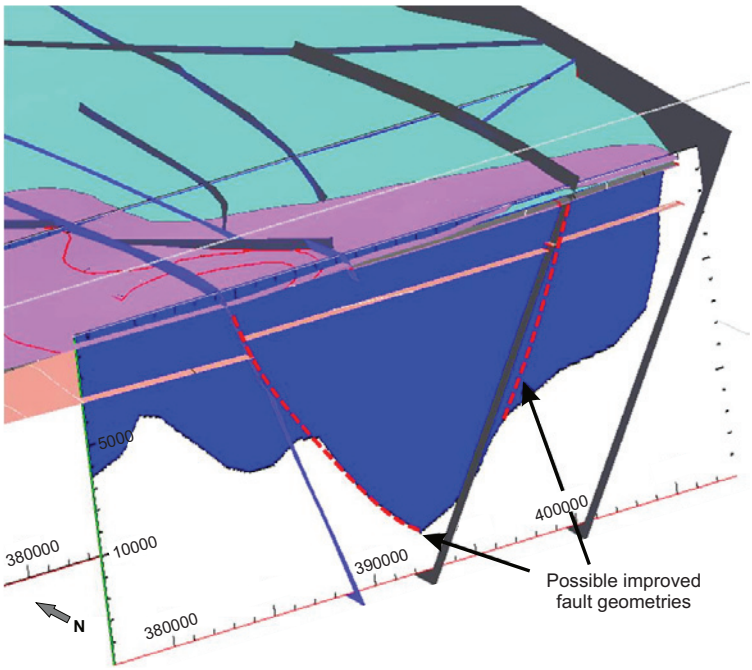

Figure 2.19: Cut-away section of the PMA model showing the position of stratigraphic boundaries and faults superimposed on 2D gravity forward model results. The faults align reasonably well with the gravity models, but could be improved by having curved fault planes at depth.

2.6 Summary

Knowledge of the structural architecture and bedrock geometry under Perth is a vital prerequisite for understanding subsurface fluid flow. This understanding is fundamental to the identification of geothermal prospects and to effective aquifer management in the metropolitan area. This study integrates information from geology, hydrogeology, digital elevation data and new potential field and seismic data to develop a new structural interpretation for the Perth Metropolitan Area as a subset of the whole Perth Basin. The upper part of the section (down to the top of the Yarragadee Formation) has made extensive use of the Perth Regional Aquifer Model (Davidson and Yu, 2006) and this has been used to produce a new 3D computer model using Skua software. The lower part of the section (from the Yarragadee Formation downwards) has made use of a newly acquired gravity survey of the Perth Metropolitan Area. The results of two vertical seismic profiling experiments using boreholes at St Hilda's School in Mosman Park and a Department of Water borehole in Kensington were inconclusive. The gravity survey was on a 1.5 km x 1.5 km grid and has been used to develop 'worms' and forward models of 2D gravity profiles. Modelling of the new gravity data shows that bedrock is shallower near the coast and this is consistent with previous offshore gravity studies. The new geophysical data have been integrated with existing stratigraphic data from 6 petroleum wells and approximately 180 water boreholes, maps of surface geology and geomorphology to allow us to make a completely new interpretation of the fault network and produce a 3D geological model of the Perth Metropolitan Area. The newly identified faults strongly influence the geometry of confined aquifers in the Perth Basin, and specifically the Perth metropolitan area and, therefore, could be highly significant in controlling the palaeo- and modern day fluid flow in areas relevant to geothermal exploration. The new 3D model provides an entirely new insight into the tectonics and stratigraphic architecture of the subsurface geology in the Perth Metropolitan Area. The resulting structural model enables 3D fluid flow and thermal transport simulations and provides a context in which to explain empirically-determined geothermal anomalies in the Perth Metropolitan Area.

3. CHARACTERISATION OF THE SEDIMENTARY/LITHOLOGICAL HETEROGENEITY OF POTENTIAL GEOTHERMAL TARGET ROCKS IN THE PERTH METROPOLITAN AREA

3.1 Introduction

The Perth Basin has a deep (up to 15 km) and varied (Permian-Recent) sedimentary fill, including numerous unconfined and confined groundwater aquifers (Crostella and Backhouse 2000, Davidson 1995, Harris 1994, Playford et al. 1976), some of which are also important hydrocarbon reservoir units. The Triassic Lesueur Sandstone and Jurassic Yarragadee are two of the most important aquifer units, with thicknesses of up to 2,000 m, and subsurface depths between 50 ->2,000 m, respectively. Therefore, these units are key potential targets for shallow geothermal heat extraction. A predominantly fluvial origin has been inferred for the Lesueur Sandstone and Yarragadee Formation. However, significant spatial and temporal variations in sedimentology, porosity and permeability have been identified (Brownhill 1966, Davidson 1995, Johnson 1965, Jones and Nicholls 1966, McWhae et al. 1958, Playford et al. 1976, Smith 1967). Sedimentary depositional environments exert primary control lithology and rock unit geometry, and lithological variations exert a first order control on permeability in sedimentary rocks. Improved understanding of lateral and vertical variations in depositional settings and their influence on lithological heterogeneity and sedimentary geometries are essential to better characterise flow variability and connectivity within the system. Examination of spatial and temporal changes in depositional setting will also be pertinent to evaluating controls on environmental change and Mesozoic basin evolution in Western Australia.

This study focuses on the Mesozoic stratigraphy of the greater Perth metropolitan area (central Perth Basin), which is of significant interest for geothermal exploration. Several petroleum exploration wells intercept the early Mesozoic stratigraphy in the region of interest (Fig. 3.1). Of these, core was recovered from four wells. From south to north, these are Pinjarra-1, Cockburn-1, Gingin-1 and Gingin-2, intersecting Triassic to Jurassic stratigraphy assigned to the Lesueur Sandstone, Eneabba Formation, Cattamarra Coal Measures, Cadda Formation and Yarragadee Formation (Brownhill 1966, Johnson 1965, Jones and Nicholls 1966, Smith 1967) (Fig. 3.1). Formations in the central Perth Basin wells were dated by palynology and formation boundaries were interpreted from breaks on the Induction-Electrical and Gamma-ray sonic logs (Brownhill 1966, Johnson 1965, Jones and Nicholls 1966, Smith 1967).

The sedimentology has been described in the well completion reports for each well by formation and only at a very basic level (e.g., the Yarragadee formation consists of sandstone and mudstone). A more detailed description of the sedimentology and depositional environment for these formations exists for sparse outcrops over 300 km away in the northern Perth Basin (Crostella and Backhouse 2000, Playford et al. 1976). To date, a lithofacies analysis of these key stratigraphic units is absent for these units in the central Perth Basin. This study presents new data from sedimentary logging, lithofacies analysis and interpretation of the environment of deposition, with the aim of answering the following questions:

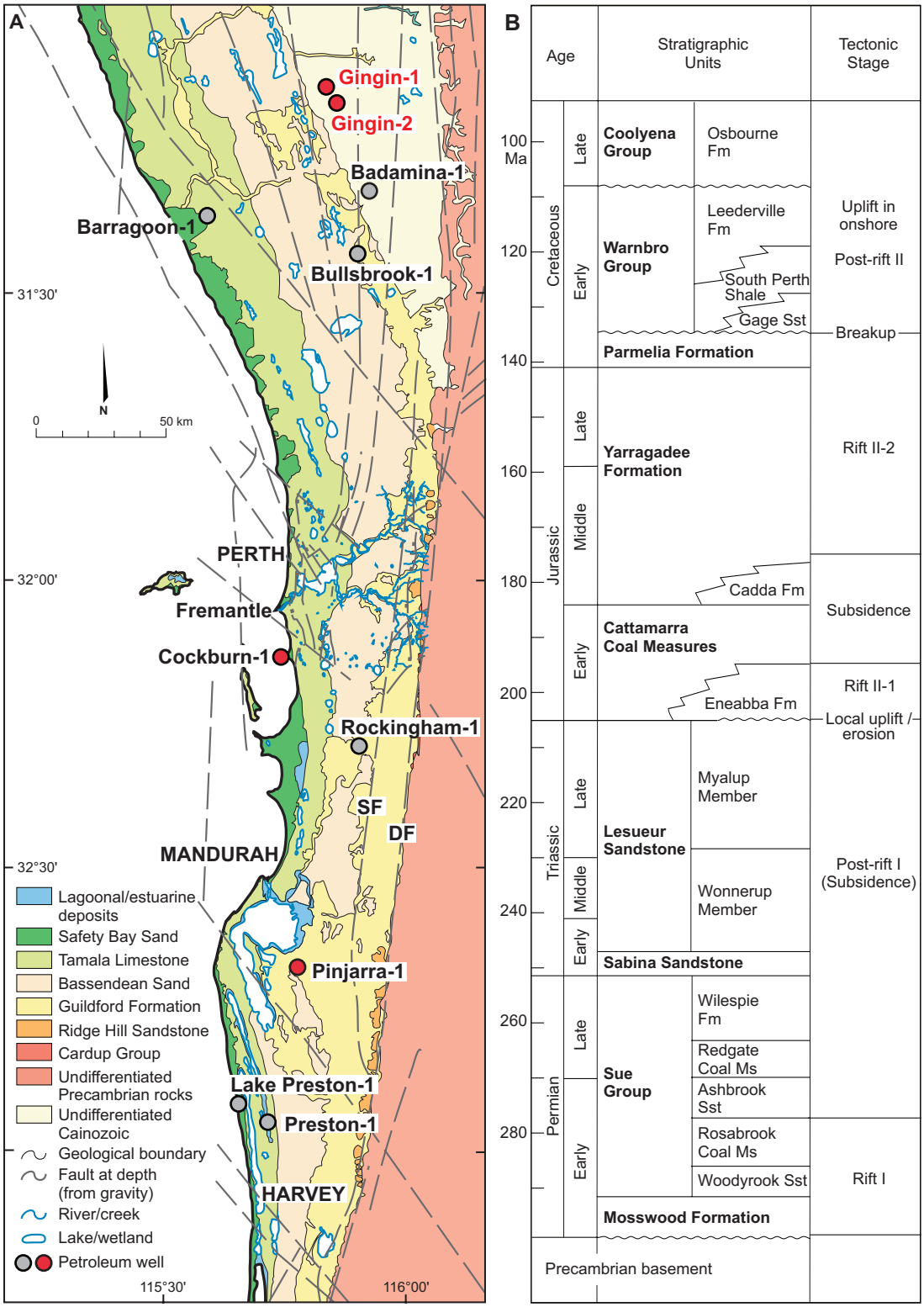

Figure 3.1: A. Geological map of the central Perth Basin showing the location of onshore petroleum wells. Wells used in this study are in red. Geology after Playford et al. (1976). 'Faults at depth' control pre-Cretaceous basin architecture and are interpreted from vertical gradient of isostatic residual gravity, after Wilkes et al. (2011). B. Generalised stratigraphy of the Perth Basin, after Crostella and Backhouse (2000). Tectonic stages after Song & Cawood (2000).

1. What is the lithological heterogeneity of each formation? What is the lithofacies variability between and within formations – are they lithologically distinctive? What are the proportions of sandstone and mudstone for each formation?
2. What sedimentary structures are present that could form flow baffles, barriers or permeability anisotropy?
3. Are there trends in lithofacies stacking over long or short term, or spatially across the basin?
4. How vertically continuous are the sandstones and mudstones? Can the units /styles be correlated between wells?
5. Can lithofacies types, associations and stacking patterns be used to predict rock unit architecture?

3.2 Summary of the stratigraphy of Pinjarra-1, Cockburn-1, Gingin-1 and Gingin-2

Pinjarra-1 is a 4572 metre-long petroleum exploration well drilled proximal to Pinjarra, Western Australia (Fig. 3.1). It intersects Quaternary sands (+11 to -14 m above sea level), the Upper Jurassic Yarragadee Formation (14-139 m below sea level), the Lower Jurassic Cattamarra Coal Measures (139 – 1192 m below sea level), Eneabba Formation (formerly 'Multicoloured' Members of the Cockleshell Gulley Formation; 1192 – 2361 m below sea level), and the Upper Triassic Lesueur Sandstone (2361 – 4562 m below sea level) (Jones and Nicholls 1966). The Yarragadee Formation is unconformable with the overlying Quaternary sands and the underlying Cattamarra Coal Measures (Ghori 2008, Mory and Iasky 1996). The cored areas of Pinjarra-1 consist only of the Cattamarra Coal Measures, the Eneabba Formation and the Lesueur Sandstone.

Cockburn-1 is the most proximal well to the Perth metropolitan area, was drilled to a depth of 3,051 m, and currently provides the best opportunity for direct observations and measurements of potential geothermal target rocks beneath Perth. Formation and member depths are summarized Table 3.2. Cockburn-1 cuts through unconsolidated sandstone and laterite, the South Perth Shale, the Yarragadee Formation, the Cadda Formation and the Cattamarra Coal Measures (formerly Cockleshell Gulley Formation) (Crostella and Backhouse 2000, Smith 1967). The Yarragadee Formation is unconformable with the overlying South Perth Shale, but conformable with the Cadda Formation. The Cadda formation is unconformable and the underlying Cattamarra Coal Measures (Crostella and Backhouse 2000, Mory and Iasky 1996). The cored intervals of Cockburn-1 consist only of the Yarragadee Formation, the Cadda Formation and the Cattamarra Coal Measures. The Yarragadee Formation is also significantly eroded at Cockburn-1, with a total thickness of only 1412 m (compared to Gingin field with a thickness of ~2970 m).

Gingin-1 and Gingin-2 are 4544 and 4482 metre-long petroleum exploration wells, respectively, that were drilled proximal to Gingin, Western Australia (Fig. 3.1). Formation and member depths are summarized Table 3.2. The wells cut through unconsolidated sandstone and laterite, the Leederville Formation (legacy, Moochamullah Sandstone), the Parmelia Group (Jervoise Sandstone and Otorowiri Formation), the Yarragadee Formation, the Cadda Formation and the Cattamarra Coal Measures (Brownhill 1966, Crostella and Backhouse 2000, Johnson 1965, Logan 1966). The Yarragadee

Formation is unconformable with the overlying Quaternary sands, but conformable with the Cadda Formation. The Cadda formation is unconformable with the underlying Cattamarra Coal Measures (Crostella and Backhouse 2000, Mory and Iasky 1996). The cored intervals of Gingin-1 consist of the Yarragadee Formation, the Cadda Formation and the Cattamarra Coal Measures, whereas the cored intervals of Gingin-2 consist only of the Cattamarra Coal Measures.

Formation	Age	Pinjarra-1	Cockburn-1	Gingin-1	Gingin-2
Yarragadee Formation	Lower Cretaceous/ Upper Jurassic	n/a	-	*Microcachryidites antarticus*	n/a
Cadda Formation	Middle Jurassic	n/a	-	*Dinophyaceae Gonyaulax*	n/a
Cattamarra Coal Measures	Lower Jurassic	*Classopollis torosus; Circulina sp.*	-	*Classopollis torusus; Circulina sp.*	*Classopollis - Circulina*
Eneabba Formation	Lower Jurassic	-	n/a	n/a	n/a
Lesueur Sandstone	Upper Triassic	*Alisporites (Pteruchipollinites); Aratrisporites paenulatus*	n/a	n/a	n/a

Table 3.1: Summary of key biostratigraphic polymorphs used to determine formation ages in each well.

Formation	Age	Pinjarra-1 Formation top height (m)		Cockburn-1 Formation top height (m)		Gingin-1 Formation top height (m)		Gingin-2 Formation top height (m)	
		Below surface	Relative to sea level	Below surface	Relative to sea level	Below surface	Relative to sea level	Below surface	Relative to sea level
Sandstone 7 laterite	Quaternary	Start of hole	+11	Start of hole	+7	Start of hole	+203	Start of hole	+266
Leederville Formation	L Cretaceous	n/a	n/a	n/a	n/a	94	+109	n/a	n/a
South Perth Shale	L Cretaceous	n/a	n/a	40	-33	n/a	n/a	n/a	n/a
Jervoise Sandstone	L Cretaceous	n/a	n/a	n/a	n/a	189	-14	280	-14
Otorowiri Formation	L Cretaceous	n/a	n/a	n/a	n/a	319	-116	401	-135
Yarragadee Formation	U Jurassic	25	-14	313	-306	356	-153	430	-164
Cadda Formation	M Jurassic	n/a	n/a	1725	-1718	3314	-3111	3399	-3133
Cattamarra Coal Measures	L Jurassic	150	-139	1914	-1907	3610	-3407	3591	-3325
Eneabba Formation	U Triassic	1203	-1192	n/a	n/a	n/a	n/a	n/a	n/a
Lesueur Sandstone	U Triassic	2372	-2361	n/a	n/a	n/a	n/a	n/a	n/a
End of hole		*4573*	*-4562*	*3054*	*-3047*	*4544*	*-4301*	*4482*	*-4216*

Table 3.2: Summary of key stratigraphic depths for each well.

Table 3.1 summarizes the key biostratigraphic *palynomorphs* used to discriminate age, listed per well and per formation. The full fossil listing may be found in each of the well completion reports. Pinjarra-1 consists primarily of the Lower Jurassic Cattamarra Coal Measures and Eneabba Formation (formerly combined as Cockleshell Gully Formation) and the Upper Triassic Lesueur Sandstone. Classopollis torosus and Circulina sp. are the key biostratigraphic indicators for the Cattamarra Coal Measures, being of Lower Jurassic age. The Upper Triassic Lesueur Sandstone is characterized primarily by Alisporites (Pteruchipollinites) and Aratrisporites paenulatus. Cockburn-1 consists of the Lower Cretaceous/Upper Jurassic Yarragadee Formation, the Middle Jurassic Cadda Formation and the Lower Jurassic Cattamarra Coal Measures. Gingin-1 consists of the Lower Cretaceous/ Upper Jurassic Yarragadee Formation, the Middle Jurassic Cadda Formation and the Lower Jurassic Cattamarra Coal Measures. Microcachryidites antarticus is a limited biostratigraphic indicator,

along with others in the assemblage, which suggests a basal Cretaceous to Upper Jurassic age. With assemblage change, this becomes progressively older downhole, towards a Middle Jurassic age, before definitively changing to the Middle Jurassic Cadda Formation. This is characterized primarily by the onset of Dinophyaceae Gonyaulax. The Cattamarra Coal Measures in Gingin-1 exhibits the same biostratigraphic indicator *palynomorphs* as in Pinjarra-1: Classopollis torosus and Circulina sp. Gingin-2 has limited core, and only contains the Lower Jurassic Cattamarra Coal Measures. Similar to the other wells, Classopollis and Circulina palynormorphs (undifferentiated) are present.

3.3 Approach

This study comprises a lithofacies analysis of the Mesozoic sediments of the central Perth Basin. Sedimentary rocks were subdivided into lithologically distinct facies (Walker and James 1992). Each lithofacies has distinct physical characteristics, such as grain size, grain sorting, sedimentary structures and colour, so that they are recognisably different in core and/or outcrop. The environment of deposition exerts a primary control on these characteristics, and so a lithofacies scheme is commonly interpreted in terms of sedimentary environment. Several facies (or sub-facies) may be produced in a given palaeo-environment, which gives rise to 'facies associations' and/or high-resolution variability within particular lithofacies, depending on how the facies scheme is developed. These key points mean that lithofacies analysis is a useful approach that (a) provides insight into the evolution of palaeo-environment in space and/or time, which in turn enables an interpretation of the likely geometry of the rock bodies, and (b) provides a physical property-based rock classification framework and a context for the interpretation of petrophysical tests, such as porosity and permeability. Note that because sedimentary structures have a key role in lithofacies analysis, this approach is generally restricted to observations made in outcrop and drill core rather than drill cuttings. Therefore, core from a very limited number of deep petroleum wells comprises the only opportunity for direct sedimentary analysis.

Sedimentary logging at approximately 1:1000 scale was done on the cored intervals from Pinjarra-1, Cockburn-1, Gingin-1 and Gignin-2 petroleum exploration wells at the Western Australia Core Library Facility, Perth. Very little core was taken in each well, with individual cored intervals typically 1-5 m long with 100-150 m spacing. Despite such an incomplete record of the central onshore Perth Basin stratigraphy in core, the regular length and spacing of the cored intervals provides a (relatively) statistically unbiased snapshot of the formations.

Core totalled 60 m from 28 intervals (with ~150 m spacing) from Pinjarra-1 that spans the Lesueur Sandstone, Eneabba Formation and Cattamarra Coal Measures; 65 m from 26 intervals from Cockburn-1, 86 m from 28 intervals from Gingin-1, and 97 m from 8 intervals from Gingin-2 wells that span the Yarragadee and Cadda Formations, and the Cattamarra Coal Measures. Note that core depths have been adjusted from those marked on the core trays for several intervals in Cockburn-1 to account for errors in the driller's depth marks during core recovery (Logan 1966). This involved subtracting 9.1 m from cores #12 (approximately 1099 m) to #17 (approximately 1913 m).

Core logging was undertaken at the Geological Survey of Western Australia core library facility in Perth. The lithology, colour, sedimentary structures, grain size, sorting, roundness/sphericity and lithofacies was recorded for each cored section. These paper logs were then digitized into WellCAD®; a digital version can be accessed through WellCAD. This provides an efficient reference, from which data is easily exported into Excel (exported in LAS format, comma delimited). Sedimentary logs were used to develop a lithofacies scheme. Logs were subsequently processed to determine (a) the cumulative downhole lithofacies distribution; (b) the cumulative lithofacies thickness per lithofacies; and (c) the continuous lithofacies thickness of each lithofacies.

3.4 Results

3.4.1 Description of the lithofacies scheme for the Mesozoic strata of the central Perth Basin

Digital copies of the original sedimentary logs, digitised WellCAD files and associated data tables can be found in Stütenbecker and Timms (2011) and Olierook et al. (2012a-d). Nine lithofacies have been identified in the cores, and are summarized in detail in Fig. 3.2. These are common in fluvial environments (Miall 1992, 1996) (Fig. 3.3), and comprise: clean medium sandstone to gravel, variably cross-bedded to homogenous barforms and fluvial channel fill deposits formed under variable energy conditions (lithofacies A-B), stacked 2D and 3D ripple cross-laminated fine sandstones associated with moderate to low energy conditions (lithofacies C), pale grey homogenised floodplain palaeosols with rootlets (Lithofacies D), brownish grey muddy bioturbated sandstone with slump and dewatering structures associated with swampy/lagoonal conditions (lithofacies E), finely interbedded trough cross-laminated fine sandstone crevasse splays and siltstone overbank deposits (lithofacies F); and mid to dark brown laminated mudstone to fine sandstone associated with swampy overbank to lagoonal conditions (lithofacies G).

Lithofacies A has been divided into three subfacies: Lithofacies Ai comprises beds of coarse sand to gravel clasts; Lithofacies Aii is typically cross bedded medium to very coarse sand with centimetre-scale fluctuations in grain size that define foresets; Lithofacies Aiii is typically massive, and predominantly coarse to very coarse sandstone. Lithofacies B is predominantly medium sand with variably preserved flaser laminations draped by clay, organic material and/or mica. Organic fragments (coal and plant debris) are common in lithofacies C to G, and thin (up to 5 centimetres thick) coal layers are commonly associated with lithofacies D and E. Grain sorting generally decreases from lithofacies A to G. Bioturbation in lithofacies E and G comprises simple sand-filled horizontal burrows with bioturbation index (Taylor and Goldring 1993) ranging from 2-4, and the occasional escape burrow. Lithofacies F is highly variable in grain size, and can appear heterolithic in places. Rare synaereses cracks found in lithofacies G indicate subaqueous shrinkage rather than desiccation, and are therefore, not an indication of subaerial exposure.

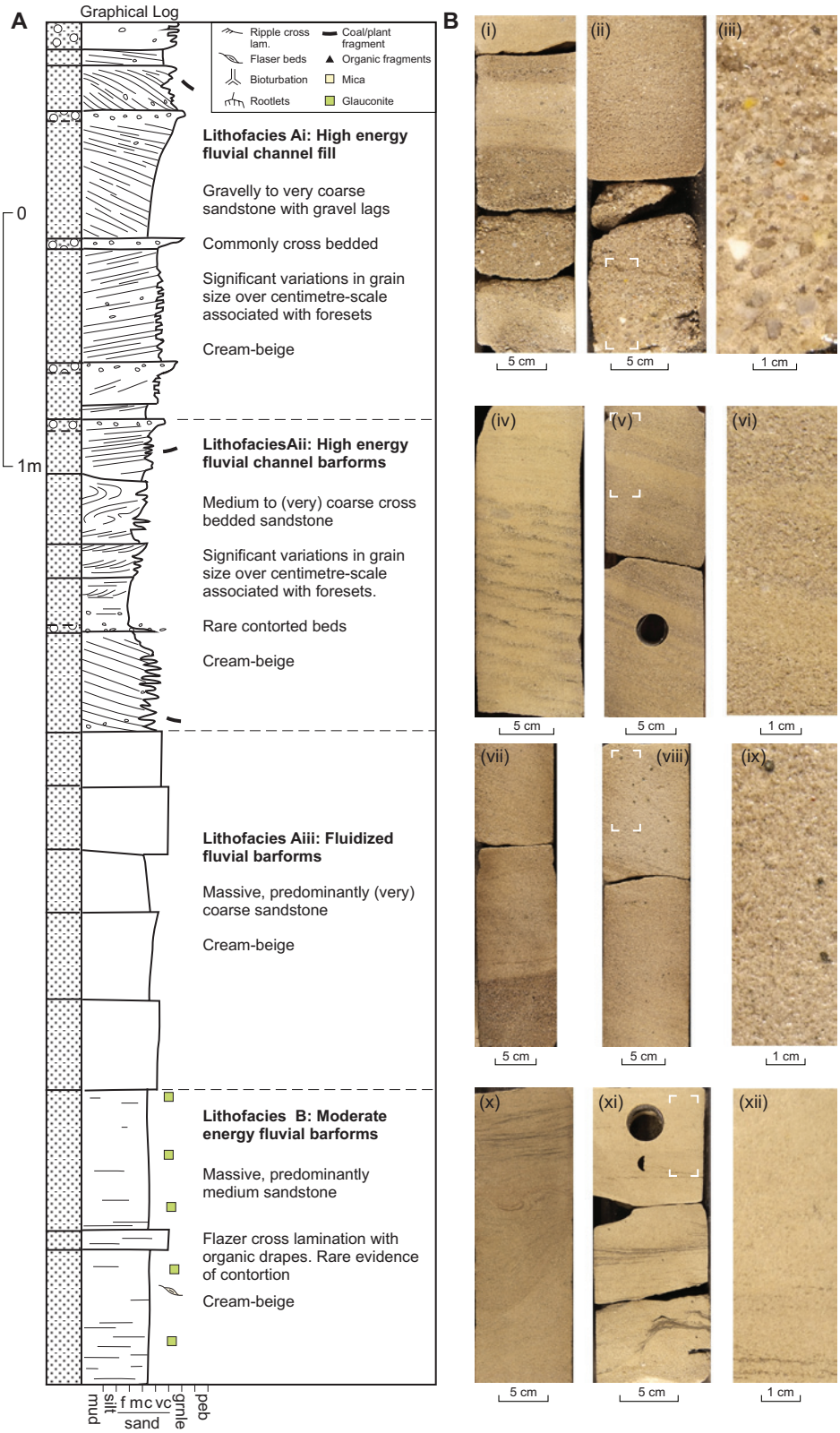

Figure 3.2: A summary of the lithofacies scheme developed for the Mesozoic stratigraphy of the central Perth Basin. A. Graphical sedimentary logs and descriptions. B. Example core photographs from Cockburn-1.

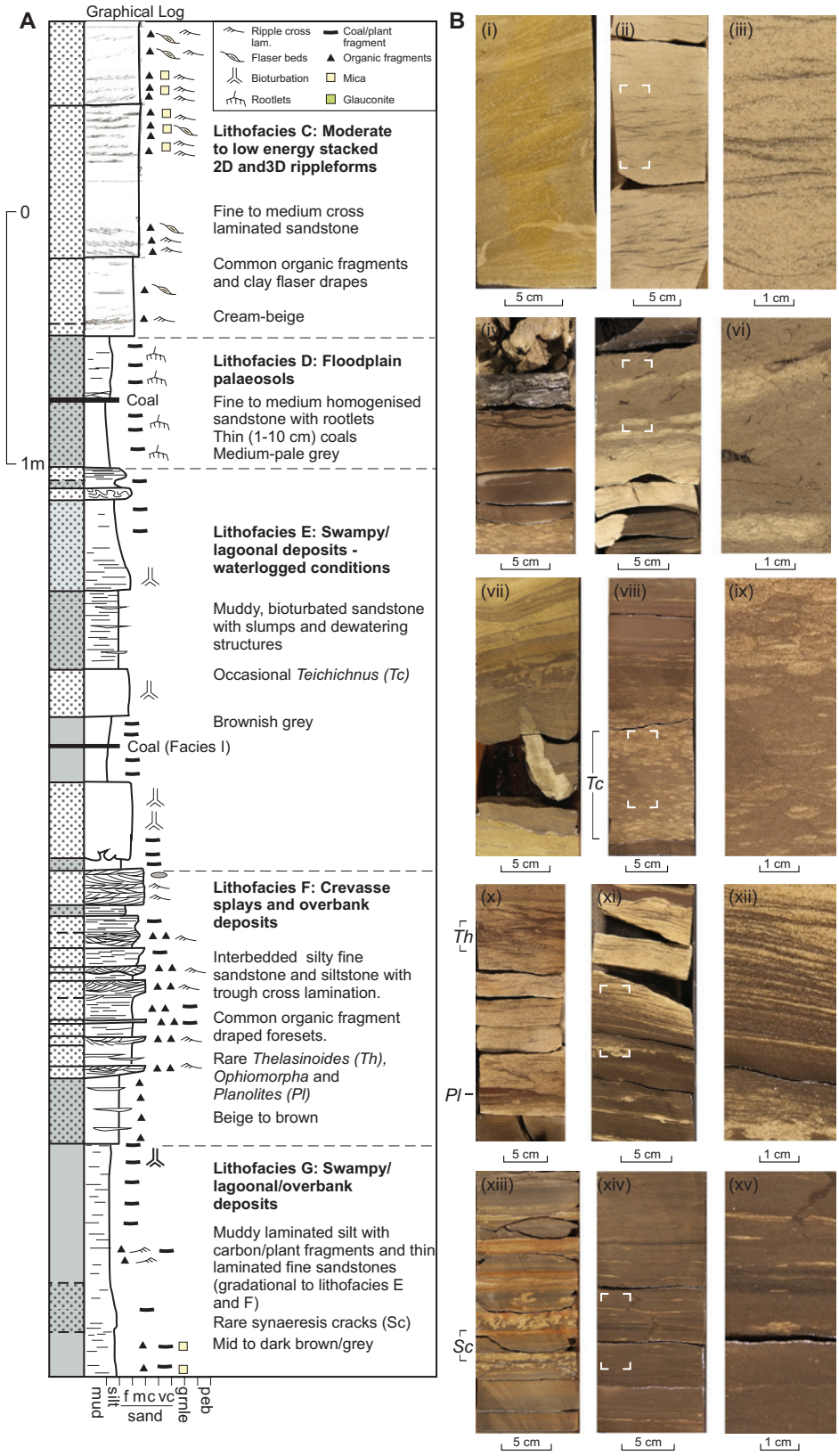

Figure 3.2 continued: A summary of the lithofacies scheme developed for the Mesozoic stratigraphy of the central Perth Basin. A. Graphical sedimentary logs and descriptions. B. Example core photographs from Cockburn-1.

3.4.2 Spatial and temporal distribution of lithofacies in drill core

The cores from all four wells show high downhole variability in lithofacies. In Pinjarra-1, over 80% of the cored intervals of Lesueur sandstone comprise sands and gravels of lithofacies A and B (predominantly Ai and Aii). These coarse facies are interspersed with intervals of lithofacies D and G in the upper part of the Lesueur sandstone. The overlying Eneabba Formation predominantly comprises lithofacies F and G (combined 67%), with 24% lithofacies A occurring lower in the stratigraphy (Fig. 3.4). The Cattamarra Coal Measures in Pinjarra-1 are dominated by fine grained and heterolithic lithofacies E, F and G (combined ~85%), with the remainder of the cored intervals only (~15%) comprising high-energy fluvial lithofacies Aiii (Fig. 3.4). By contrast, the cored intervals of Cattamarra Coal Measures in Cockburn-1 are much more variable, and have a greater proportion of high-energy fluvial lithofacies Ai and Aiii (Fig. 3.4). Almost 50% of the only cored interval of the Cadda Formation in Cockburn-1 is lithofacies G, with most of the remainder comprising palaeosols (lithofacies D) and low-energy fluvial lithofacies C (Fig. 3.4). The Yarragadee Formation above is very variable in distribution, with no particular stratigraphic succession in lithofacies types in any of the studied wells. It is dominated (~66%) by fluvial sand and gravel lithofacies, with the remainder containing significant proportions of lithofacies D to G (Fig. 3.4). Units of high energy fluvial lithofacies have variable thicknesses and are interbedded throughout the Cockburn-1 well. The clean sandstones/gravels are most abundant in cored intervals from the base of the Yarragadee and top of the Cadda Formations (Fig. 3.4).

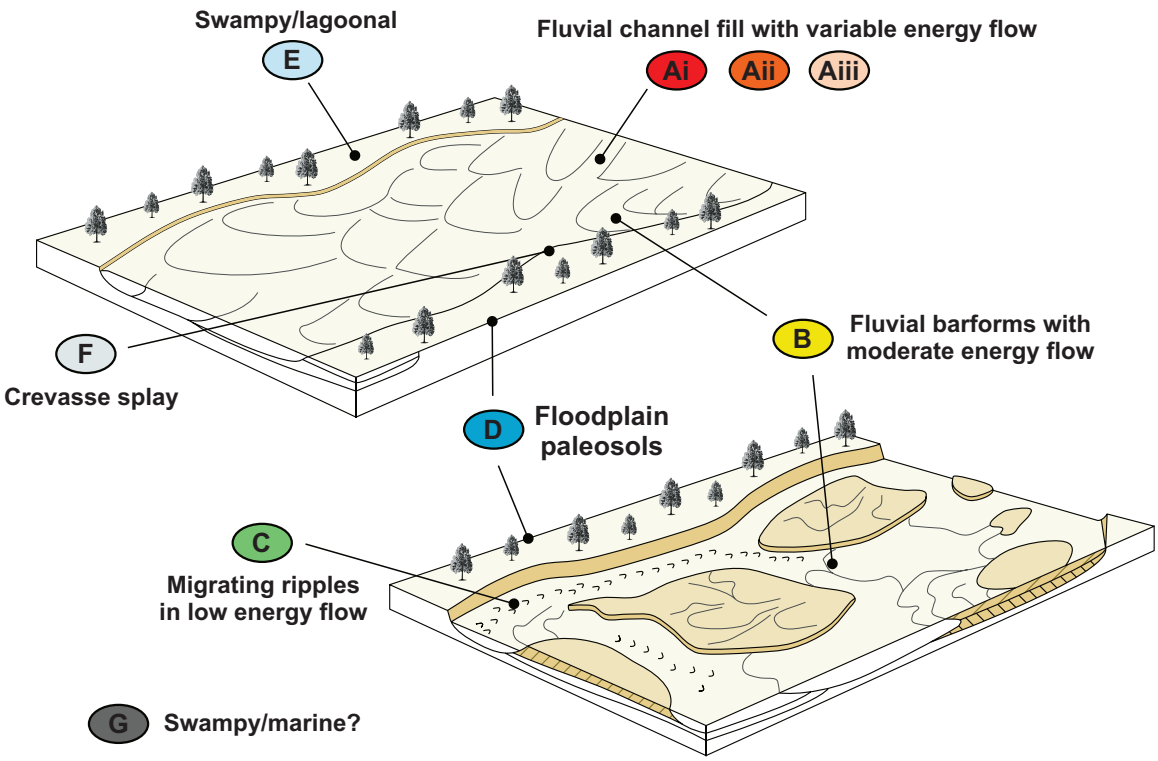

Figure 3.3: Block diagrams to illustrate the sedimentary depositional environment and architecture of lithofacies A-G. After Miall (1996).

In Gingin-1, the Cattamarra Coal Measures are almost bimodal between sandy fluvial lithofacies Aiii/B and mud/silt-dominated lithofacies G (Fig. 3.4). The only cored interval of Cadda Formation sees an appearance of cross-bedded fluvial lithofacies Aii and muddy sandstone lithofacies E (Fig. 3.4). The cored intervals of Yarragadee Formation in Gingin-1 show similar lithofacies variability as in Cockburn-1, and a similar distribution (Fig. 3.4). In Gingin-2, the only cored intervals were Cattamarra Coal Measures, and show a higher proportion of moderate to low-energy fluvial lithofacies B and C with sharp, frequent lithofacies switching (Fig. 3.4). Palaeosols (lithofacies D) are more significant in Cockburn-1 than the other logged wells (Fig. 3.4). High energy lithofacies Ai and Aii are most prevalent in the Lesueur sandstone in Pinjarra-1 (Fig. 3.5). When averaged across the four wells, the Yarragadee Formation shows quite an even distribution of lithofacies, whereas the cored intervals of Cadda Formation and Cattamarra Coal Measures contain >30% muddy/silty lithofacies G (Fig. 3.5).

When the data from the four wells are combined, the variety and proportions of different lithofacies are quite similar between the Cattamarra Coal Measures, Cadda Formation and Yarragadee Formations (Fig. 3.5). The main difference is that there are proportionally more cored intervals of lithofacies Ai and Aii for the Yarragadee Formation, largely at the expense of lithofacies Aiii, B and G, which are present to a higher degree in the Cadda Formation and Cattamarra Coal Measures (Fig. 3.5). These contrast with the Eneabba Formation and Lesueur Sandstone, which are dominated by lithofacies Ai, Aii, and G.

All of the wells show high-resolution lithofacies switching such that the mean continuous thickness of any particular lithofacies is less than 1 m (Figs. 3.6 and 3.7). Cockburn-1 has the most rapid lithofacies switching, with mean continuous thicknesses ranging from 8 to 17 cm, which is approximately the scale of the individual bedforms. The most continuous sections of lithofacies Ai/Aii are from cored intervals of the Lesueur Sandstone in Pinjarra-1, with some intervals over 4.5 m (Fig. 3.6). The cored sections of Cattamarra Coal Measures in Gingin-1 and Gingin-2 contain intervals of continuous Lithofacies Aiii and C up to 11.19 m and 7.07 m thick, respectively, although these are uncommon (Fig. 3.6). Several >2.5 m intervals of continuous lithofacies G occur in the Cattamarra Coal Measures of Pinjarra-1, Gingin-1 and Gingin-2 (Fig. 3.6).

3.4.3 Bedform thickness analysis of Cockburn-1 core.

The thicknesses of individual bedforms in Cockburn-1 have been quantified sedimentary logging (Fig. 3.8). The mean thicknesses of beds from all lithofacies types vary from 8 to 17 cm. Beds within each lithofacies show similar ranges and very rarely exceed 1 m. Note that the coarsest-grained lithofacies Ai and Aii have mean bed thicknesses of 8 and 11 cm, respectively, in the Yarragadee Formation in Cockburn-1. Beds of the Cattamarra Coal Measures from the all lithofacies except C and D tend to be slightly thicker (higher facies mean thickness) than the equivalent lithofacies in the Yarragadee Formation above.

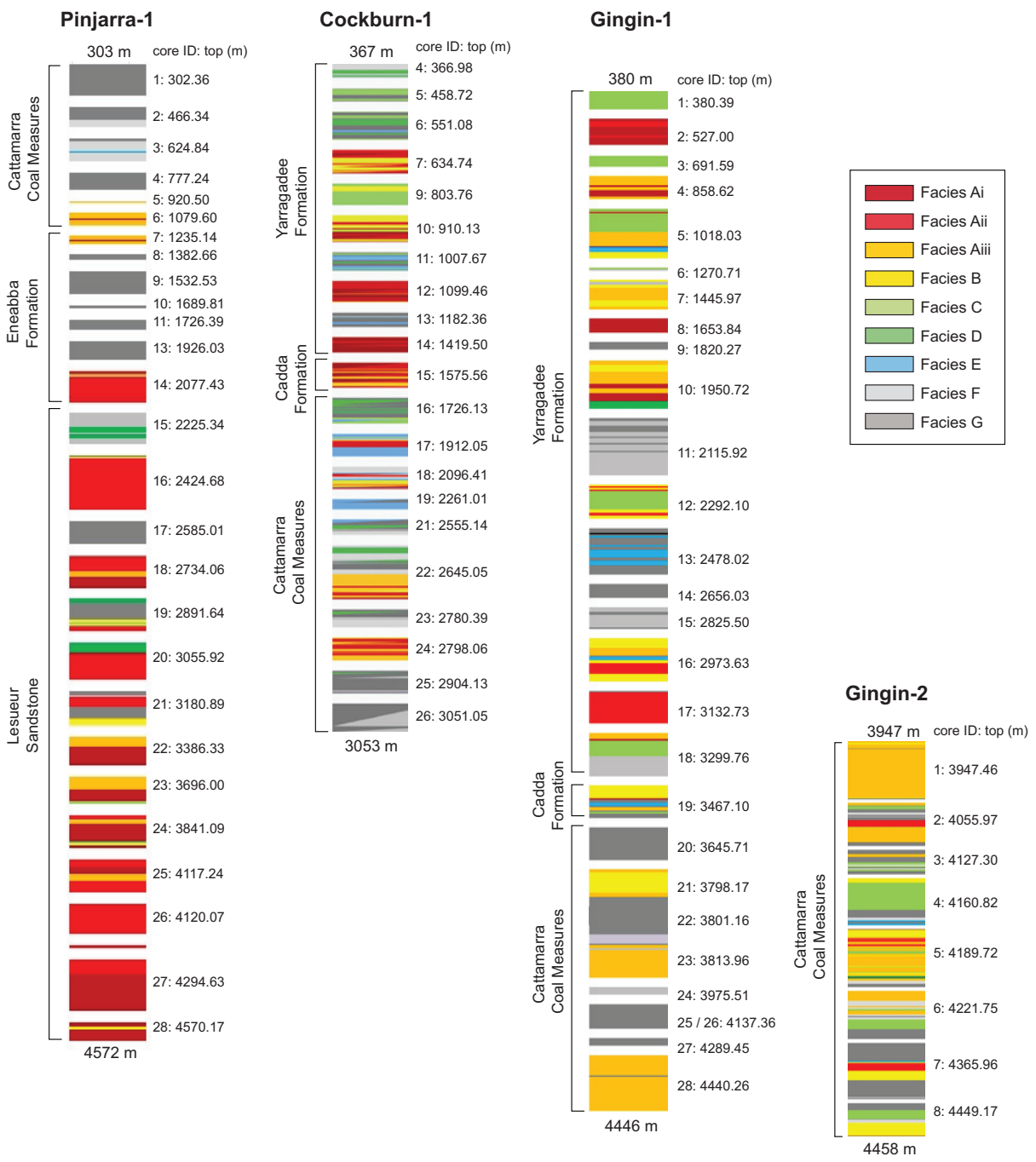

Figure 3.4: A summary of the lithofacies assigned to cored intervals of the studies wells from sedimentary logging. (a) Pinjarra-1. (b) Cockburn-1. (c) GinGin-1. (d) GinGin-2. Numbers adjacent the charts refer to the original core IDs and depth of the top of the cored section.

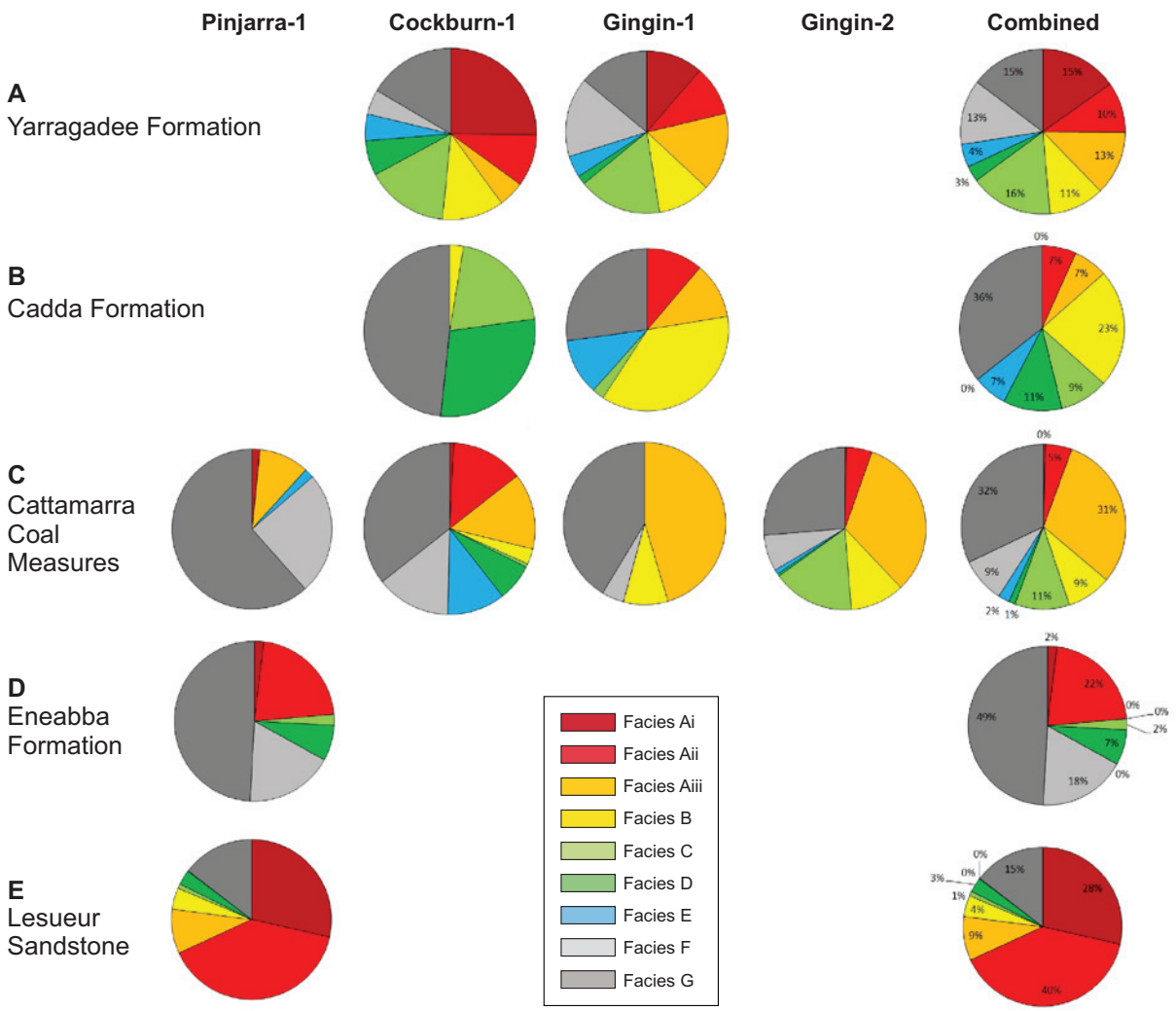

Figure 3.5: A-E Pie charts show the proportion of different lithofacies for combined cored intervals of each stratigraphic formation represented in each well and combined across the four wells. Note that the Eneabba Formation and Lesueur Sandstone only occur in Pinjarra-1.

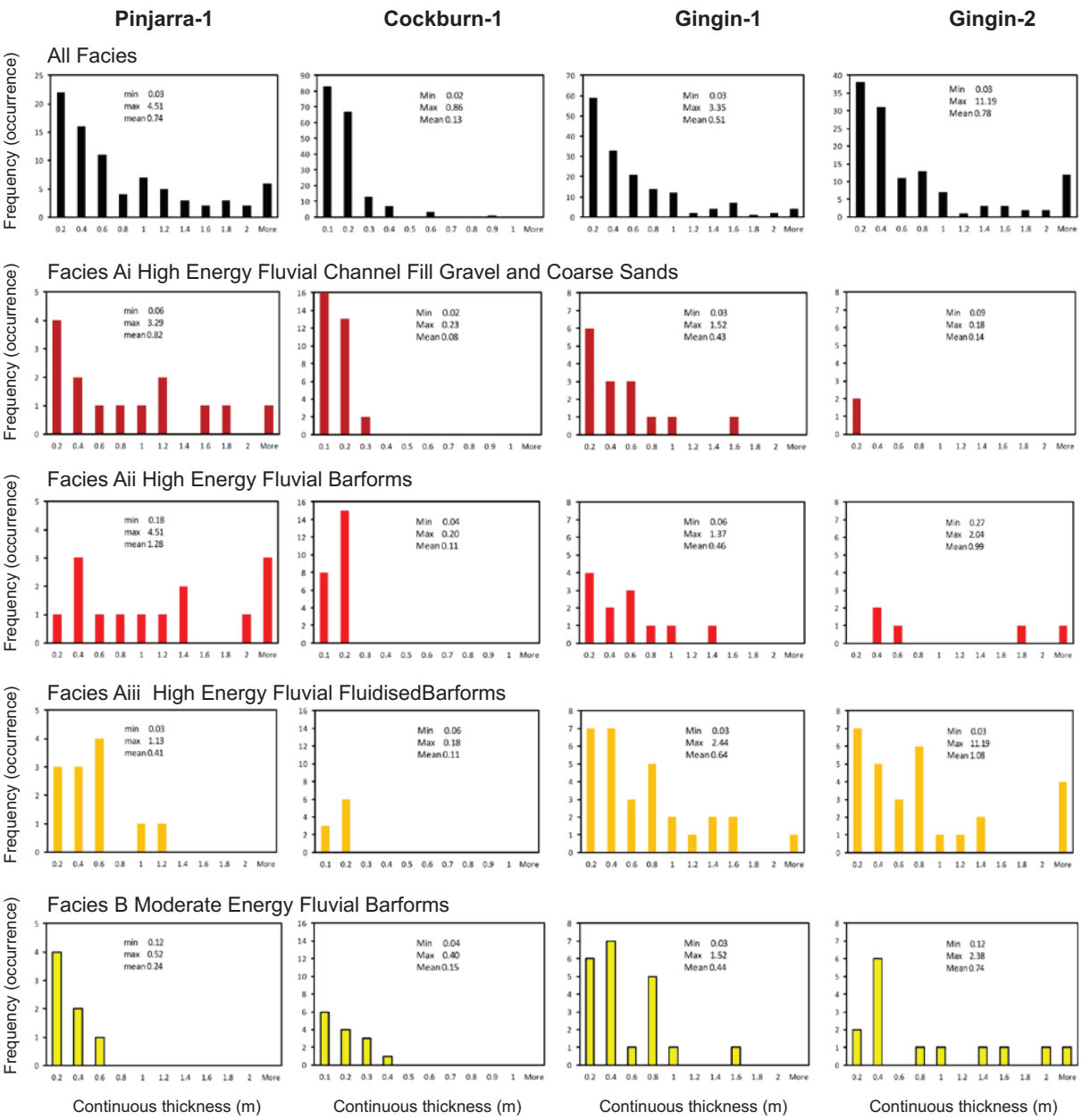

Figure 3.6: Charts of the frequency of continuous intervals of each lithofacies. A. Pinjarra-1. B. Cockburn-1. C. Gingin-1. D. Gingin-2. See text for discussion.

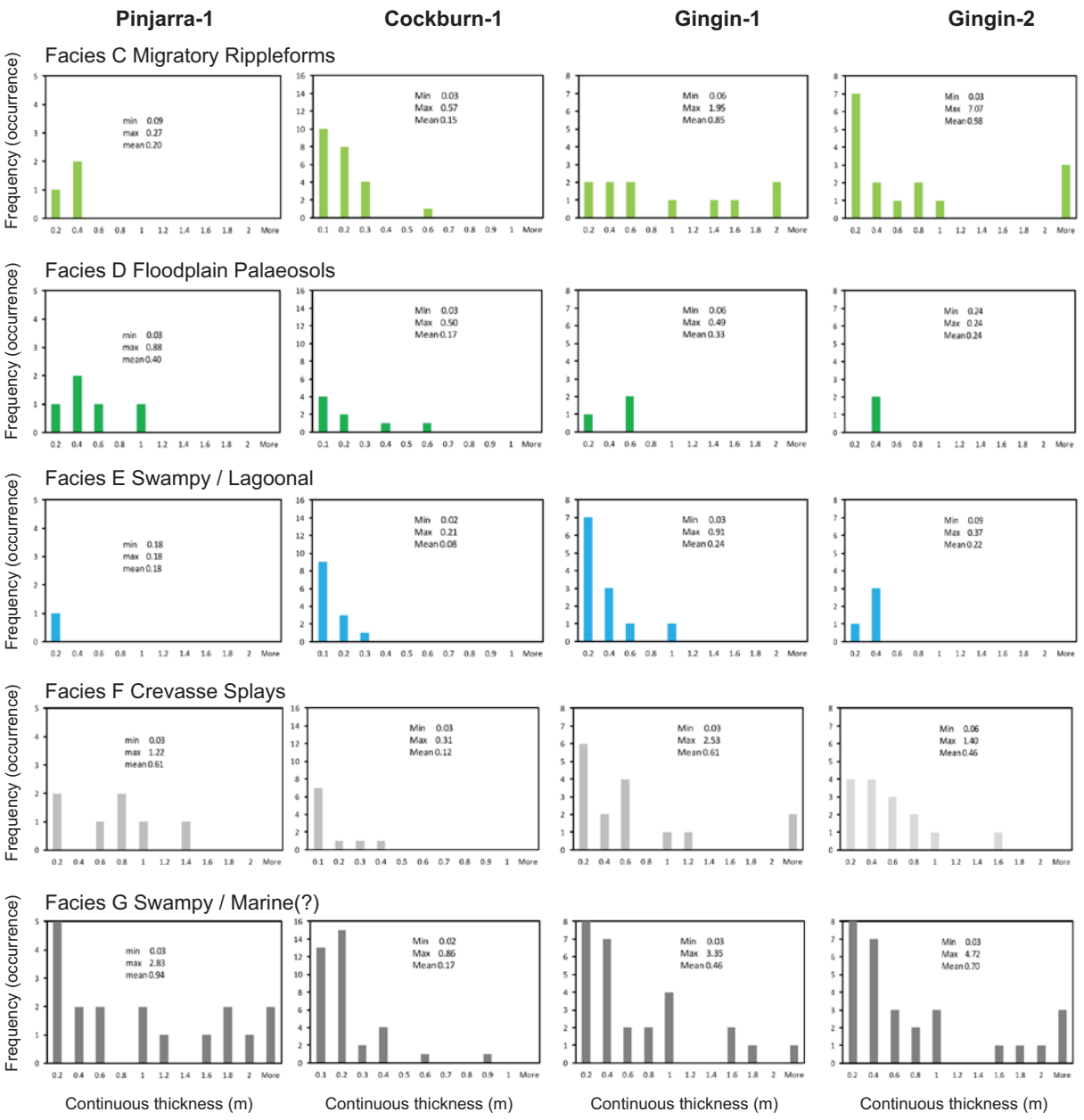

Figure 3.6 continued: Charts of the frequency of continuous intervals of each lithofacies. A. Pinjarra-1. B. Cockburn-1. C. Gingin-1. D. Gingin-2. See text for discussion.

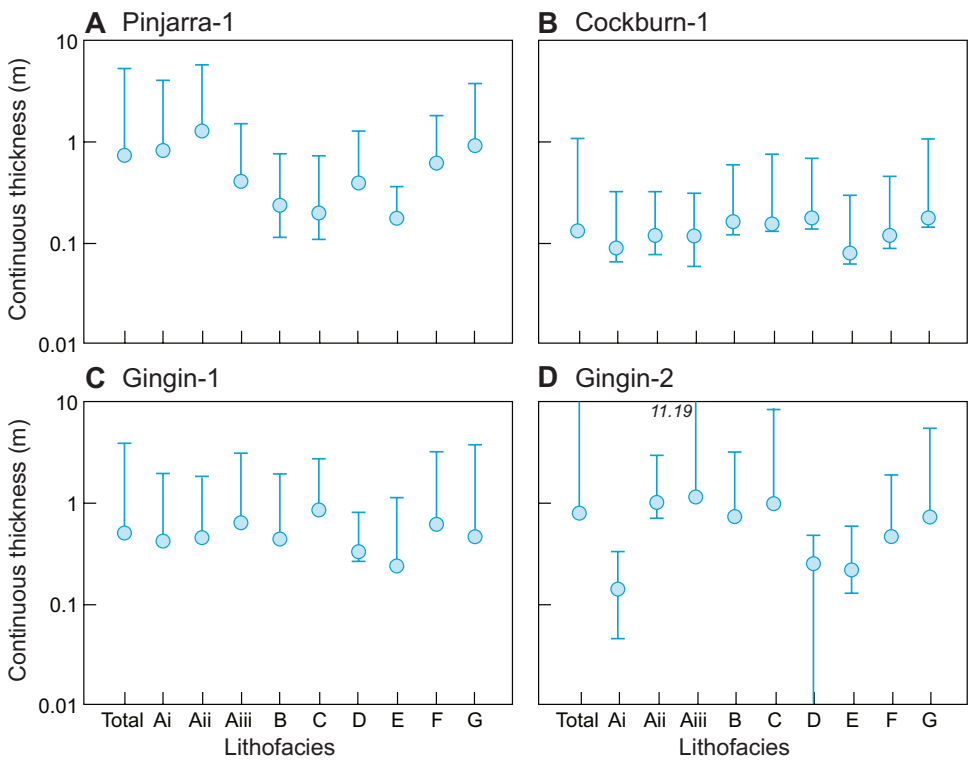

Figure 3.7: . Charts to summarise the mean, minimum, and maximum continuous intervals of each lithofacies. A. Pinjarra-1. B. Cockburn-1. C. Gingin-1. D. Gingin-2. See text for discussion.

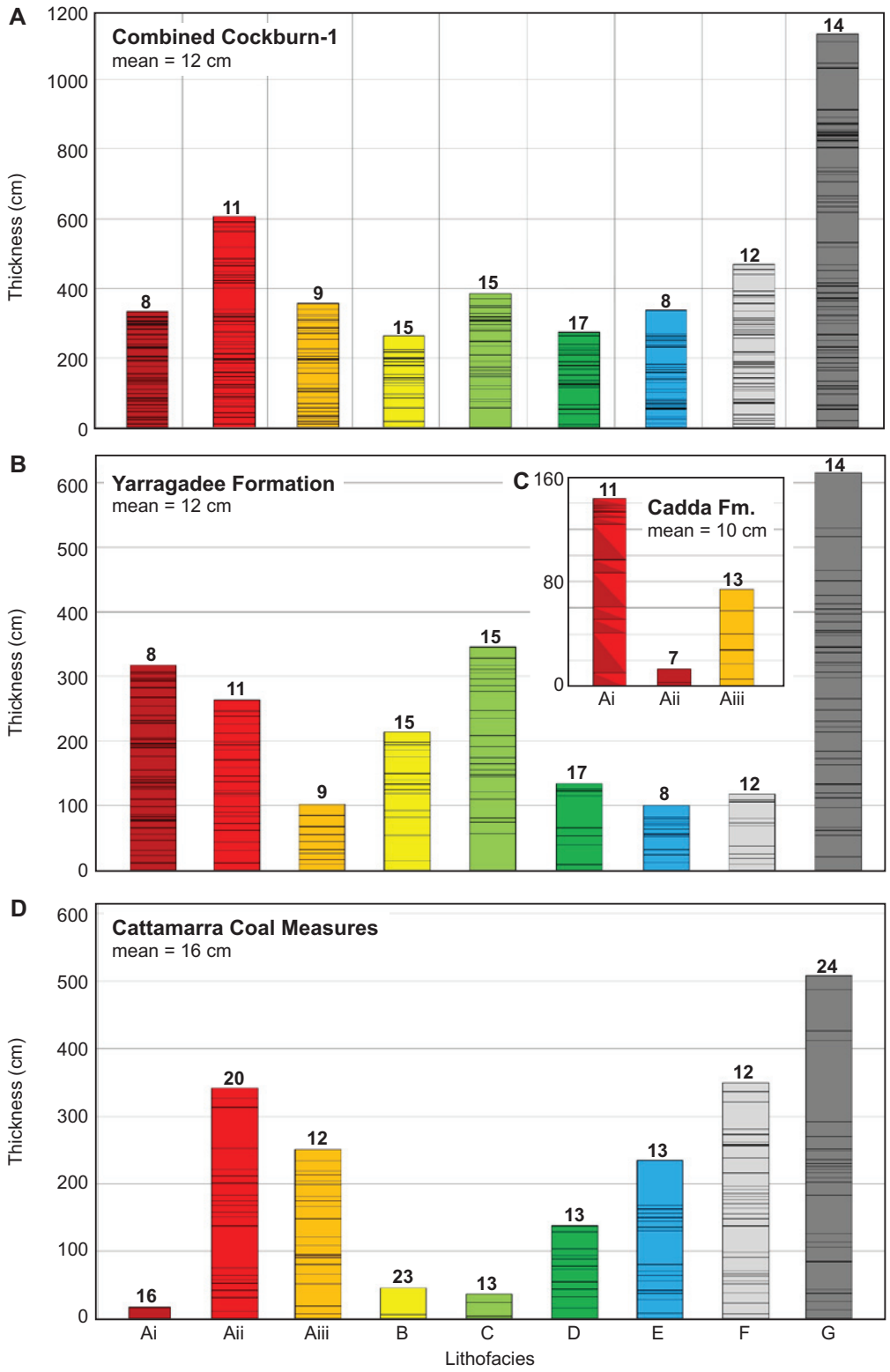

Figure 3.8: Charts to show bedform thickness variations for different lithofacies in Cockburn-1. Numbers above bars are mean bed thicknesses in cm.

3.5 Discussion

3.5.1 Evaluation of spatial and temporal variations in lithofacies

All of the studied formations have high lithological variability throughout all four wells (where present). There do not appear to be any systematic trends in the relative proportions of mud/silt-dominated versus sand-dominated lithofacies with depth, neither over the vertical distance of a core nor as a longer-term trend through the depth intervals of the whole formations. The Lesueur Sandstone and Eneabba Formation present in Pinjarra-1 are lithologically distinctive from the other formations in that they are dominated by coarse sands and gravels of lithofacies A and silts/muds of lithofacies G with an approximately bimodal distribution. The Yarragadee Formation, Cadda Formation and Cattamarra Coal Measures are indistinguishable in terms of lithofacies. They contain the same set of lithofacies with approximately similar proportions, stacking patterns, and bed thicknesses. The conclusion is that, from the logged core intervals, there are no clear lithological differences between these formations.

3.5.2 Implications for the evolution of depositional environment during the early Mesozoic

All lithofacies are attributed to fluvial-alluvial systems with no clear, unequivocal evidence of tidal or wave influence (e.g., (Homewood and Allen 1981, McIlroy et al. 2005). It is possible that some intervals of lithofacies G represent marine incursions, although there are no clear indicators of marine conditions. The sedimentary depositional environment was probably a low-lying fluvio-deltaic coastal plane with braided streams, overbank floodplains, swamps and lagoons - much like the current environment of the central Perth Basin. The change from coarse-grained lithofacies that typifies the Triassic Lesueur Sandstone to mixed lithofacies during the Jurassic could be due to any or all of: (a) change in sediment supply rate from the same source; (b) a change in depositional environment from, e.g., fluvio deltaic conditions to a mixed coastal plane setting; or (c) a switch in detrital provenance caused by tectonic factors. However, the results of this study are unable to resolve this issue.

One implication of the observations that the Yarragadee Formation, Cadda Formation and Cattamarra Coal Measures are lithologically indistinguishable with no long term stacking trends is that approximately similar depositional environments persisted across the central Perth Basin during the duration of the Jurassic. This is consistent with steady filling of continuously generated accommodation space during subsidence associated with a rift phase of basin development during this period (Harris 1994, Song and Cawood 2000).

The rapid vertical facies switching suggests a complex 3D architecture. It is not possible to predict the lateral continuity and, consequently, vertical connectivity of the lithofacies from the data without further constraints, such as lithofacies interpretations of wireline logs and seismic sections, or stratigraphic forward models that would provide statistics on likely dimensions of rock bodies. It is highly unlikely that lithostratigraphic units identified in this study persist across the distance between wells. Nevertheless, this study provides ideal data to benchmark wireline logs and very detailed stratigraphic forward models. However, the data from this study suggests extreme lithological variability far beyond resolution of seismic data.

3.5.3 Identification of sedimentologically-favourable potential geothermal targets

Assuming that the coarse-grained lithofacies are the most permeable (although this requires verification - see Section 5 of this report), then most of the Lesueur Sandstone in Pinjarra-1 and the thickest continuous intervals of lithofacies A within the Eneabba and Yarragadee Formations seem promising candidates for high permeability reservoirs. However, the vertically discontinuous nature of the cored intervals inhibits an adequately thorough analysis of sedimentologically suitable geothermal targets based entirely on the data from this study. One of the limitations involved in statistical analysis of the cored intervals is that the maximum continuous length of beds and lithofacies cannot be accurately determined due to the length of individual sections of drill core. These is especially pertinent in sections of core in Pinjarra-1, for example, where they comprise entirely of one lithotype and, therefore, are likely to be significantly longer than can be supported from the available cores alone. As a result, the average continuous length of a specific facies is likely to be significantly longer than estimated here. This could be important if the main reservoir/aquifer horizons are dominated by relatively few thick units. Therefore, porosity and permeability characteristics of each lithofacies and vertically continuous record of rocks types are required to satisfactorily identify suitable aquifers (see Sections 5 and 6 of this report).

3.5.4 Sedimentary structures as potential flow baffles, barriers and causes of permeability anisotropy in coarse-grained lithofacies

Cross bedding and flaser bedding in sandstones assigned to lithofacies B, C, and F are commonly draped by clay, organic fragments and mica. It is anticipated that these sedimentary structures could form bedform-scale permeability baffles where they are less well developed or even barriers where drapes are thick and continuous. Flow will be hampered perpendicular to the cross bedding foresets. Furthermore, the centimetre-scale cross bedding that is common in lithofacies Ai and Aii is defined by variations in grain size which could form permeability anisotropy where permeability is maximum parallel to the foresets. The integrated permeability anisotropy generated by cross bedding depends entirely on the foreset orientation, ultimately controlled by palaeocurrent directions. The studied core was not orientated, and so palaeocurrents could only be assessed qualitatively. The orientation of foresets in each cored section interval showed limited ranges in orientations consistent with bulk unidirectional flow, consistent with some fluvial systems. However, these cores cannot be used to assess syn-depositional palaeoflow evolution over large intervals.

3.5.5 Goals for future research

- The results of this study have been used as a framework for all rock physics measurements from core samples (see Section 4 of this report). The lithofacies assignment described herein could be used as a context for all future analyses of core from the studied wells.
- The vertical lengthscales of lithofacies switching and stacking patterns could be used to benchmark forward stratigraphic models for the central Perth Basin (see section 6 of this report).
- Lithofacies analysis is a useful approach that could be applied to other cored wells to determine

the nature of lithological variability of potential target formations elsewhere.

- The possibility of interpreting lithofacies from wireline logs to get continuous vertical lithofacies log for each well could be investigated
- Lateral variations in lithofacies could be investigated by integrating lithofacies analysis from core or wireline logs with vertical seismic profiles (e.g., Section 2 of this report) from the same well.
- It could be possible to apply the lithofacies scheme (with some limitations) to cuttings from other wells in the Perth Basin. This could fill data gaps and provide insight into broad-scale vertical and lateral varaitions in lithofacies for target formations.

3.6 Summary

Assessment and successful exploration for- and exploitation of aquifers in the Perth Basin requires knowledge of their physical (sedimentological) characteristics and geometry. The sedimentology of key geothermal target formations in the central Perth Basin has only ever been described at a very basic level, and/or extrapolated from outcrops many hundreds of kilometres away. This study addresses this via a sedimentological and lithofacies analysis of core from four deep legacy wells to quantify sedimentary variability in three dimensions, and provides an insight into changes in depositional environment over time and space. A fluvial-dominated lithofacies scheme has been developed and applied to the Yarragadee Formation, Cadda Formation, Cattamarra Coal Measures, Eneabba Formation and Lesueur Sandstone recovered from Pinjarra-1, Cockburn-1, Gingin-1 and Gingin-2 wells. The results show that the Yarragadee, Cadda and Cattamarra Coal Measures have a wide variety of lithofacies types in very similar proportions. The Lesueur Sandstone is dominated by coarse-grained high energy fluvial deposits. Complex switching of lithofacies on the order of 10 cm to approximately 2 m vertical scale is observed in all formations and wells, which indicates auto-cyclic avulsion of different depositional environments, probably with an intricate 3D architecture. Given that sedimentology commonly exerts a first order control on many rock properties, the lithofacies analysis of this study provides a framework in which to interpret petrography, mineralogy and laboratory-measured petrophysical data and wireline logs (see Sections 4 and 5 of this report, respectively).

4. MINERALOGY, DIAGENESIS AND PETROPHYSICAL PROPERTIES OF POTENTIAL GEOTHERMAL TARGET ROCKS IN THE CENTRAL PERTH BASIN

4.1 Introduction

Petrography, mineralogy and permeability are key considerations for geothermal exploration. Knowledge of grain size distribution and cements is vital for assessment of the physical integrity of potential geothermal reservoirs. The mineralogy of potential geothermal reservoirs and/or aquitards is useful for assessment of fluid-rock reactions during geothermal production, and could yield information about sedimentary provenance, which is useful for stratigraphic forward modelling. Knowledge of the porosity, permeability and thermal conductivity structure of target rocks is essential for modelling fluid and heat flow in steady geothermal scenarios. For transient simulations, e.g. how we can extract/reinject heat associated with geothermal production, extra parameters such as matrix compressibility, density, and heat capacity are required. Aquifer permeability and thickness, thermal conductivity and heat capacity and fluid properties (e.g., density and viscosity) determine the relative contribution of thermal convection and conduction on the thermal regime and the motion of the pore fluid (i.e., the Rayleigh number) (Reid et al., 2012).

Very little has been reported on the petrography and mineralogy of the Mesozoic rocks of the central Perth Basin, which contain major 'deep' aquifers such as the Lesueur Sandstone and Yarragadee Formations (Davidson 1995). The legacy porosity and permeability data that exists for these rocks is of unknown quality and shows a wide range of values (Brownhill 1966, Johnson 1965, Jones and Nicholls 1966, Smith 1967). For example, the Yarragadee Formation crossed by Cockburn-1 well shows 5 orders of magnitude variation in permeability that does not have a simple relationship with depth. The principal cause(s) of this variation is unknown, but is likely to be related to primary lithological characteristics (e.g., grain size, sedimentary structures) and/or diagenetic and post deposition effects (e.g., authigenic cements, fractures, etc.). The available data for intrinsic thermal conductivity of rocks in the central Perth Basin are scarce and/or unreliable. The need for improved petrophysical characterization of the target geothermal formations is clear.

Recent research by WAGCoE shows wide variations in the sedimentology of these rocks that reflect spatio-temporal variations in primary depositional setting (see Section 3 for details). However, the links between sedimentology, porosity and permeability had not been systematically examined. Furthermore, there are no previous studies of the diagenetic fabrics of the central Perth Basin, and their effects on porosity and permeability have not been assessed. All material properties depend on pressure, temperature and chemistry. Measuring variations within this parameter space is difficult, and it hasn't even been attempted in the WA context. In this study, WAGCoE and the CSIRO Petrophysics group have commenced the process by performing an initial study of the key exploration parameters (mineralogy, petrography, porosity, permeability and thermal conductivity) of rock samples from potential deep geothermal targets in the central Perth Basin. This is the first stage in a larger effort to develop a detailed understanding of the rock property characteristics salient to

geothermal exploration and production in the Perth Basin. In doing so, it will answer the following specific questions:

- What is the petrography and mineralogy of the sediments, and what are the implications for (a) detrital provenance, (b) diagenesis, (c) thermal conductivity?
- What are the effects of the diagenetic history on the modern day fluid flow properties in the central Perth Basin?
- What are the relationships among porosity, permeability, thermal conductivity, lithofacies, depth, and latitude within the central Perth Basin, i.e., what are the main controls on permeability and thermal conductivity in the central Perth Basin?

4.2 Geological background

The central onshore Perth Basin comprises an asymmetric graben known as the Dandaragan Trough, which is an axis-parallel sub-basin bound to the east by the N-S trending Darling Fault, and compartmentalised to the north and south by major oblique fault zones (Cockbain 1990, Harris 1994, Playford et al. 1976, Wilde and Nelson 2001). The eastern margin of the Dandaragan Trough is taken to be the South Turtle Dove Ridge – an inverted half graben which separates the Dandaragan Trough from the offshore Vlaming sub-basin (Cockbain 1990, Lockwood and Iasky 2004). The Dandaragan Trough is the deepest part of the Perth Basin where up to 15 km of sedimentary succession was deposited from the Permian to Recent (Cockbain 1990, Tech 2005); Section 1 of this report).

There are several possible provenance sources of sedimentary detritus in the central Perth Basin. The Yilgarn Craton directly to the east of the onshore Perth Basin consists of many greenstone belts intruded extensively by multiple pulses of granitoids with different geochemical characteristics (Myers and Hocking 1998, Wilde and Nelson 2001). Three geologically, geophysically, and geochronologically distinct crustal components make up the southwest Yilgarn Craton; from west to east these are the Balingup, Boddington and Lake Grace Terranes (Wilde 1999, 1996). The Balingup Terrane is made up of belts of turbiditic metasediments and intensely deformed orthogneisses, such as the Chittering, Balingup and Jimperding Metamorphic Belts, intruded by younger granites such as the Logue Brook Granite (~2.690 to ~2.616 Ga; (Nemchin and Pidgeon 1997). Multiple sets of mafic dyke swarms intruded the assembled craton during Proterozoic times (i.e., post ~2.4 Ga) (Wingate and Giddings 2000). Rocks of the Albany-Fraser Orogen occur to the south of the Yilgarn Craton and outcrop along the southern margin of Western Australia. In the southwest, an inlier known as the Leeuwin complex consists of Late Mesoproterozoic to Neoproterozoic (1100-500 Ma) orthogneiss and granite (Collins 2003, Jansen et al. 2003).

The depositional environment in the central Perth Basin was fluvial-dominated from the Permian to the Jurassic, with possible marine incursions, resulting in the deposition of the Lesueur Sandstone, Eneabba Formation, Cattamarra Coal Measures, Cadda Formation and Yarragadee Formation (Crostella and Backhouse 2000). These formations were deposited during the main rift phase of basin development as greater India and Australia separated during the breakup of Gondwana (Harris 1994). The persistent fluvial setting of sedimentation implies that sedimentary fill approximately kept track

with rift-related accommodation space generation. The Dandaragan Trough has been somewhat compartmentalised by syn-rift faulting, and the drainage patterns during the Permian to Jurassic are not clear. Consequently, the provenance of the sediments is unknown. Potential detrital source rocks include the Archaean rocks of the Yilgarn Craton, the Leeuwin Block, the Albany Fraser belt, the East Antarctic Craton or Greater India (Cawood and Nemchin 2000, Kohn et al. 2002, Sircombe and Freeman 1999, Veevers et al. 2005).

The burial history of the central Perth Basin is not well understood. Average burial rates for the deepest parts of the Dandaragan Trough (12 km) must have been approximately 40 m/Myr, assuming continuous linear burial rates since the Permian. However, actual burial rates could vary significantly from this value across the central Perth Basin due to unknown additional overburden prior to Neocomian uplift and erosion, and differential subsidence related to local faulting. Apatite fission track data from the northern Yilgarn Craton suggests slow, continuous denudation of the craton during the Early Permian through to Mid-Late Jurassic, which was considered to be due to removal of a sedimentary blanket rather than erosion of cratonic material (Weber et al. 2005). Vitrinite reflectance data from the Permian coal measures in the nearby Collie Basin indicate the presence of an extra ~1.4 km of sedimentary cover to achieve the inferred maximum burial temperatures of ~100 °C (Le Blanc Smith 1993). However, it is unclear whether this history also applies to the onshore Perth Basin.

4.3 Approach

This study utilises cores recovered from the four petroleum wells that penetrate the deep aquifers of the central Perth Basin, from south to north, Pinjarra-1, Cockburn-1, Gingin-1, and Gingin-2 (Fig. 3.1). A sedimentological and lithofacies analysis of these wells is presented in Section 3, and summarised in Fig. 4.1. Core plugs of approximately 1” length and 1-1.5” diameter with their long axes parallel to bedding were taken to span a range of lithofacies and depths from each well. 23 core plugs were taken from Pinjarra-1, 48 from Cockburn-1, 67 from Gingin-1, and 47 from Gingin-2. The end section of each core plug (perpendicular to bedding) was removed with a trim saw, impregnated with blue resin and used to make polished petrographic thin sections.

4.3.1 Mineralogy

Modal mineralogy was determined using two methods: Point counting and automated mineral analysis.

Point counting method: Optical photomicrographs with a spatial resolution of 2 µm were taken of all thin sections using a Zeiss Axio Imager II at CSIRO, Perth. Modal mineralogy was determined from the digital photomicrographs by point counting using J MicroVision© (Roduit 2006). A rectangular area was selected for each thin section for 400 counts, with a random grid. The following minerals were counted: quartz, feldspar, clay minerals, opaque minerals, organic carbon, other minerals (micas, zircon, Ti-oxides); additionally, ‘partially occluded porosity’ (pale blue-green resin, clay minerals present) and ‘clear porosity’ (strong primary blue resin) were quantified.

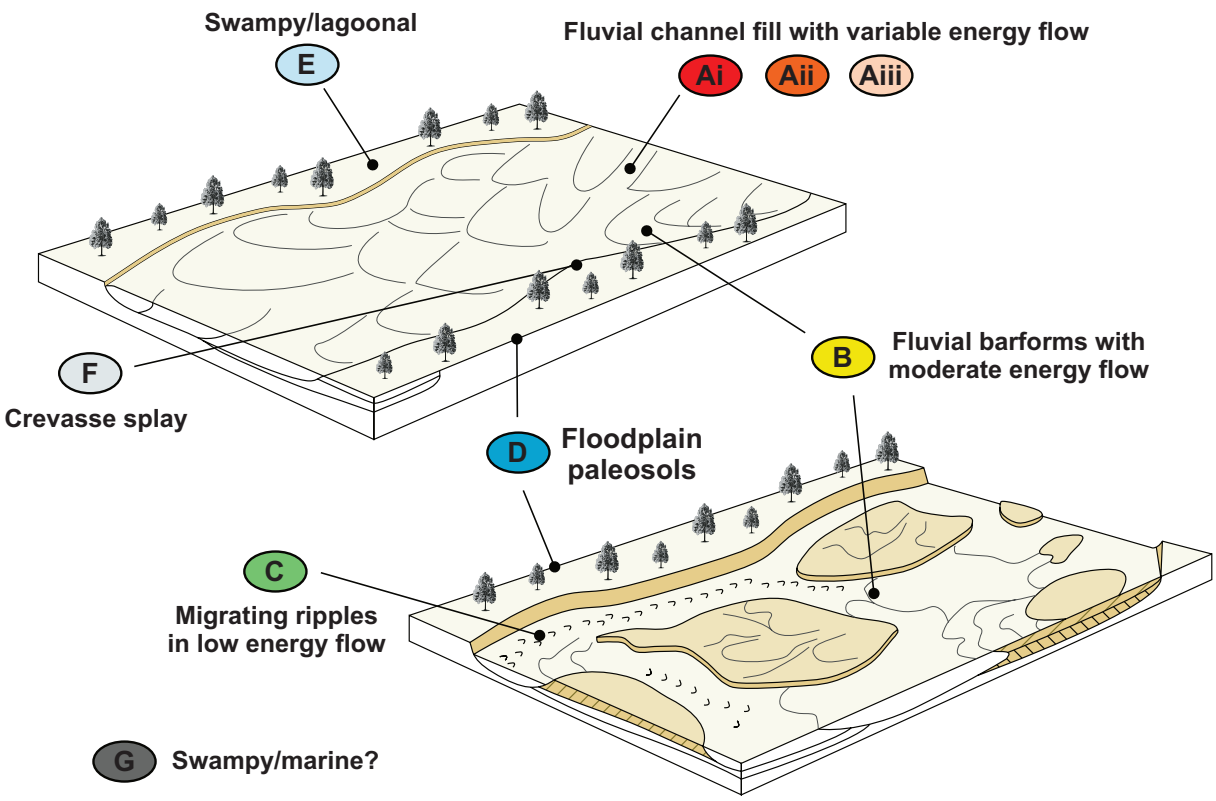

Figure 4.1: Summary of the lithofacies scheme developed for the Mesozoic stratigraphy of the central Perth Basin. After Miall (1996). See Section 3 for further details.

Automated mineral analysis method: The modal mineralogy was determined for 47 samples from Pinjarra-1, Cockburn-1 and Gingin-1 using automated mineral analysis (Dilks and Graham 1985, Goldie Divko et al. 2010, Messent and Farmer 2008, Reid 1989) using an FEI E430 QEMSCAN® (QS) at ALS Ammtec Pty Ltd, Perth, Western Australia. The instrument comprises a scanning electron microscope (SEM) with four energy dispersive X-ray spectrometers (EDX). The spacing of analytical points was set at 5 µm or 10 µm depending on whether the area for analysis appeared fine grained or coarse grained, respectively. The data were processed using FEI's iDiscover off-line image analysis software. During automated analysis, spectral data collected at each point were classified using a detailed chemical-based mineral database. Data processing software allows for the simplification of these mineral species into a manageable format, by creation of mineral groupings. The additional benefits of this technique over point counting are that it can yield (a) data on mineral compositions, such as garnet; (b) quantification of the modal proportions of trace minerals; and (c) data on the location and abundance of clay minerals. Disadvantages of the technique include (a) an inability to distinguish between some phases (e.g., kyanite and sillimanite); (b) an inability to distinguish clast from overgrowth cement; and (c) an inability to identify organic material because of the signal from the carbon coat.

4.3.2 Logging of diagenetic structures / fabrics

Each core interval was logged for natural (i.e., non-core handling induced) fractures and stylolites. These data are presented as structures per metre, and apply to cored intervals only. The moderate to poor condition of many intervals precluded identification of natural fractures with confidence. Some weakly developed stylolites were visible via optical microscopy only, and are reported as structures per thin section.

4.3.3 Porosity characterisation by image analysis

Porosity was quantified in 2D via image analysis of petrographic thin sections using ImageJ® software. The percentage of blue-dyed resin (porosity) was calculated in transmitted, plane polarized light images, using the Threshold Colour plug-in of Rasband (2011) (Fig. 4.2). The software was used to threshold the images to isolate domains of impregnated blue resin based on hue, saturation and luminosity, convert the threshold areas to monochrome and quantify the area as a percentage of total. The plug-in offers the flexibility to account for variations in resin colour between samples, and permits the quantification of the fraction of porosity that is partially occluded by clay minerals (appears pale blue-green) (Fig. 4.2).

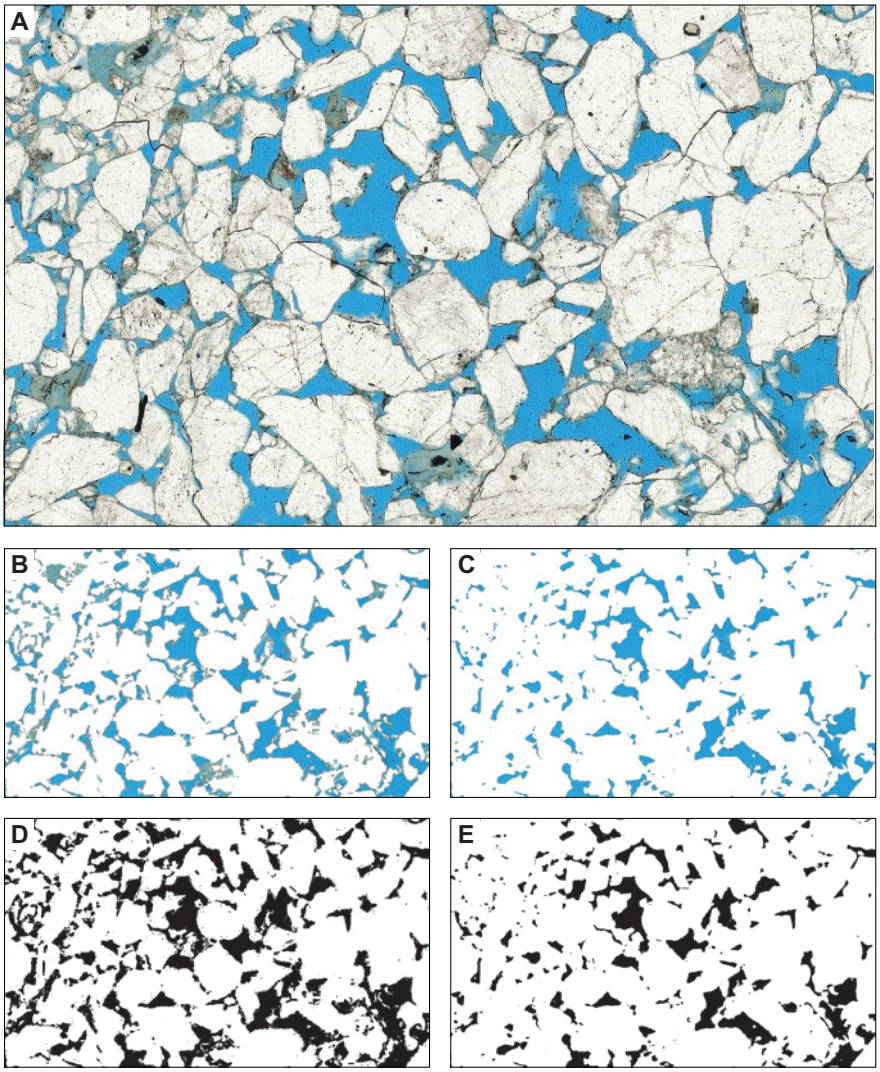

Figure 4.2: Example of image analysis technique to derive 2D porosity.
A. Photomicrograph of a petrographic thin section from Cockburn-1. The sample was impregnated with blue resin prior to sectioning to highlight porosity.
B. 'Total porosity' area selected using the threshold colour plugin for ImageJ.
C. 'Clear porosity' area selected by adjusting the threshold parameters to highlight a narrow range of blues.
D. A binary image generated from B used to calculate area percent porosity. This range rejects the light blue domains where clay minerals partially occlude the porosity.
E. A binary image generated from C used to calculate area percent porosity.

4.3.4 Porosity imaging by scanning electron microscopy

Images of the 3D pore spaces in sandstone were acquired via secondary electron imaging using a Zeiss EVO scanning electron microscope at the Electron Microscope Facility at Curtin University. Images were acquired using carbon coated broken, surfaces of core samples using 15 kV acceleration voltage, 425 spot size, an aperture optimised for depth, and working distances that ranged from 29 to 30 mm. Mineral phases were verified in spot mode using an Oxford Instrument AZTEC energy dispersive X-ray spectrometry (EDX) system.

4.3.5 Laboratory measurements of porosity and permeability

Porosity and permeability were measured simultaneously in the laboratory using a CoreTest AP-608 automated permeameter-porosimeter from Core Test Systems Inc. at CSIRO, Perth. The instrument precisely measures permeability in the range <0.001 mD to >10 D, therefore extending the range of data available from previous open access reports. In a standard test a rock sample is loaded into the core holder and flooded with inert Helium gas from both ends of the sample. The permeameter-porosimeter works on a transient pulse decay method and takes into account the gas slippage for output permeability, the so-called Klinkenberg effect (Tanikawa and Shimamoto 2006). It thus records the equivalent liquid permeability, or Klinkenberg corrected permeability. Further details of the permeability methodology are presented elsewhere (Israni and Delle Piane 2011). Helium expansion is monitored and the pore volume (i.e. porosity) of the rock sample is calculated following Boyle's law:

$$V_1 = \frac{P_2.V_2}{P_1}$$

where V_1 is the volume of Helium permeating the rock sample; P_2 and V_2 are the pressure and the calibrated volume of Helium before being released into the sample; and P_1 is the pressure of gas after sample infiltration.

Porosity and permeability of each of the cores were measured at increasing isotropic pressure to: i) simulate overburden pressure; ii) evaluate the pressure sensitivity of the measured transport properties. The confining pressures (P_c) were arbitrarily chosen to be 500, 1000 and 2000 psi corresponding to 3.4, 6.9 and 13.8 MPa, respectively, and the pore pressure (P_p) is always 250 psi. Hence the effective pressure (P_{eff}) applied on the plugs was:

$$P_{eff} = P_c - P_p$$

The P_{eff} were hence 250 psi, 750 psi and 1750 psi applied sequentially on each plug during the helium gas porosity measurements. Using a basic equation, depths corresponding to the effective pressure can be calculated:

$$P = (\rho_{rock} - \tilde{n}_{fluid}).g.h$$

and $$h = P/[(\rho_{rock} - \rho_{fluid}).g]$$

where P is pressure (Pa), g is the gravitational constant (9.81 m/s^2), h is depth (m), ρ_{rock} is the average density of rocks to depth h (kg/m^3)and ρ_{fluid} is the density of the pore fluid (kg/m^3). Using ρ_{rock} = 2400 kg/m^3 and ρ_{fluid} = 1000 kg/m^3, the effective pressures represent depths of approximately 248, 502 and 1005 m, respectively. The complete dataset can be found in (Israni and Delle Piane 2011). However, only the high pressure data are presented in this report because they are closest to the conditions of interest.

4.3.6 Thermal conductivity

175 new core plugs were acquired from the four wells via the Geological Society of Western Australia (GSWA) core library facility. Some very coarse grained sandstone half-plugs were in relatively poor cohesive condition, but suitable enough for thermal property measurements. The plugs from the other rock types were all in good condition.

Thermal conductivity (λ or TC) of the core plugs was measured at room conditions under dry and water saturated condition using a high resolution Optical Thermal Scanner, OTS (Popov et al. 1999) at the School of Earth Sciences, University of Melbourne. This non-destructive and non-contact apparatus is based on a movable heat source coupled to infrared detectors which measure the temperature of the sample before and after heating. The optical scanner yields a continuous profile of thermal conductivity along the core axis of the sample to high precision and accuracy of 1.5% within a thermal conductivity range of 0.1-70 W.m^{-1}.K^{-1} (Popov 1997). OTS provides rapid data acquisition without sample preparation with a minimum sample length of 1 cm. The temperature sensors can penetrate at a depth of 50 mm into the core from the surface when composed of pure quartz (i.e. the most thermally conductive mineral). Results were calibrated against two standards of known thermal conductivity both at the beginning and end of a scan with the λ matching as close as possible λ of the studied rock. Raw data were processed using TSC software by Schlumberger Ltd., which calculates minimum, maximum, mean, standard deviation and inhomogeneity of λ within each sample. After a series of tests, an optimum thermal scanning velocity of approximately 1-2 mm/s and heat spot-temperature recording distance of about 50 mm gave the best signal/noise ratio. The high contrast of temperature changes generated when the probe sensor is approaching the edge of the sample between air and sample (i.e. edge artefacts) are limited with such optimum settings. This allows a thermal scanning close to the very edge of the sample for a better thermal conductivity profile along the quasi full length of the sample. The heat penetration inside the sample combined to the velocity of the temperature probing give a maximum thickness of investigation of about 0.5-1 cm (i.e., 0.5-1 cm^3).

Thermal conductivity was measured on dry core plugs painted black to avoid heat reflection from the sample surface. The samples were then immersed in fresh water under air vacuum during 24 hours, weighed to check the degree of water saturation, and immediately measured with OTS along the same line previously measured under dry conditions to permit comparison between dry and saturated datasets.

Several problems arise from the room conditions and techniques to perform reliable thermal

conductivity measurements. The in-situ conditions are difficult to replicate in laboratory tests. For example, physical stresses, such as the regional lithostatic stress state, are relaxed and natural and anthropogenic crack damage can lead to increased porosity-permeability of the sample at laboratory conditions. The thermal conductivity is susceptible to these changes.

4.4 Results

4.4.1 Petrography and mineralogy

Details of the petrography and mineralogy of all four wells can be found in Olierook et al. (2012a-d) and Stütenbecker and Timms (2011). All of the lithofacies from the studied wells are quartz-dominated and contain sub-angular to sub-rounded grains with moderate sphericity (Figs 4.3-4.5). With the exception of a few large lithic clasts from lithofacies A and rare mud clasts in finer-grained lithofacies, clasts are monomineralic. Lithic fragments, where present, comprise crystalline aggregates of quartz and feldspar (now kaolinite) ± zircon, indicative of a granitic source rock. Cross bedding in lithofacies Aii is defined by changes in grain size. In many samples of lithofacies A from Gingin-1, the grain size appears to be polymodal and consequently poorly sorted (Fig. 4.5). Laminations in lithofacies C, D, E and F are defined by detrital clays, organic fragments and/or heavy minerals such as rutile and zircon (Figs 4.3-4.5).

Point count data from optical microscopy shows a lithofacies control on mineralogy and 2D porosity, with little systematic variation with depth for each studied well (Fig. 4.6).

Pinjarra-1: With the exception of lithofacies D and G, Pinjarra-1 comprises 62-82% quartz, 2-13% alkali feldspar and 10-20% clay minerals. Lithofacies D and G are clay-dominated and contain <30% and <40% quartz, respectively (Fig. 4.6). Clay minerals significantly occlude the primary porosity in all lithofacies in Pinjarra-1, with residual porosities <10%.

Cockburn-1: In Cockburn-1, quartz ranges from 50-70% and alkali feldspar is 2-30% in lithofacies A and B. Lithofacies D to G contain much less quartz, virtually no alkali feldspar and up to 17% mica (Fig. 4.6). Lithofacies A, B C, D and F have the highest primary porosity. However, porosity occlusion by clay minerals generally increases with depth in lithofacies A and B, and lithofacies C, D and F show significant porosity occlusion by clay minerals at most depths. Despite the presence of porosity-occluding clays, residual 2D porosity remains high in lithofacies A and B to several kilometres (Fig. 4.6).

Gingin-1: Gingin-1 shows similar mineralogy to Cockburn-1. Partial pore occlusion by clay minerals occurs across all lithofacies, and residual porosities are generally lower than for equivalent lithofacies in Cockburn-1.

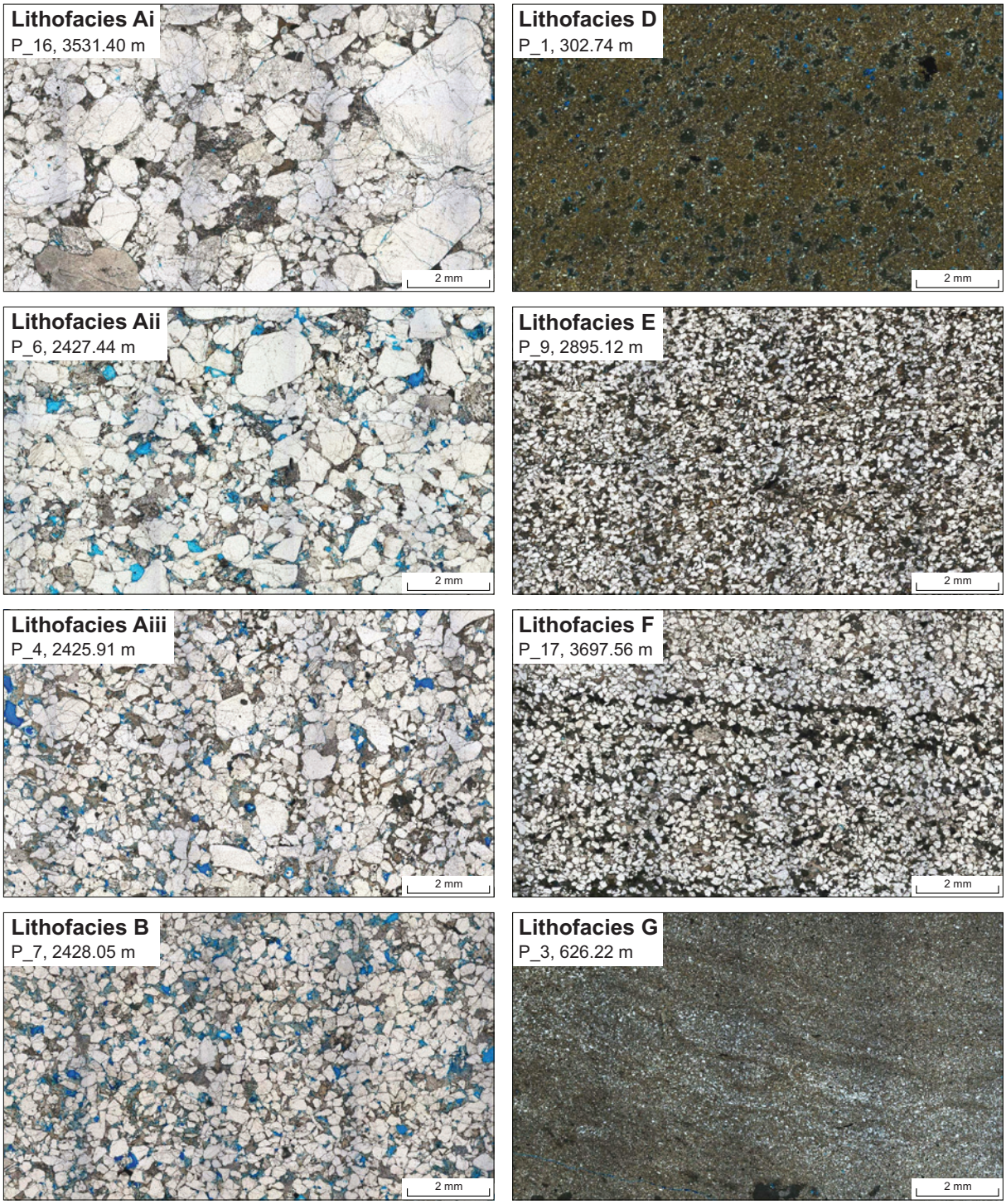

Figure 4.3: Optical photomicrographs and mineral maps of representative samples from each lithofacies in Pinjarra-1. Samples have been impregnated with blue resin to show porosity.

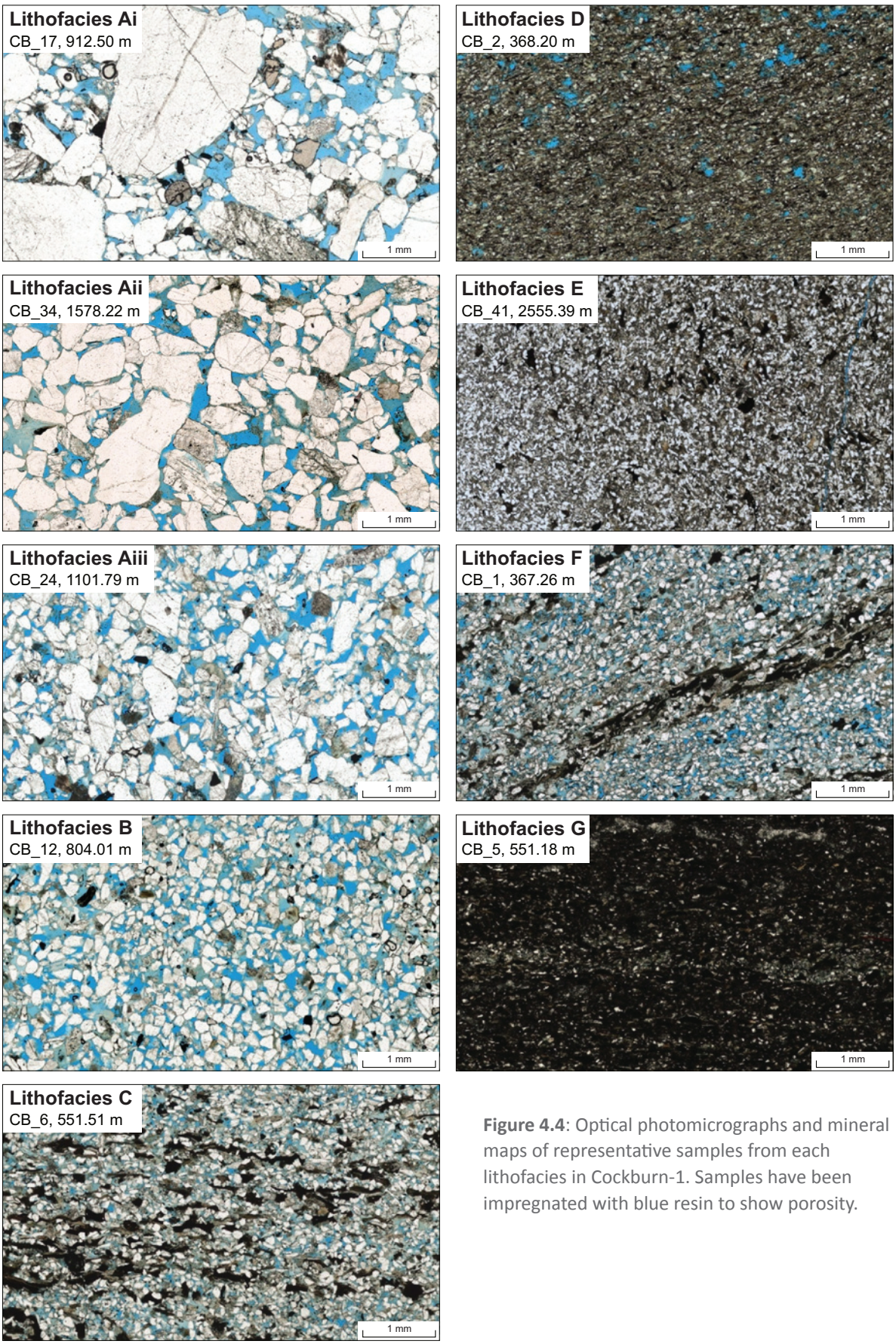

Figure 4.4: Optical photomicrographs and mineral maps of representative samples from each lithofacies in Cockburn-1. Samples have been impregnated with blue resin to show porosity.

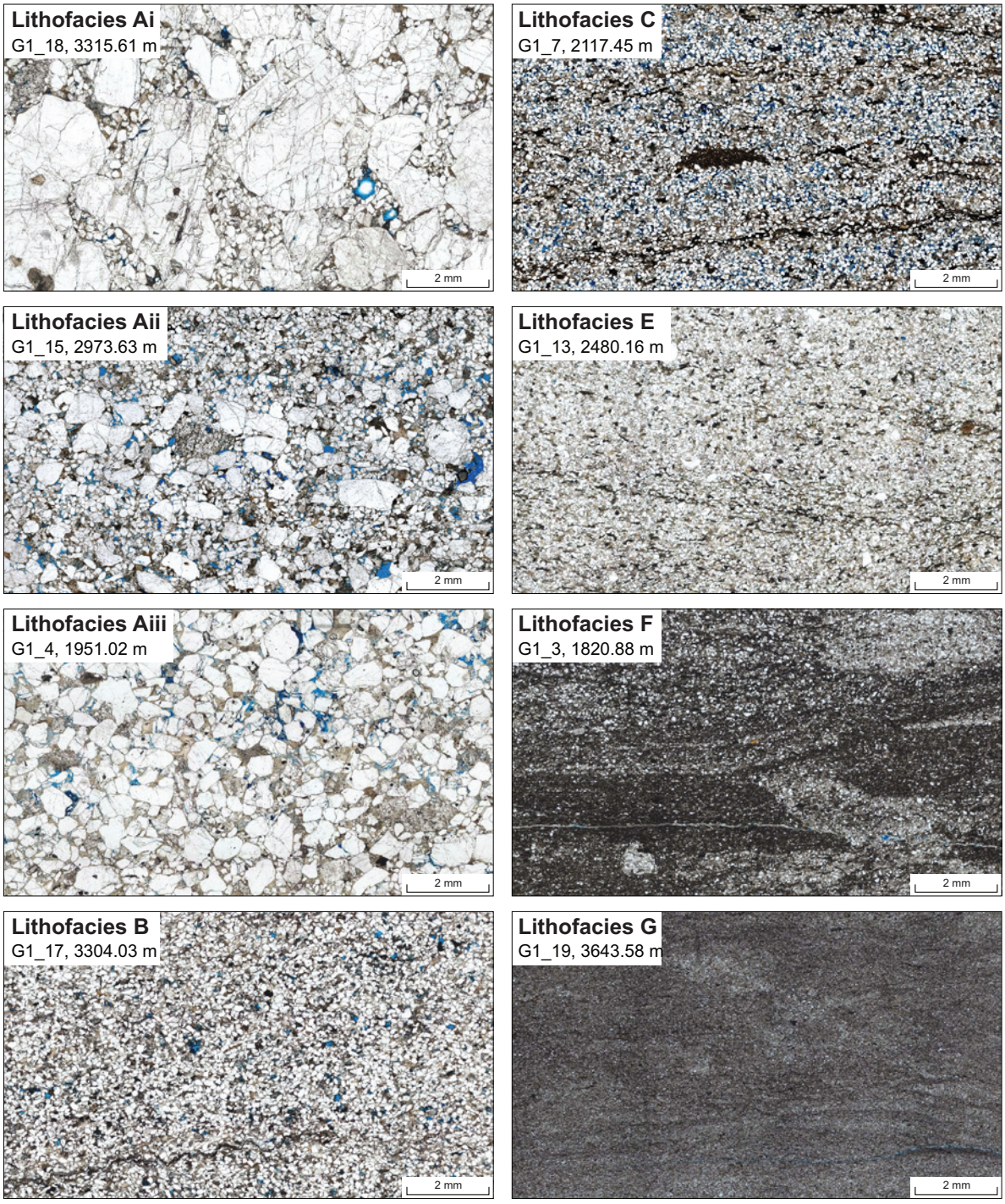

Figure 4.5: Optical photomicrographs and mineral maps of representative samples from each lithofacies in Gingin-1. Samples have been impregnated with blue resin to show porosity.

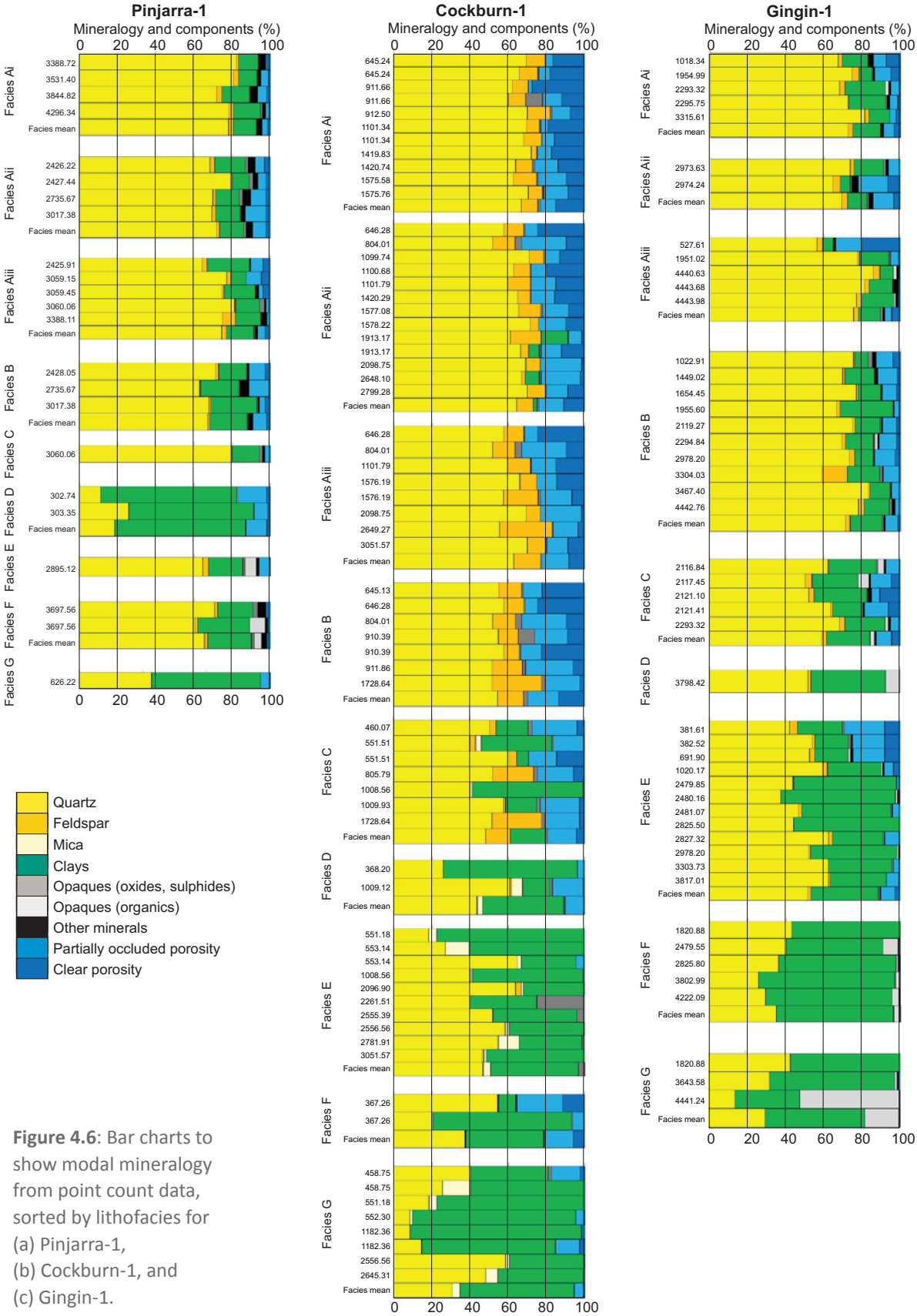

Figure 4.6: Bar charts to show modal mineralogy from point count data, sorted by lithofacies for (a) Pinjarra-1, (b) Cockburn-1, and (c) Gingin-1.

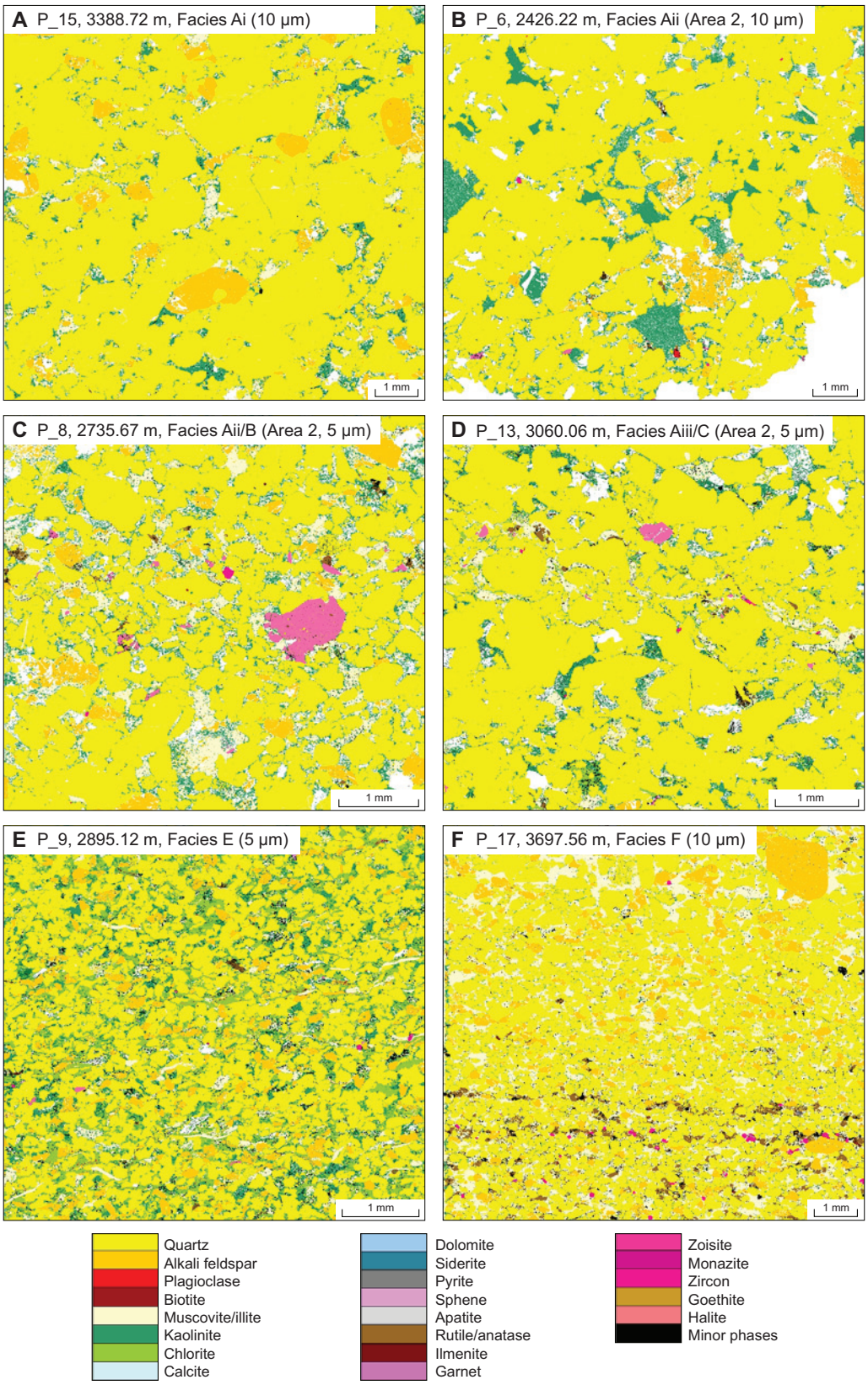

Figure 4.7: Representative automated mineral analysis maps for different lithofacies in Pinjarra-1. Sample I.D., downhole depth, facies and analytical step size are indicated.

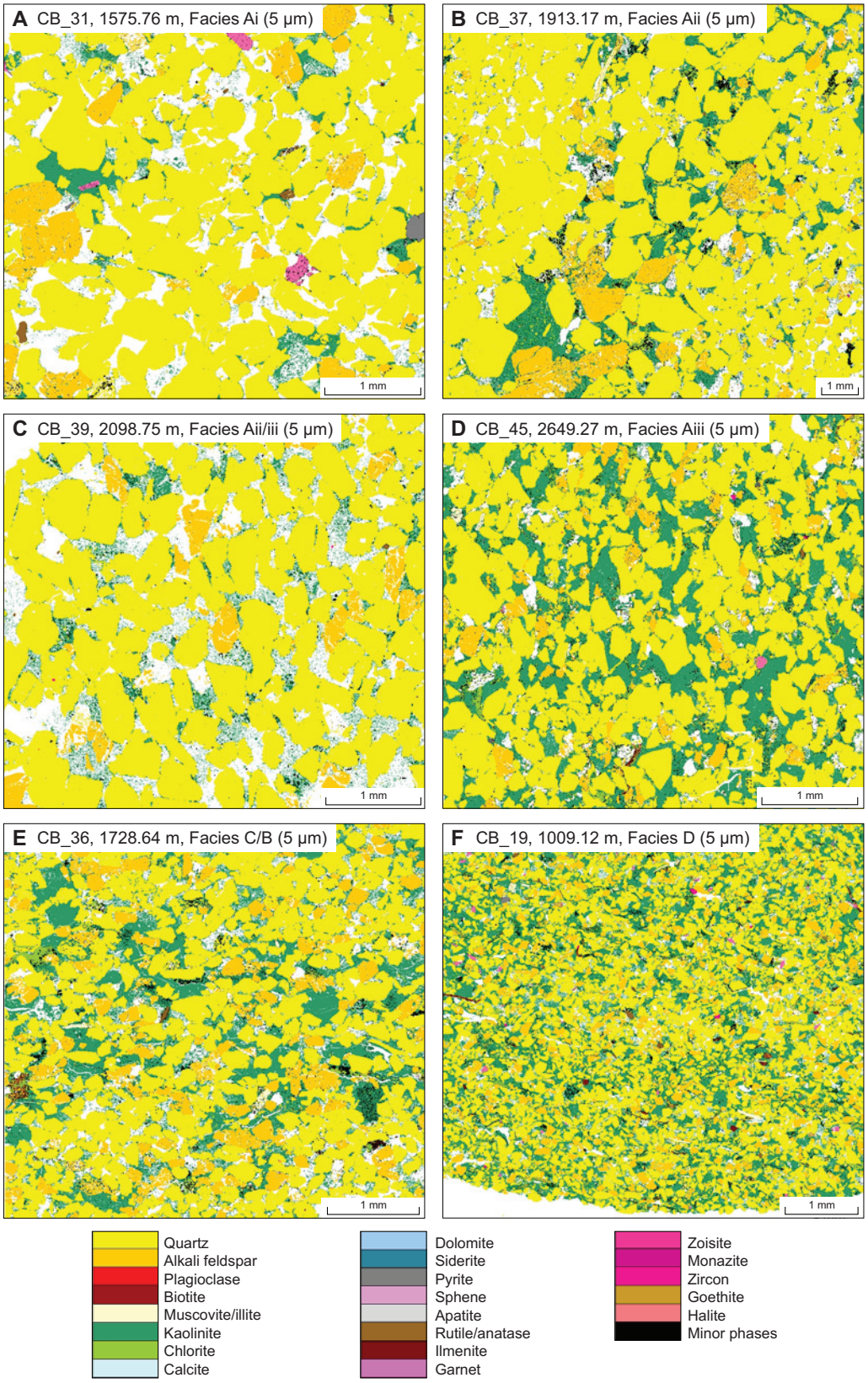

Figure 4.8: Representative automated mineral analysis maps for different lithofacies in Cockburn-1. Sample I.D., downhole depth, facies and analytical step size are indicated.

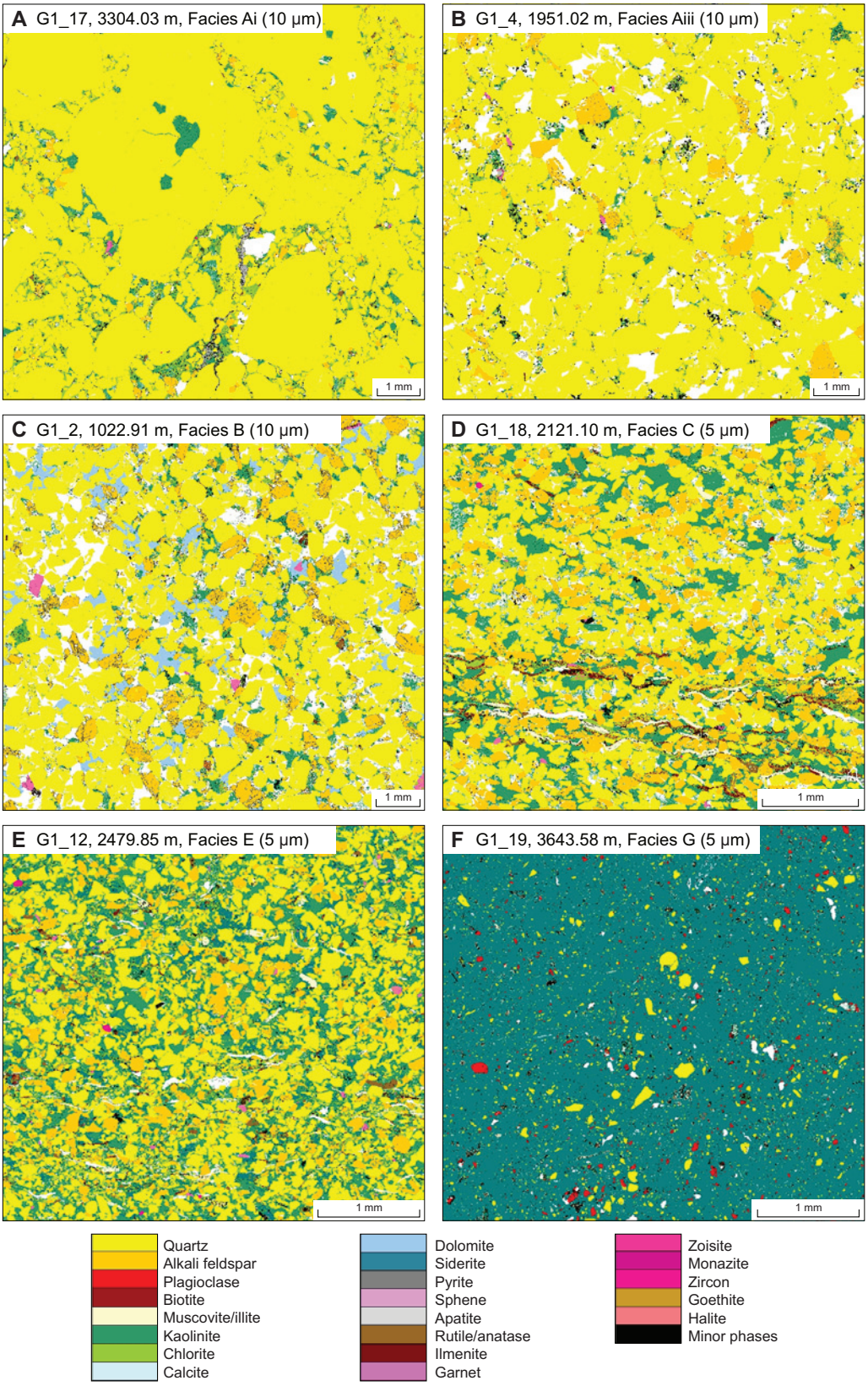

Figure 4.9: automated mineral analysis maps for different lithofacies in Gingin-1. Sample I.D., downhole depth, facies and analytical step size are indicated.

Automated mineral mapping of selected samples from Pinjarra-1, Cockburn-1 and Gingin-1 provides a more statistically robust mineralogy dataset than point count data (Figs 4.7-4.9). This approach permits the quantification of the proportion and textural context of major and trace minerals (Figs. 4.10 and 4.11). These data confirm that quartz and alkali feldspar are the main framework minerals across the three wells, which comprise 42 to 92% and 2 to 21% of the total mineral abundance, respectively (Fig. 4.10). One sample in Gingin-1 is exceptional in preserving plagioclase (3.7%), which has an albite composition. Elsewhere, plagioclase is not present as a major framework mineral. Minor amounts (<1%) of detrital biotite and muscovite are present in all three wells. Variations in mineralogy are best explained by a lithofacies control rather than systematic variations with depth. Detrital garnet grains occur in many of the samples up to approximately 2% (Fig. 4.10). Other heavy minerals of notable trace abundance in all three wells include monazite, zircon, ilmenite and TiO_2 minerals (rutile and anatase) (Fig. 4.11). Areas mapped as TiO_2 have the appearance of large detrital rutile grains as opposed to the typical euhedral microcrystal appearance of diagenetic anatase (Figs 4.7-4.9). Pyrite and apatite occur at trace levels (<0.1%) in Cockburn-1 and Gingin-1, and goethite occurs in three samples from Gingin-1 (Fig. 4.11). Chlorite is generally of low abundance (<2%), and is most abundant in lithofacies E in Pinjarra-1 (12%) and Gingin-1 (1.5-3.6%). In sample P_2895.12 m, chlorite is Fe-rich, which is the composition for formation in sedimentary environments. It is spatially associated with detrital biotite and muscovite and has probably formed as a diagenetic alteration of these micas.

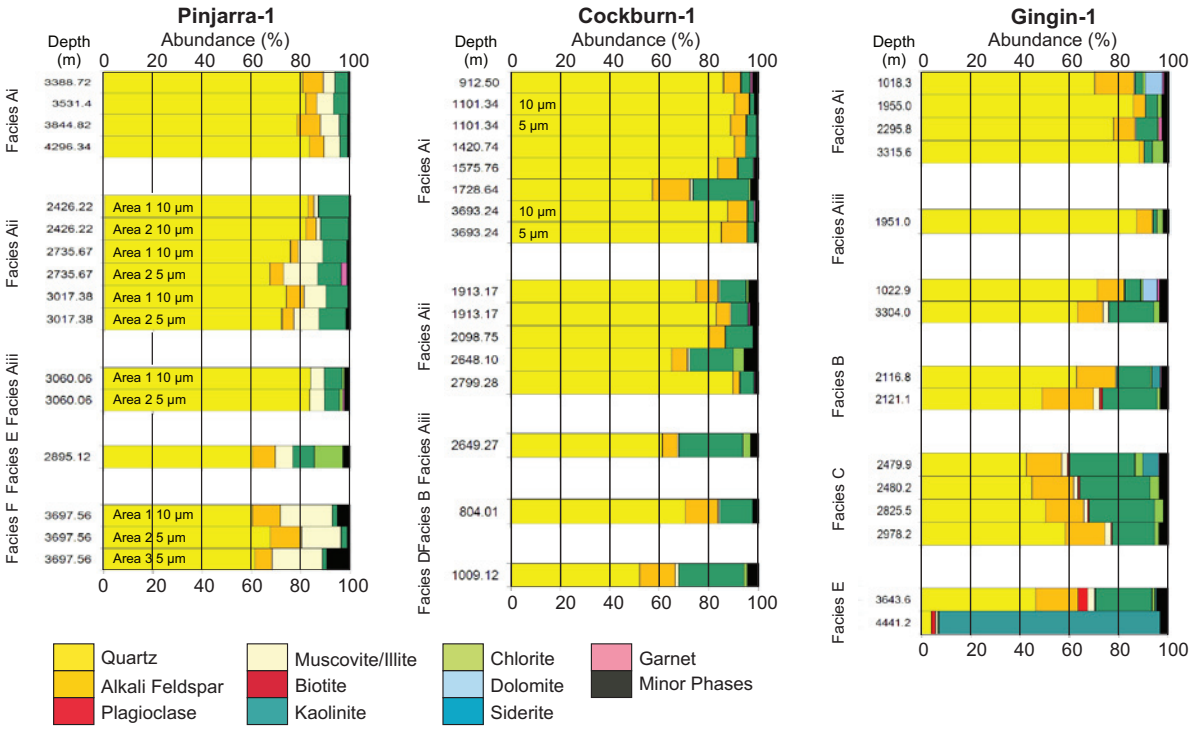

Figure 4.10: Bar charts to show modal mineralogy from automated mineral analysis, sorted by lithofacies for Pinjarra-1, Cockburn-1, and Gingin-1.

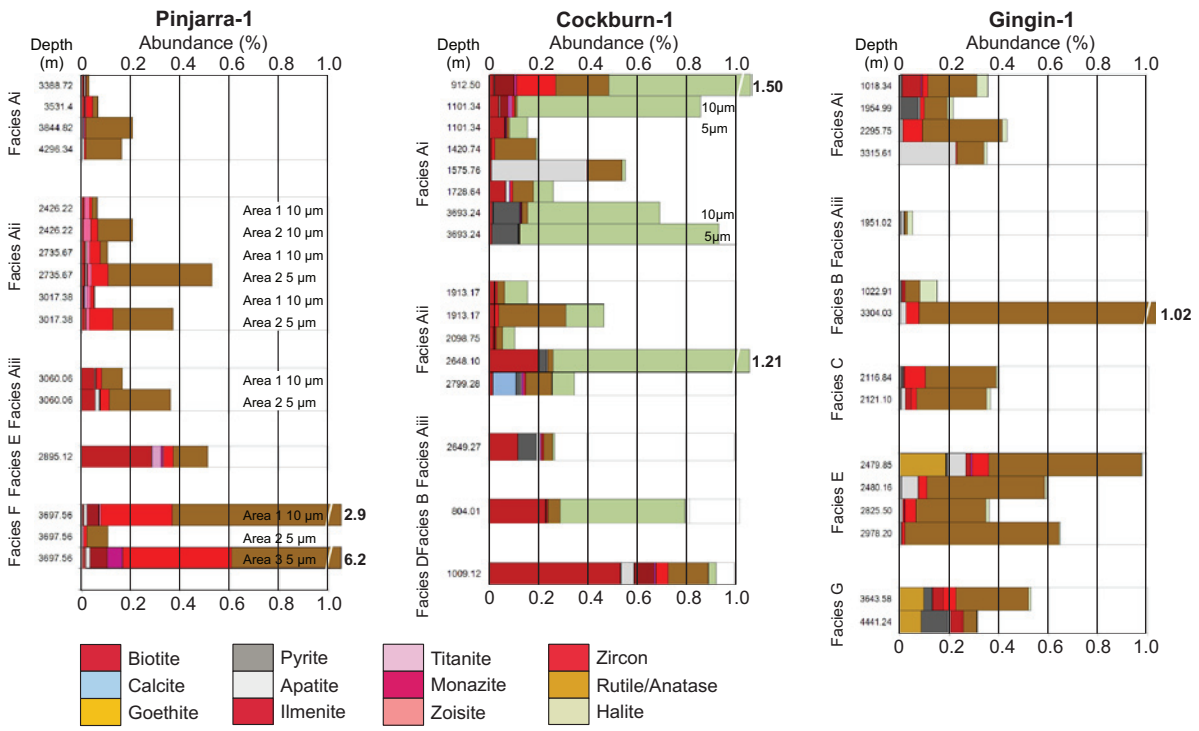

Figure 4.11: Bar charts to show modal trace mineralogy from automated mineral analysis, sorted by lithofacies for Pinjarra-1, Cockburn-1, and Gingin-1.

4.4.2 Diagenesis

Kaolinite is the main clay mineral in all three wells (Figs 4.7-4.10, 4.12, 4.13), and commonly occurs as microcrystalline coatings on the detrital grains and in heterogeneously distributed pore-occluding clots, probably precipitated locally after dissolution of detrital plagioclase feldspar clasts (Fig. 4.12a-c) (Worden and Morad, 2003). Some alkali feldspars are skeletal and/or contain kaolinite domains, and appear to have been partially dissolved, probably indicating the preferential removal in solution of feldspar lamellae of a particular composition in originally perthitic grains. Al and Si liberated from dissolved feldspar probably provided the source for kaolinite. Image analysis and point count data shows that the proportion of skeletal feldspar and primary porosity that has been partially occluded by clays (kaolinite) increases with depth across all lithofacies and wells (Fig. 4.6).

Quartz overgrowth cements are minor, patchy and relatively early in the studied wells (Figs 4.3-4.5, 4.12f-g, 4.13). This could be due to early development of kaolinite (after plagioclase dissolution) that coated grains and inhibited the development of quartz overgrowths (Fig. 4.13). Pore-occluding domains mapped as muscovite/illite common in Pinjarra-1 samples (e.g., Fig. 4.12d) are likely to be diagenetic illite due to its size and shape. Illite has formed after kaolinite grain coatings (Fig. 4.12d). Illite does not occur in Cockburn-1 or Gingin-1. A patchy, pore occluding dolomite cement at approximately 6-7% occurs in two samples at approximately 1020 m in Gingin-1 (Figs 4.9 and 4.12e). These dolomite cements do not overgrow grain coatings of kaolinite and are interpreted to have formed earlier than kaolinite. No carbonate cements have been observed in Pinjarra-1 or Cockburn-1.

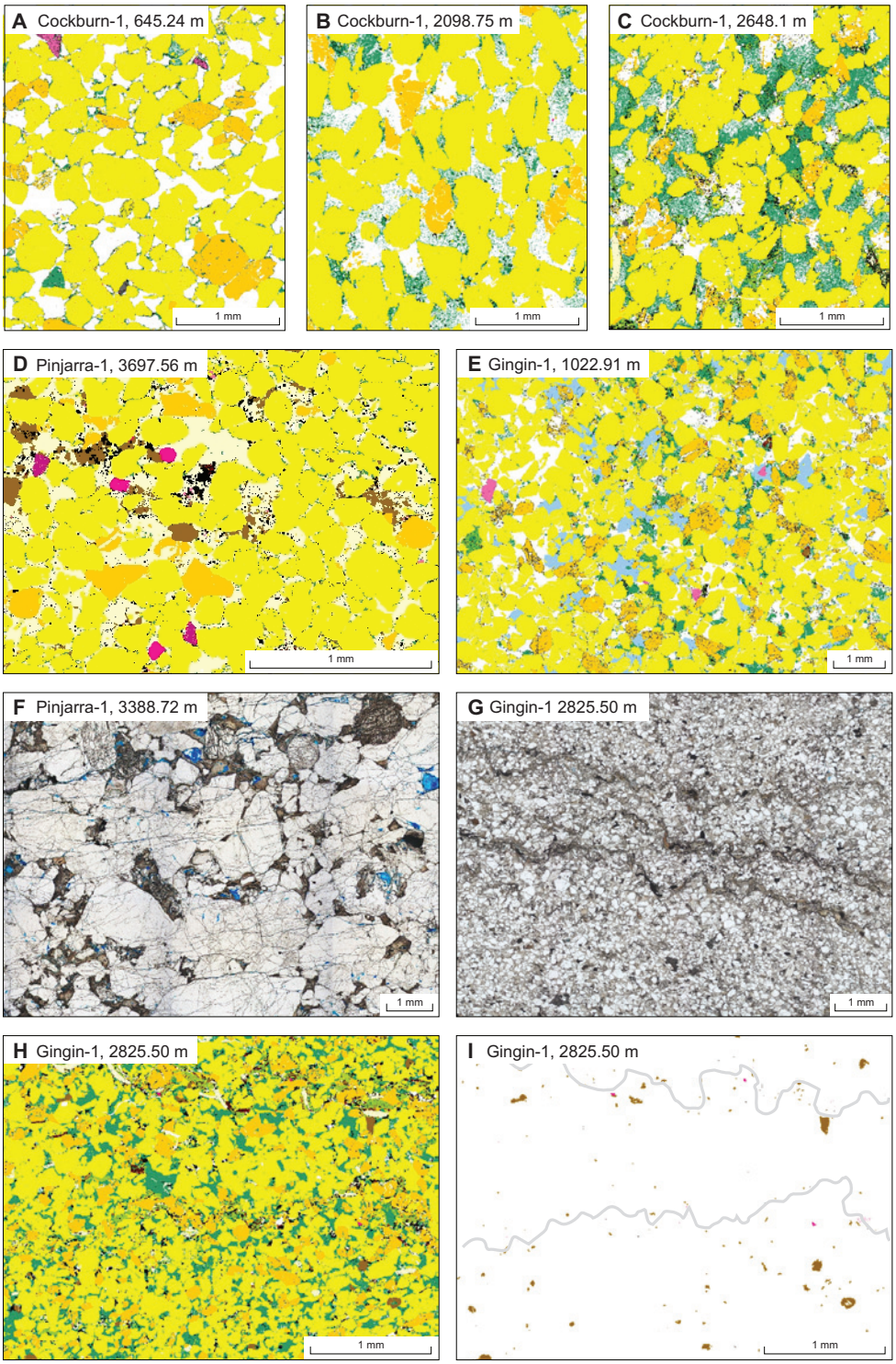

Figure 4.12: Summary images of diagenetic features of the central Perth Basin. A-C. Authigenic kaolinite cementation present to varying proportions in Cockburn-1. D. Kaolinite grain coatings and pervasive illite cement present in Pinjarra-1. E. Patchy dolomite cement present in two samples in Gingin-1. F. Pervasively fractured grains typical in coarse grained rocks from deeper intervals in Pinjarra-1 and Gingin-1. G. Clay-rich stylolites in fine sandstone. H. Automated mineral analysis map of stylolites showing weak enrichment in trace minerals. I. As in H but with major minerals plotted white to reveal the distribution of trace minerals.

Minor amounts, (up to 1%) ,of halite were noted in all samples in Cockburn-1 and some samples in Gingin-1 (< 0.1%) (Fig. 4.11). Its origin is unknown but it may be a contaminant from the drilling process. However, records of the drilling fluid, etc., from the time of drilling are not available. Sample G1_14571 is distinctly different from other samples. It has 90% siderite and contains 1.5% plagioclase with an albite composition, which is not present in all but one of the other samples (Fig. 4.9f). This sample is probably a siderite concretion formed early during diagenesis that protected plagioclase from contact with burial fluids and, consequently, reaction to kaolinite.

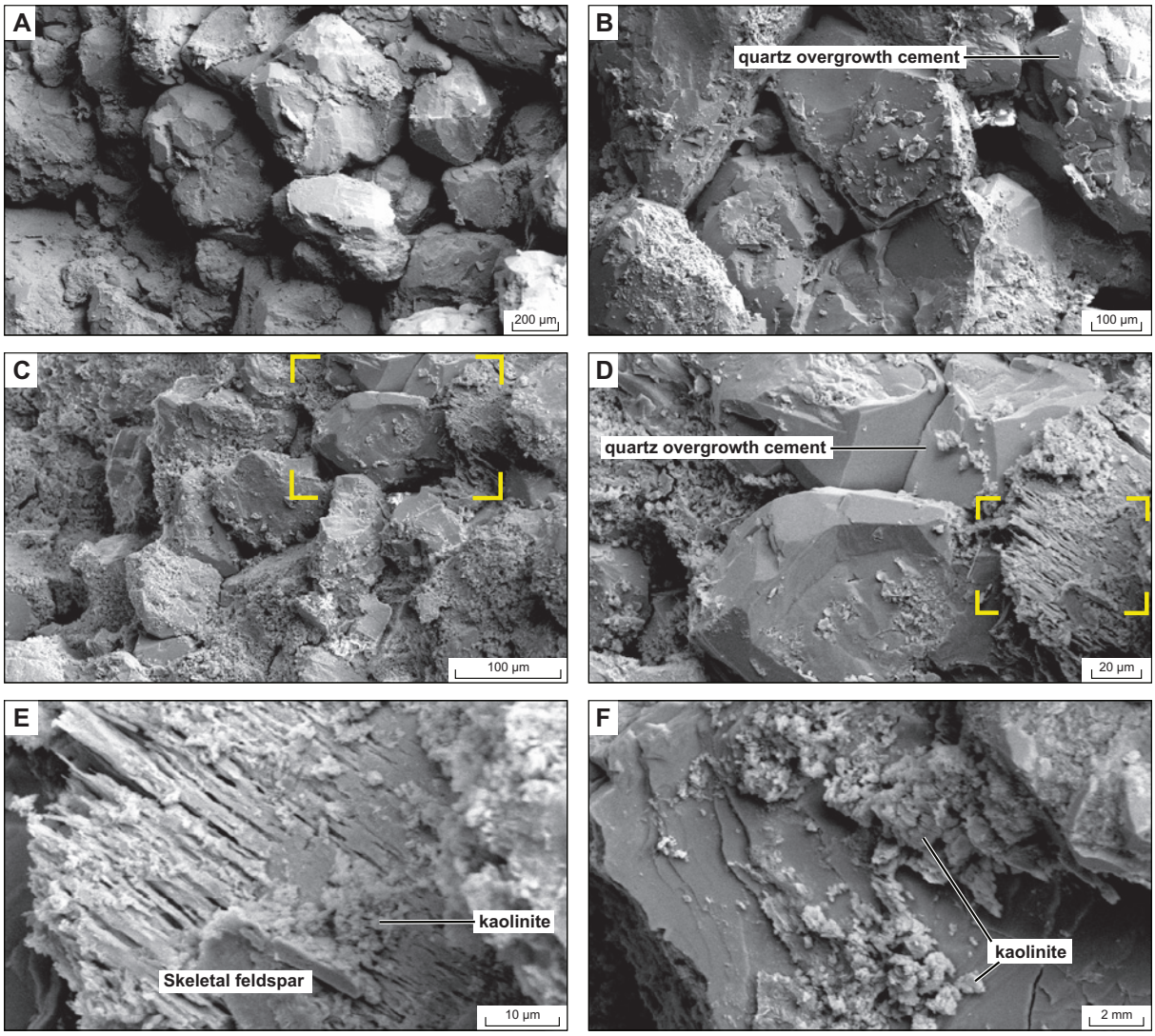

Figure 4.13: Secondary electron images of a broken surface of a core sample showing the nature of the 3D pore spaces in a cross-bedded sandstone sample typical of lithofacies Aii from Cockburn-1. A. Clean, well sorted, coarse grained part of the sample with well-preserved porosity. B. Detail of the clean, well-sorted domain showing some faceting of the grain surfaces by minor authigenic quartz overgrowth cement. C. Fine grained, clay-rich domain showing grains with patchy coating of authigenic kaolinite. Kaolinite commonly fills the pore throats at grain contacts. D. Detail shown by white box in C showing well-faceted authigentic quartz overgrowths with patchy kaolinite coatings. E. Detail shown by white box in D showing skeletal feldspar with micrometer-scale blocky kaolinite. F. Surface of a grain with micrometer-scale blocky kaolinite and poorly-developed booklets of kaolinite. Sample is from 912.26 m depth.

Compaction-related textures such as elongate grain boundaries and reduced primary porosity increase with depth, particularly in Pinjarra-1 and Gingin-1. Samples from Cockburn-1 seem to be less affected by compaction at equivalent depths. Grains in the deepest coarse grained samples from Pinjarra-1 and Gingin-1 are significantly fractured by multiple fracture sets (Fig. 4.12f). Aligned 'fracture zones' commonly cut across several grains. These have probably formed in response to compaction-related stresses during burial.

Stylolites have developed along sub-horizontal clay-rich laminations in all wells at depths below ~2200 m (Figs 4.12g and 4.14). Stylolites are generally weakly developed, discontinuous, and contain greater abundance of micas, pyrite and heavy minerals (Fig. 4.12h-i). The thickest (i.e., most developed) stylolites can be observed hand samples of core and occur at depths greater than 3800 m in Gingin-1 and Gingin-2 (Fig. 4.14).

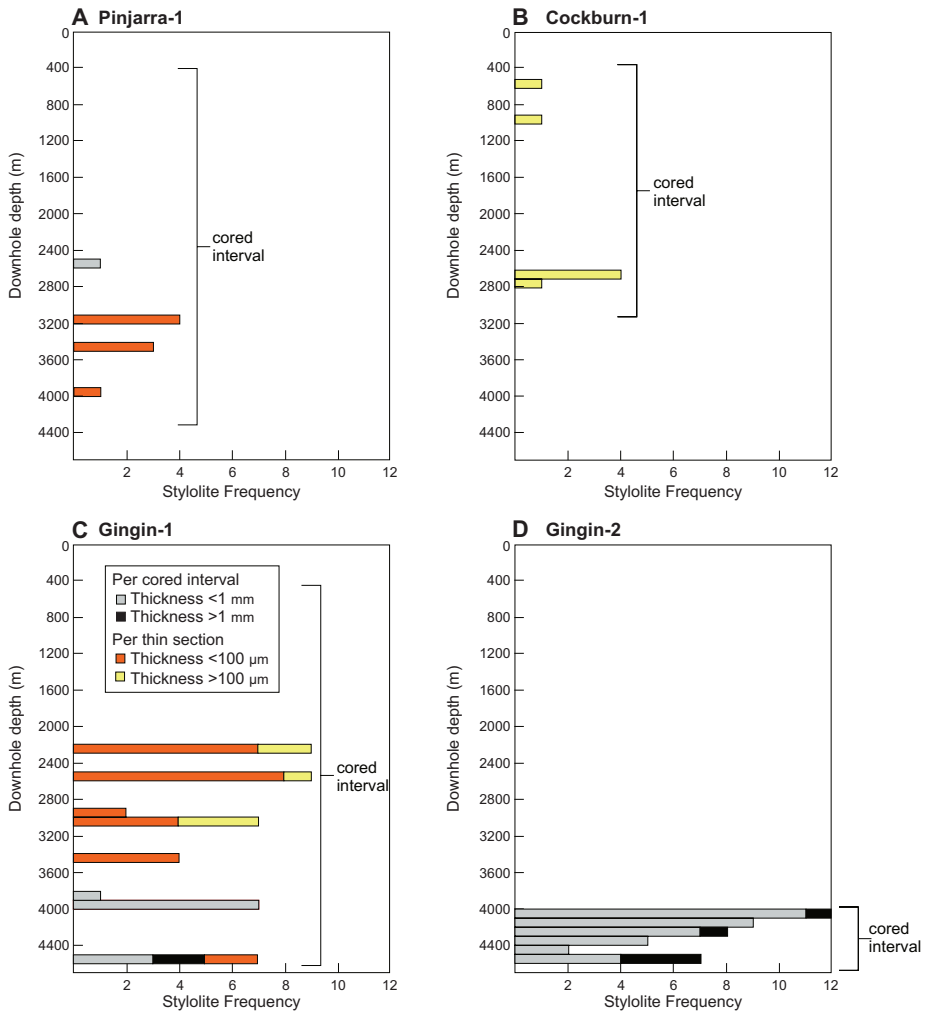

Figure 4.14: Frequency histograms of stylolites with downhole depth.
A. Pinjarra-1. B. Cockburn-1, C. Gingin-1, D. Gingin-2.
The depths sampled by core are indicated by grey lines.

4.4.3 Porosity and permeability data

3D (volumetric) porosity and permeability data can be found in Israni and Delle Piane (2011), and have been plotted against downhole depth by lithofacies in each of the studied wells (Fig. 4.15). Porosity varies from 0.5-15%, 0.1-25%, 0.5-20%, and 0.1-10% in Pinjarra-1, Cockburn-1, Gingin-1 and Gingin-2, respectively (Fig. 4.15a,c,e,g). Israni and Delle Piane (2011) show little dependence of porosity on confining pressure, such that there is a strong correlation between measurements made at 500 and 2000 psi with R2 = 0.99.

Generally, 3D porosity diminishes with depth for each lithofacies with an approximately linear trend, consistent with the estimates of 2D porosity from image analysis (Figs 4.6 and 4.15). Lithofacies A, B, and C are the most porous and lithofacies F and G are the least porous for a given depth in each hole. Lithofacies D and E have moderate porosity values with significant variability, as expected from the lithological variability within these lithofacies.

Permeability values range over six orders of magnitude (Fig. 4.15b,d,f,h). Broadly, linear trends of the logarithm of permeability with depth can be seen for each lithofacies. For a given depth in each well, lithofacies systematically reduce in permeability from A (most permeable) through to G (least permeable) (Fig. 4.15). The most permeable values at each depth could be used to generate an upper bound trend line for permeability with depth. However, it should be noted that several highly porous, coarse grained samples were damaged during testing (i.e., data from these samples are missing), and so any extrapolation based on the current data will likely result in an under-estimation of the maximum permeabilities present in the wells. Therefore, this analysis was not done.

3D porosity was plotted against the logarithm of permeability by lithofacies as a combined dataset across all wells (Fig. 4.16a). The maximum, minimum and mean porosity and permeability values and porosity-permeability relationships for different lithofacies from the combined dataset are summarised in Table 4.1. An exponential trend line can be fitted to the combined dataset with a reasonable correlation factor $R^2 = 0.7914$ (Fig. 4.16a, Table 4.1). Different lithofacies show systematic deviation from this 'global' trend line, and most lithofacies-specific trend lines lie sub-parallel to it and have higher R^2 values up to 0.9604 (Fig. 4.16a, Table 4.1). A systematic reduction in permeability for a given porosity value can be seen from lithofacies A through D. Trend lines for lithofacies E, F and G have poor fit statistics, with $R^2 = 0.2695$, 0.2547, and 0.3413, respectively. These lower values could be because of the low porosity and permeability values and significant scatter for these lithofacies, which are most likely caused by fine grain sizes, high initial mud contents, and primary lithological variability.

Variations in the porosity and permeability data plotted for each individual well also show a strong lithofacies control in a similar way as has been described for the combined dataset (Fig. 4.16b-e). The coarser grained lithofacies A tend to lie above the mean trend lines for each well (black lines on Fig. 4.16b-e), i.e., they are more permeable for a given porosity than the other lithofacies. Lithofacies E, F and G consistently have low porosity (<10 %) and permeability values (<0.7 mD). Variability along the trend lines has a reasonable relationship with downhole depth, as shown in Fig. 4.15. The absolute porosity and permeability values for lithofacies A vary systematically with depth (red dashed line

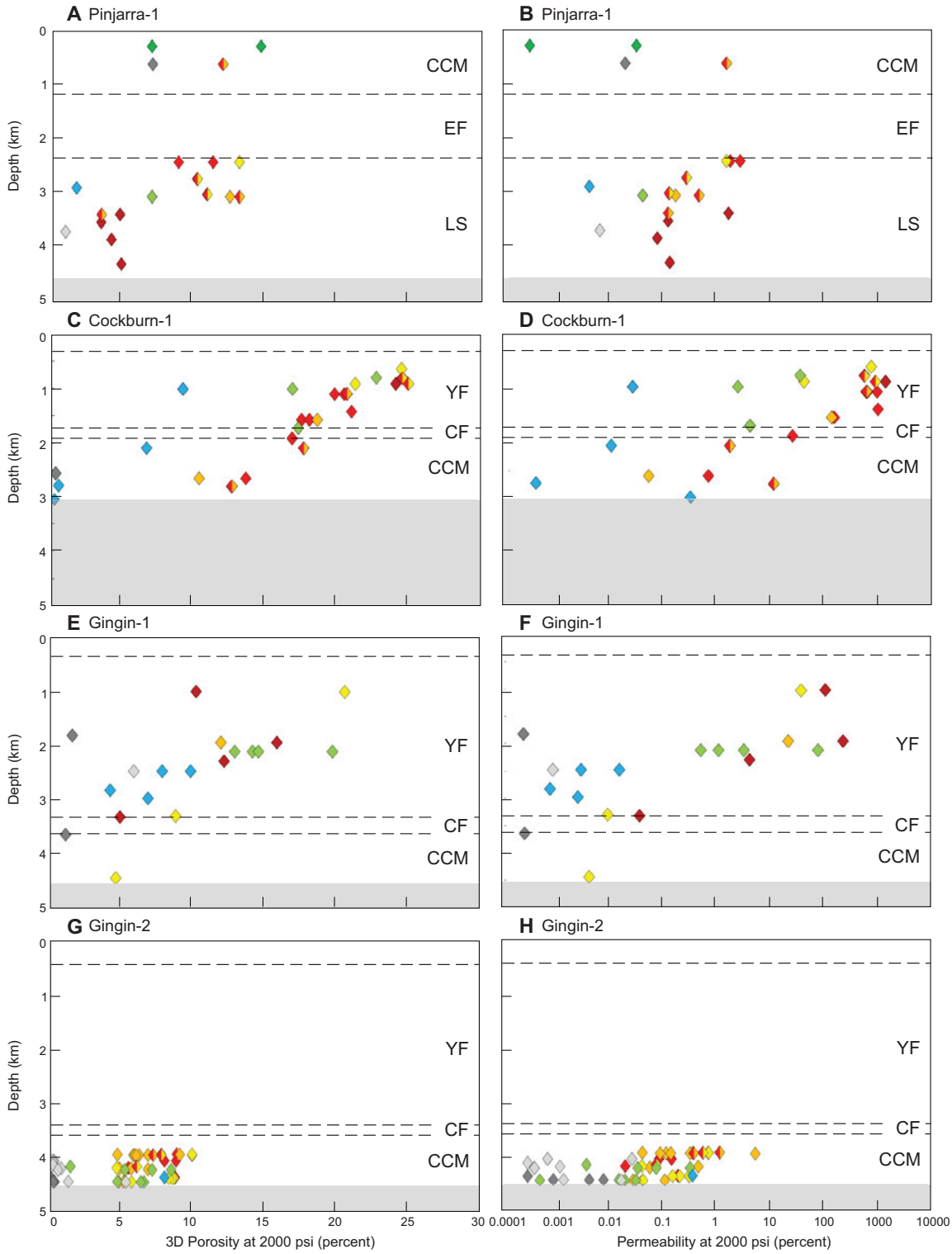

Figure 4.15: Relationship between 3D porosity (A, C, E, G), logarithm of permeability (B, D, F, H) and depth. Data are coloured for lithofacies. Porosity and permeability values are 2000 psi data, and permeability data are Klinkenberg-corrected. Dashed lines denote stratigraphic subdivisions. LS = Lesueur Sandstone; EF = Eneabba Formation; CCM = Cattamarra Coal Measures; CF = Cadda Formation; YF = Yarragadee Formation. Areas of the charts that are beyond the end-of-hole are shaded grey, for which there are no data.

contours on Fig. 4.16b-e). Cockburn-1, Gingin-1 and Gingin-2 have similar porosity and permeability depth contours for lithofacies A, whereas Pinjarra-1 shows anomalously low values for equivalent depths. Given the similarities in other textural properties between the wells (e.g., grain size, sorting, clast mineralogy) this phenomenon is most likely to be linked to the presence of pore occluding illite in Pinjarra-1 (Figs 4.7, 4.10 and 4.12), which is not present in the other wells at similar depths.

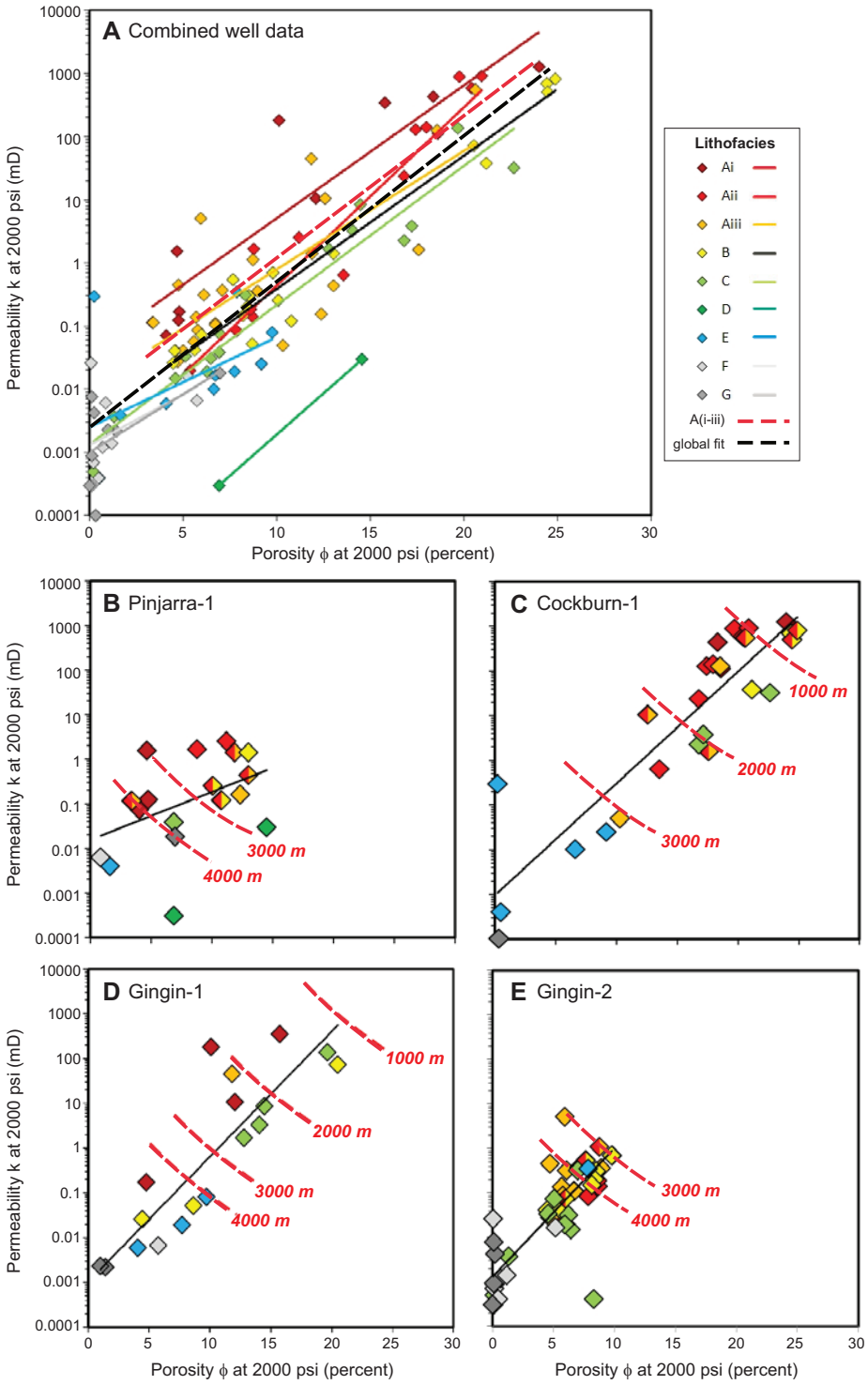

Figure 4.16: Porosity-permeability plots coloured for different lithofacies.
A. Combined data for all wells,
B. Pinjarra-1. C. Cockburn-1. D. GinGin-1.
E. GinGin-2. Exponential relationships for trend lines are given in Table 4.1. Depth contours (red dashed lines) on B-E are approximate and refer to lithofacies A (combined) only.

Facies	Porosity, ϕ (percent)			Permeability, k (mD)			Relationship exponential	Correlation factor (R^2)
	Min	Max	Mean	Min	Max	Mean		
Ai	3.36	23.98	10.95	0.0719	1260.6	213.0	$k=0.0406e^{0.4842\phi}$	0.8398
Aii	5.34	24.45	14.09	0.0196	915.7	187.0	$k=0.0007e^{0.6497\phi}$	0.8617
Aiii	3.37	20.59	8.98	0.0274	549.9	27.54	$k=0.0107e^{0.4315\phi}$	0.5886
A (group)	3.36	24.45	11.12	0.0196	1260.6	117.71	$k=0.0064e^{0.5214\phi}$	0.741
B	4.46	24.87	12.53	0.0257	804.2	11.31	$k=0.003e^{0.4858\phi}$	0.9604
C	0.19	22.64	10.17	0.0005	137.6	1.17	$k=0.0014e^{0.5075\phi}$	0.9164
D*	6.89	14.53	10.71	0.0003	0.0295	0.0149	$k=5E\text{-}06e^{0.6006\phi}$	1*
E	0.08	9.72	4.22	0.0001	0.351	0.0641	$k=0.0025e^{0.3275\phi}$	0.2695
F	0.08	5.74	1.59	0.0003	0.0259	0.0061	$k=0.0013e^{0.3697\phi}$	0.2547
G	0.00	6.96	1.26	0.0001	0.0183	0.0045	$k=0.001e^{0.4229\phi}$	0.3413
Global fit	0.00	24.87	9.12	0.0001	1260.6	71.91	$k=0.0021e^{0.5426\phi}$	0.7914

* based on 2 data points only.

Table 4.1: Porosity-permeability relationships for different lithofacies in the central onshore Perth Basin. Combined data from Pinjarra-1, Cockburn-1, Gingin-1, and Gingin-2 samples.

4.4.4 Thermal conductivity data

A detailed description and interpretation of the thermal conductivity results can be found in Esteban et al. (2012). Raw OTS-measured thermal conductivity values under dry and water saturated conditions are presented with depth from each well (Figs 4.17 and 4.18). The mean dry raw thermal conductivity from the integrated dataset ranges from 2.76 to 3.29 W/m/K and from 4.27 to 4.43 W/m/K in saturated conditions (Table 4.2; Fig. 4.18). Within each well and each unit, significant variations of thermal conductivity are observed (in particular for Gingin-1 and Gingin-2 wells). These variations are a function of different lithofacies types and depth (Table 4.2; Figs 4.17 and 4.18). The standard deviation of the mean thermal conductivity values in dry and saturated conditions for each formation is high, indicating that assignment of average thermal conductivity values based on stratigraphic formation may be misleading. Nevertheless, the Yarragadee Formation clearly records the lowest thermal conductivity across the wells under dry conditions (around 2.7 W/m/K) and saturated conditions (4.3 W/m/K). The measured thermal conductivity increases with depth (due to decreasing porosity with depth), with saturated thermal conductivity higher than dry thermal conductivity by approximately 1.5 W/m/K. More details of the statistics of thermal conductivity by formation and well is provided in (Esteban et al. 2012).

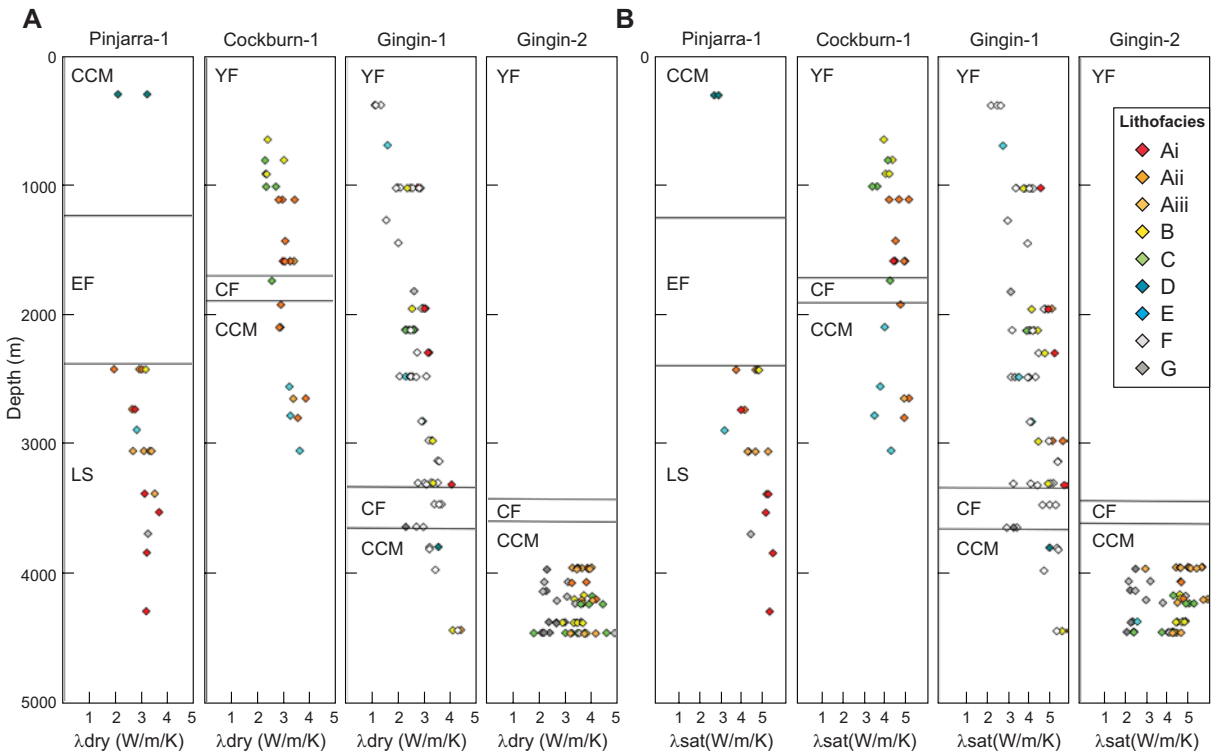

Figure 4.17: Laboratory-measured thermal conductivity variation with depth for dry and water saturated conditions for samples from Pinjarra-1, Cockburn-1, Gingin-1, and Gingin-2 wells. Data points are coloured according to the lithofacies scheme outlined in Section 3 of this report.

Well	Formation	Number of samples	Dry Thermal Conductivity $Wm^{-1}K^{-1}$		Water saturated Thermal Conductivity $Wm^{-1}K^{-1}$	
			Mean	Std. Dev.	Mean	Std. Dev.
Pinjarra-1	All	23	2.91	0.49	4.36	0.82
	Cattamarra Coal Meas.	0	-	-	-	-
	Eneabba	5	2,72	0.64	3.74	0.85
	Lesueur	18	2.96	0.44	4.54	0.74
Cockburn-1	All	27	2.94	0.45	4.34	0.57
	Yarragadee	17	2.80	0.43	4.28	0.61
	Cadda	1	3.54	0	4.303	0
	Cattamarra Coal Meas.	9	3.27	0.36	4.46	0.59
Gingin-1	All	67	2.76	0.68	4.43	0.85
	Yarragadee	52	2.57	0.59	4.28	0.78
	Cadda	5	3.51	0.35	5.17	0.49
	Cattamarra Coal Meas.	10	3.38	0.69	4.87	1.04
Gingin-2	Cattamarra Coal Meas.	60	3.29	0.66	4.27	1.07
Combined	Facies Ai	11	3.16	0.38	5.04	0.50
	Facies Aii	19	3.17	0.57	4.75	0.47
	Facies Aiii	27	3.50	0.39	4.95	0.64
	Facies B	19	3.05	0.56	4.56	0.49
	Facies C	16	3.05	0.84	4.22	0.67
	Facies D	3	2.92	0.76	3.54	1.33
	Facies E	11	2.81	0.59	3.84	0.54
	Facies F	12	3.06	0.76	3.44	0.69
	Facies G	11	2.57	0.51	2.89	0.54

Table 4.2: Laboratory measured thermal conductivity statistics per stratigraphic formation, per well for the central Perth Basin sample suite.

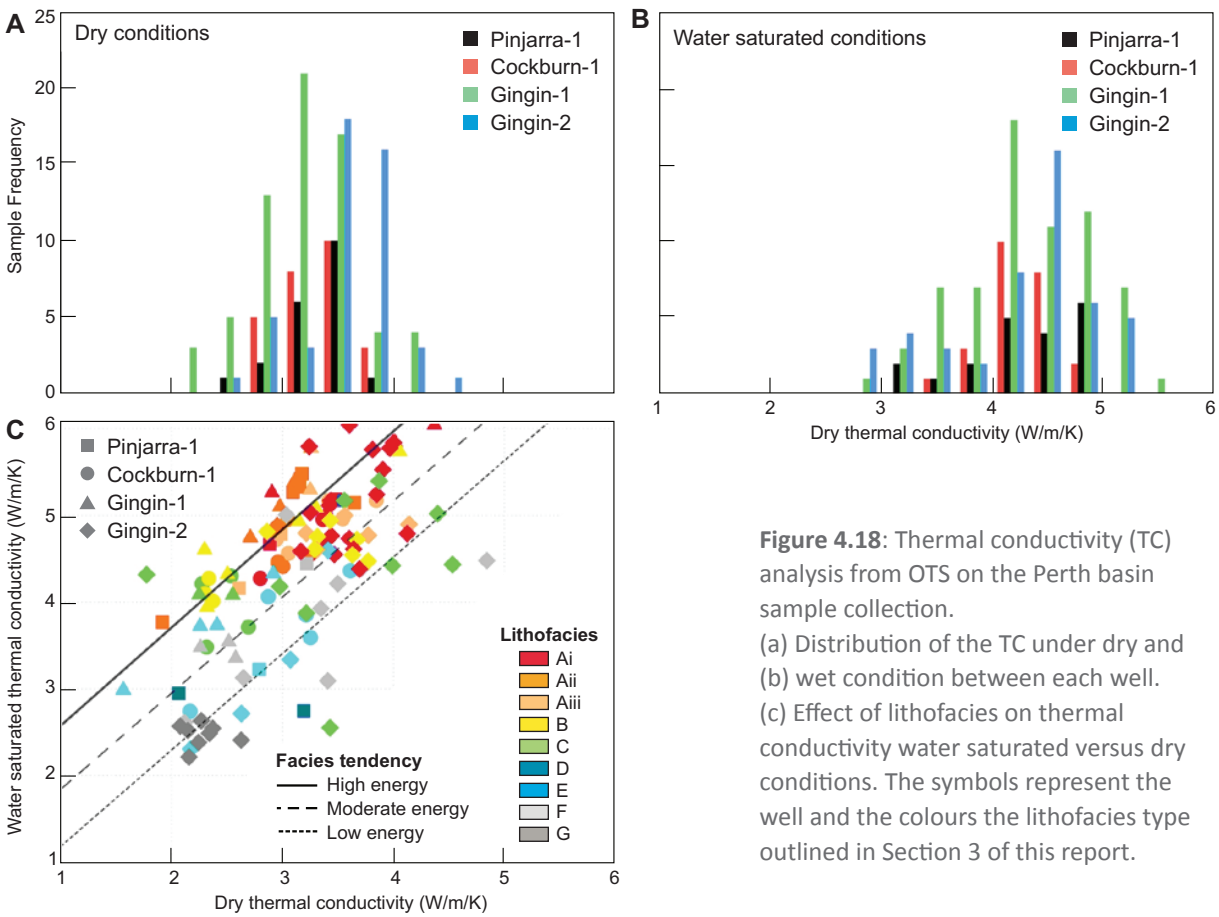

Figure 4.18: Thermal conductivity (TC) analysis from OTS on the Perth basin sample collection.
(a) Distribution of the TC under dry and (b) wet condition between each well.
(c) Effect of lithofacies on thermal conductivity water saturated versus dry conditions. The symbols represent the well and the colours the lithofacies type outlined in Section 3 of this report.

4.5 Discussion

4.5.1 Detrital mineralogy

The detrital mineralogy of samples from Pinjarra-1, Cockburn-1, and Gingin-1 is dominated by single-crystal quartz, with rare polycrystalline quartz, a moderate amount of alkali feldspar and very minor amounts of garnet, organic fragments, muscovite and biotite, and rare albite in Gingin-1. Trace (<1%) zircon, rutile, monazite, apatite and titanite are common. In general, alkali feldspar is more abundant northward. However, there does not seem to be any other systematic changes in mineralogy across the four wells. Mineralogy changes heterogeneously with depth in all four wells. These variations are consistent with a strong lithofacies control on mineralogy. Lithofacies A tends to be the most quartz-rich, which probably reflects greater winnowing associated with high energy channel fill processes. Finer-grained lithofacies D-G have variable but low proportions of quartz, and significant amounts of clays (kaolinite). Lithofacies E-G contains more detrital mica and organic fragments, which tend to be abundant on lamination surfaces. The high proportion of authigenic clays in most samples prevents the use of traditional ternary classification schemes for sandstones (Selley 1988).

Overall, the detrital mineralogy is consistent with cratonic and/or metamorphic sources. Other than garnet, no specific metamorphic indicator minerals were present. It is difficult to precisely pinpoint the exact provenance of the sediments. They could have been sourced from any or all of the Yilgarn

Craton, the Northampton Block, the Leeuwin block, Antarctica or Greater India, which would all have granitic composition rocks with garnet-rich metamorphic rocks.

Most quartz grains in the sandstones are sub-angular, with some sub-rounded. This indicates moderate distance from source. The source of sediment is probably the Yilgarn Craton or re-worked from younger rocks overlying the Yilgarn, suggesting that fluvial systems transported sediment from source to deposition (Miall 1996). The Cadda Formation in Gingin-1 has >80% quartz in its two samples and is significantly more rounded, even for gravel-sized grains. Furthermore, it is better sorted than other sandstones. This suggests better winnowing, further transport from site, and therefore is more likely to be of beach to shallow marine origin.

4.5.2 Diagenesis

Prevalent and early-formed authigenic kaolinite (after feldspar) has had an important role in the evolution of porosity within the sandstone samples. The kaolinite in the sandstones does not have the appearance of inherited detrital clay coats because it is not present at grain-grain point contacts. Either detrital clay coats were uncommon, or have been removed in the high energy fluvial environment. Kaolinite in these rocks has a book-like habit, and is consistent with development via eogenetic dissolution of feldspars by the action of low-pH groundwater in humid climate conditions (Worden and Morad, 2003). This process is more prevalent in permeable sediments, such as channel sand deposits (Worden and Moarad, 2003). The presence of kaolinite-filled skeletal feldspars in the low energy, swampy and lagoonal facies indicates that some of the kaolinite is eogenetic. However, a proportion of the total clay content could have resulted from flocculation of riverbourne clays in estuarine conditions, or grain coating by percolation of mud-rich surface waters in floodplain environments (Worden and Morad, 2003). The uncommon presence smectite and/or Fe sulphides and/or early carbonate cements and/or glauconite could indicate occasional influence of marine conditions (Worden and Morad, 2003).

Early (eogenetic) grain coating by kaolinite probably inhibited quartz overgrowth cementation (Worden and Morad, 2003). However, increased abundance of kaolinite with depth is a major factor in the reduction of porosity with depth across all wells. Patchy dolomite cements and siderite nodules are rare in the region, and are most likely to have formed later than eogenetic kaolinite. Previous x-ray diffraction studies in the Cattamarra Coal Measures (below 3600 meters) found that on average each sample from Gingin-1 (and Gingin-2 at equivalent depth) contained 75% kaolinite, 23% chlorite, and 2% illite relative concentrations (Macchi 2000). One sample in coarse-grained sandstone contained 65% illite/smectite and 35% kaolinite. The development of illite has significantly reduced the porosity in Pinjarra-1, but is generally not present in Cockburn-1 or Gingin-1. This suggests that this well has undergone a different burial and/or thermal history to the other wells. Transformation of kaolinite to illite is prevalent at temperatures greater than approximately 70 °C and pervasive at temperatures greater than 130 °C (Worden and Morad, 2003). This would imply that temperatures have remained below 70 °C at the depths sampled by Cockburn-1 and Gingin-1, whereas the presence of illite implies relatively higher temperatures in Pinjarra-1. Greater burial and subsequent uplift of Pinjarra-1 is consistent with the change in depth of the stratigraphic formations across

the four wells. However, there is no significant difference of the upper limit of stylolite formation between the wells, as could be expected for differential burial/exhumation histories between the wells. Alternatively, Pinjarra-1 could have experienced higher temperatures during diagenesis due to underlying basement rocks with higher heat production. It is possible that the Logue Brook Granite, which outcrops to the east of the Darling Fault at the same latitude as Pinjarra-1 (Nemchin and Pidgeon 1997, Wilde 1999, Wilde and Nelson 2001), extends beneath the region of Pinjarra-1 to the west of the Darling Fault. However, this is difficult to verify due to the thickly developed succession in this part of the basin. Buried granites of the Northampton Complex have been suggested as an influence on the anomalously high apparent modern day heat flow in the northern Perth Basin north of latitude 30°00' (HDRPL 2008).

Burial-related stylolites are weakly developed in the central Perth Basin, and it is anticipated that stylolites are unlikely to have significant effects on the vertical permeability at depths <3800 m. Pervasive, burial-related intra-grain fractures of coarse grained sedimentary rocks at depths greater than 2,900 m in Gingin-1 and 2,400 m in Pinjarra-1 could contribute to a decrease in bulk strength and increase in dynamic permeability, depending on the cohesive properties of the fractures. Figure 4.19 summarises the paragenetic sequence in the central Perth Basin.

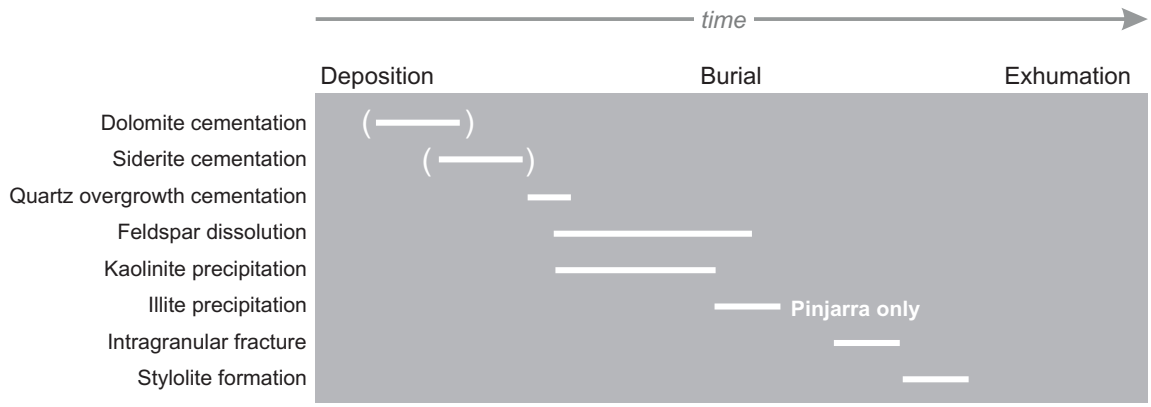

Figure 4.19: Paragenetic sequence for the central Perth Basin.

4.5.3 Controls on porosity and permeability

The main controls on the highly variable porosity in all four wells are lithofacies (i.e., depositional environment and depth). With a few exceptions, porosity has a broadly linear relationship with depth for each lithofacies. Lithofacies type primarily controls grain size and sorting, with coarse grain sizes and good sorting corresponding to high porosity. Porosity occlusion by clay minerals and compaction increases with depth.

The corresponding effect on permeability is a lithofacies-related variability (at a given porosity) of approximately two orders of magnitude, and depth-related variability (for a given lithofacies) of five orders of magnitude. For example, the permeability for lithofacies A at 1000 m and 3000 m is on the order of 100 mD and 1 mD, respectively, for Cockburn-1, Gingin-1, and Gingin-2. For Pinjarra-1, the permeability of lithofacies A is on the order of 0.1 mD, and these lower values are probably due to illite cementation.

4.5.4 Controls on thermal conductivity

The thermal conductivity variations in the Perth Basin samples are related at first order to the decrease of porosity, a relationship that has been described elsewhere (Pagoulatos and Sondergeld 2004). Therefore, the strong pattern of increased compaction and authigenic clay mineral development, and hence decreasing porosity with depth exerts a fundamental control on thermal conductivity in the Perth Basin. The thermal conductivity is known to be affected by mineralogy (Clauser 2006, Clauser and Huenges 1995, Tong et al. 2009). Several authors used this assumption to determine with a good approximation the thermal conductivity by knowing the dominant phase of the studied rock and neglecting the influence of the other minerals (Abdulagatova et al. 2009, McKenna et al. 1996, Ozkahraman et al. 2004). In the Perth Basin, quartz is the dominant phase across all of the studied formations, with the exception of some shales (Fig. 4.10). The dependency of the thermal conductivity on lithofacies type is mostly controlled by the depositional energy conditions, with a shift toward the highest thermal conductivity corresponding to an increase of the grain size and quartz mineral content (Fig. 4.18; Table 4.2). Only Gingin-1 and Gingin-2 record very low energy facies with low thermal conductivity around 2 W/m/K.

4.5.5 Goals for future research

- Dating of detrital minerals such as zircon and monazite could provide better constraints on sediment provenance.
- Modal proportions of alkali feldspar, mica, zircon and monazite could be used to calculate the in situ heat production from the sedimentary rocks of the central Perth Basin.
- Modal mineralogy could be used to calculate thermal conductivity.
- Lithofacies- and depth-specific porosity-permeability relationships could be used to improve numerical models of heat transport and fluid flow, and to validate stratigraphic forward models.
- Methods for estimating thermal conductivity from wireline logs could be explored.
- Measurement of sediment heat capacity should be pursued in order to support reservoir engineering studies.
- Petrophysical measurement programmes should be extending to consider the effects of elevated temperature and pressure on rock properties.

4.6 Summary

The Triassic and Jurassic sedimentary rocks of the central Perth basin have been identified by Western Australia Geothermal Centre of Excellence as potential targets for geothermal exploration. However, previous investigations report wide ranges of key petrophysical properties such as porosity and permeability, and there is little data on the mineralogy and intrinsic thermal conductivity for these formations. This study presents new data on petrography, mineralogy, porosity, permeability and thermal conductivity data from core samples that encompass a variety lithofacies types (identified in Section 3 of this report) and depths from Pinjarra-1, Cockburn-1 and Gingin-1 wells to determine the influence of primary sedimentary variations and diagenesis on key parameters for geothermal exploration and production. The detrital mineralogy acquired by point counting and automated

mineral analysis of samples from Pinjarra-1, Cockburn-1, and Gingin-1 is dominated by single-crystal quartz, with rare polycrystalline quartz, a moderate amount of alkali feldspar and very minor amounts of garnet, organic fragments, muscovite and biotite. These data show a lithofacies-dependence of the modal proportion of minerals, with little variation between equivalent lithofacies from different depths, formations or wells. Lithofacies type primarily controls grain size and sorting, and consequently has first order control on porosity. Each lithofacies type shows a trend of decreasing porosity and permeability with depth due to the increasing effects of compaction and authigenic clay mineral development. Cementation by quartz and carbonates is rare. The corresponding effect on permeability is a lithofacies-related variability (at a given porosity) of approximately two orders of magnitude, and depth-related variability (for a given lithofacies) of five orders of magnitude. Variations in thermal conductivity are related at first order to the decrease of porosity, grain size and quartz mineral content. This study shows that consideration of lithofacies and burial depth is vital for understanding the variability in petrophysical properties for geothermal exploration of the Perth Basin.

5. CALIBRATING POROSITY AND PERMEABILITY FROM WIRELINE LOGS: A CASE STUDY OF COCKBURN-1 WELL

5.1 Introduction

To make predictions about fluid flow and heat transport in the Perth Basin requires information about the variation in permeability in three dimensions. The facies analysis and porosity-permeability measurements presented in Section 4 of this report provide detailed but discontinuous information about the variability of porosity and permeability with depth in each well. Wireline logs can be used to convert this information into a continuous record of permeability with depth in each well, taking us a step closer to a full 3D model of permeability in the basin. We illustrate this approach in the Cockburn-1 well by using the sonic log to estimate porosity, then estimating permeability using the porosity-permeability relationship derived from Cockburn-1 samples (see Fig. 4.16). The result is a profile of porosity and permeability with depth over the same interval and with the same vertical resolution as the sonic log (0.1524 m).

5.2 Approach

The first step is to calculate porosity from the available wireline logs. Porosity can be determined from the sonic, density or neutron logs if the lithology is known, or from a combination of two or more of these logs if the lithology is unknown (Schlumberger, 1989). Density and neutron logs produce the most reliable results. Unfortunately the density log exists to only 915 m depth in Cockburn-1 and there is no neutron log, therefore the sonic log was used to estimate porosity in this study.

Porosity was calculated in Paradigm's Geolog software (www.pdgm.com) using the Wyllie method corrected for shale content (Dresser Atlas, 1979; Wyllie et al., 1956). The Wyllie time-average method gives the porosity of a clean, consolidated porous rock ($Ø_W$) as:

$$\phi_W = \frac{\Delta_t - \Delta_{tma}}{\left(\Delta_{tf} - \Delta_{tma}\right)} \qquad (5.1a)$$

where Δ_t, Δ_{tma} and Δ_{tf} are the sonic transit times of the fluid-saturated rock (i.e. the value recorded by the sonic log), rock matrix and pore fluid, respectively (Wyllie et al., 1956). A correction is applied to give the porosity of a shaly formation, $Ø_{DA}$:

$$\phi_{DA} = \phi_W - V_{sh}\frac{\Delta_{tsh} - \Delta_{tma}}{\left(\Delta_{tf} - \Delta_{tma}\right)} \qquad (5.1b)$$

where V_{sh} is the shale volume fraction and Δ_{tsh} is the sonic transit time of shale (Dresser Atlas, 1979). V_{sh} can be estimated by various methods from wireline logs. In this study we used the smallest value of V_{sh} obtained from three different methods using the gamma ray and spontaneous potential logs. Taking the minimum value is justified on the basis that shale indicators tend to overestimate shale content, therefore the lowest estimate is likely to be the most valid (e.g. Adeoti et al., 2009). Geolog then applies a maximum porosity cut-off to give the final value of sonic porosity, Øs:

$$\phi_s = \min\left[\phi_{DA},\ \phi_{s\max}\left(1 - V_{sh}\right)\right] \qquad (5.1c)$$

where ϕ_{smax} is the maximum allowable porosity of a shale-free rock. Table 5.1 lists the parameter values that were used.

Parameter	Value
Δ_{tf}	Sonic log
Δ_{tsh}	140 µs/ft (from sonic log)
Δ_{tma}	55.5 µs/ft (Schlumberger, 1989)
Δ_{t}	189 µs/ft (Schlumberger, 1989)
Φ_{smax}	1
V_{sh}	Minimum of values derived from spontaneous potential and gamma ray logs

Table 5.1: Parameter values used to calculate sonic porosity in Geology.

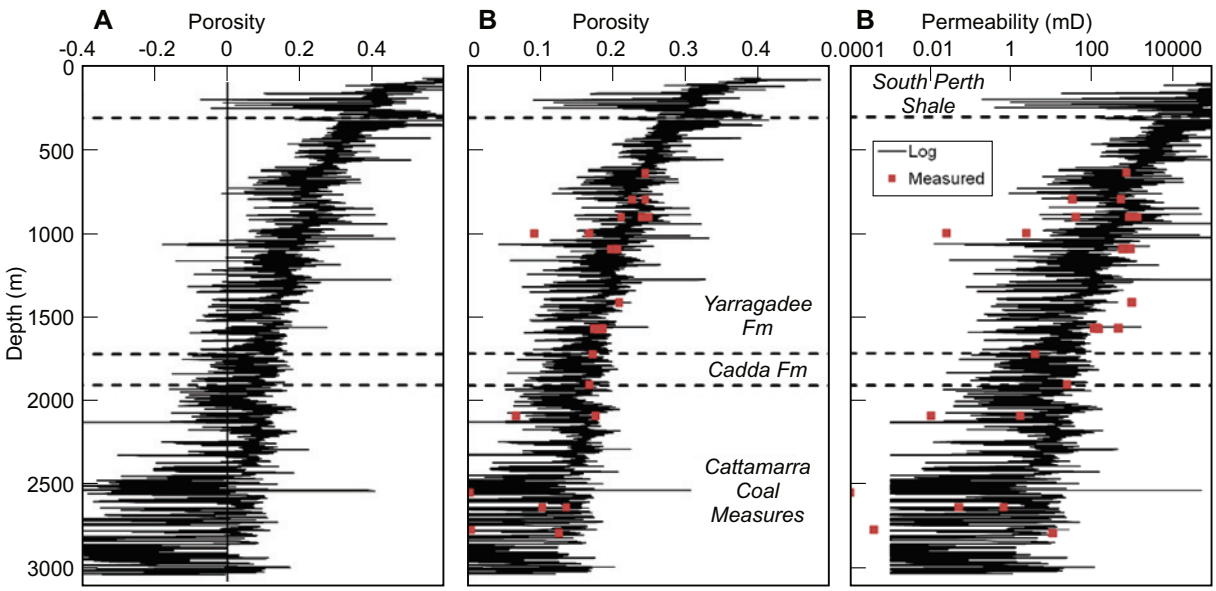

Figure 5.1: Porosity and permeability profiles obtained from the sonic log in Cockburn-1. Dashed lines indicate formation boundaries. Red squares indicate measured values. (A) Porosity calculated from sonic log using the Wyllie method. (B) Adjusted sonic porosity. (C) Permeability calculated from adjusted sonic porosity.

The resulting sonic porosity profile is shown in Figure 5.1A. Formation boundaries are shown for reference. The overall trend of decreasing porosity with depth is reasonable, but the range of values is not. Clearly the negative values must be incorrect, and the largest positive values are unrealistic. Therefore it was necessary to apply a correction to the sonic porosities. The appropriate correction was identified by plotting measured porosity against sonic porosity and fitting a linear trend line to the data (Fig. 5.2). The depths of the measured porosities do not correspond exactly to depths in the sonic log, therefore a weighted average of the sonic porosities immediately above and below each sample depth was used for comparison with the measured porosity. When all data points are included the correlation between measured and sonic porosities is poor (R^2 = 0.52; red crosses and dashed line in Fig. 5.2). A much stronger correlation is achieved if certain data points are excluded

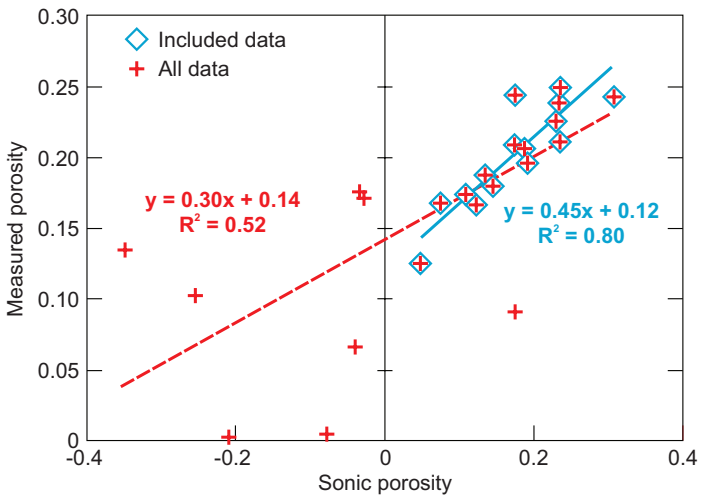

Figure 5.2: Comparison of measured and sonic porosity in the Cockburn-1 well. See text for explanation of "Included data".

(R^2 = 0.80; blue diamonds and solid line in Fig. 5.2). The excluded points are those with negative sonic porosities, and those where the difference between the sonic porosities immediately above and below the sample depth exceeds 0.01. The best-fit line for the reduced data set has the following equation:

$$\phi_{adj} = 0.45\phi_s + 0.12 \qquad (5.2)$$

where ϕ_{adj} is the adjusted sonic porosity. Applying this equation to the sonic porosities resulted in a more realistic porosity-depth profile, although some small negative values remained. Therefore a minimum porosity cut-off of 0.001 was imposed. The resulting adjusted porosity profile is shown in Fig. 5.1B, showing good agreement with the measured porosities (red squares in Fig. 5.1B).

Permeability was calculated from the adjusted porosity using the porosity-permeability relationship derived from Cockburn-1 samples (Fig. 4.16). The resulting permeability-depth profile is shown in Figure 5.1C, with measured permeabilities displayed as red squares.

5.3 Analysis of porosity-permeability profiles in Cockburn-1

The general trend is one of decreasing porosity and permeability with depth, as expected in sedimentary basins. There is no distinct change in porosity or permeability at formation boundaries, except the change from relatively low porosity and permeability in the South Perth Shale to higher values in the underlying Yarragadee Formation. Averages for each formation are listed in Table 5.2, but these averages are not particularly useful because they mask important variation within formations. For example, the averages imply that the South Perth Shale has much higher permeability than the underlying Yarragadee Formation, yet the permeability-depth profile (Fig. 5.1C) shows that the bottom half of the South Perth Shale has much lower permeability than the top part of the Yarragadee Formation. It is this low permeability that dominates the hydraulic relationship between these two formations, with the South Perth Shale acting as a confining bed at the top of the Yarragadee Aquifer (Davidson, 1995; Davidson and Yu, 2007).

Formation	Porosity	Permeability (arithmetic mean; mD)	Permeability (harmonic mean; mD)
South Perth Shale	0.33	75000	91
Yarragadee Fm	0.21	3000	8.2
Cadda Fm	0.15	14	1.3
Cattamarra Coal Measures	0.11	24	0.0062

Table 5.2: Average porosity and permeability by formation.

Instead of calculating averages by formation, a more useful representation of the permeability-depth profile is provided by moving averages. Figure 5.3A shows two moving averages of permeability: the arithmetic mean and the harmonic mean. Both were calculated over 50 m intervals. The arithmetic and harmonic means are known as the Wiener Bounds, which represent upper and lower limits on the effective permeability of a heterogeneous system (Renard and deMarsily, 1997). For the case of a horizontally layered system in which all layers have homogeneous isotropic permeability and infinite lateral extent, the arithmetic and harmonic means represent the effective horizontal and vertical permeabilities of the layered system, respectively (McKibbin and Tyvand, 1982; Wooding, 1978). In sedimentary basins the layers are discontinuous, thus the arithmetic mean represents an upper limit on the horizontal permeability and the harmonic mean represents a lower limit on the vertical permeability (Ababou, 1996; Michael and Voss, 2009). The ratio of horizontal to vertical permeability based on Wiener Bounds therefore represents an approximate upper bound on large-scale permeability anisotropy. This ratio ranges from ~2 to ~100 over most of the depth interval of Cockburn-1 (Fig. 5.3B), with higher values occurring in low-permeability horizons. The true anisotropy is likely to be smaller due to the discontinuous nature of low and high-permeability layers in sedimentary basins. Small-scale anisotropy within layers would also influence the large scale behaviour, but was not considered here due to lack of information about anisotropy on this scale.

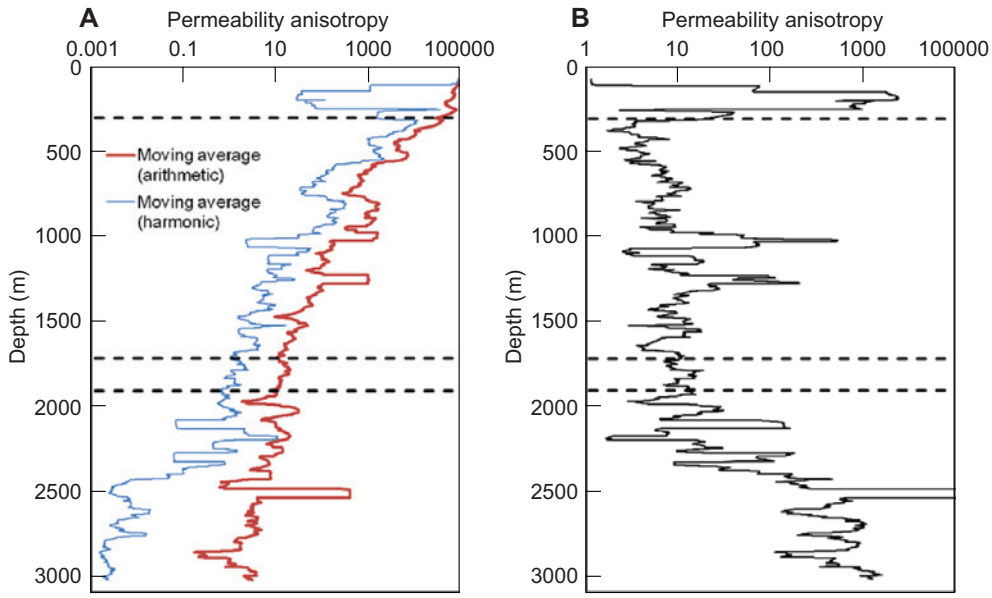

Figure 5.3: (A) Arithmetic and harmonic moving averages of permeability in the Cockburn-1 well. Averages calculated over 50 m intervals. (B) Permeability anisotropy based on the Wiener Bound moving averages in (A). Formation boundaries as in Fig. 5.1.

Superimposed on the general decrease in porosity and permeability with depth are smaller-scale variations spanning a few tens of centimetres to a few metres (Fig. 5.4). The length scale of these variations is consistent with the range of continuous facies thicknesses recorded in Cockburn-1 (~10 cm to 1 m; Figs 3.7 and 3.8). Figure 5.4 also demonstrates the relationship between measured and calculated values, with porosities showing very close agreement in the 1574-1580 m interval, while calculated permeabilities are approximately an order of magnitude smaller than measured values in the same interval. This order-of-magnitude discrepancy arises from the spread of data in the porosity-permeability data set, with permeabilities spanning at least an order of magnitude above and below the trend line (Fig. 4.16).

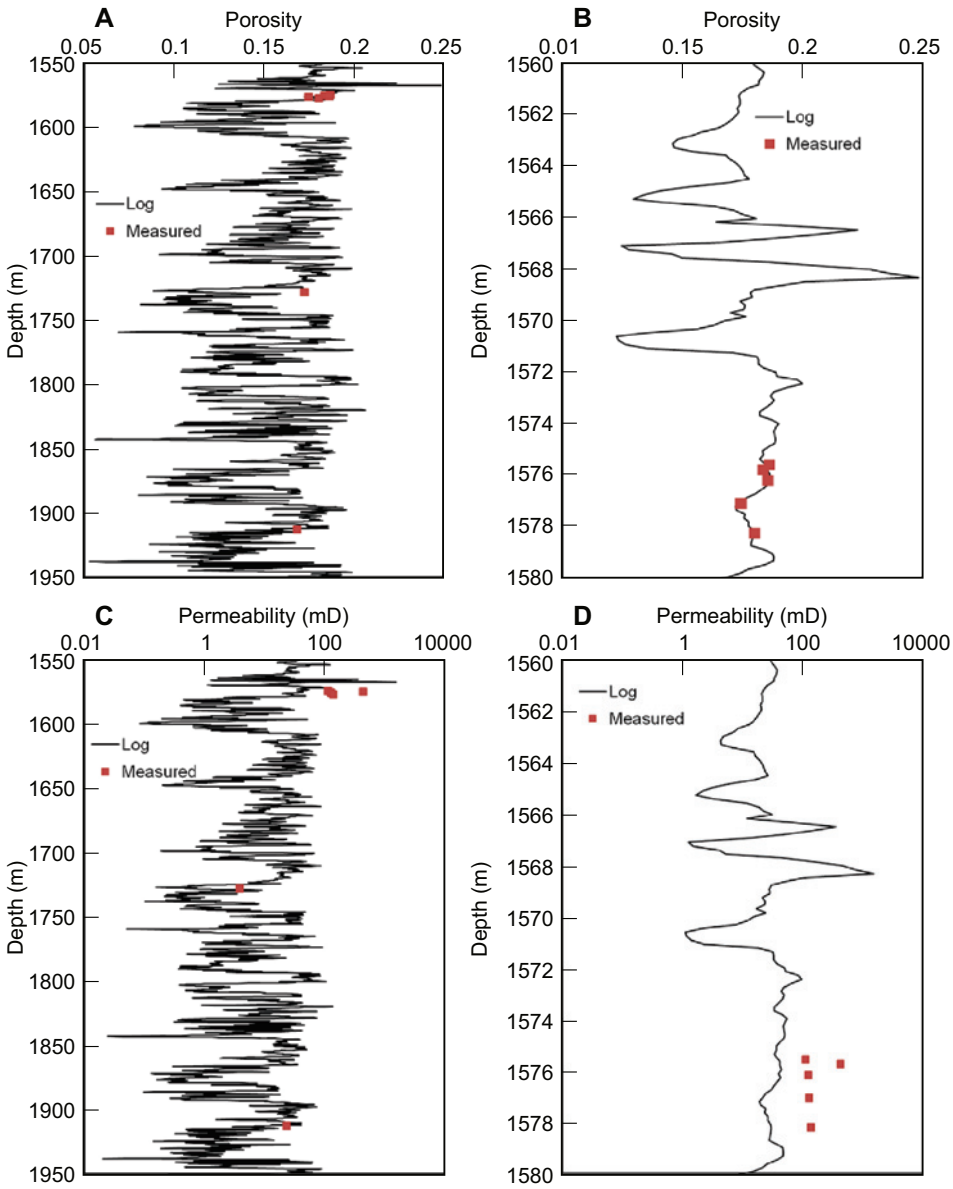

Figure 5.4: Small-scale variations in sonic-derived porosity and permeability in Cockburn-1. Red squares indicate measured values. (A) Porosity 1550-1950 m depth. (B) Porosity 1560-1580 m depth. (C) Permeability 1550-1950 m depth. (D) Permeability 1560-1580 m depth.

5.4 Discussion

The method described above combines information from laboratory measurements of porosity and permeability with wireline logs to create a picture of the variability of porosity and permeability with depth at a single well location. This information could be used in simulations of heat transport and fluid flow in the Perth Basin, which in turn can be used to inform geothermal exploration. However, the method does not provide information about the lateral variability of porosity and permeability.

5.4.1 Limitations

Accuracy of the porosity-permeability profiles obtained using the method described above is limited by several factors:

1. Porosity-permeability measurements recorded at 2000 psi were used to calibrate the sonic porosity curve and to constrain the porosity-permeability relationship. Ideally these measurements would have been adjusted to reflect in-situ pressure at the depth of each sample, however it was not obvious how this adjustment should be carried out. A linear extrapolation to in-situ pressure based on the measured values at 500, 1000 and 2000 psi resulted in negative values in some cases, and there were insufficient data points to constrain a non-linear relationship between pressure and porosity or permeability. Using the 2000 psi values means that the sonic-derived porosities and permeabilities may be higher than their in-situ values.
2. Use of the sonic log in isolation to calculate porosity. Ideally the sonic log should be used in conjunction with density and/or neutron logs to determine porosity (Schlumberger, 1989), however only the sonic log was available in Cockburn-1.
3. Limitations of the Wyllie method (e.g. Kamel, 2011; Schlumberger, 1989). Geolog provides the Raiga-Clemenceau method as an alternative to the Wyllie method for deriving porosity from the sonic log, which may produce superior results in some cases (Raiga-Clemenceau et al., 1988). However the Raiga-Clemenceau method could not be used in this study because Geolog truncates the porosity to zero when applying this method, which would have yielded minimum porosities of ~15% when calibrated with the experimental data.
4. Poor correlation between measured and sonic porosity at low porosity (Fig. 5.2). This problem might be improved by using other methods to calculate porosity from wireline logs (see points 2 and 3 above).
5. Spread of porosity-permeability data around the trendline (Fig. 4.16), which implies at least an order of magnitude variation in permeability either way for a given porosity in Cockburn-1.
6. No attempt was made to capture the variation in porosity-permeability relationship with facies. This could be addressed by devising a scheme to identify facies from wireline logs.
7. Lack of information about anisotropy on the sample scale. Permeability was measured in only one direction on each sample, therefore there was no information about small-scale anisotropy. This would influence the estimates of large-scale effective permeability and permeability anisotropy based on moving averages.

Nonetheless, the calculated porosity-permeability profiles provide some insight into the variation of these properties with depth in Cockburn-1, representing a step towards a comprehensive 3D model of permeability in the Perth Basin.

5.4.2 Goals for future research

- Apply the porosity-permeability analysis to other petroleum wells in the Perth Basin.
- Use the resulting depth profiles to inform statistical representations of porosity and permeability in the basin, which in turn could be used to explore heat transport and fluid flow in scenarios representing aspects of the basin, e.g. assessing the potential for convection with vertically varying permeability.
- Use the depth profiles in conjunction with 3D forward stratigraphic models produced by SEDSIM (see Section 6 of this report) to create a 3D model of porosity and permeability in the basin. This in turn could be used for simulations, building on the results produced in Project 3 (see Reid et al., 2012).

5.5 Summary

Wireline logs from the Cockburn-1 well were used to estimate porosity and permeability, providing insight into the variation of these parameters with depth. Porosity was estimated from the sonic log using the Wyllie method with a shale correction, then the resulting profile was calibrated using laboratory measurements of porosity. Permeability was calculated from the calibrated porosity profile using the porosity-permeability relationship derived from laboratory measurements on Cockburn-1 samples. The resulting profiles show porosity and permeability generally decreasing with depth with no marked changes at formation boundaries other than at the top of the Yarragadee Formation. Averages by formation mask important variations within formations that are likely to influence the hydrothermal regime. Moving averages provide a more useful representation of the data. The ratio of horizontal to vertical permeability is estimated to be about 2 to 100. The length scale of porosity-permeability variations with depth is consistent with the range of continuous facies thicknesses in Cockburn-1. The porosity-permeability-depth profiles provide detailed information about the variation of these parameters with depth at one well location; the same technique could be applied to other wells but other methods must be used to provide information about lateral variability between wells.

6. HOT SEDIMENTARY AQUIFER CHARACTERIZATION USING STRATIGRAPHIC FORWARD MODELLING, PERTH BASIN, AUSTRALIA

6.1 Introduction

Most sedimentary basins in Australia have been explored for petroleum prospectivity at some stage. Although geothermal and petroleum exploration differ in the resource they are looking for – high-temperature water versus hydrocarbons, most data collected for petroleum exploration can and have been used for geothermal exploration (Deming, 1989). However, as opposed to petroleum fields, viable geothermal fields need to be close to consumers, especially for direct use applications. Using petroleum data becomes then more challenging, as the closer petroleum exploration is conducted to cities, the sparser the resulting data.

The most common approaches used to spatially characterize sedimentary architectures are currently geostatistics and object-based stochastic modelling (De Marsily et al., 2005). These structure-imitating approaches do directly invoke the physical processes by which sediment bodies and stratal architecture formed. In this paper, we describe the use of a Stratigraphic Forward Modelling program (Sedsim) to characterize potential geothermal fields using geological process understanding. The dataset generated by Sedsim, can then be used for simple static geothermal assessments, as discussed in this paper, or for more complex coupled heat and fluid flow simulations.

6.2 Stratigraphic Forward Modelling

Stratigraphic Forward Modelling (SFM) is a sedimentary process simulation that replays the way that stratigraphic successions develop and are preserved. It reproduces numerically the physical processes that eroded, transported, deposited and modified the sediments over varying time periods. In a forward modelling approach, data are not used as the anchor points for facies interpolation or extrapolation, but to test and validate the results of the simulation. Stratigraphic forward modelling is an iterative approach, where input parameters have to be modified until the results are validated by actual data. The workflow is described in Figure 6.1.

One of the major benefits of using SFM to characterize sedimentary successions is the fact that the results will always make sense from a geological point of view. It is also possible to test different geological scenarios, environments or conceptual models, to assess their impact on the stratal geometry and better understand the depositional processes. Ultimately, it enables the prediction of facies and porosity distributions in areas where data are sparse, unevenly distributed, or at inappropriate resolution.

For this study we used the Sedsim three-dimensional stratigraphic forward modelling package that was developed originally at Stanford University by D. Tetzlaff and J. Wendebourg under the supervision of Prof. J. Harbaugh. It has since been modified and extended at the University of Adelaide and CSIRO by C. Dyt, F. Li and T. Salles (Griffiths et al, 2001). Sedsim enables the simulation of major depositional processes including marine, lacustrine, aeolian, fluvial, density flow, carbonate, vegetation and others.

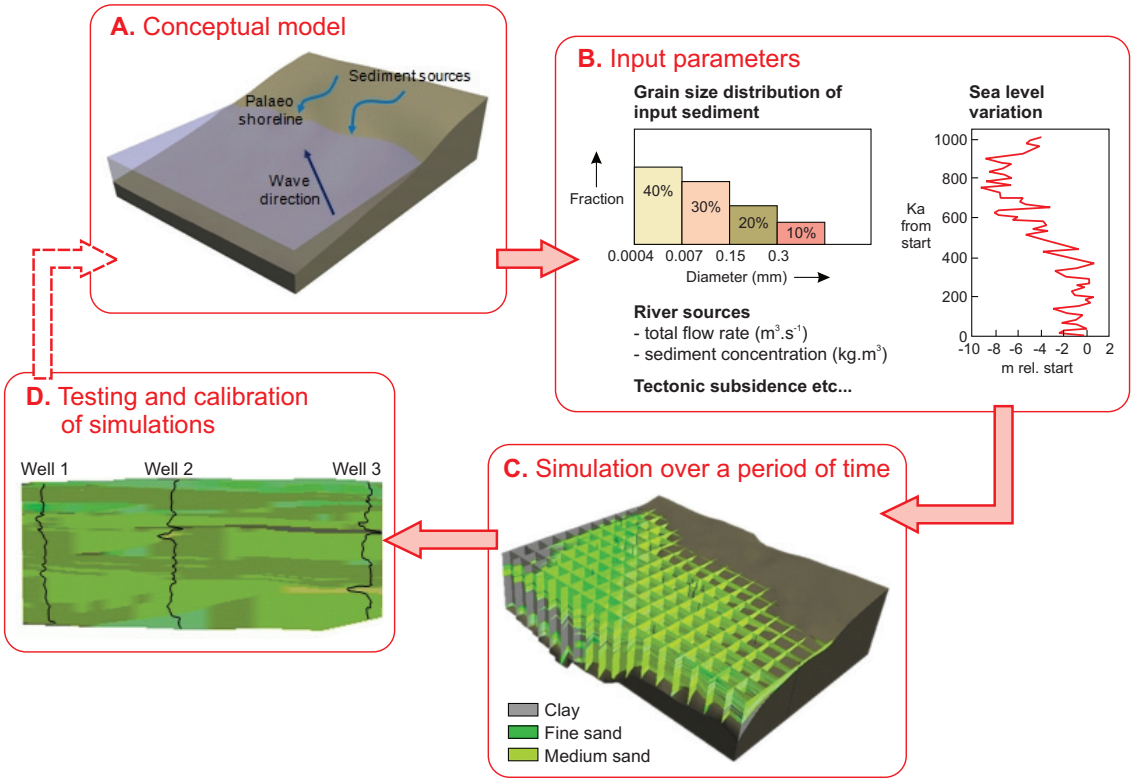

Figure 6.1: Stratigraphic Forward Modelling has a four step iterative workflow. The simulation workflow is repeated while modifying the conceptual model and input parameters until appropriate convergence with available data is achieved.

6.3.1 Basic principles of Sedsim operation

The initial background to, and the basic principles of operation of, Sedsim are described in Tetzlaff and Harbaugh (1989). A synopsis and recent updates to the numerical code are included below.

6.3.1.1 Fluid Flow

Hydrodynamics make up the core of the Sedsim program and utilize an approximation to the Navier-Stokes equations. The full Navier-Stokes equations describing the fluid flow in three dimensions are currently impossible to solve due to limitations in computer speed (it would take longer to simulate a flow than the real event). Sedsim instead simplifies the flow by solving the shallow water equations, utilizing isolated fluid elements to represent continuous flow (Tetzlaff and Harbaugh, 1989, Chapter 2). This Lagrangian approach to the hydrodynamics allows for a significant increase in the speed of computation and the simplification of the fluid flow equations. The downside of this approach is that individual events such as a rapid variation in fluid flows caused by brief downpours and unexpected short term river meanders can not be modelled. However, as the timing of these events is impossible to predict, this is a small loss. Simulations over geological periods can at best hope to capture the mean conditions and create a general pattern of sediment distribution, rather than capture the exact timing of each individual pulse of material. With this in mind, the approach utilized by Sedsim will accurately model the 'mean' physics in the simulation.

Modelling of the fluid flow is performed by allowing fluid elements to travel over the grid describing the topographical surface, reacting to the local topography and conditions such as the flow density and the density of the medium through which the element is passing (eg. air, sea water, or fresh water). The fluid elements are treated as discrete points with a fixed volume, an approach known as "marker-in-cell". As mentioned, several simplifications are made to the Navier Stokes equations, comprehensively described in Tetzlaff and Harbaugh (1989) with the most important of these being that the flow is expected to be uniform in the vertical direction (ie. the whole of the fluid element has the same velocity), and that the friction experienced by the fluid element is controlled by Manning coefficients. The net result of these simplifications is that the Navier Stokes equations are modified into non-linear Ordinary Differential Equations (ODEs). These equations are now solved using a modified Cash-Karp Runge Kutta scheme (Press et al., 1992) which ensures stable and accurate 4th order in time solutions.

The resolution of the simulation has an influence on the results. There are two discretisations which must be examined in Sedsim; the temporal and spatial. The spatial resolution is perhaps the most obvious. Because the fluid elements use the grid topography to determine their flow characteristics, features smaller than the grid resolution have no influence upon the flow. The temporal aliasing comes in several forms which can be controlled by the user:

- The choice of "display interval" in years simulated time (this is equivalent to the temporal resolution in cross-sectional models). This controls how often the data are output from the model. All sediments deposited during a time interval are lumped together in a single layer. Thus multiple events occurring within a display interval are seen as one integrated event (bed).
- The choice of "flow sampling interval". This represents the interval between releases of new fluid elements. For example setting this to 100 years would mean that a new fluid element would be released every one hundred years. That fluid element would then contain the volume of water and sediment as if the original source had flowed for 100 years. As it is moved about the topography it is assumed to flow at each point for 100 years.
- Time step. The time step controls how far the simulation advances in time with each iteration. This variable is automatically calculated by Sedsim, and is chosen to be as large as possible whilst ensuring that the simulation remains numerically stable and accurate. It is also chosen so that no topographical features are by-passed by the fluid elements. It is indirectly controlled by the accuracy factor, which specifies to what precision any change in the flow must be calculated.
- The choice of "extrapolation factor" (ratio of computing time to simulated time). Because of the large geological time scales over which Sedsim must run, a simplification is introduced where the conditions for one time-step are thought of as being representative of the flow over that area for a multiple of that time given by the extrapolation factor. The main purpose of this extrapolation is to allow the fluid elements to interact with other processes (such as sea level movement) which typically occur on much longer time scales by keeping the fluid element in the system for a longer time. It does not affect the number of fluid elements released or the speed of the computations.

- The choice of "parametric sampling interval". This variable affects how often in simulated time other effects such as sea level change, tectonic movement, wave/wind effects and slope instabilities are calculated. These values are generally chosen to be much shorter than the rate at which these events may be observed in the stratigraphic record. For example change in sea level is typically referenced once every 100 years.

6.3.1.2 Sediment Transport

Sediment is transported across a bathymetry or topography (bypassed), deposited on its surface, or eroded from the surface, according to the principle of conservation of mass. In other words, for each time interval:

sediment in + sediment eroded = sediment in the fluid + sediment deposited + sediment out

In Sedsim the sediment moves at exactly the same rate as a fluid element, because there is neither a velocity gradient in the fluid, nor any distinction between the rate of transport by the fluid element of the suspended and bed load. Because of the use of the flow sampling interval (described above), this crude approximation has little effect on the results, as the fluid flow represents a time averaged response. The boundary between erosion and transportation is determined by the critical shear stress, calculated as a function of particle diameter (threshold shear stress increases linearly with particle diameter above 0.1 mm). The rate of sediment deposition or erosion is proportional to the excess "effective sediment concentration". This is the difference between the actual sediment load within the fluid element and its capacity to hold sediment. This capacity is a function of the water density, the velocity, and average fall rate of the contained sediment and the buoyancy of the flow. Sediment sinks within a fluid element as a function of its excess density over the fluid, its diameter, and the viscosity of water at 15 °C. For more detailed consideration of the algorithms used by Sedsim the reader is referred to Tetzlaff and Harbaugh (1989). Sedsim is typically run using four different siliciclastic grain sizes specified by the user. In addition to this is the option to include growth of two types of carbonates (for example coral and forams) and two types of organic material (for example algae and vegetation), and their resultant clastic grains after erosion.

After initial deposition from fluid elements the sediments can still be re-deposited due to slope angle tests in the local environment. The sediment can be diffused many grid cells until it deposits at a user-defined stable slope angle.

6.3.1.4 Wave effects

The wave routine is designed to simulate longshore transport of sediment deposited by a fluid element in a shore-face setting. Waves can be introduced in a number of ways, from detailed information at every grid point varying in time, through to just a single transport rate and direction constant throughout the simulation. Effects such as wave refraction and the shadowing of water bodies by land can also be introduced. The parameters used are: angle of incidence, transport rate or wave height, wave-base, depth of mobile bed, berm height and the wave calling interval. The net effect of the wave module is to transfer sediment exposed to the prevailing wind and wave directions, and above wave base, alongshore. Depending on the simulation, this can be a dominant process.

6.3.1.5 Aeolian processes

Aeolian sediment transport and landscape development by wind presents a rich mixture of complex systems at various spatial and temporal scales. Sand transport by wind is a classic dissipative process with non-linear dynamics, while dune field evolution is a prototypical self-organisation phenomenon. Form and process in aeolian geomorphology have in the past largely been treated separately, landforms and dune field evolution principally being understood by means of (static) morphometric descriptions while sediment transport is captured in reductionist (dynamic) process models. Recent advances in numerical modelling have facilitated investigation of dune field evolution and dune migration dynamics as process (either with reductionist simulation models or with self-organising cellular automata), and advances in field experimentation and instruments have allowed recognition of form in sediment transport, such as aeolian streamers and patterning in spatial and temporal transport variability. An aeolian model has been developed to investigate both environmental and geological issues such as the role of climate variability and human activities on dune-field evolution or improvement in the predictive modelling of aeolian sands reservoirs.

6.3.1.6 Temporal aliasing/time sampling sensitivity

There are two types of temporal aliasing to consider. The first concerns the relationship between flow time-step and the maximum slope over which sediment will flow. For steep slopes, and irregular bathymetry, the flow needs to be calculated more frequently to ensure realistic sediment geometries. This problem is automatically handled by the code as discussed in the section on fluid flow. A reduction of the flow time-step makes the simulation more stable, and potentially provides marginally higher resolution in the output geometries. A consequence however, is a significant increase in computing time. The second factor influencing temporal aliasing is the display interval. Temporal aliasing is the ability to model a given time event. If it is believed that a fan developed in ten years, its geometry and composition could not be simulated with a time step greater than five years. The consequence of choosing a display interval of 5 ka, therefore, is that the minimum temporal depositional event that can be modelled is one with a duration of 10 ka. If the aim is to model the effect of orbital forcing on high-frequency sedimentation cycles, then a display interval of at most 10 ka would be needed to capture the effects of the 19-21 ka cycle. The "parametric sampling interval" is the time interval at which the sea-level curve is sampled, wave influences calculated, slope stability's checked, compaction calculated etc. The smaller the parametric sampling interval, the higher the resolution of the events that can be modelled, but the penalty is a slightly longer computing time.

6.3.1.7 Tectonic subsidence

Sedsim can incorporate vertical tectonic movement in a simulation. A subsidence/uplift value is defined for each individual grid node in the initial topography, and these arrays of values can be changed at any time in the simulation, independently of either the display or parametric sampling interval.

6.3.1.8 Compaction

Compaction during the simulation is calculated using a "look-up table" containing porosity values as a function of effective stress and grain size. For each display interval, the lithostatic pressure is

calculated from the overburden. Compaction is controlled by this pressure and the actual grainsize deposited. Burial compaction has to be applied after the simulation by an additional program.

6.3.1.9 Loading / Isostasy

Loading effects on stratal geometries can be included in a simulation, as a function of mantle density and flexural rigidity. For simulation areas of the order of a hundred kilometres isostatically-driven elastic deformation of the basement will be small for less than a kilometre of sediment load. (Li et al., 2004)

6.3.1.10 Slope Failure and Turbidites/Gravity Flows

Slope failure within Sedsim is triggered by over-steepening of sediment due to tectonic movement or the exposure of sediment due to sea level fall. The composition of the underlying sediment also plays a strong role in failure prediction in Sedsim. The failed sediment is transferred into a new fluid element (or series of fluid elements), and then treated in the same way as other fluid elements. Due to the high sediment concentration, these flows can often lead to large gravity flows, provided gradients are sufficient.

6.3.1.11 Carbonates and Organics.

Sedsim models the accumulation of carbonates and organic material. Sedsim is capable of modelling the in situ accumulation of two types of carbonates (for example coral and forams) and two types of organic material (for example algae and vegetation), and their resultant clastic grains after erosion. The major problem with attempting to represent the growth of carbonates and organics mathematically is the wide range of ecological niches in which they may or may not develop. Prediction of carbonate and organic production and accumulation therefore tends to be descriptive, for example "reefs grow at a rapid rate in warm climates, in locations where there is with little sediment input". In order to deal with the inexactness of descriptive language, we turn to Fuzzy logic, inspired by the stratigraphic modelling package 'Fuzzim' (Nordlund 1996, 1999). Fuzzim utilizes fuzzy logic to model depositional system behavior including the siliciclastic transport as well as carbonate growth and erosion. However, Sedsim only models production of carbonates and organic material using fuzzy logic, leaving all the other processes to the existing hydrodynamic code. An advantage of the use of a fuzzy system is that the code executes very rapidly and so adds little in computational time to the already heavy load imposed by the fluid dynamics. The challenge in this modelling lies in developing the correct set of rules to model the simulation.

6.4 Method

The Sedsim computer program discussed above was used to explore conceptual depositional concepts in the Perth Basin by producing numerical stratigraphic forward models based on the current understanding of the stratigraphy and depositional systems within the Perth Basin. Three-dimensional stratigraphic forward modelling enables us to study, at geological time scales, the combined influence of a variety of inter-dependent basin processes and factors on basin fill. The results reflect possible changes in sediment distribution over time as a function of changes to the depositional environment.

Input data included a range of initial surface bathymetries, grain-size distributions and sediment supply rates linked to climate proxies provided from palynology and global sea-level curves. All other input parameters were iteratively tested.

Sedsim is a comprehensive process-based stratigraphic forward model, as described above. The program models sediment erosion, transport and deposition, and predicts clastic and carbonate sediment distribution on a given bathymetric surface. In Sedsim the Navier-Stokes equations and the continuity equation are simplified and solved by using a marker-in-cell technique in two horizontal dimensions (Tetzlaff and Harbaugh, 1989). Flow velocity, water depth and sediment load are represented at points that move with the fluid. At each time step the position and velocity of each fluid element are recalculated, and the sediment transfer between the surface and the fluid element is calculated at the grid points. This technique combines the advantages of Eulerian and Lagrangian representations of fluid flow.

Past studies that have demonstrated the value of using Sedsim modelling include those by Griffiths et al. (2001), Li at el (2005), Griffiths and Dyt (2001), Griffiths and Paraschivoiu (1998), Koltermann and Gorelick (1992) and Martinez and Harbaugh (1993), Meyer et al (2011), Salles et al (2009, 2011a, 2011b). Any computer modelling is only as good as the validity of the input data and the algorithms used in the program. The Sedsim program has been shown to predict sediment distributions in a range of depositional environments and at scales from a few centimetres to several kilometres. The derivation of input data for computer models should be no more onerous than that required for a conceptual geological model of an area. However, the need for quantitative data forces the geologist to a greater degree of commitment than may otherwise be the case.

6.5 Application to the Yarragadee Formation, Perth Basin

The Yarragadee Aquifer in the Perth Basin has been used for geothermal purposes for a few decades now. It is currently the source for six direct use geothermal projects in Perth vicinity (Pujol, 2011), mainly swimming pool heating. Although the upper part of the aquifer is well characterized in the Perth Metropolitan Area (PMA) thanks to water supply exploration and development, the deeper parts of the Yarragadee Formation have been only poorly explored. As shown in Figure 6.2, only two petroleum wells are available in the PMA to help characterize the deep part of the Yarragadee Formation. However, petroleum wells intersecting the Yarragadee Formation are spread over the entire Perth Basin.

Using the Yarragadee Formation as a case study, we investigated the use of Stratigraphic Forward Modelling to characterize poorly explored aquifers for geothermal purposes. Modelling the sedimentation of the Yarragadee Formation over the entire Perth Basin enabled us to better understand the sedimentation process, characterize the Yarragadee Formation in the Perth Metropolitan Area, and predict porosity and permeability distributions away from well data and below seismic resolution.

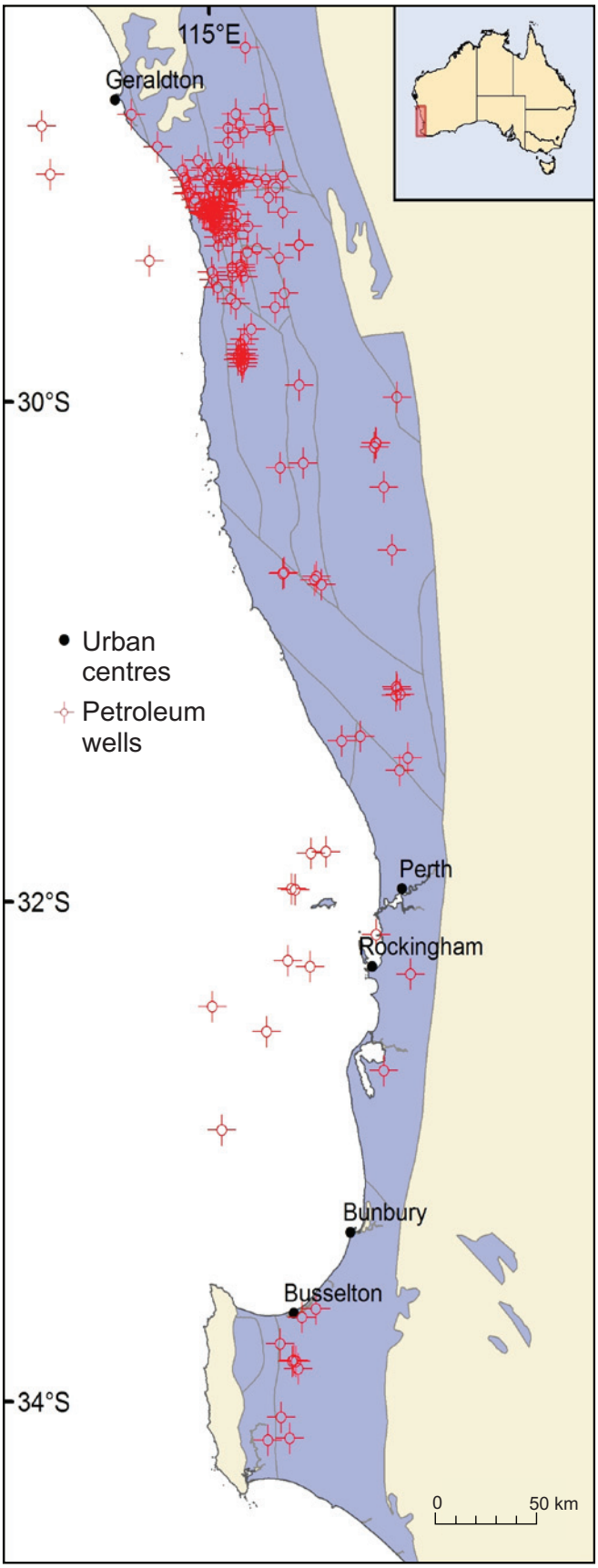

Figure 6.2: Location of petroleum wells intersecting the Yarragadee Formation over the entire Perth Basin.

6.5.1 Conceptual model presentation

In the middle Jurassic period (160 Ma) during which the Yarragadee Formation was deposited, the Perth Basin is believed to have been a vegetated floodplain traversed by meandering rivers. At that time Antarctica, Australia and Greater India still formed one continent and a large fluvial system drained northwards from Antarctica into the rift system between Greater India and the current Yilgarn Block, Australia (Fig. 6.3). Some small alluvial fans and tributary rivers are also believed to have formed at the time along the flanks of the rift (Tait 2007). Although no evidence has yet been found in support, it is possible that some sediments were sourced from Greater India.

The simulation was run for 15.8 Ma, from the Middle Jurassic at 160 Ma to the Late Jurassic at 144.2 Ma. The modelled area included the entire Perth Basin in order to capture the complexity of the sedimentary processes, although the main focus was the Perth Metropolitan Area. The grid spacing was set at 3710 m, yielding 179 x 61 cells to cover the entire area of 660 km x 225 km.

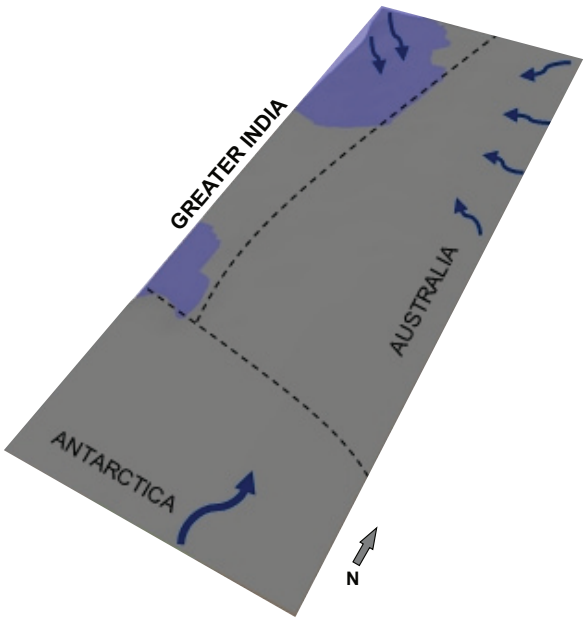

Figure 6.3: Conceptual model for the Yarragadee Formation deposition.

6.5.2 Review of input parameters

Like any other computer modelling process, Stratigraphic Forward Modelling predictions are only as good as the validity of the input data and our understanding of the processes involved. Therefore a thorough analysis of available data is necessary before determining the main input parameters. The parameters are here reviewed in no specific order:

- **Sediments** - Four siliciclastic grain sizes were used, based on sample data from petroleum wells (Table 6.1).

	Coarse sand	Medium sand	Fine sand	Clay
Diameter (mm)	0.45	0.15	0.03	0.0003
Density (kg.m^{-3})	2650	2600	2600	2550

Table 6.1: Grain size parameters.

- **Sediment sources** – The location of the main source was decided from the literature. The minor sources from the Yilgarn Block (Beard, 1999) were derived partly from the location of palaeo-river valleys related to the present-day rivers. The sources from Greater India were added after several simulation runs showed a sediment deficiency to the western side of the basin. These proposed sources have yet to be verified by field observations.

- **Topography** – The form of the initial topography was based on current basement shape from OZ SEEBASE™ (FrogTech, 2005). The magnitude of the relief was determined by well observations that the sediments were fluvial/lacustrine. This gave some initial indications of height above sea level and local gradients. These were then tested and refined by the initial sedimentation runs.
- **Subsidence and Uplift** – Initial subsidence rates were computed from seismic and well data and subsequently modified after several simulation runs. The locations of tectonically active cells were determined from the OZ SEEBASE™ (FrogTech, 2005). The timing of uplift or subsidence was interpreted from seismic data and biostratigraphic data from wells. Where available, the presence or absence of biostratigraphic zones, and evidence of erosion from seismic, were used to constrain erosion due to uplift or non-deposition of a particular interval at a particular location.
- **Sea level** - The Haq and Schutter (2008) eustatic sea level curve was used as the basis of low frequency base-level changes. This curve was then modulated with Milankovich frequencies and resampled at 40 ka to provide a high-frequency base-level oscillation. Note that although the Mid to Late Jurassic sediments in the Perth Basin were mostly of fluvial to lacustrine origin, and thus accommodation was not directly affected by sea level, the rate of change of sea level was used to control river flow volumes throughout the simulation. This is predicated on the assumption that during periods of rapid sea-level fall river supply fell, and during periods of rapid rates of sea-level rise the river supply increased. The fact that marine conditions have not been identified in preserved sediments of the Mid to Late Jurassic in this part of the Perth basin despite the amplitude of eustatic sea level variation, is itself a valuable indication of the minimum altitude of the basin floor during the simulated period.
- **Porosity table** – The rate of porosity reduction due to overburden stress was calculated from a porosity–depth curve derived from Cockburn-1 and Gingin-1 wells (Fig. 6.4).
- **Compaction** – Sedsim simulates both syn- and post-depositional compaction by calculating the reduction of porosity due to overburden stress for different grain-size ratios. Post-depositional compaction was calculated on the basis of preserved Yarragadee tops. Porosity reduction due to cementation was not modelled in this simulation.

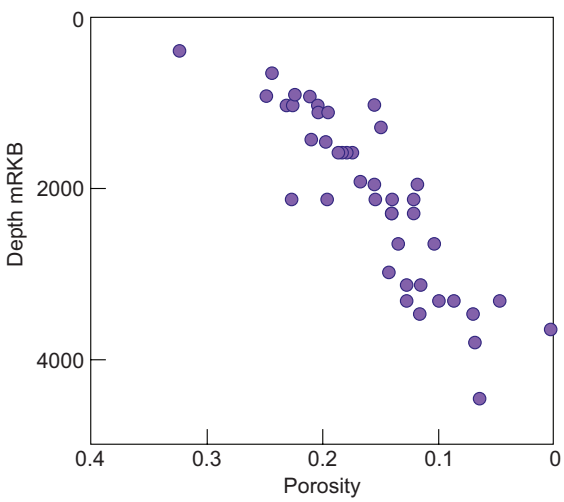

Figure 6.4: Core plug porosity values for Yarragadee Formation samples in Cockburn 1 and Gingin 1 wells, for samples with an estimated mean grain size above 0.15 mm.

6.5.3 Stratigraphic Forward Modelling Results

SFM simulations can provide several types of output. The standard output for each time step, for each grid node, includes; siliciclastic grain size distribution, carbonate and organic content, porosity, sediment sorting, facies (distance from shore, water depth), and age of preserved sediment. Additional outputs such as net:gross, permeability, acoustic impedance etc. can also be generated from the standard output provided local calibration from well data are available within the simulation area. Post-depositionally, Sedsim is also able to uplift, erode and compact the sediments to their present-day state. The resulting grid and its properties can be imported into any 3D geological package such as Petrel, RMS, Eclipse, GoCad etc. for further analysis, reservoir simulation, and display.

For the Yarragadee Formation simulations, the main outputs were the grain size distribution (Fig. 6.5) and the porosity distribution. A permeability distribution was also computed, using porosity-permeability relationships based on core data from a few petroleum wells (Israni and Delle Piane, 2010).

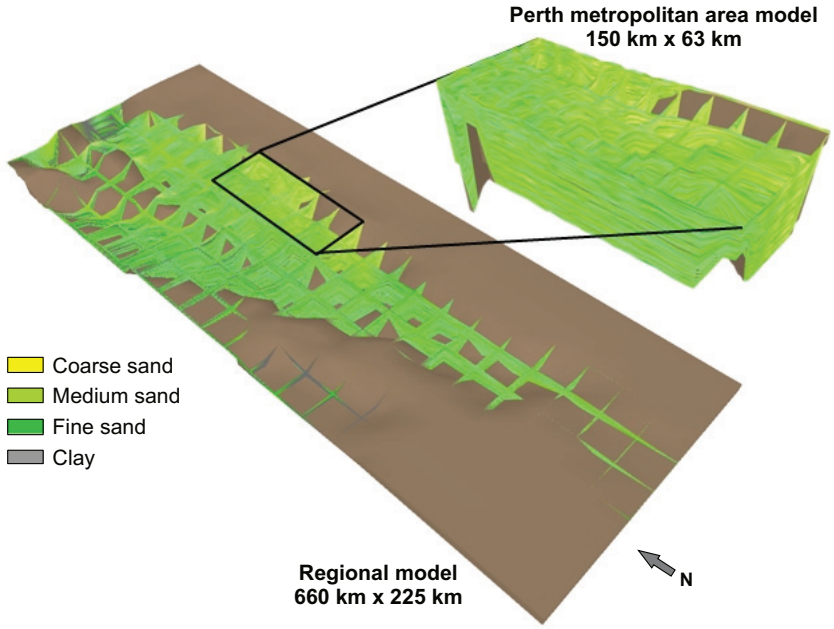

Figure 6.5: Display of predicted grain size distribution of the Yarragadee Formation over the entire Perth Basin and Perth Metropolitan Area. The regional model has a resolution of 14840 m on a 45x17 grid, while the Perth Metropolitan grid is nested within this simulation with a resolution of 3710 m on a grid of 41 x 17.

6.5.4 Testing and calibration of simulations

Sedsim output enables simulations to be verified in many ways. It is possible to generate both synthetic seismic and 'pseudo-seismic' profiles from the simulation, to compare the stratal architecture to actual seismic lines. It is also possible to generate synthetic petrophysical logs, such as gamma-ray and porosity, to compare with petrophysical wire-line logs from petroleum wells. However, the synthetic logs are recorded at preserved geological time steps (every 50 000 years in this case) which at any one location may result in a single bed 10 m thick or a layer 2 mm thick at one time step. This makes direct comparison with wireline logs challenging, apart from the fact that the wireline tool has sampled a cross-sectional area of significantly less than 10 m^2 while in the present

simulation the Sedsim grid node represents a sediment cross-sectional area of over 15 km^2. However, in the case of a grid node being close to a well location, and the rate of lateral change of facies thickness being low then a Sedsim net to gross may be compared to the upscaled values from the wireline logs that would be used in a reservoir simulator block.

The simulation results of the Yarragadee Formation were validated against a 2D seismic profile available just south of the Perth Metropolitan Area (Fig. 6.6) and against petrophysical logs (Fig. 6.7) available from petroleum wells unevenly spaced in the Perth Basin.

Over 50 calibration runs were necessary to obtain results in accord with the available data. During the test and calibration stages, the parameters requiring most adjustment were the sediment sources, the deposition parameters of the main source, and the subsidence rate. As discussed above, a Sedsim petrophysical record at a grid node in this simulation can be thought of as representing an upscaled sample of 15 km^2 compared to the wireline sample of less than 10 m^2 . In Figure 6.7 the Sedsim porosity prediction trend is apparently more linear and steeper than the wireline porosity trend. This is because the porosity-stress relationship curves used in this simulation were calibrated using core-plug data rather than wireline data. The core plug porosities diverge in a similar way from the wireline porosities. This may indicate a matrix composition shift that was not allowed for in the wireline calculation of porosity from petrophysical response.

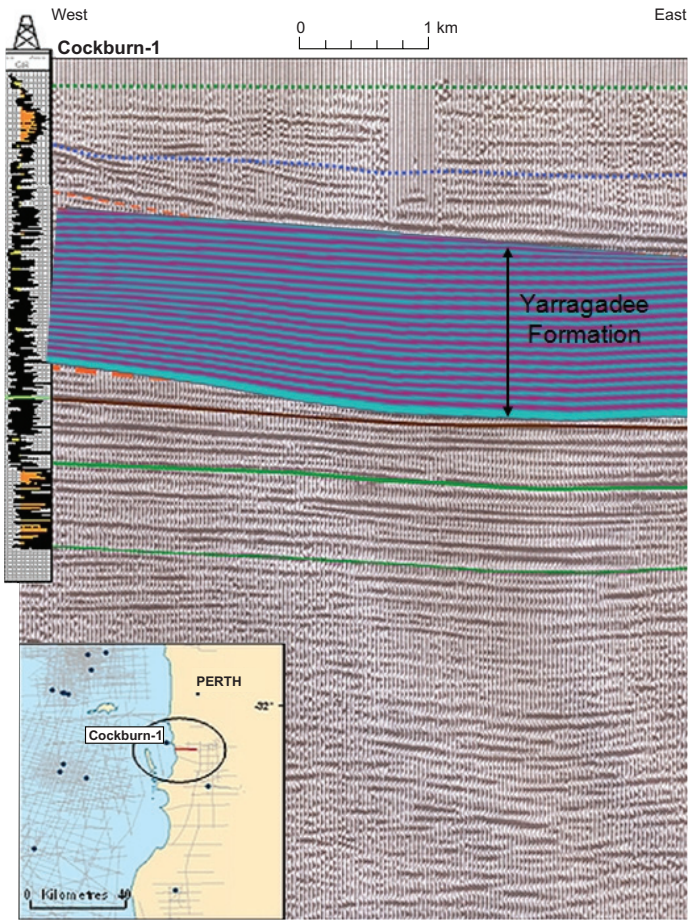

Figure 6.6: Comparison of stratal geometries from pseudo-seismic generated from Sedsim results and a seismic line south of the Perth Metropolitan Area (modified from Causebrook et al., 2006). The pseudo-seismic is simply the pattern of alternate time layers generated by the simulation coloured alternately red and blue. The geological time interval simulated is outlined in yellow on the seismic section and can be compared to the Sedsim output over the same geological time interval to the right.

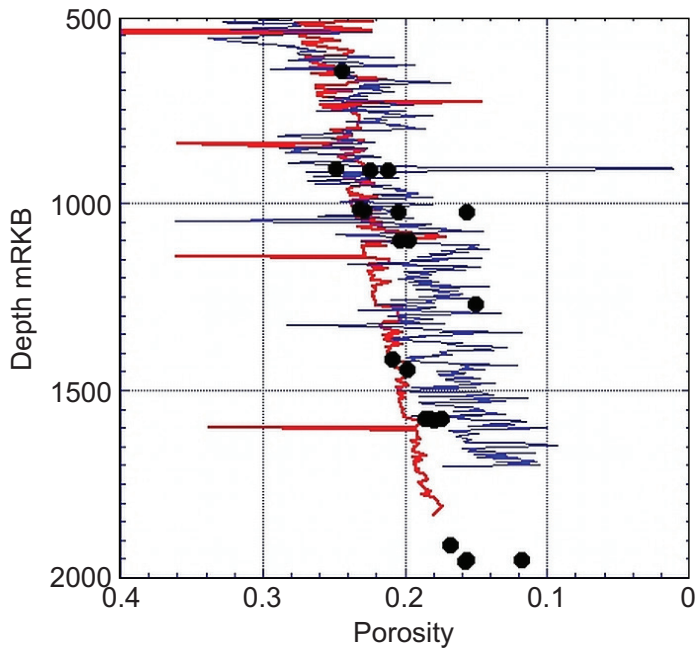

Figure 6.7: Comparison at petroleum well Cockburn 1 of Sedsim porosity (in red), wireline porosity (in blue) and core porosity (in black).

6.6 Results

In areas of sparse well coverage, and given the need for the prediction of lateral facies distributions and associated porosities and permeabilities below seismic resolution, or in the absence of seismic data such as beneath urban areas, then the alternatives to process-based stratigraphic forward modelling are either geostatistical interpolation, or a linear interpolation of facies boundaries.

The simulation described here initially modelled an area of the Perth Basin 660 km by 220 km at 3710 m resolution from 160 Ma to 144.2 Ma at 50 ka resolution giving a regional model of middle to late Jurassic stratigraphy. This regional model was used to test the validity of the conceptual model of a major river system flowing from Antarctica providing most of the sediment into the Perth Basin, with lateral alluvial fans supplementing this depositional system from the Yilgarn fault scarp. These fans are predicted to have lower Vshale, better porosity, and a permeability that may provide optimum petrophysical properties for convective geothermal cells (Fig. 6.8).

Once the regional model had been adequately constrained, by observations at well locations and on seismic sections, then a new regional simulation was run at 14840 m resolution on a 45 x17 grid, within which a 3.7 km resolution model on a 41 x 17 grid was nested (Fig. 6.5). Such nested grids are not interpolations between the coarser grids but are separate simulations that use the hydraulics at the coarse node locations as boundary conditions for the higher resolution simulation. This means that if there is a 3D seismic surface available in the higher-resolution area then the additional information about local surface gradients, subsidence history and river flow conditions, can be used at that resolution. Without additional information, a nested grid is still possible but will extrapolate processes away from coarse nodes rather than lithofacies.

Work at Curtin University and CSIRO (see Sections 3 and 4 of this report) on core data from various wells in the Perth Basin developed a porosity/permeability/lithofacies/depth model that was

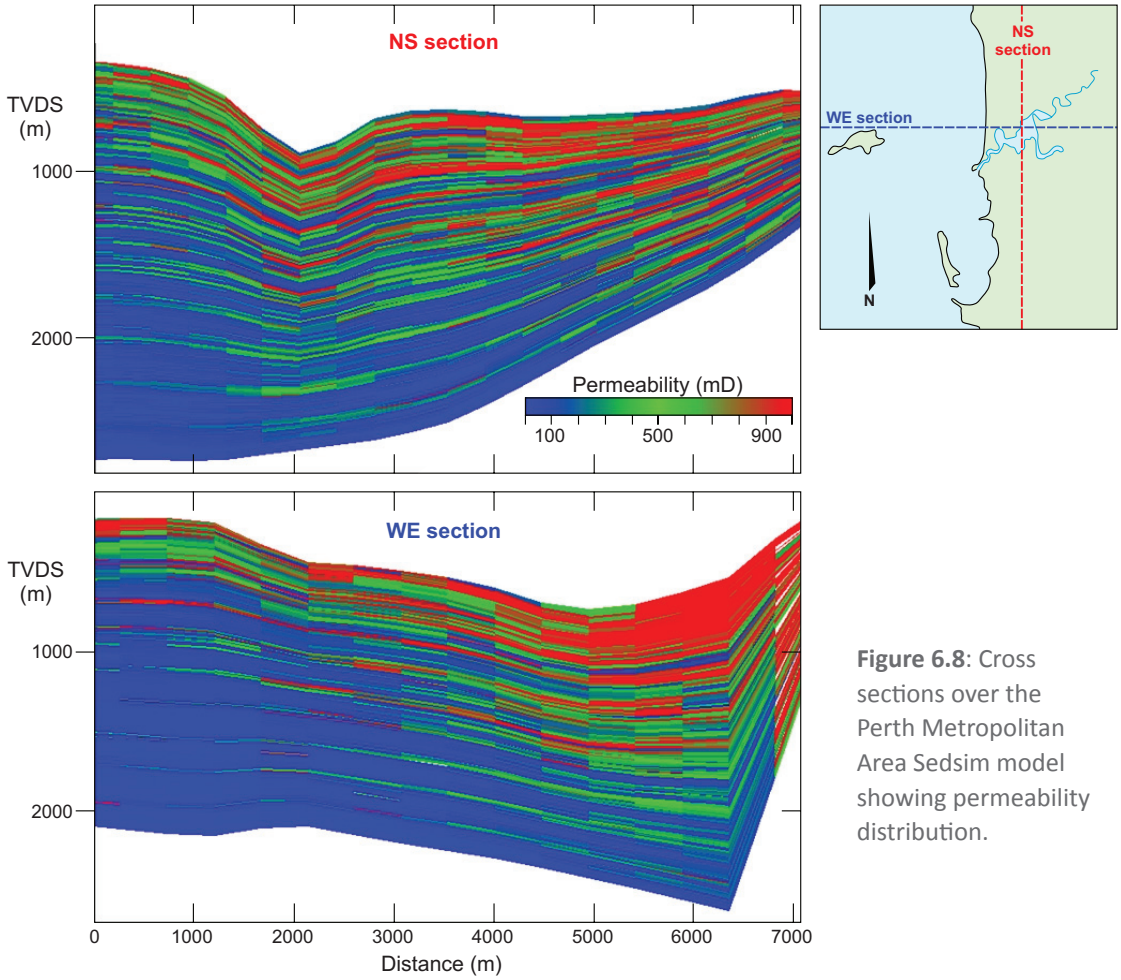

Figure 6.8: Cross sections over the Perth Metropolitan Area Sedsim model showing permeability distribution.

translated into the Sedsim input files to control the relationship between grain-size distribution, burial depth, and initial porosity both during the simulation and as a function of post-depositional compaction. The permeability/porosity relationship from core data was applied to the output files post-simulation.

Permeability and porosity volumes have been prepared as a result of this work. 3D volumes of porosity, lithofacies, and permeability are now available. Example cross-sections through these volumes (Fig. 6.8) and 3D visualisations show that this Sedsim simulation predicts an optimum permeability zone about 10 to 15 km west of the Darling Fault zone, in an area that is more-or-less continuous in a north-south direction, but has greater volumes where paleo-river systems draining the Yilgarn Craton formed alluvial fans on the Perth Basin plain.

Stratigraphic Forward Modelling of the Yarragadee Formation suggests that under the Perth Metropolitan Area, the aquifer cannot be treated as a single reservoir. Three main silty bodies divide the formation into four sub-reservoirs. Other smaller impermeable bodies with smaller extents should also be taken into account for flow and transport simulations, although they do not compartmentalise the reservoirs.

6.7 Discussion and Conclusion

This project set out to investigate the possibility of using stratigraphic forward modelling to develop a static geological model of lithological facies, porosity and permeability at scales that were appropriate for quantitative evaluation and location of potential geothermal resources in a hot sedimentary aquifer beneath Metropolitan Perth. The results show that this technology can contribute to both an understanding of the processes that controlled the stratigraphy of the aquifer, and make quantitative predictions about porosity, permeability, and lithofacies distributions at appropriate scales.

Stratigraphic Forward Modelling was successfully applied to characterize the unexposed and poorly quantified Yarragadee Formation in the Perth Basin. It proved its efficiency at predicting grain size and porosity distributions based on understanding of depositional processes rather than interpolation between sparse data. It provided insight into, and numerical predictions of, the distribution of sediments and their petrophysical properties below ground, in areas where wells and seismic data did not exist, and will be challenging to obtain in future due to urban development.

Although SFM ensures that simulation results make geological sense, the simulation quality is highly dependent on the input data and the expertise of the modeller. Permeability distribution is also not computed during the simulations, but can only be calculated post-simulation using empirical porosity-lithology-permeability relationships based on core data.

Stratigraphic Forward Modelling generates high resolution datasets of porosity, grain size and depositional facies that can be used to produce 3D synthetic seismic volumes and synthetic petrophysical logs for validation. Such extensive datasets may potentially reduce risk for geothermal exploration which always suffers from a lack of subsurface data. Those results were used to quickly assess the geothermal potential of an area for a given application, given an understanding of the processes involved and minimal well and seismic data (see Ricard et al. 2012).

The major advantage of Stratigraphic Forward Modelling is the fact that it directly uses and tests our understanding of the sedimentary processes that led to the preserved depositional succession. Petroleum wells intersecting the Yarragadee Formation in the Perth Basin are unevenly distributed, with only one within 20 km of Perth city centre. Because we have tested our understanding of how the basin was filled, and the model has been validated against available data throughout the entire basin, we have increased confidence in the results (Fig. 6.8) in the Perth Metropolitan Area even with no data available yet in that specific area.

Stratigraphic Forward Modelling output could also be used for more complex geothermal exploration purposes, either at reservoir or basin scale. Most geothermal simulations are run using laterally homogeneous layering, while Stratigraphic Forward Modelling results can help identify lateral porosity and permeability variation, baffles, and highly permeable layers to provide more realistic models.

6.8 Summary

Several geothermal projects in the Perth Metropolitan Area, Western Australia, have already demonstrated the geothermal potential of the area for aquifers down to 1 km depth. The Western Australian Geothermal Centre of Excellence (WAGCoE) was tasked with assessing the potential of deeper aquifers. Members of WAGCoE, in collaboration with CSIRO, investigated the use of stratigraphic forward modelling (SFM) techniques combined with geothermal reservoir definition to identify potential geothermal reservoirs in locations where data are sparse.

The major aquifer and low-temperature geothermal target in the Perth Basin, the Yarragadee Aquifer, provides a major portion of Perth's drinking water. Although the shallow part of the Yarragadee Aquifer has been well studied by hydrogeologists (Davidson and Yu, 2006), the deeper part is still poorly characterized. Using the stratigraphic forward modelling package Sedsim, the sedimentation of the Yarragadee Formation was simulated over a period of 15.8 Ma commencing in the middle Jurassic period. The simulation was calibrated against sparse seismic surveys, petroleum wells and core data. The final simulation volume was uplifted and eroded to the current state of the Yarragadee Formation, providing estimates of facies, grain size and porosity distributions for the entire formation.

Once the simulation of the Yarragadee Formation was achieved, the identification of geothermal reservoirs was attempted. This required investigating the suitability of the subsurface to deliver the energy required for candidate geothermal applications. Based on simple assumptions such as constant thermal conductivity, uniform geothermal gradient, and using pre-defined geothermal production design settings such as flow rate and maximum pressure drop, parameters such as reservoir temperature and the reservoir producible power were evaluated. As different geothermal applications have different subsurface requirements, reservoirs were individually investigated for specific geothermal applications. This methodology has been developed to allow rapid investigation of the local geothermal potential while changing the surface geothermal application requirements.

7. FAULT-RELATED DAMAGE AND DIAGENESIS AND IMPLICATIONS FOR FAULT PERMEABILITY IN THE NORTH PERTH BASIN

7.1 Introduction

The Perth Basin is an extensive north-south sedimentary basin that has significant well exploration and extraction of hydrocarbons in reservoirs (Crostella and Backhouse, 2000). Their small size, in comparison to other Australian examples, is thought to be due to fault-induced permeability baffles, rather than juxtaposition of reservoir-seal rocks (Johnson, 2002, King et al., 2008, Mory and Iasky, 1996, Song and Cawood, 2000). In terms of geothermal exploration, this implies that there may be difficulties associated with the transfer/extraction of deep, hot water to shallower depths at economical speeds. Limited prior work on the assessment of permeability around major faults has been done in the Perth Basin. However, significant work around the world has aided in reducing the risk in petroleum and geothermal exploration and extraction (Billi et al. 2003, Fisher and Knipe 1998, 2001, Neuzil 1986, Odling et al. 2004).

The established view of faults and fault zone architecture is that they comprise a 'core zone' associated with a principal displacement surface (tens of centimetres, even for very large displacement faults), and are surrounded on both sides by broadly tabular 'damage zones' – essentially where the host rocks contain structures (minor faults, extensional and shear fractures, stylolites, etc.) that accommodate some strain but considerably less than the principal displacement surface(s) (Ben-Zion and Sammis 2003, Billi et al. 2003, Kim et al. 2000, Kim et al. 2004, Mooney et al. 2007). Damage zones are considered to be relict 'process zones' – damage that occurs ahead of the fault tip, modified as the fault accumulates displacement by many slip events. The assessment and characterisation of meso- and microstructures and diagenesis is useful in determining the strain accommodation in fault damage zones, including the assessment of structural modification of reservoirs and aquifer fluid flow properties and interaction with diagenesis (Bonson et al. 2007, Johansen et al. 2005, Johnson 2002, Kim et al. 2004, Mory and Iasky 1996, Tada and Siever 1989). Burial history, in terms of formation of diagenetic fabrics and structural deformation, is fundamental in the understanding of permeability around faults (Billi et al. 2003, Faulkner et al. 2010, Fisher and Knipe 1998, 2001, Kim and Sanderson 2010, Odling et al. 2004, Peacock et al. 1998, Volk et al. 2009). It is often difficult to predict the permeability of fault zones because they often form complex, three-dimensional arrays of fractures that evolve throughout a fault's history, relative to the orientation of the applied stress field (Fisher and Knipe 2001, King et al. 2008). Clastic sedimentary rocks, such as found throughout the Perth Basin, respond to faulting differently based upon depositional lithology, diagenesis and pre-existing structural deformation (Lewis et al. 2002, Lloyd and Knipe 1992). Therefore, these are important factors for characterizing an aquifer's permeability history (Fisher and Knipe 2001, Hayon 1999, Johnson 2002).

The aim of this study is to perform an integrated analysis of sedimentology, petrography, diagenetic fabrics, meso- and microstructures of potential aquifer/reservoir rocks in the damage zone of a large fault in the northern Perth Basin to enable an assessment of the controls on aquifer quality with the

aim of reducing risk associated with geothermal exploration and extraction. This has been achieved by a detailed analysis of core retrieved from an exploration hole Apium-1 (2749-2782 m) drilled proximal to a fault identified from 3-D seismic data (Fig. 7.1). The overall objective was to characterize the orientation and downhole distribution of stylolites, fractures and faulting-related microstructures both proximal (via Apium-1 well) and distal (via Centella-1 and Mondarra-4 wells) to a normal fault in the northern Perth Basin, and assess their effects on porosity and permeability, and hence the evolution of reservoir quality. This study represents the first analysis of a fault zone in the Perth Basin, and is compared with models for fault damage zone deformation mechanisms around sedimentary basins elsewhere.

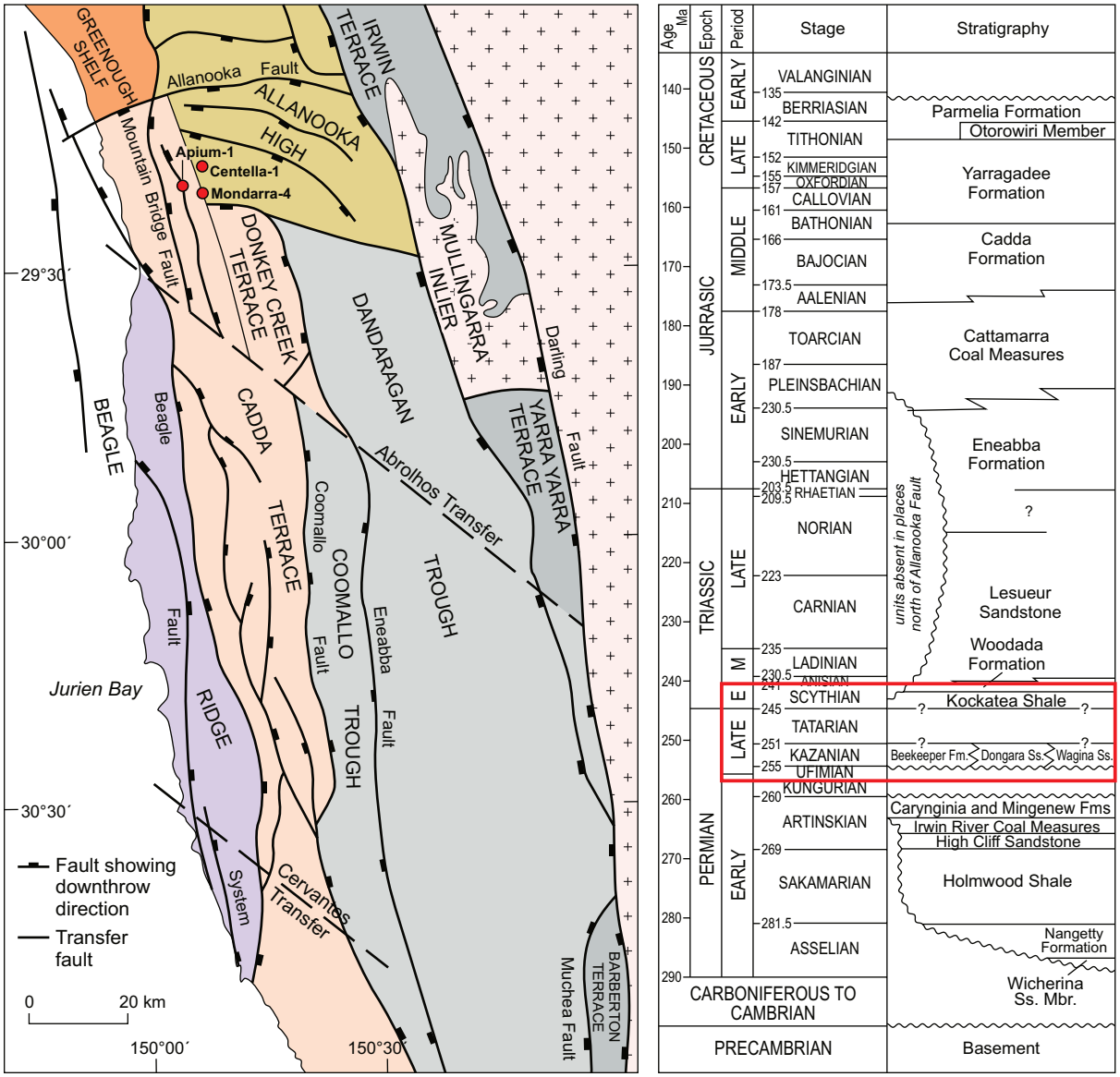

Figure 7.1: (A) Basin subdivisions in the northern Perth Basin. Apium-1, Mondarra-4 and Centella-1 (yellow dots) is located in the Beharra Springs Terrace, east of an unnamed major fault, modified from Crostella and Backhouse (2000). (B) Stratigraphy of the northern Perth Basin; cored Apium-1 is taken from the base of the Early Triassic Shale and the top of the Late Permian Dongara Sandstone, modified from Mory & Iasky (1996).

Apium-1, Mondarra-4 and Centella-1 are located in the Dandaragan Trough/Beharra Springs Terrace, Northern Perth Basin, and are 1.0, 4.8 and 5.4 km to the east and in the hangingwall block of an unnamed NNW-trending fault, respectively (Fig. 7.1 A, C). The unnamed fault is to the east of and sub-parallel with the Mountain Bridge Fault. It is orientated favourably for reactivation in the modern day stress field (King et al. 2008). The fault is approximately 50 km long, with a maximum, predominantly dip-slip net displacement of 800 m along the fault plane approximately 10 km to the south of Apium-1. The net displacement along the fault adjacent to Apium-1 is approximately 600 m identified from seismic imaging. Apium-1 is located on an uplifted fault block with 4 way-dip closure, bound by the NNW-trending unnamed fault to the west, a NNW-trending fault to the east, an E-trending fault to the south and a WNW-trending fault to the north (Fig. 7.1 C). Centella-1 and Mondarra-4 are located in the same fault block as Apium-1 and are more distal to the main NNW-trending fault. All three wells intersect the Late Permian Dongara Sandstone, which is overlain by the Early Triassic Kockatea Shale (Fig. 7.1 B)(Mory and Iasky 1996, Owad-Jones and Ellis 2000). The Dongara Sandstone consists of shallow marine to foreshore beach unit sandstone of varying maturity, with minor shale interbeds, has previously been targeted as a petroleum reservoir, and is the focus of this study (Mory and Iasky 1996).

7.2 Approach

The sedimentology and mesoscopic structures were characterized by sedimentary and structural logging of core recovered from Apium-1, Centella-1 and Mondarra-4 (Fig. 7.2). Core logs of Centella-1 and Mondarra-4 were used to assess the lateral and spatial extent of the damage zone around the major regional fault.

Lithologies are described in terms of grain-size (Wentworth scale), sorting, rounding/sphericity and modal mineralogy, using Folk's sandstone classification scheme (Folk 1965, Wentworth 1922). Ultraviolet light images of Apium-1 core were used to identify the presence of petroleum residue and diagenetic minerals (such as barite and siderite). The orientation and depth of faults, fractures, stylolites and other pressure solution features were measured, in terms of angle from core margin. Depth, orientation, amplitude and any cross-cutting relationships were recorded. The method of measuring two angles and one length in half-core to constrain the orientation of structures was used, which has a low degree of uncertainty (Blenkinsop and Doyle 2010). The plunge of Apium-1 and Centella-1 is 85° and 74°, respectively, which been accounted for in orientation data. The fluorescence, amplitude (in the case of stylolites), and the presence of diagenetic pyrite nodules and their size and distribution were recorded.

Laboratory measurements of porosity and permeability from Apium-1 core plugs were done by ARC Energy Ltd® using mercury injection capillary pressure. 24 samples were taken between 2758.50 and 2781.90 m, impregnated with blue resinand used to make polished thin sections to examine the petrography and microstructure in Apium-1. High resolution (2 µm) optical photomicrographs of the whole thin sections were acquired using the Zeiss Axio Imager 2 microscope at CSIRO, Perth (see Olierook (2011) for a full catalogue). Transmitted and cross polarized light images were used for

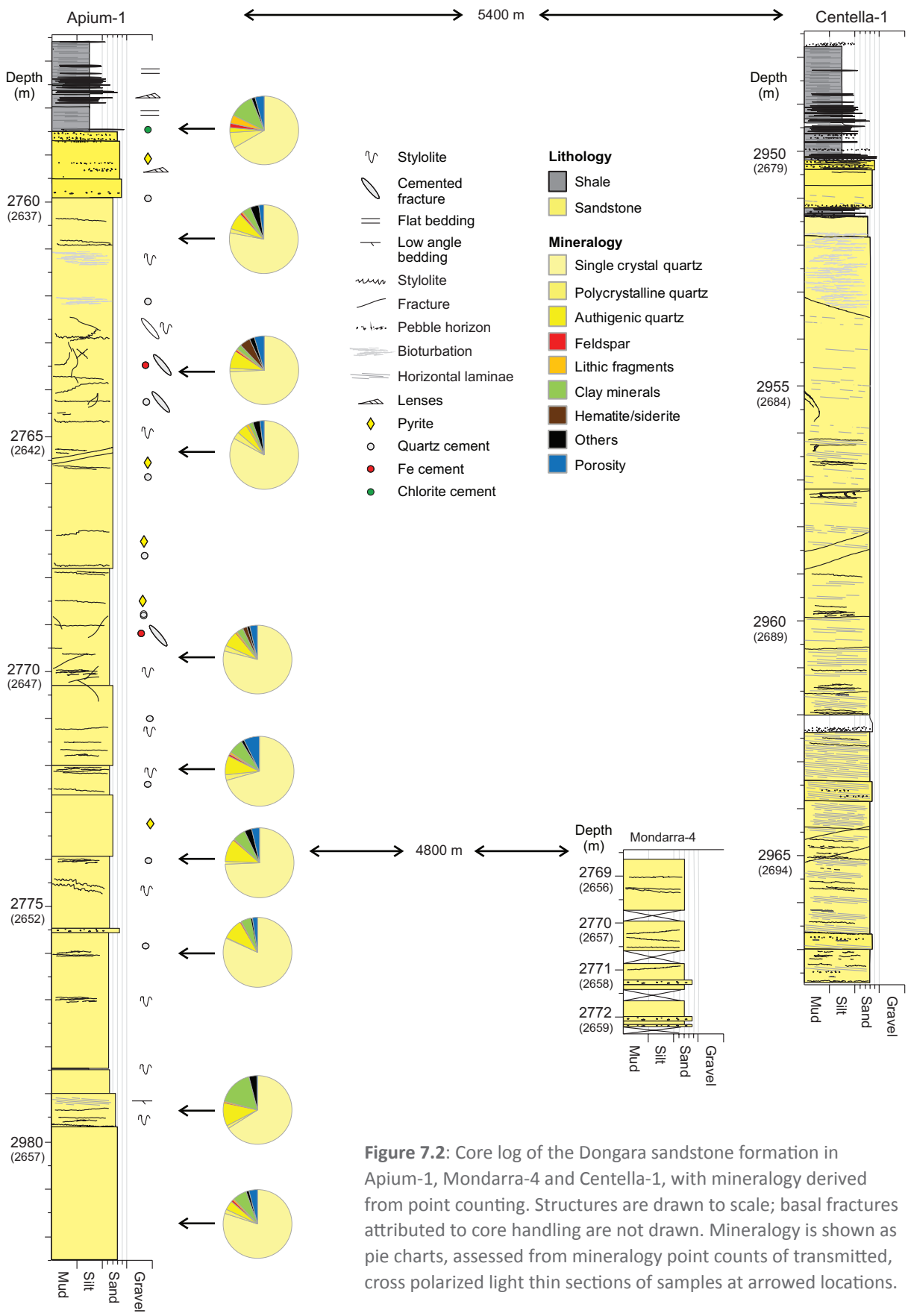

Figure 7.2: Core log of the Dongara sandstone formation in Apium-1, Mondarra-4 and Centella-1, with mineralogy derived from point counting. Structures are drawn to scale; basal fractures attributed to core handling are not drawn. Mineralogy is shown as pie charts, assessed from mineralogy point counts of transmitted, cross polarized light thin sections of samples at arrowed locations.

point counting to determine modal mineralogy, as these are able to differentiate between detrital and quartz overgrowths. Porosity was measured from thin sections via an image analysis technique using ImageJ® software (Rasband 2011). The 'Threshold Colour' plug-in (Landini 2010) permits the area fraction of blue resin, and thus porosity, to be determined. Two values for porosity were discriminated: 'blue resin' and 'green-blue resin', which represent clear and partially clay-occluded porosity, respectively. This 2D porosity values show a good correlation with core plug porosity values (Olierook, 2011).

Cathodoluminescence imaging (CL) was used to investigate quartz overgrowths/cements because it is sensitive to variations in trace elements and defects, and unlike most other techniques, it provides strong contrast between detrital and diagenetic phases and can resolve syntaxial veins and overgrowths in quartz (Augustsson and Bahlburg 2003, Kwon and Boggs 2002, Lloyd and Knipe 1992). CL images were collected at Curtin University using a Philips XL30 scanning electron microscope (SEM) fitted with a KE developments cathodoluminescence detector with working distances between 14.5 and 16.9 mm, a spot size of 6 and accelerating voltages of 10.0 – 12.0 kV.

Crystallographic mapping was done to characterise microscopic deformation mechanisms in the vicinity of damage in key samples via electron backscatter diffraction (EBSD) at Curtin University, using the Zeiss EVO SEM with Oxford Instruments EBSD system (Channel 5.10). This is a quantitative technique that can resolve mineral phases, grain geometry statistics, intra-grain deformation (e.g., lattice strain and dauphiné twins (60°/<0001>) in quartz), and crystallographic preferred orientation data. EBSD utilized a working distance of 15.0 mm, a spot size of 5.5, a stage tilt of 70.0° and an accelerating voltage of 20.0 kV. EBSD data were collected and processed using the Oxford Instruments' software using routine procedures (see Olierook (2011) for further analytical details) (Prior et al. 1999, Reddy et al. 2007). Visual comparison of the processed data with optical photomicrographs indicates that no significant artefacts were introduced. Dauphiné twins were redrawn from EBSD maps due to a systematic misindexing issue that affected some grain that resulted in false isolated 60°/<0001> data points due to close rotational crystal symmetry of quartz.

High-resolution (2 µm step-size) quantification of major and trace mineralogy in two stylolite regions was done to assess the degree of enrichment of immobile detrital minerals (e.g., zircon and TiO_2), and thus quartz dissolution associated with stylolitization. This was done via automated mineral analysis (AMA) (Goldie Divko et al., 2010; Messent and Farmer, 2008; Dilks and Graham, 1985; Reid, 1989) using four light-element, energy dispersive X-ray spectrometers (EDX) on the FEI QEMSCAN® at Ammtec Ltd®. This was performed quantitatively using calibration with a copper standard to determine the chemical composition. QEMSCAN® utilizes a software suite (iMeasure) controlling automated data acquisition. Modal mineralogy was determined from spectral data using iExplorer. The working distance was 23 mm, with an accelerating voltage of 15 kV and a probe current of 3 nA. Samples were coated using a 10 nm-thick evaporative carbon coat to disperse electron charge induced in the SEM. Note that EDS cannot differentiate between minerals of the same/similar chemistry, such as anatase and rutile, or illite and muscovite.

7.3 Results

7.3.1 Sedimentary Logging and Petrography

Seven distinct sedimentary units were identified during photo-interpretation and core logging of Apium-1 (Fig. 7.2). The units are: (1) Shale, with some sandstone lenses towards the base. (2) The shale gradates into a very coarse-grained sublitharenite. It has poor sorting, with sub-angular grains. The base of the unit is marked with a pebble horizon. Clay minerals are interstitial, consisting primarily of kaolinite, with significant chlorite in a small interval. Units (3) – (7) are very similar, all classed as quartz arenites, which are separated based on their grain size. Sorting is moderate to good, with sub-rounded grains and moderate to good sphericity. Sandstone units are predominantly massive with sparse, weakly-developed sedimentary structures (Fig. 7.2). Point counting of thin sections shows that the Dongara Sandstone in Apium-1 is dominated by single crystal quartz (67-84%), with very minor amounts of detrital feldspar, lithics, rutile and zircon, and authigenic quartz cement and clay minerals (Fig. 7.2). The sandstones are classified as quartz arenites, after Folk (1965), and between proto-quartzite and ortho-quartzite, after Selley (1988), with very little mineralogical variation between all units.

7.3.2 Diagenetic minerals and fabrics

Relict detrital quartz grain boundaries were identified by thin haematitic coatings in optical photomicrographs, which reveal that optically continuous, authigenic overgrowth cements are common. The detrital to authigenic quartz ratio varies from 4:1 in fine grained units, 16:1 in medium grained units, and 18:1 to 28:1 in coarse grained units. Up to four quartz overgrowth zones were identified by CL, and quartz grains typically show one or two overgrowth phases (Fig. 7.3). The diagenetic clay assemblage consists of 1-5% pore-filling kaolinite booklets that post-date quartz overgrowth cements (Fig. 7.3 B). Large biogenic/diagenetic pyrite nodules (up to 80 mm across) occur between 2765 and 2770 meters (unit 3 and 4), and show distinctive pyrite rimming. Timing relationships with these pyrite nodules is poorly constrained.

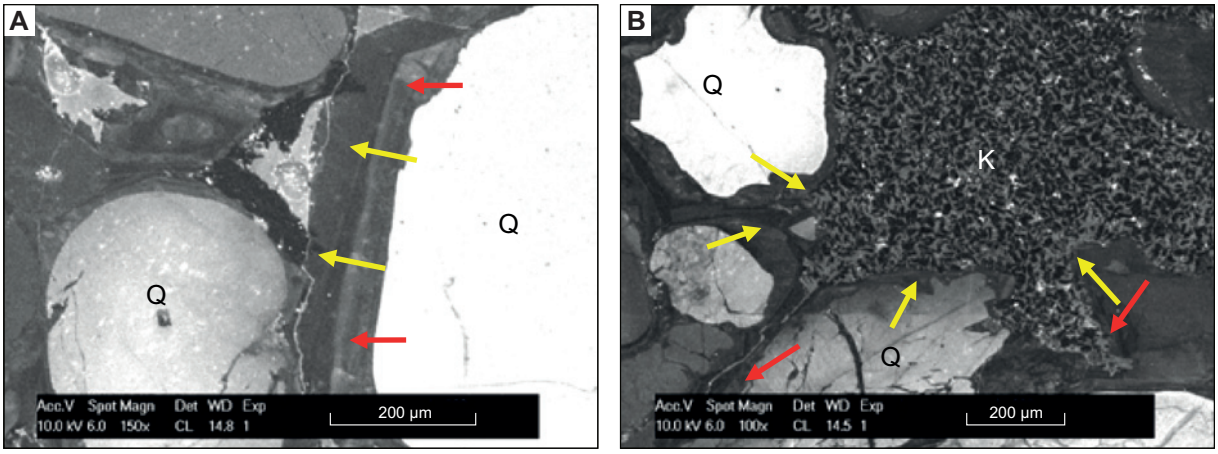

Figure 7.3: (A) Quartz (Q) has up to four overgrowth stages, divided into two mains phases: an early phase (red arrows) and later phase (yellow arrows). (B) Kaolinite (K) partially-occludes pore spaces that have been previously intruded by both early (red arrows) and later (yellow arrows) quartz (Q) phases.

7.3.3 Meso-scale structural analysis

Fractures and stylolites were observed in Apium-1. Stylolites and fractures decrease from holes proximal to the major regional fault (Apium-1), when compared to distal holes (Centella-1 and Mondarra-4) (Fig. 7.4). Apium-1 has higher densities of stylolites than the other two wells, with 3.5 stylolites per metre compared to 1.9 stylolites per metre in fine to medium grained sandstone, respectively. Similarly, Apium-1 has 0.4 fractures per metre, whereas Centella-1 and Mondarra-4 contain none. This suggests that the regional fault has a significant damage zone, with the formation of stylolites and fractures at least 1 km into the hangingwall block.

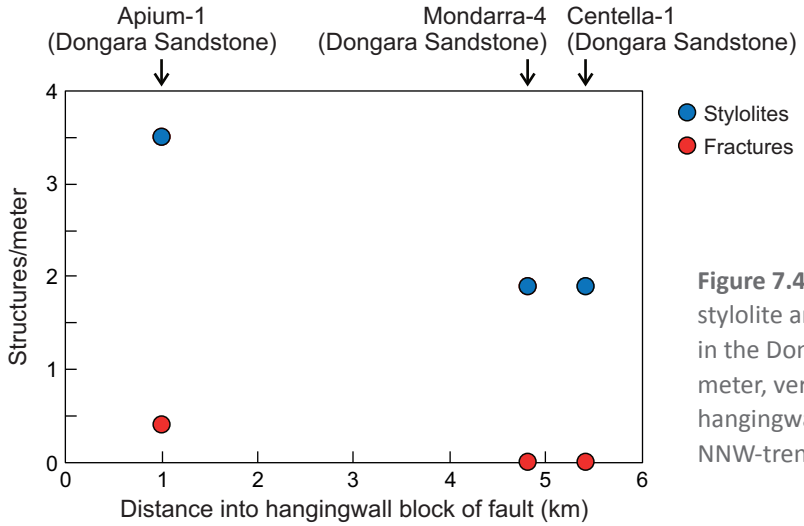

Figure 7.4: Graph showing the stylolite and fracture populations in the Dongara Sandstone per meter, versus the distance into the hangingwall block of the major NNW-trending regional fault.

At the mesoscopic scale, fractures occur as cemented, steeply-dipping shear fractures and open sub-horizontal extensional fractures (Fig. 7.5). Cemented shear fractures are limited to fine to medium quartz arenite (unit 3 and 4). They are cemented by either red-brown siderite and quartz or black organic carbon and clay. Open extensional fractures show no evidence of prior cementation. These are typically sub-horizontal, although occasionally steeply-dipping. They are far more abundant in shale (~22 open fractures per metre) than in sandstone (1.2 open fractures per metre).

Three types of stylolites are identified in Apium-1. Type (a) stylolites are common in fine to medium grained homogenous quartz arenite, in units 3 and 4 (Fig. 7.6 A, B & Fig. 7.7 A, B). They are variably filled with predominantly organic carbon and clay minerals, but minor amounts of other framework grains are present. Type (b) stylolites (muddy) contain significantly more clay and organic carbon (Fig. 7.6 C, D). These occur predominantly in unit 5 and 6, which contain minor clay horizons (0.1-5 mm). Stylolites localize on these clay horizons, since clay is known to enhance quartz pressure solution (Sibley and Blatt 1976, Tada and Siever 1989). Type (c) stylolites (ribbon) have one or two stylolites over one millimetre in thickness and up to ten 'proto-stylolites' (precursors to more well defined type (a) and (b) stylolites) (Fig. 7.6 E, F). Proto-stylolites are significantly thinner, less than 0.5 mm and commonly less than 0.1 mm in thickness. Stylolites of similar orientations are locally clustered, but there is no systematic distribution within the logged intervals (Fig. 7.7 B).

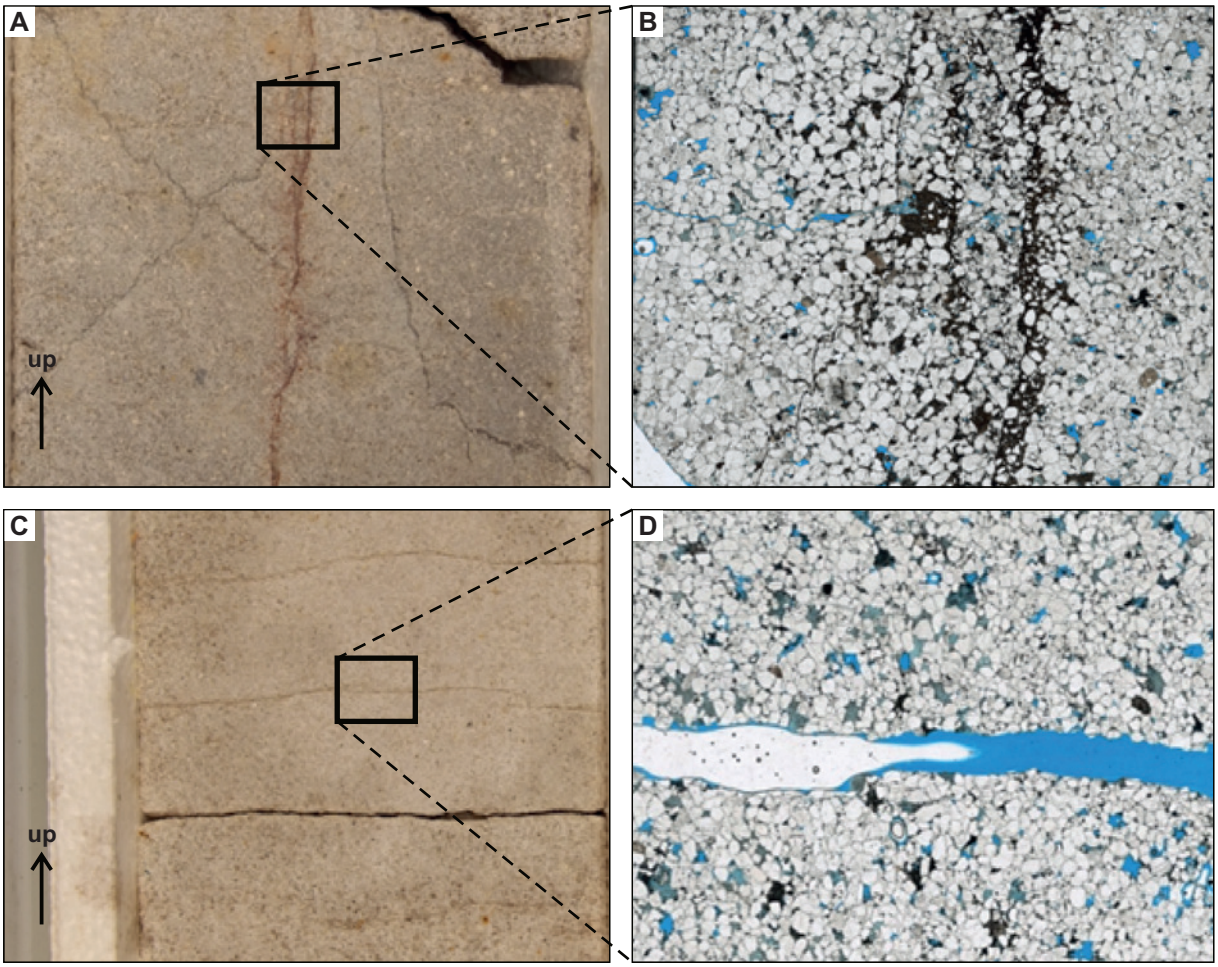

Figure 7.5: Core (A) and transmitted, plane polarized light (B) images of a typical cemented fracture, and; core (C) and transmitted, plane polarized light (D) images of a typical open fracture (mineralogy changes are not apparent across fractures). The black boxes represent the approximate locations of samples. Arrow indicates up direction. Samples have been impregnated with blue resin to highlight porosity.

Siderite-cemented, organic and clay-'lined' shear fractures have variable dips and generally strike NW, parallel to minor faults in the region (Fig. 7.8 A). These fractures become locally orthogonal to bedding-parallel stylolites. Sub-horizontal, uncemented extensional fractures, less than 1mm wide, are perpendicular to the present day maximum principal stress (King et al. 2008), and are therefore likely to be drilling-induced (Fig. 7.8 D). Stylolites in Apium-1 and Centella-4 are most commonly bedding-parallel (sub-horizontal), but are orientated at higher angles, up to orthogonal to bedding, proximal to cemented shear fractures (Fig. 7.8 B, C). 75% of stylolites are sub-horizontal in Apium-1 and independent of other deformation structures, and the remainder form at the tip zone of fractures with dips of up to 60°. Sub-horizontal stylolites vary systematically in dip with a mean dip of 4° and consistent strike (sub-)parallel to the main regional fault (Fig. 7.8 B). Stylolites in Centella-1 are less systematically oriented, with a mean dip of 16° (Fig. 7.8 C). Mondarra-4 shows only a few bedding-parallel stylolites.

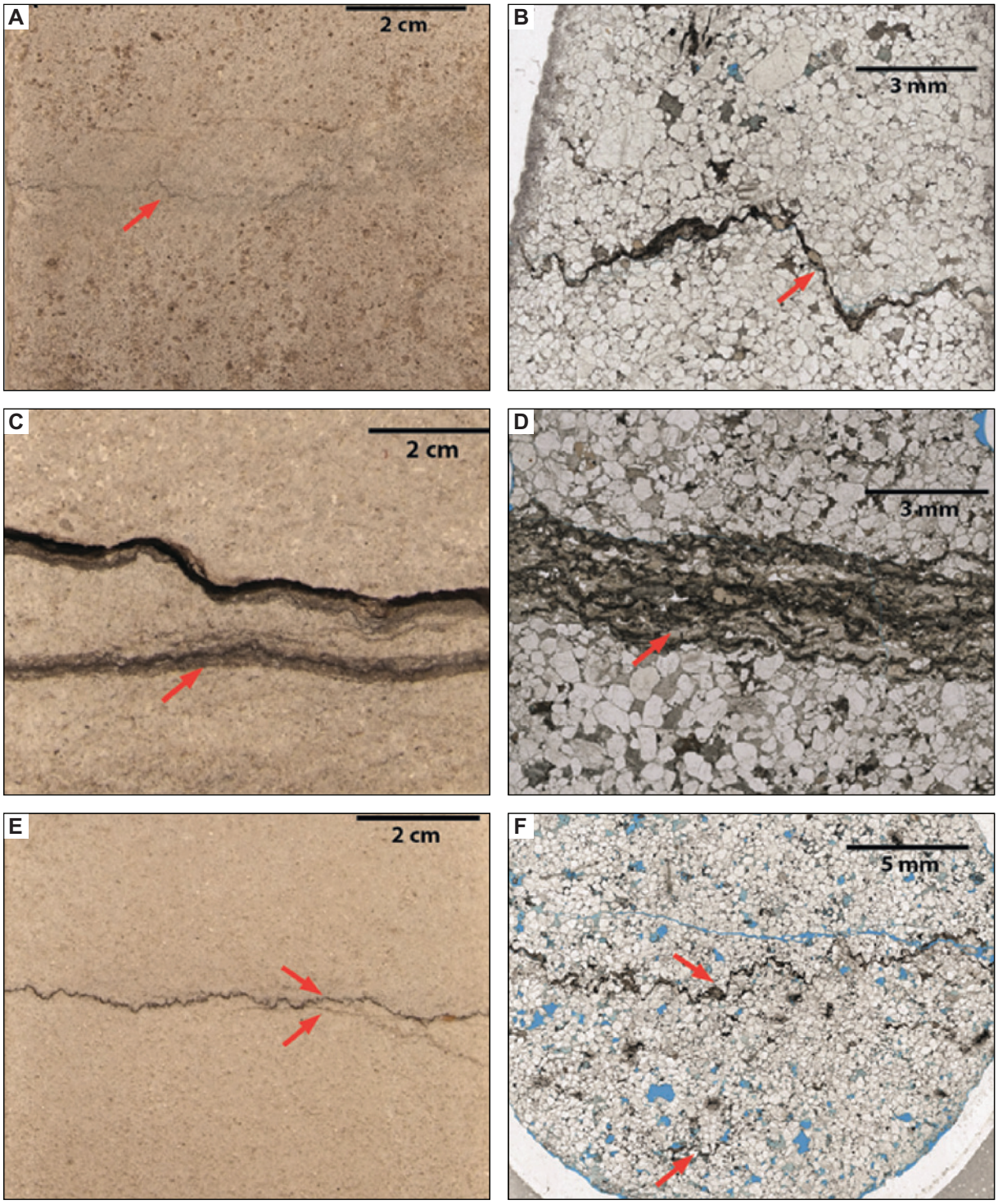

Figure 7.6: Core photographs (A, C, E) and respective sample photomicrographs in transmitted plane polarized light (B, D, F) of type (a), (b) and (c) stylolites. A and B are from sample location 3 (2760.85 m) in unit 3, showing type (a) stylolites; C and D are from sample location 23 (2779.25 m) in unit 6, showing type (b) stylolites, and; E and F are from sample 17 (2774.10 m) in unit 5, showing type (c) stylolites. Red arrows show stylolites in core and respective photomicrographs.

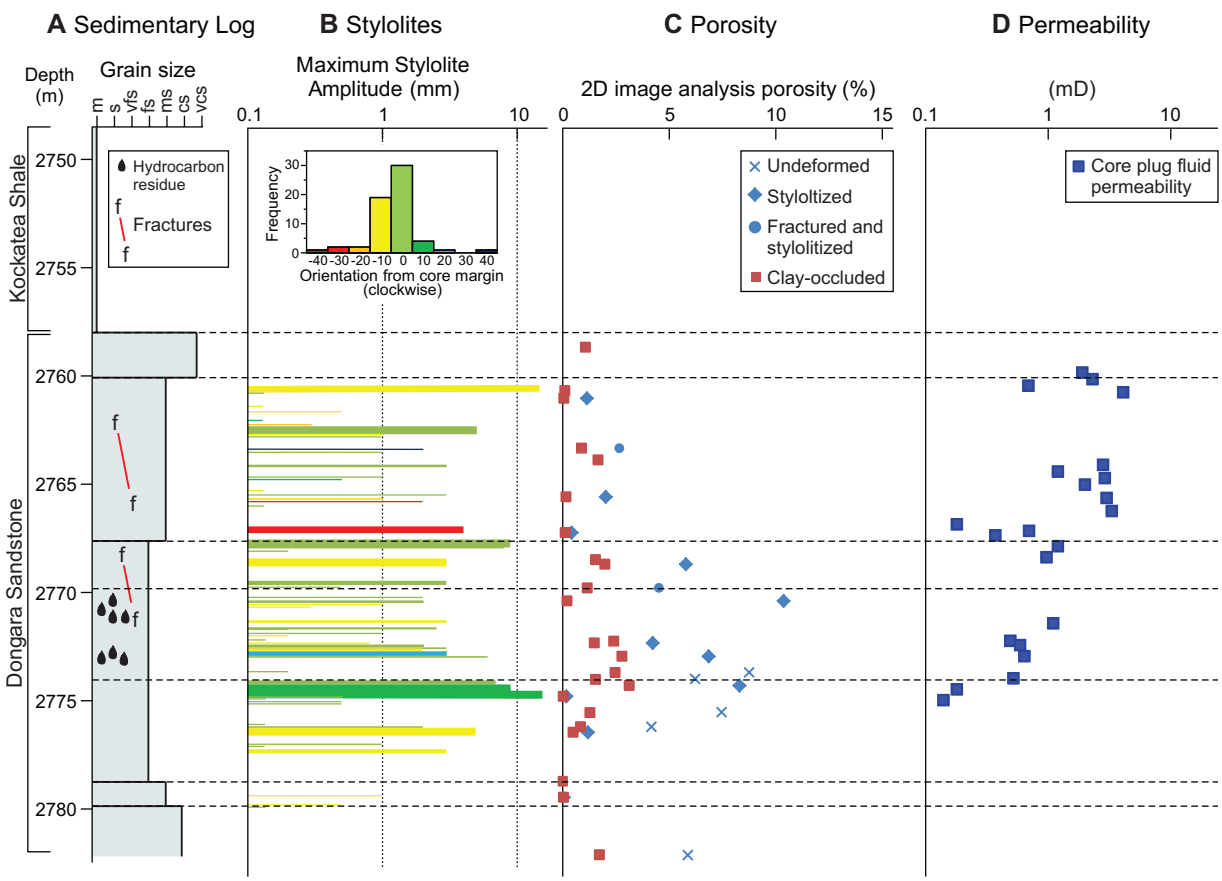

Figure 7.7: Graphical representation of the effect of lithology and stylolites on porosity and permeability: (A) Sedimentary Log; (B) Stylolite distribution (thickness of bars represents average thickness of stylolites, to scale); (C) Porosity versus depth, and; (D) Permeability.

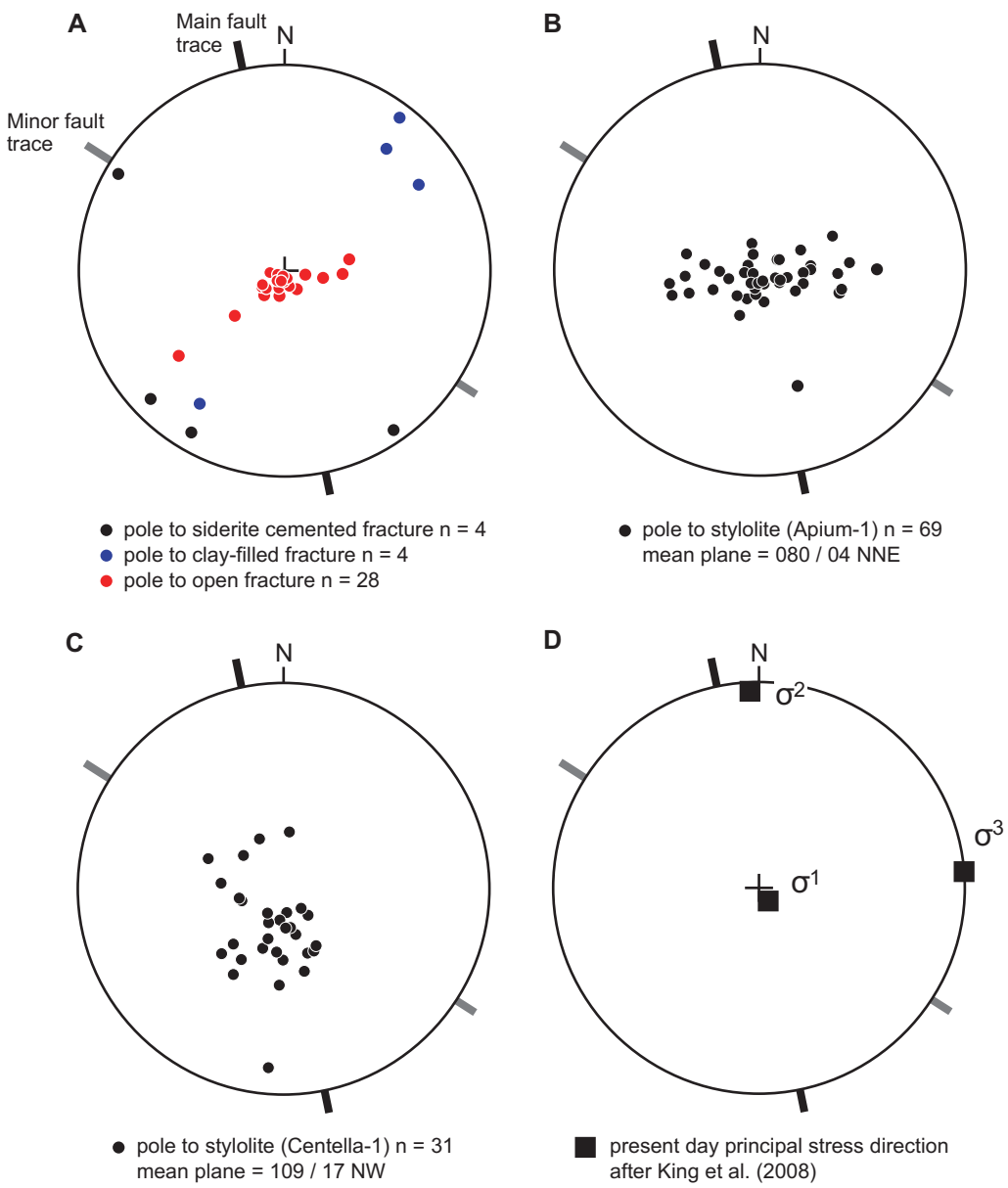

Figure 7.8: Stereographic projection of fracture and stylolite orientations in Apium-1 using GEOrient©. The trend of a major regional fault is denoted by a black line, striking NNW. The smaller scale regional fault, NW-striking is also marked on with a grey line (see Fig. 7.1). (A) Poles to fractures in Apium-1; (B) Poles to stylolites in Apium-1; (C) Poles to stylolites in Centella-1, and; (D) Present day principal stress direction, after King *et al*. (2008).

7.3.4 Microstructural analysis of fractures and stylolites in Apium-1

Microstructural analysis of Apium-1 samples shows that meso-scale shear fractures are accommodated by micro-brecciation along fracture surfaces and have damage zones containing intragranular extensional fractures filled with quartz cement (i.e., veins) and dauphiné twins localized at grain boundaries and triple junctions, and weakly-developed intragrain crystal-plastic strain (Fig. 7.9). Quartz veins cross cut quartz overgrowth cements and are predominantly oriented

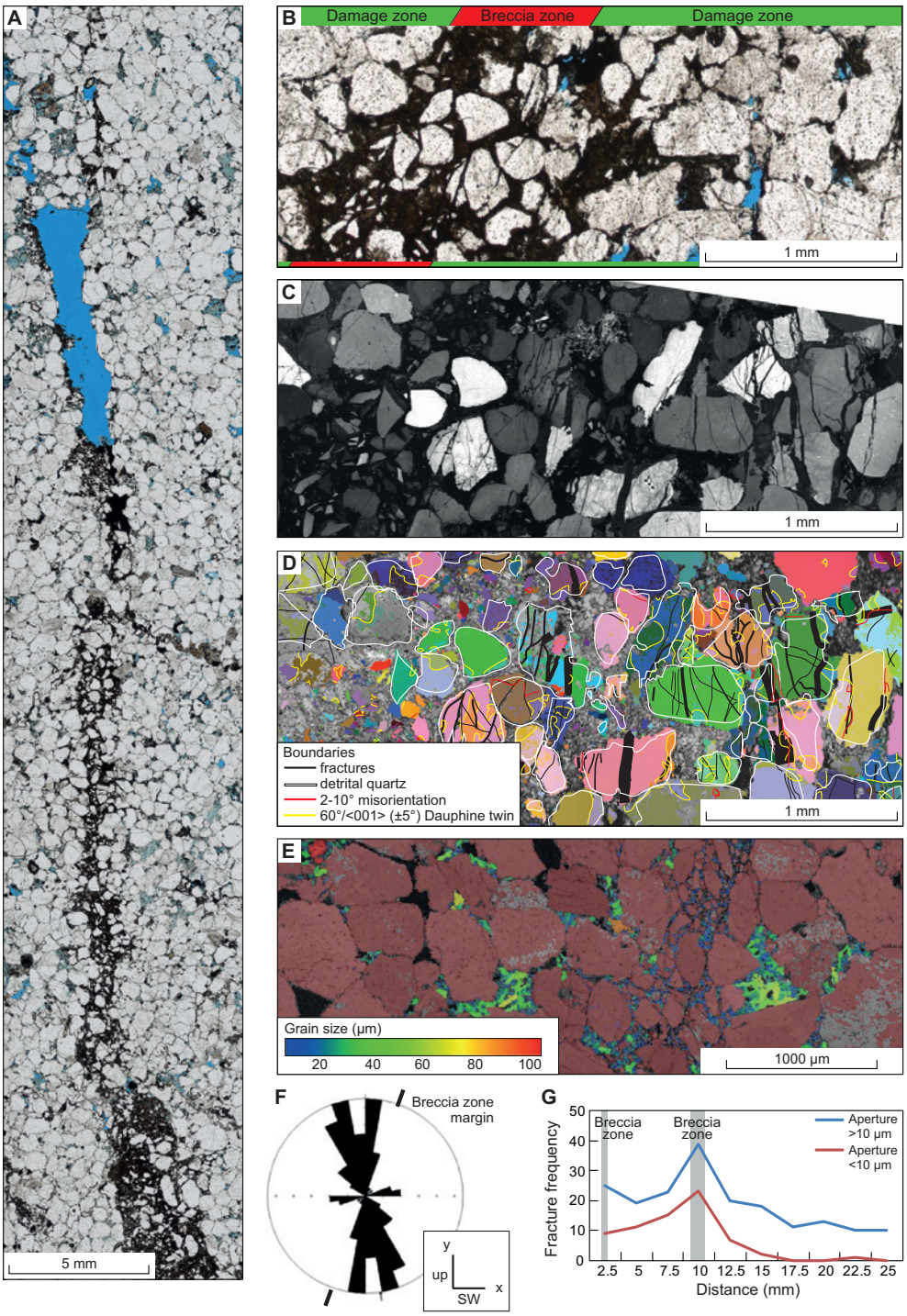

Figure 7.9: Fractures are exhibited different microstructures that are shown to reduce porosity. (A) Siderite-filled breccia zone with significant quartz comminution, in thin section, under plane polarized light. (B) Zoom-in of siderite-filled breccia zone in thin section, also showing open microfracture in breccia zone. (C) CL image of B, showing syntaxial quartz veins, oblique to brecciazone. (D) EBSD image of B, highlighting detrital quartz veins, syntaxial quartz veins, low angle misorientation boundaries and dauphiné twinning. (E) Different breccia zone with quartz (dark red) and drusy to anhedral siderite cement, coloured for grain size. (F) Rose diagram showing orientations of tensile fractures (both open and quartz-filled) in relation to the breccia zone margin in a breccia zone transect. (G) Tensile fracture frequency distribution across two breccia zones.

at 25-35° to mesoscopic shear fracture planes, which is consistent with formation perpendicular to σ3, in the same stress field as the mesoscopic shear fractures (Anderson 1942) (Fig. 7.9 C, F). The density of quartz veins increases toward meso-scale fracture surfaces (Fig. 7.9 G). Total extension accommodated by quartz veins in the damage zone of the shear fracture is estimated at 5.2%. Micro-breccia zones occur in discrete 0.1 to 2 mm bands that are associated with mesofractures that are cemented with siderite. Significant disaggregation and minor cataclasis has occurred along slip surfaces, where grains have been reduced in size. These breccia zones are often soft-linked in relay zones, with stylolites splaying out of tip zones. Siderite forms a drusy, spar-texture of red-brown, rhombic to anhedral crystals characteristic of carbonates and is found along shear fractures (Fig. 7.9 E). Partially-filled pores adjacent to fracture breccia zones are filled with siderite and kaolinite, with kaolinite being early-formed. Siderite has formed after two quartz overgrowth phases and brecciation. Open, unsealed intragranular fractures are extremely rare in all samples except in unit 2 (very coarse grained sublitharenite) or occasionally as refractured cements in wide tensile fractures.

UV images show that hydrocarbon residue is clustered into two sections. Both are approximately 1.5 m thick, between 2770.8 and 2772.1 m and between 2772.5 and 2774.1 m. Stylolites sharply bound hydrocarbon-rich domains and is evidence that stylolites inhibited migration of hydrocarbons (Fig. 7.10 A, B). Stylolites show a strong relationship between thickness and amplitude, which suggests an evolution to thicker, high amplitude stylolites over time (Fig. 7.10 H). All stylolites have strongly anastomosing sutured quartz grains along their interfaces indicative of quartz dissolution, and authigenic quartz is precipitated in rock volumes on both sides of stylolites (Fig. 7.10). Optical microscopy and AMA shows that stylolites consist of mainly organic carbon and illite (Fig. 7.10 C, D). AMA shows concentrations of accessory phases in stylolites, including TiO_2 (rutile/anatase), zircon and pyrite (Fig. 7.10 C, D, E). The anhedral form of TiO_2 is thought to be the diagenetic form, anatase. Anatase is confined to stylolites, very-fine grained, ranging from 3-15 µm, and typically subhedral (Fig 7.10 E). A 'titanium silicate' was found during automated mineral analysis. Optical microscopy confirmed that there was no interaction of framework titanium oxide and quartz phases, hence the interference is presumed to arise from commonly occurring rutile needles in quartz. Rutile needles provide the titanium necessary for formation of authigenic anatase. The most likely source of titanium for authigenic anatase is the localised dissolution of rutilated quartz grain boundaries because rutile diffusion in quartz is negligible under 600 °C (Cherniak et al. 2007). Anatase is only confined to stylolites because this is the only site with significant quartz pressure solution to liberate Ti from rutile. Pyrite identified under optical and SEM microscopy is located in stylolites, typically subhedral and 50-100 µm in diameter. It is also located as an anhedral pore-filling phase and fine remnant of incomplete alteration to siderite near siderite-cemented fracture zones.

7.3.5 Porosity and Permeability characterisation

Two-dimensional measurements of porosity from analyses of optical photomicrographs vary between 0 and 20% (Fig. 7.7 C). Maximum porosity values are controlled by grain size, with higher values from coarser grained units. However, there are strong variations in porosity within units of similar lithology and grain size. This variation is due to the presence of fractures and stylolites. Porosity reduction

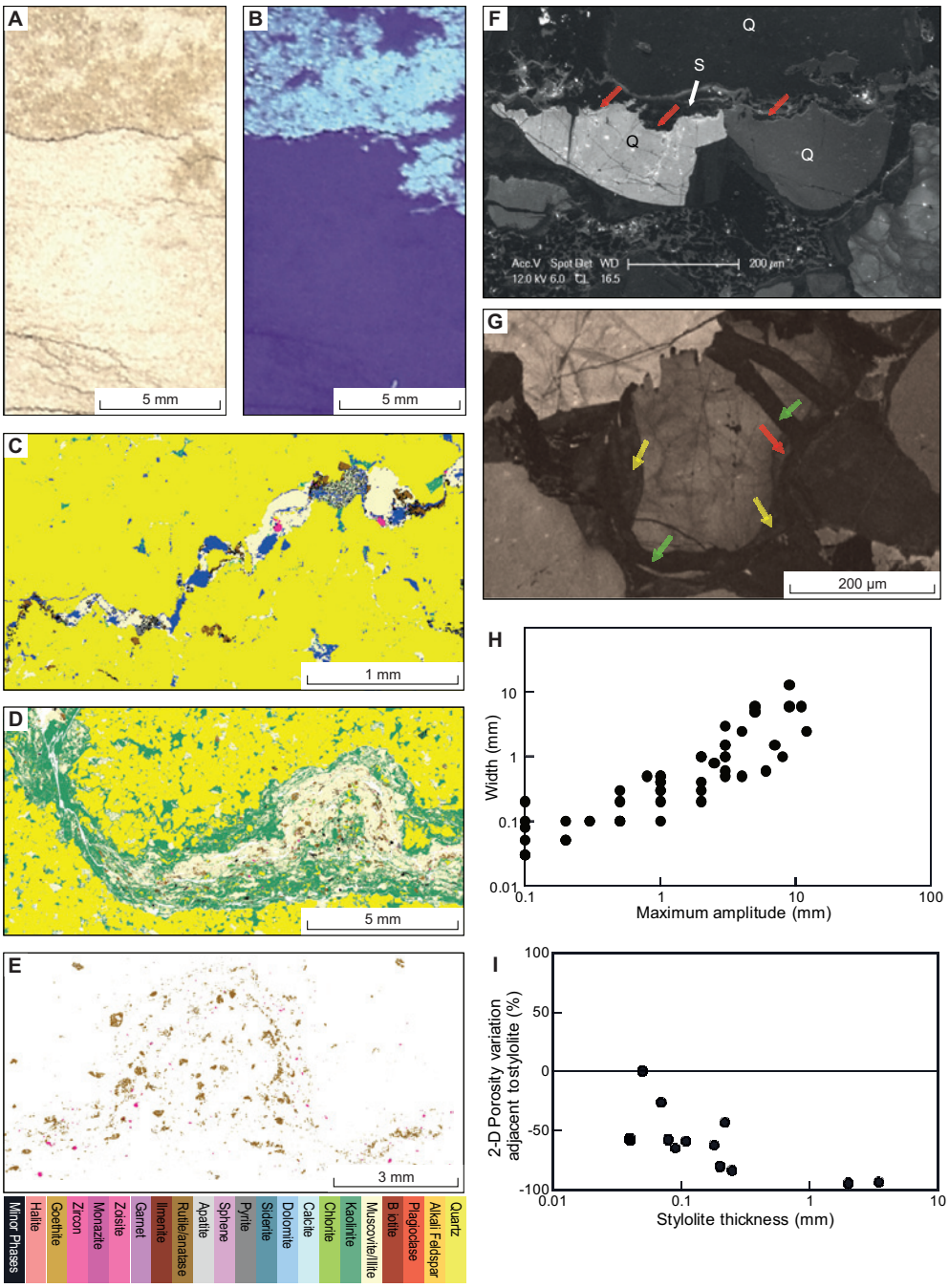

Figure 7.10: Stylolites are shown to reduce porosity on the micro-scale. Note that the mineralogy legend is applicable for C, D and E. (A) & (B) Core photograph in plane polarized light of stylolite bounding oil residue, under normal light (A) and ultraviolet light (B). (C) AMA of small stylolite shown to be filled with illite, pyrite, rutile/anatase, zircon and siderite. (D) AMA of larger stylolite enriched heavily in illite, kaolinite and accessory minerals. (E) AMA of D, showing only zircon and rutile/anatase, highlighting enrichment in stylolite as opposed to surrounding host rock. (F) CL image showing highly sutured quartz grains at quartz-stylolite interfaces (red arrows). (G) Syntaxial quartz veins (green arrows) overprinting early (red arrows) and later (yellow arrows) quartz overgrowth phases. The second quartz phase is similar in brightness to stylolites in F, under the same brightness/contrast settings. (H) Maximum amplitude of stylolites is proportional to stylolite width. (I) Stylolite thickness is proportional to porosity reduction.

in fractures is due to siderite, pyrite, and minor quartz cementation which as significantly reduced the porosity of fractures. Domains adjacent fractures typically do not show significant reduction in porosity. Stylolites exhibit lateral porosity reduction within 1-20 mm (or more, outside the thin section area), dependent on the maximum thickness of the stylolites. Halos of reduced porosity are commonly asymmetrically developed. There is a strong correlation between the thickness of stylolites and porosity reduction (Fig. 7.10 I). Porosity measurements in the nearest 2 mm of stylolites have a proportional reduction when plotted against thickness of stylolites. Stylolites formed along mud beds were differentiated from those formed in homogenous sandstone. Thicker and higher amplitude stylolites, and those that formed along muddy beds, have wider halos of decreased porosity. Stylolites in quartz arenite have distances between 1 and 20 mm, where porosity is significantly reduced. Stylolites in mud horizons are thicker and have >20 mm reduction in porosity (outside the area of the thin section). Away from stylolites, porosity can be partially occluded by interstitial kaolinite (and minor illite?). Grain plucking prior to resin impregnation has generated anomalously high porosity values from image analysis (and a high clear to partially-occluded porosity ratio), and is entirely an artefact of poor sample preparation.

Permeability studies show variable permeability across the core, with semi-distinct boundaries between units (Fig. 7.7 D). Primary permeability was calculated from the maximum permeability observed in each unit. However, within a unit permeability varies by one to two orders of magnitude, which is controlled by structures and lithology. Fractures are cemented, filled with siderite and quartz cement, but have permeable linkage zones. Permeability plugs taken at or in close proximity (5 cm) to stylolites typically show an order of magnitude reduction from the maximum permeability in undeformed samples. Permeability plugs at fractures show permeability increases because they tend to be broken due to core extraction and handling. Increased silica overgrowths, characterized by vitreous rims on quarts grain in core samples, reduce permeability by up to two orders. Authigenic quartz overgrowths in thin sections show a modal percent increase in samples that contain stylolites.

7.4 Discussion

7.4.1 Facies and environment

The shale and the sandstone identified in Apium-1 are the Kockatea Shale and the Dongara sandstone, according to palynology studies by Origin Energy Ltd (Mitchell 2004). The seven distinct units in Apium-1 can be split into three facies. (1) Unit 1 is part of an offshore marine facies, consisting of shale with lensoidal intercalations of medium to coarse grained sandstone. This ranges from an offshore marine shelf (wholly shale), to lower offshore (< 5 cm lenses of sand) to rare upper offshore (10 cm bed of sandstone). (2) Unit 2 is part of a transgressive shoreface deposit consisting of coarse to very coarse grained, friable, chlorite-cemented sandstone. (3) Units 3 to 7 are part of a foreshore facies, consisting of massive, fine to medium grained quartz arenite. There is a low order sequence stratigraphic boundary present between facies 1 and 2, marking a change from a highstand systems tract (Dongara sandstone) to a transgressive systems tract (Kockatea Shale) (Mitchell 2004, Mory and Iasky 1996).

7.4.2 Relative structural and diagenetic history

The diagenetic and structural history is established from timing relationships of diagenetic phases and structures and an interpretation of the origin of diagenetic phases in a framework of structural history. Six distinct events were determined (Fig. 7.11).

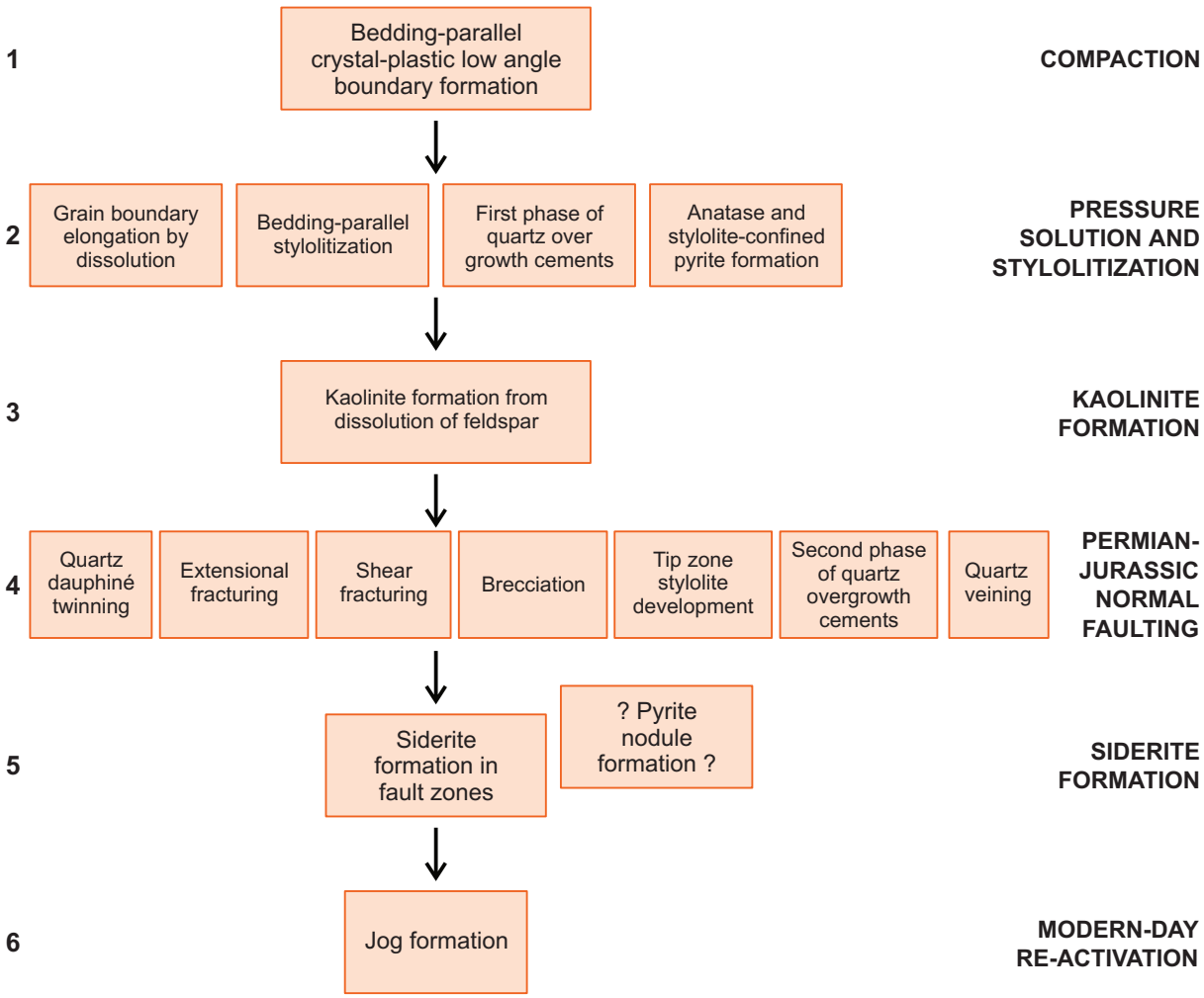

Figure 7.11: Flow chart showing interpreted burial history of Apium-1.

1. Randomly orientated crystal slip boundaries are present in the majority of quartz grains, suggesting that crystal-plastic deformation was inherited from pre-deposition. A second, bedding-parallel crystal-slip event occurred, propagating across multiple grain boundaries, suggesting that this was compaction-related.
2. An early quartz overgrowth cement phase is crosscut by breccia, stylolites and all other diagenetic phases. Grain-grain contact pressure solution could have been triggered during compaction, seen by long and sutured grain contacts throughout the host sandstone. The first quartz phase occasionally displays up to four separate overgrowths on a single quartz grain indicating that cementation was spatially and temporally heterogeneous (Gratier et al. 2005).

Stylolitization begins to occur at ~ 1000 m depth in quartzose sandstone basins implying that heterogeneous compaction-related pressure solution probably preceded it. Compaction, pressure solution and stylolitization processes involve dissolution along quartz-quartz contacts and re-precipitation in adjacent pore-quartz contacts (Knipe 1989, Lloyd and Knipe 1992). This supports isochemical models of quartz cementation in reservoir sandstones, which suggests that it is unlikely that quartz cement originated from external fluids flowing along fractures (Fisher et al. 2000). Localized pressure solution would have led to grain boundary elongation, with syntaxial quartz overgrowth precipitated at quartz-pore interfaces. Automated mineral analysis showed that zircon and rutile concentrated in stylolites is 1-2 orders of magnitude (up to 35 times higher) than the surrounding quartz arenite. This suggests that it is residual from the removal of large volumes of quartz by pressure solution (Hamilton et al. 2011). Titanium to form anatase is then likely found from rutile needles in quartz grains, shown by presence of quartz-TiO_2 chemistry; this also implies anatase formed during stylolite formation.

3. Kaolinite formed between the two quartz phases, creating and partially-filling in situ pore spaces. The most likely origin for this book kaolinite is from in situ feldspar dissolution for the following reasons: (a) the pore shapes that host kaolinite are subhedral, retaining pseudo-habits of feldspars with similar size to surrounding framework grains; (b) the first quartz overgrowth phase is impeded against kaolinite-pore spaces, suggesting that original framework feldspars were still present, and; (c) booklets of 5-30 platelets are randomly oriented (Górniak 1997, Wilson and Pittman 1977). The second quartz overgrowth cements still grow into pore-spaces, suggesting that feldspar dissolution was already occurring or complete during later authigenic quartz formation, such that a second phase of quartz rim cements were unimpeded by feldspars at grain-grain contacts.
4. The second quartz phase formed from stylolite-derived quartz and continued pressure-solution, post-fracturing, but prior to siderite formation. Initial normal faulting occurred during Permian to Jurassic rifting, probably creating subsidiary, core-scale transgranular fractures (Song and Cawood 2000). These stylolites either: (a) post-date the Permian to Jurassic normal faulting event, using the deformed fracturing surfaces as lower energy nucleation sites (Gratier et al. 2005, Song and Cawood 2000); or (b) stylolites nucleated and propagated syn-faulting, forming in the tip-zone of soft-linked fractures (Canole et al. 1997, Labaume et al. 2004, Rispoli 1981). The latter mechanism is more likely, considering steeply-dipping stylolites, those expected to form at tip zones, vary 40-50° in strike to sealed fractures. This strike variation is expected in stylolites located in tip damage zones of normal and strike-slip faults (Peacock et al. 1998). Tip-zone stylolites experience a local perturbation of the stress field, where the maximum principal stress, $\sigma 1$, is not vertical. Since cathodoluminescence increases with increased rare earth or trace element content, this explains the dark cement of the second phase, undeformed by significant fracturing, and the more luminescent first quartz phase (Augustsson and Bahlburg 2003). Regional normal faulting also resulted in the onset of dauphiné twinning, low angle grain boundary slip sub-parallel to faulting, tensile and shear fracturing. Shear fracture accumulation then led to brecciation. Dauphiné twins are clearly crosscut by quartz veins (representing low angle grain boundaries) and the second phase of overgrowth.

5. Fracture breccias are filled with late siderite. Siderite tends to form through either pyrite reacting with CO_2-rich fluids or carbonate alteration (Schenau et al. 2002, Xiao et al. 2010). Presumably, siderite is derived from centimeter-scale biogenic pyrite nodules reacting with CO_2-rich fluids, since no other carbonates are found in Apium-1. Siderite is also found locally to alter from anhedral pyrite and this may therefore be another source of iron.
6. Lastly, modern day stresses (transitional reverse to strike-slip) re-activated steeply-dipping sealed fractures to create jogs in releasing bends (Kim et al. 2004, King et al. 2008). Quartz veins were not observed in these fractures, suggesting that stylolitization had ceased before modern-day stress state has been established.

7.4.3 Mass transfer associated with stylolitization

The intensity of stylolitization in Apium-1 is characterized by the condensation of heavy minerals along a stylolites seam via automated mineral analysis (Heald 1955, Tada and Siever 1989). If it is assumed that in homogenous sandstone (unit 3 and 4), detrital clays and heavy minerals were originally evenly distributed, then zircon and titanium oxides were enriched between 6 and 35 times in stylolites as to adjacent host rock. The mechanism for this enrichment is via quartz dissolution and removal. Sample 6 and sample 13 have been analysed. Sample 13 has stylolite enrichment ratios of 6 and 8, whereas sample 6 has stylolite enrichment ratios of 35 and 22, for zircon and rutile, respectively. The enrichment factor is proportional to the thickness of the stylolites, suggesting that the accumulation of detrital material is as a result of quartz (and feldspar) dissolution. This implies that one to two orders of magnitude of quartz have been dissolved, when compared to the area of the image, to produce this enrichment of detrital minerals. This is equivalent to 50 to 70 mm of quartz lost vertically in sample 13 and 200 to 300 mm of quartz lost vertically in sample 6. In clay-rich sandstone, zircon and titanium oxides were enriched between 30 and 57 times, respectively, in stylolites as adjacent to host rock through quartz dissolution. Sample 18 has stylolite enrichment ratios of 54 and 33, whereas sample 23 has enrichment ratios of 30 and 57, for zircon and rutile, respectively. The discrepancy is thought to arise from probable authigenic anatase production, enriching TiO_2, or the non-uniform initial distribution of zircon and rutile.

7.4.4 Porosity and permeability evolution

Microstructural controls on diagenetic mineral assemblages have affected porosity, and consequently permeability, over time. Modern-day average 2-D porosity in undeformed quartz arenite was calculated to be 4.5% in medium-grained sandstone, 5.8% in fine-grained sandstone and 8.0% in sandstone with oil-residue. Average porosity calculations from point counting show a large discrepancy to CL porosity calculations, reflecting poor detrital to authigenic quartz calculations. Therefore, quantitative porosity determined in section of sample 5 (2763.70 m) is the best means of determining porosity reduction over time.

Three main porosity reduction events identified (authigenic quartz, kaolinite and siderite) were quantitatively investigated in fractured and undeformed regions where CL imaging and EBSD mapping were performed (Fig. 7.12). Only one fractured area was investigated due to the high

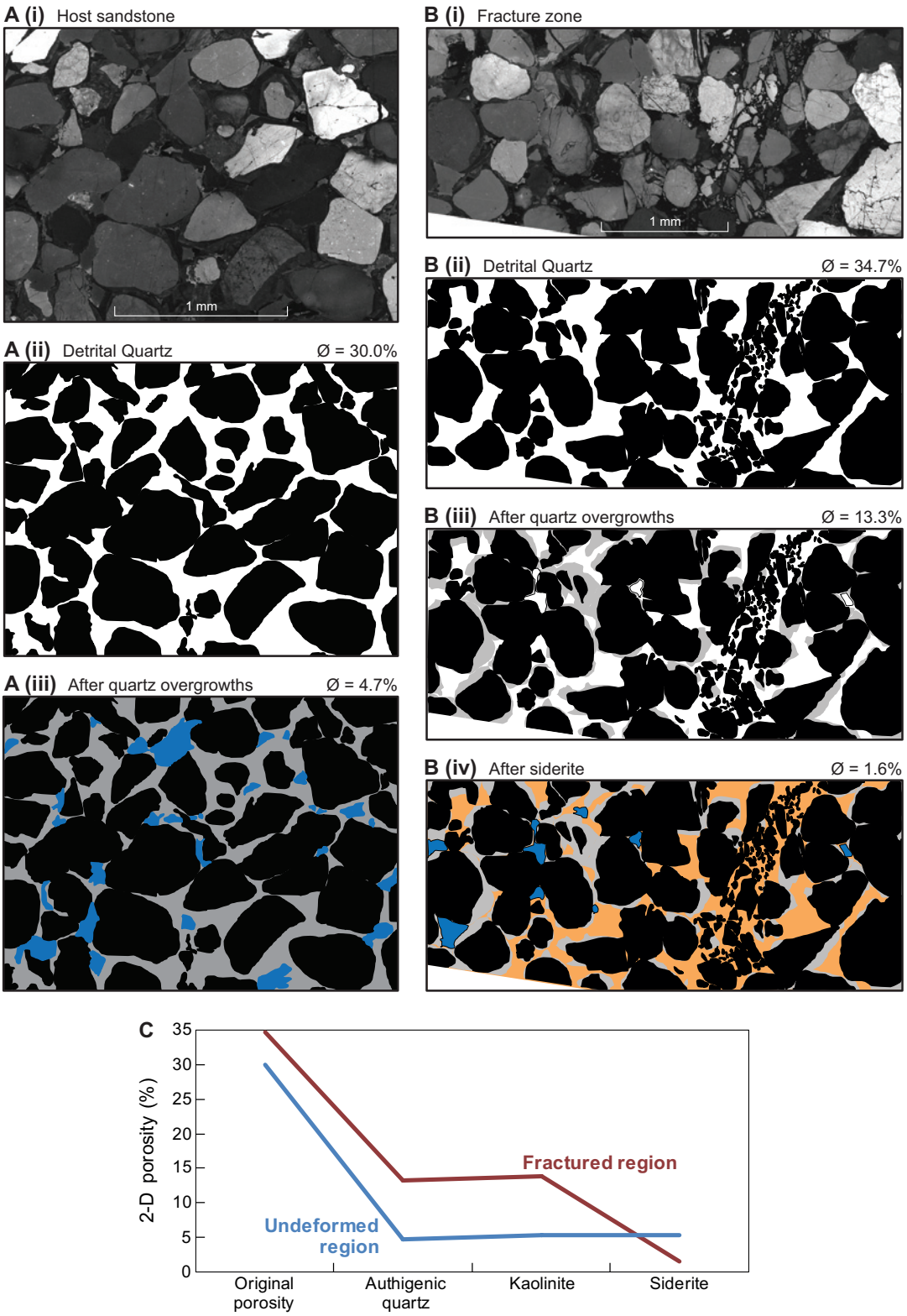

Figure 7.12: Quantitative porosity of (A) the host sandstone and (B) a brecciated fracture zone. Note that the breccia zone in B only formed between the quartz overgrowth and siderite phases, and hence is excluded in (i) to (iii). (C) Graph showing the porosity evolution of time for the undeformed (A) zone (blue) and the fractured (B) zone (red).

indexing of quartz and because siderite was indexed in only this area with EBSD. One undeformed region was analysed due to available time constraints. The area percentage of detrital quartz is calculated by tracing a CL image and calculating its fraction to the entire section. Kaolinite formation was analysed by calculating the porosity gained through feldspar dissolution from individual pores and subsequently extrapolated for the entire thin section. Feldspar dissolution produced kaolinite, which occupies a smaller volume and therefore kaolinite-occluded pore spaces reflect an increase in porosity.

Primary 2-D detrital quartz was 65.3% and 70.0% in fractured and undeformed medium-grained quartz arenite, implying a primary 2-D porosity of 34.7 and 30.0%, respectively. This estimate may be slightly high, because it assumes that all cement intruded into pore space, where it is likely that some of the authigenic quartz was initially detrital quartz. Authigenic quartz is thought to be locally sourced by diffusive mass transfer from detrital quartz and syntaxially re-precipitated during stylolitization and compaction, reduced porosity to 12.6% and 4.7% for the fractured and undeformed regions, respectively. This fraction of authigenic quartz would account for the detrital grain material lost. Nevertheless, pre-diagenetic porosity with tangential contacts would still be higher prior to the onset of diffusive mass transfer to relocate quartz cements, increase compaction and consequently reduce volume (Bathurst 1987, Mørk and Moen 2007, Renard et al. 2000).

The percentage area of kaolinite of two individual pore spaces (pseudo-feldspar habit) in sample 2 and sample was 81.4% and 83.7%, an average 82.6%. Assuming feldspar completely filled these pore spaces before dissolution to kaolinite, this suggests an average porosity increase of 17.4% in each partially-occluded pore space. Clay in undeformed samples varies between 2.2 and 6%, averaging 3.4%; sandstone absent from stylolites contains insignificant amounts of clay minerals relative to authigenic kaolinite. This means an average porosity increase of 0.4% to 1.1%, with an average increase of 0.6%. Siderite formation occurred after breccia fracture formation, reducing porosity in the fractured region from 13.9% to 1.6%. This clogged up any remaining primary and secondary porosity.

7.4.5 Hydrological properties of faults/fault zone structures in the present day Perth Basin

Fractures and stylolites in the damage zone of this major fault have shown to be sealed. Extensional cracks have been sealed by quartz precipitation, shear fractures locally preserve brecciation and are always filled with siderite cement, and stylolites are common and contain halos of quartz cementation. In each case, porosity was reduced to approximately 1%. Reduction of fracture porosity from about 10% to approximately 0% by pressure solution of quartz would take on the order of one month to seal 10 µm wide fractures, and 1000 years to seal 100 µm wide fractures (Gratier and Gueydan, 2007). However, the rate of sealing is modelled to decay exponentially with time (Gratier and Gueydan, 2007). The host rock consists of fine to medium sandstone dominated by quartz grains, which probably had good aquifer/reservoir properties prior to faulting (Fig. 7.12). However, dissolved SiO_2 material from faulting-related stylolitzation has been re-precipitated in the remaining pore space of the surrounding rock volume, significantly reducing porosity. Where coeval stylolites and factures intersect, 'crack seal systems' were established that completely compartmentalize the reservoir on

a fine scale, effectively reducing the finite permeability to almost zero. Using porosity-permeability relationships for sandstones, a porosity of 1% would equal a permeability of << 0.01 mD. Finally, fluids that migrated through faults active during the Mesozoic also precipitated exotic authigenic cements (e.g., siderite, and event pyrite) along transmissive shear fractures shortly after their formation. In summary, sealing of faults may have developed over a broad range of timescales from several days (self-healing of fractures) to a thousand years (pressure solution sealing of SiO_2). Given the interconnected structures observed in the core are likely to form a dense 3-D network (steeply dipping fractures and shallowly dipping stylolites), the bulk permeability of the damage zone would reflect the permeability of the fractures and stylolites. Therefore, it is highly likely that 'fossil' (i.e., inactive) faults have impermeable fault cores and an interlocking network of impermeable structures in their damage zones, irrespective of their orientation to the present day stress field. In summary, most, if not all of the Mesozoic faults in rocks of similar mineralogy and grain size in the northern Perth Basin would be sealing.

7.4.6 Goals for future research

- Further studies into Centella-1 and Mondarra-4 to measure the porosity and permeability in order to assess the lateral variation in fault damage zone permeability.
- Apply the fault permeability findings to wells of similar lithology and burial history to different scales and depths in the north Perth Basin, to assess the locations of permeability baffles and conduits.
- Test this approach to wells within the central Perth Basin areas to assess their geothermal potential.
- Recent mineralogical studies show that the Jurassic stratigraphic units in the central Perth Basin (e.g., Lesueur Sandstone, Cattamarra Coal Measures and Yarragadee Formation) have significantly more modal proportions of feldspar, mica and clay minerals than the Dongara Sandstone in Apium-1 (Sections 4 and 5 of this report). The effects of these differences in mineralogy to the damage response during faulting – particularly stylolite development – remain to be tested.

7.5 Summary

Faults and their associated damage zones in sedimentary basins can be sealing, impeding fluid flow and creating permeability barriers, or open, creating permeable fluid pathways. This impacts the aquifer/reservoir potential of rocks in fault damage zones. Stylolitization and fracturing severely impacted permeability through compartmentalization and cementation of Apium-1, an exploration hole drilled in the northern Perth Basin, Western Australia. Drill core samples (from Apium-1 well) situated 1 km into the hangingwall block damage zone of a major NNW-trending normal fault were qualitatively and quantitatively characterized via sedimentary and structural logging, and microstructural and porosity analysis. Apium-1 core consists of fine to medium grained quartz arenite (Dongara Sandstone) that is overlain by a coarse-grained lag and capped by impermeable shale (Kockatea Shale).

Fractures and stylolites in the damage zone of this major fault have shown to be sealed. Extensional cracks have been sealed by quartz precipitation; shear fractures locally preserve brecciation and are always filled with siderite cement; stylolites are common and contain halos of quartz cementation. In each case, porosity was reduced to approximately 1%, equalling a permeability of <<0.01 mD. The host rock consists of fine to medium sandstone, which probably had good aquifer/reservoir properties prior to faulting. Given the interconnected structures observed in the core are likely to form a dense 3-D network (steeply dipping fractures and shallowly dipping stylolites), the bulk permeability of the damage zone would reflect the permeability of the fractures and stylolites. Furthermore, faults striking north to north-west are in a favourable orientation for re-activation in the present day stress field, suggesting that there would be even less chance for dilatant fractures. In summary, most, if not all of the Mesozoic faults in the northern Perth Basin would be sealing.

8. QUANTIFICATION OF MAGNITUDE AND LENGTH SCALE VARIATION OF HEAT PRODUCTION FROM THE BASEMENT ROCKS OF THE PERTH BASIN

8.1 Introduction

The Perth Basin covers an area of around 4000 km^2, and is comprised of up to 12 km thickness of Phanerozoic sedimentary rocks. A significant proportion of these units have relatively high permeabilities and form good aquifers (Davidson, 1995). There is, therefore, significant potential for HSA (Hot Sedimentary Aquifer) geothermal energy extraction in the Perth Basin.

Successful prediction of the geothermal potential of the Perth Basin requires knowledge of a wide variety of parameters; the parameter of interest for this study is the heat production potential of the crystalline basement to the Perth Basin. If the basement is rich in heat-producing elements such as U, Th and K then the basement will provide enhanced heat flow to the overlying sediments, which will increase the viability of geothermal energy applications.

In addition to the magnitude of the heat producing capacity, it is necessary to determine the spatial variation of this parameter. Natural variations occur as a function of changes in rock type, both laterally and vertically, and the magnitude and typical length scale of these variations will determine if the geothermal potential of the Perth Basin is evenly distributed, or varies only on short length scales (less than tens of metres). If this is the case then locations for drilling are likely to be determined by factors such as site accessibility and the geology of the Perth Basin sediments. If, on the other hand, heat production varies significantly on length scales large enough to influence fluid temperature (tens of kilometers upwards), then it is worth focusing effort into location of hot spots, and further investigation of the Perth Basin geology.

Unfortunately, the basement to the Perth Basin is largely inaccessible because of the thick sedimentary cover, and there have been relatively few measurements of the heat production of the basement. The purpose of this study is to combine new and existing measurements of heat production from the Perth Basin, and from rocks deemed to be equivalent that are exposed elsewhere. The data compilation is then used to investigate the likely distribution of heat production in the Perth Basin basement, and to estimate the probable dominant length scale and magnitude of variation. This information can then be used to develop stochastic models of heat production that can be used to constrain models of heat flow in the Perth Basin.

8.2 Geological Background

The Perth Basin sedimentary sequence overlies crystalline basement that is thought to form part of the Pinjarra orogen (Fitzsimons, 2002). The Pinjarra orogen lies at the current western margin of the Yilgarn Craton, and is at least 1500 km long. The orogen, in Australia, is bounded by the Darling Fault to the east, and by the ocean to the west, and is thought to extend along the whole length of the western continental margin (Fig. 8.1).

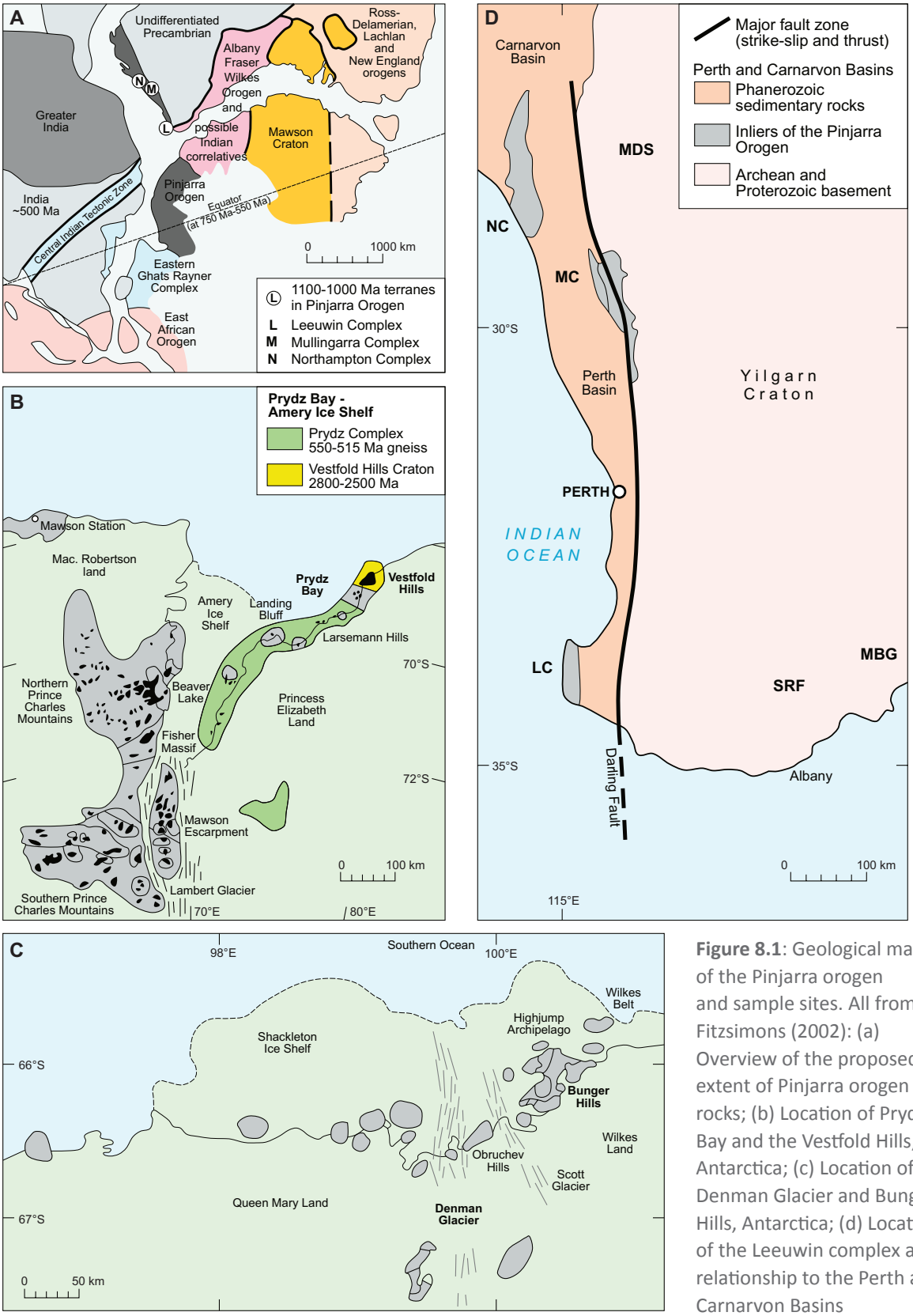

Figure 8.1: Geological map of the Pinjarra orogen and sample sites. All from Fitzsimons (2002): (a) Overview of the proposed extent of Pinjarra orogen rocks; (b) Location of Prydz Bay and the Vestfold Hills, Antarctica; (c) Location of the Denman Glacier and Bunger Hills, Antarctica; (d) Location of the Leeuwin complex and relationship to the Perth and Carnarvon Basins

The Pinjarra orogen is a N-S-trending tectonic boundary that records deformation, magmatism at 1080 and 750 to 500 Ma (Fitzsimons, 2002; Myers, 1990). The Darling Fault, at the western margin is, most recently, a Phanerozoic structure with a record of normal displacement during Gondwana breakup.

Exposure of the orogen is poor, however, and outcrops are found only in the Northampton and Mullingara complexes. The Leeuwin complex has rocks that have been produced and metamorphosed at similar ages to those included in the Pinjarra orogen, but the precise relationship of this block to the Pinjarra orogen is controversial (e.g. Wilde, 1999).

It has been proposed that the Pinjarra orogen extends into Antarctica (Fig. 8.1; Fitzsimons, 2002; Boger, 2011), and is exposed in the region of the Denman Glacier. It has also been proposed that rocks in the Prydz Bay area, the Vestfold Hills and the Bunger Hills may form part of the orogen (Fitzsimons, 2002; Boger, 2011), but poor exposure of the regions between these areas of outcrop preclude definitive attribution of areas such as the Vestfold and Bunger Hills to the Pinjarra orogen. Antarctic evidence suggests that the Pinjarra orogen was a major orogen that divides East Gondwana in two, and may record either Mesoproterozoic collision (1080 Ma) followed by intracratonic reactivation in the Neoproterozoic, or a major Neoproterozoic suture that incorporates Mesoproterozoic terranes.

The Northampton and Mullingara complexes are mostly composed of psammitic paragneisses, with subordinate conformable lenses of pelite, quartzitic and mafic gneisses (Myers, 1990). The Leeuwin complex is different in that the most common rock type is felsic orthogneiss, with mafic, intermediate, and anorthositic units (Fig 8.2; Myers, 1990; Wilde and Murphy, 1990; Collins, 2009).

Variably deformed felsic plutonic rocks are the most common rock type in the Denman Glacier area. These are associated with lesser quantities of hornblende-biotite orthogneisses, and psammitic and pelitic gneisses. The Prydz bay region comprises interleaved ortho- and paragneisses which have been metamorphosed at granulite facies and intruded by Neoproterozic granites. The Vestfold Hills, which lie within the greater Prydz Bay region, contain much older Archean cratonic rocks (2800 – 2500 Ma), and include tonalitic and monzonitic gneisses, plus younger basic intrusions. The Bunger Hills contains Archean – Palaeoproterozoic crust that was reworked by both the Albany-Fraser and Pinjarra orogens. The basement in this area is granulite-facies tonalitic to granitic orthogneisses, plus layered psammitic and pelitic paragneisses. This basement has been intruded by gabbroic to granitic plutons (Fitzsimons, 2002).

Only a small number of rocks from the basement to the Perth region have been described (HDR, 2008). The rock types noted are garnet- and sillimanite-bearing paragneisses, granites, and quartzites (Fletcher and Libby, 1993).

The variety of rocks exposed in known and proposed areas of the Pinjarra orogen suggest that the heat production of this basement is highly variable. Archean and Palaeoproterozoic fragments in the Bunger and Vestfold Hills would have relatively low heat producing capacity, while regions of felsic paragneisses, such as those in the Northampton and Leeuwin complexes would be expected to have heat production similar to that of the upper crust today.

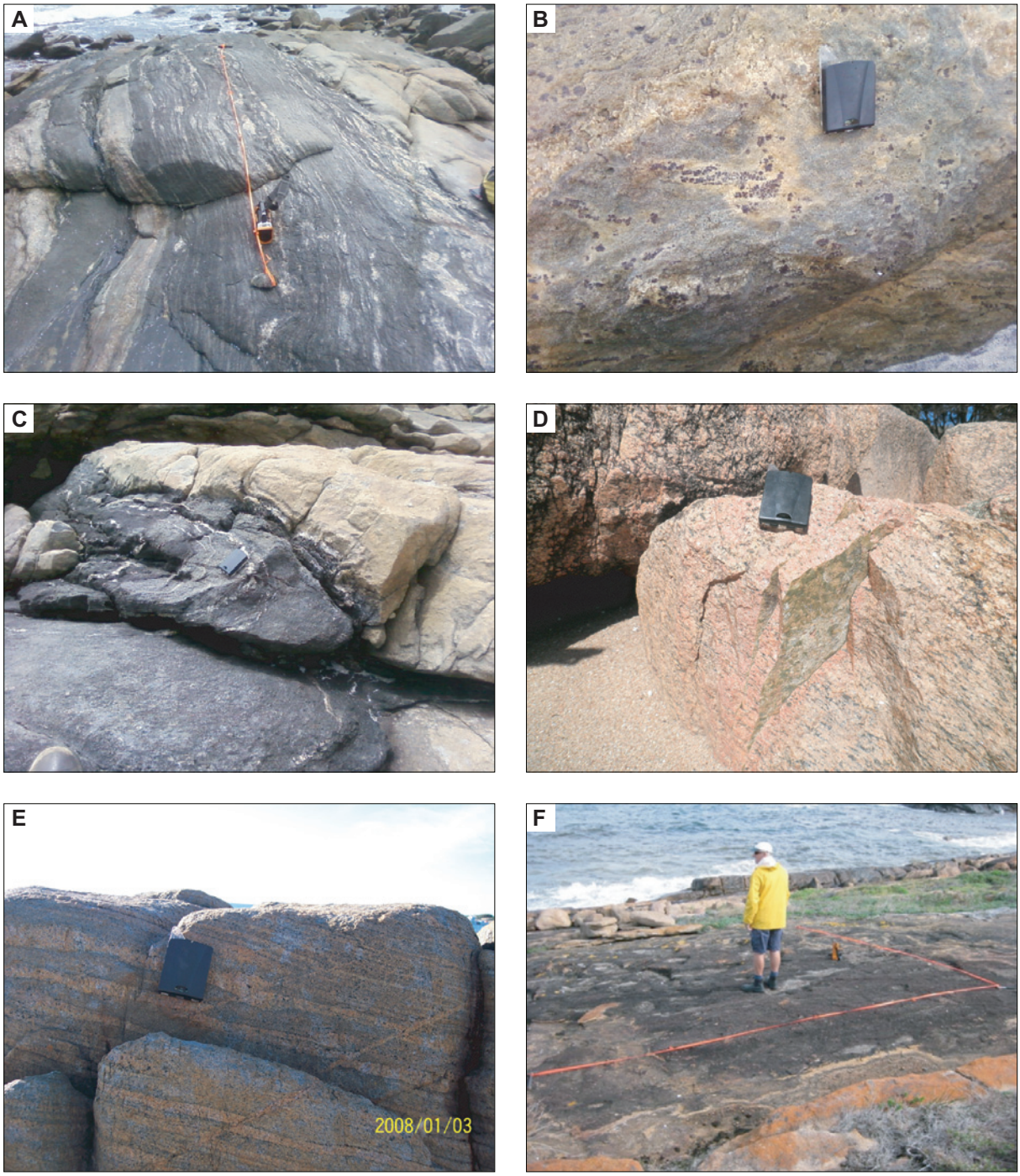

Figure 8.2: Rocks of the Leeuwin complex: (a) interlayered mafic and intermediate rocks at Skippy Rock, SW Australia; (b) garnet-bearing felsic gneiss at Skippy Rock, SW Australia; (c) folded mafic and felsic gneisses at Skippy Rock, SW Australia; (d) ksp-porphyritic granite, Bunker Bay, SW Australia; (e) layered ksp-rich and dioritic gneisses at Sugarloaf rock, SW Australia; (f) typical sample layout for GRS analysis on the Leeuwin anorthosite complex near Augusta, SW Australia.

8.3 Methods

Literature data was collected, where available, for the Mullingara, Northampton, Leeuwin complexes, the Perth region, and the proposed areas of Pinjarra orogen in Antarctica. Data is relatively sparse for these areas, particularly the Northampton and Mullingara complexes. Data for the Antarctic exposures was obtained from the Geoscience Australia database, filtered by latitude, longitude and locality.

New data was collected from the Leeuwin complex. Fieldwork was undertaken using a RS-125 super spec gamma ray spectrometer (GRS) from Radiation Solutions INC (Fig. 8.2f). This device uses a 6.3 cubic inch sodium iodine detector and a 1024 channel spectrometer to detect gamma ray emitting elements and gives their abundance in a sample. It has a detection range of 3 foot (~92 cm) radially from the detector (Radiation Solutions, 2009). The detector was normalized to the background at each new location before the actual measurements to remove the effects of background radiation.

Measurements were taken on outcrops of Proterozoic basement. Nine measurements were taken at each locality to ensure a representative result was obtained at each location. This strategy was employed in order to gain information on spatial variability of heat production at relatively short length scales; the heat-producing elements U and Th are expected to be heterogeneously distributed because they generally occur in accessory minerals which may not be spread homogenously throughout the outcrop.

The criteria used to select measurement localities were that the top surface of the outcrop should be relatively flat, and big enough to accommodate 9 measurements including the ~1 metre buffers to account for the measurement volume. Care was also taken to ensure that there were no holes underneath the outcrops or that they were at least ~1 metre thick.

The nine measurements were arranged, where possible, in an L configuration with five and four measurements taken on each arm. The GPS position was taken at the ends of each line segment (Fig. 8.2f). The average and standard deviation of the concentrations of the three main heat producing elements, K, U and Th, were calculated for each outcrop, and these data were used to calculate the heat production in $\mu W\ m^{-3}$, assuming a density of 2800 $kg\ m^{-3}$.

Rock samples were also gathered at selected localities but, due to the flat nature of the outcrops suitable for measurement, it was often necessary to travel up to 30 m from the GRS site to find an in-situ site where a sample could be taken. Twenty rock samples were collected, and these were subjected to bulk composition analysis. The crushed sample was fused with lithium tetraborate to form glass discs, which were then analysed by a combination of ICP-OES (Inductively Coupled Plasma Optical Emission Spectrometry), for the major elements and ICP-MS (Inductively Coupled Plasma Mass Spectrometry) for rare earth elements and for trace elements such as U and Th. Analysis was undertaken by Intertek-Genalysis commercial laboratories in Perth. Repeat analysis of selected samples and of known secondary standards indicated that accuracy and precision of the analysis was satisfactory.

The mineral hosts for U, Th and K in the Leeuwin sample rocks were determined using a combination

of optical microscopy and scanning electron microscopy. Data was collected using the Zeiss Evo scanning electron microscope at the Centre for Materials Research at Curtin University. The analysis was completed with an accelerating voltage of 20 kV, a working distance of between 8 and 9 mm. The contrast was increased and brightness decreased to reveal likely minerals containing heat-producing elements, as U and Th have a high atomic number and thus appear bright in the SEM image with these settings. Element-specific mapping using the EDS system was also used to locate mineral phases that contain uranium and thorium.

Analyses by GRS and ICP were compared to allow validation of the GRS technique. Hand-held field equipment provides a valuable means to obtain large amounts of information quickly in the field, but it is necessary to evaluate the accuracy and precision of this data if it is to be combined with data obtained using other sources. The spatial variability of the distribution of heat producing elements was determined on the outcrop scale, by examination of the standard deviation of the nine measurements taken for each outcrop. Histograms were used to assess variability on the 10 – 100 km, and orogen length scales, and to examine the differences in distribution of heat producing elements as a function of rock type. Heat production was plotted as a function of longitude and latitude to determine any systematic spatial variation in its distribution, and probability plots were constructed to allow the best estimate of heat production for the areas examined to be determined.

8.4 Results

8.4.1 Leeuwin Complex: Comparison of laboratory analyses with GRS results

GRS results correlate well with laboratory analyses for K, but the data is more scattered for U and Th (Fig. 8.3). Some degree of scatter is expected, because the samples are not taken from sites identical to those sampled with the GRS, so it is useful to compare the extent of scatter with the standard deviation for measurements from single outcrops (Fig. 8.4). The mode of the standard deviation for K is about 10%, relatively, while standard deviations for U and Th are around 50 and 20% relative, respectively. The larger scatters for U and Th are expected given the low concentrations of these elements and the likely heterogeneous distribution of these elements within the rock.

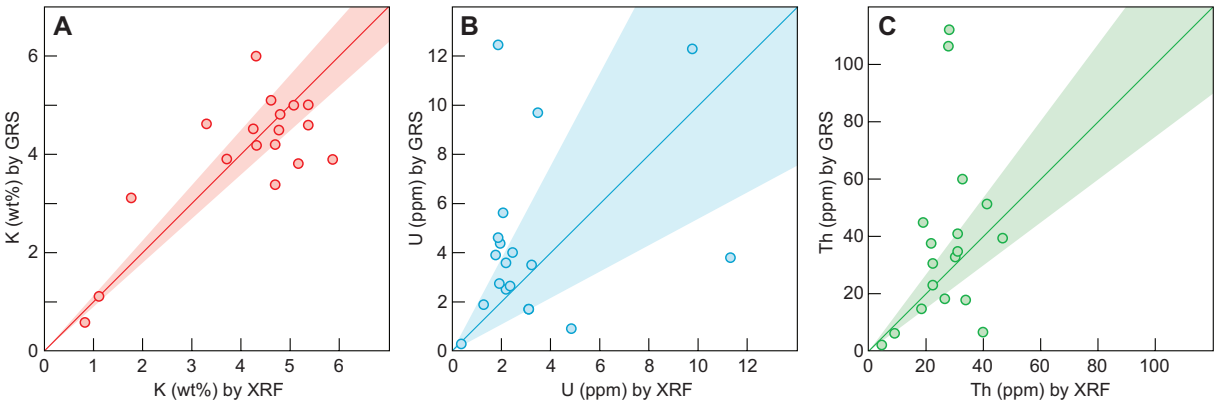

Figure 8.3: Comparison of element concentrations measured by hand held gamma ray spectrometer and by ICP-MS. Shaded region indicates estimate of spatial variation (1 sd) at each outcrop based on 9 measurements: (a) potassium; (b) uranium; (c) thorium.

If variation within an outcrop is taken to account then the bulk of measurements lie within the expected region. However, the GRS may systematically overestimate U and Th contents, since more samples lie above the line of GRS = ICP-MS than below it for both these elements, although the number of samples that lies outside the expected envelope above and below the line is similar. In the case of U, there are two cases where the GRS appears to significantly overestimate the Th concentration but it is difficult to determine if this is due to real heterogeneity or a systematic analytical issue with the GRS.

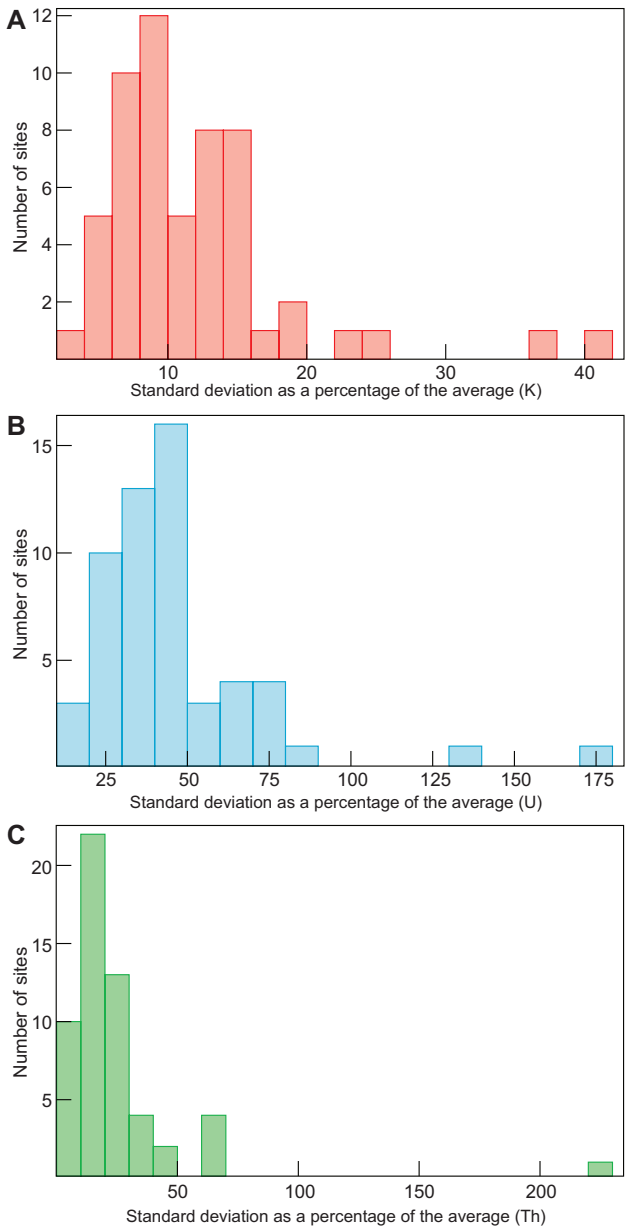

Figure 8.4: Histograms of the variation in GRS measurements from the 9 data points taken at each outcrop: (a) potassium; (b) uranium; (c) thorium.

8.4.2 All samples: heat production

The mean heat production for all 678 samples is 1.7 ± 2.56 µW m^{-3} (1 standard deviation), which is somewhat lower than an estimate of the crustal average of 1.9 ± 1.4 µW m^{-3} (Beardsmore and Cull, 2001), or the average for granitic rocks of 2.82 ± 1.03 µW m^{-3} (Beardsmore and Cull, 2001). These low values are heavily influenced by large numbers of samples from the Archean Bunger Hills and Vestfold Hills areas, with values of 1.3 ± 2.75 µW m^{-3} (246 samples) and 0.69 ± 0.77 µW m^{-3} (277 samples) respectively (Fig. 8.5). Samples from the Perth region are most similar to those from the Prydz Bay area; the 13 samples from the Perth region have a value of 2.38 ± 3.04 µW m^{-3}, while the Prydz Bay samples give 2.56 ± 2.55 µW m^{-3} (30 samples). This does not imply that the two regions come from the same original terrain, though this is not impossible. However, it is more likely that the similar values arise from common genetic processes that occurred at different times and in different places,

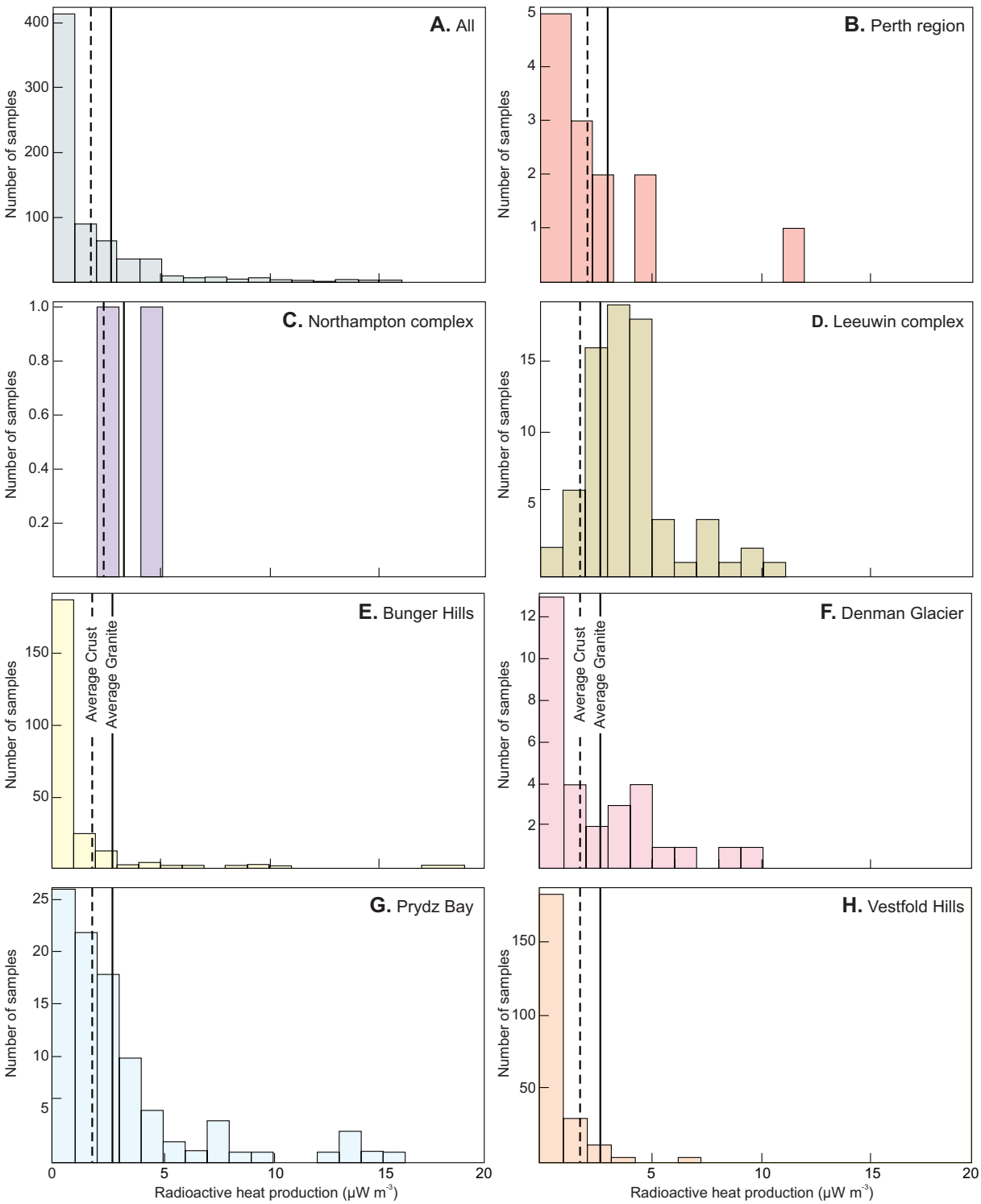

Figure 8.5: Histograms of the calculated heat production for the seven regions studied and for the whole sample set: (a) all samples; (b) Perth region; (c) Northampton complex; (d) Leeuwin complex; (e) Bunger Hills; (f) Denman Glacier; (g) Prydz Bay; (h) Vestfold Hills. Average crust and average granite values are from Beardsmore and Cull (2001).

rather than a close spatial relationship at some point in time. Heat production in the Perth basin basement and Prydz Bay fall between those for the crustal average and the average for granitic rocks. Samples from the Denman Glacier, the Northampton complex and the Leeuwin complex all have heat production values that are higher than the granite average, although the low number of samples (2) for the Northampton complex precludes any reliable determination of the average heat production.

If the analyses are divided into mafic and felsic rock types (Fig. 8.6) then it can be seen that the felsic rocks have distinctly higher heat production than the mafic rocks, and that the number of mafic rocks sampled is much greater than the number of felsic rocks sampled, in spite of descriptions of the various areas which suggest that felsic rocks are more common.

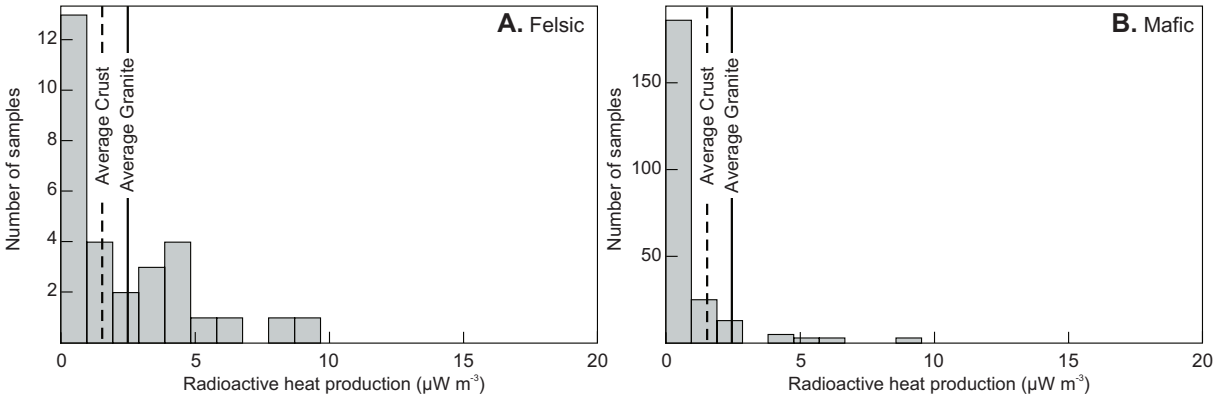

Figure 8.6: Histograms of calculated heat production split by rock type: (a) felsic; (b) mafic.

There was no systematic variation of heat production with longitude or latitude (Fig. 8.7), either within Australia, Antarctica, or where data for the two continents was combined, although the Australian samples cluster at slightly higher heat production values, because of the lack of low heat production Archean craton material. There is no significant difference between heat production in the Perth region, the Northampton complex and the Leeuwin complex.

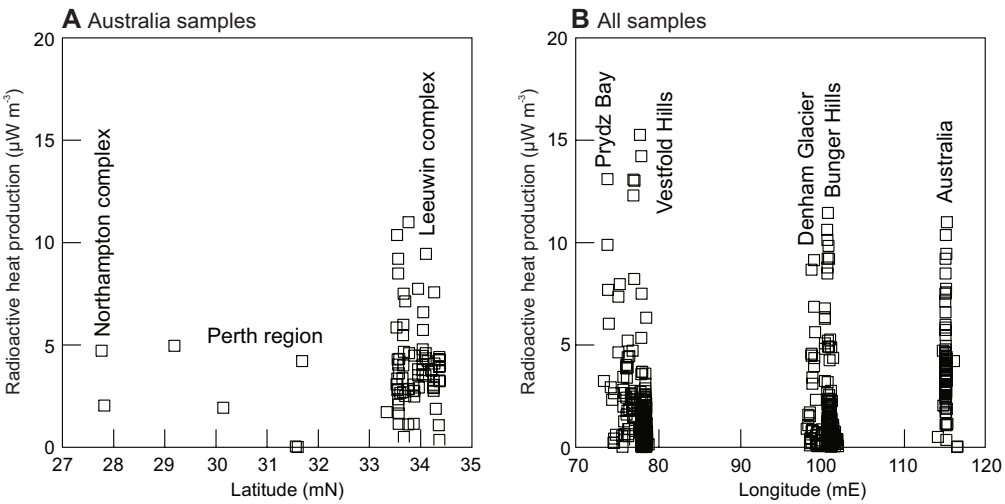

Figure 8.7: Calculated heat production plotted against longitude and latitude: (a) Australian samples only; (b) all samples.

Cumulative frequency plots (Fig. 8.8) reveal that the Perth region and Prydz Bay regions have a similar distribution of heat production, with a steep climb in heat production above the 50th percentile, although the Perth region plot is less well defined because of the low number of samples. The Leeuwin complex samples have a distinctly different frequency plot, with a much more consistent gradient, and less of an "S" shape to the frequency plot, as does the Denman Glacier. This grouping reflects that of the overall heat production, with the Perth region and Prydz Bay regions having similar heat production, and the Leeuwin complex and Denman Glacier region having higher heat production (>3 µW m^{-3}).

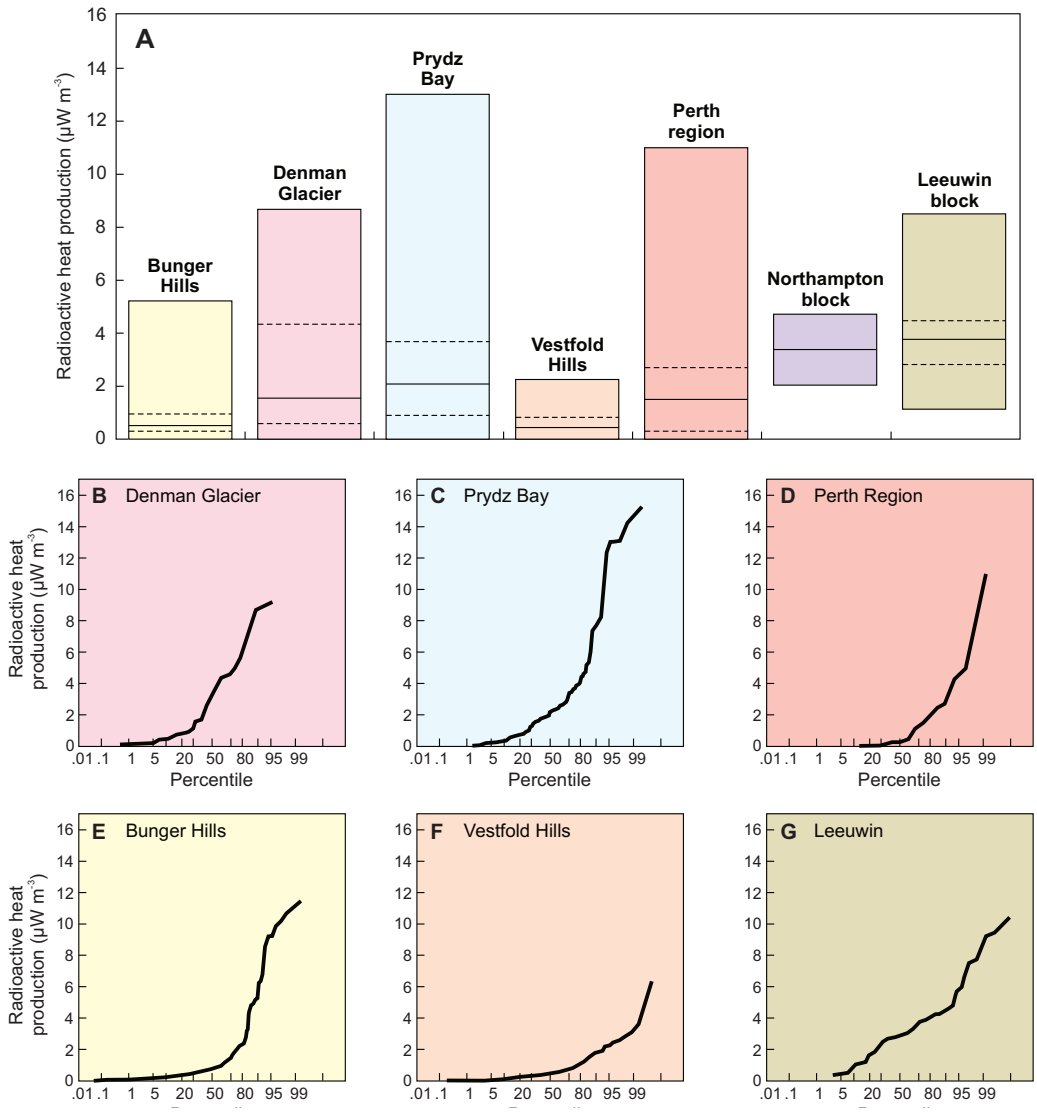

Figure 8.8: Box plots and frequency plots of heat production from the different regions considered. (a) Box plot comparing all regions; the thick line in each box is the median value, the dashed lines are the 1st and 3rd quartiles, and the end of the boxes are the 5th and 95th percentiles. Cumulative frequency plots for (b) the Denman Glacier; (c) the Prydz Bay region; (d) the Perth region; (e) the Bunger Hills; (f) the Vestfold Hills; (g) the Leeuwin complex.

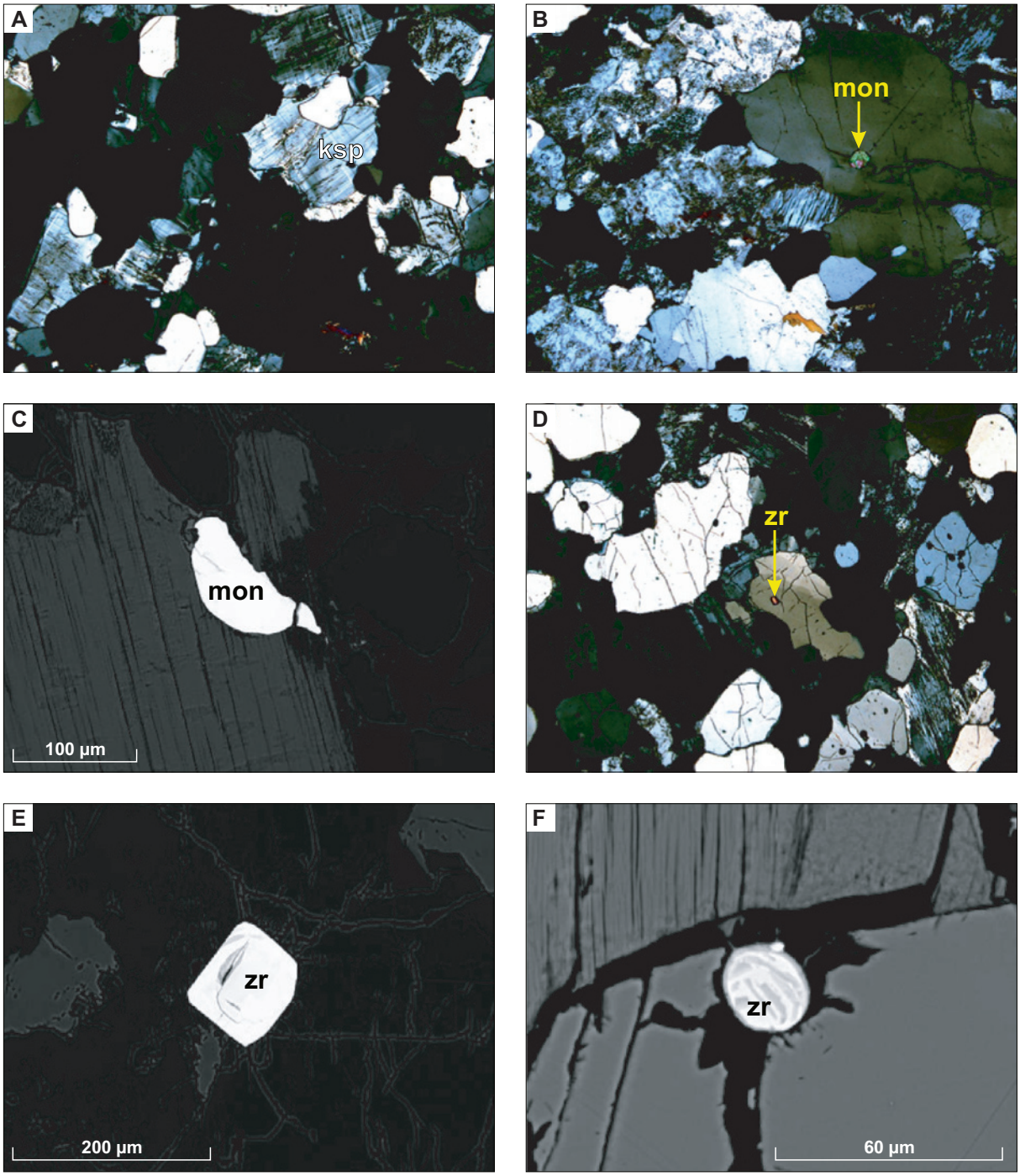

Figure 8.9: Mineral hosts for heat producing elements in Leeuwin complex samples. (a) photomicrograph of perthitic, alkali feldspar and microcline in sample CNCL-1205-09, FOV is 23mm, XP; (b) photomicrograph of monazite hosted in quartz in sample CNCL-1905-20, FOV is 23mm, XP; (c) Back scattered SEM image of monazite on margin of a mica grain in sample CNCL-1305-11; (d) photomicrograph of equant zircon included in quartz in sample CNCL-1105-07, FOV is 23mm, XP; (e) Back scattered SEM image of equant zircon in sample CNCL-1305-11; (f) Back scattered SEM image of rounded zircon with magmatic zoning in sample CNCL-1005-05.

8.4.3 Mineral Hosts

Mineral hosts to the heat producing elements are typical of those in high grade gneissic terranes (Fig. 8.9). K is hosted by k-feldspar (Fig. 8.9a), biotite and muscovite. U is hosted by zircon, and Th is hosted by monazite (Fig. 8.9b, c) and xenotime. There is considerable variation in zircon morphology; equant, cubic grains (Fig. 8.9d, e) and rounded magmatically zoned grains (Fig. 8.9f) were observed.

8.5 Discussion

8.5.1 Comparability of GRS and ICP data

K concentrations compare well between GRS and ICP methods. The means of the two datasets are well within error of each other, the t-test probability that the means of the two sample sets are the same is 88%, and the correlation coefficient is 0.83, which is significant at the $P<0.0005$ level.

U and Th correlations compare less well. The mean of the GRS dataset is higher for both U and Th than for the ICP dataset, although the values are within a single standard deviation of each other for both elements so the overestimation is not necessarily systematic. The t-test for U and Th is 24 and 19% respectively, which is too low to state convincingly that the two data sets are the same, but also too high to reject the hypothesis that they are different. The correlation coefficient for both U and Th is 0.36, which is slightly lower than that required for a $P<0.05$ probability of correlation, which requires a correlation coefficient of 0.39. These data suggest that either the GRS does not measure U and Th very accurately, or that the spatial variation within an outcrop is sufficiently large to destroy the correlation and provide difficulties with representative sampling.

To distinguish between these possibilities, the average standard deviation of the 9 GRS analyses for each outcrop was used to place uncertainty bounds on Fig. 8.3. If the variation observed is due only to the natural variability rather than to a systematic error then we would expect to see about a third of the samples plotting outside the shaded area, and indeed the proportion plotting outside is about a third, so the GRS method is likely to be acceptable. However, the small number of very high Th values is a concern so further work may be necessary to test the comparability of the two methods.

8.5.2 An analogue for the Perth Basin Basement?

Determination of the probable heat production of the Perth Basin basement requires assessment of the degree to which the various datasets utilized here are likely to represent that below the Perth Basin.

Datasets from the low heat production Archean craton material in the Bunger and Vestfold Hills seem unlikely to represent the Perth Basin basement, as the small existing dataset (13 samples) from the Perth basin basement has quite different rock types, in that there is a lack of monzonitic and tonalitic material, and the average heat production is much higher than that from the Bunger and Vestfold hills.

The dataset from the Leeuwin, which has relatively high heat production is on average higher, the central 50% of its data distribution does not overlap with that of the Perth basin basement (Fig. 8.8a), and it has quite a different distribution to that of the small dataset for the Perth region on a cumulative probability plot (compare Figs 8.8b and c). The high heat production samples in the Leeuwin come from outcrops dated as Neoproterozoic (~650 – 750 Ma; Collins, 2009). These rocks have the geochemical signature of A-type granites (Fitzsimons, 2000), and may be related to accretion of the Northampton and Mullingarra complexes to the Yilgarn craton, and, in this case, may not be spatially as widespread as older Mesoproterozoic rocks which may underlie the Perth Basin. It may, therefore, be unwise to use the Leeuwin complex as a model for the Perth Basin basement.

The Northampton complex dataset is too small to assess in any meaningful way. The Denman Glacier and Prydz Bay datasets, show similar averages to the small Perth Basin dataset and the Prydz Bay dataset shows a similar cumulative frequency curve. It therefore seems likely that these datasets are the most likely to provide a plausible analogue for the Perth Basin basement. This proposal is consistent with the similarity of T_{DM} Nd model ages for the Denman Glacier to those from granitic Perth Basin basement (2200 Ma – 2000 Ma; Fletcher et al., 1985; Fletcher and Libby 1993).

8.5.3 Typical Length Scale of Variation

A simple exercise was undertaken to investigate the typical length scale of variation. For the dataset of interest, a list of all pairwise permutations of sample numbers was generated. For each pair of samples, the distance between the samples, and the difference in heat production (ΔHP) between the samples was calculated to produce a dataset in which each data point was a pair of {distance, ΔHP} values. This dataset was then sorted and averaged to give an estimate of the distribution of heat production variation for length scales of 10 m to 10 000 km (Fig. 8.10).

With this type of plot, low values of ΔHP are expected if the area under investigation is homogenous on that length scale considered, whereas high values would be expected if the area is highly heterogeneous on the length scale of interest. Low values may result due to large continuous areas with similar heat production or to repetition on the length scale of interest.

Results indicate that ΔHP generally increases with length scale, with two exceptions, which will be discussed below. Significant jumps in ΔHP are observed on length scales of 1 – 100 km for most datasets investigated (Fig. 8.10a, c, d), which suggests that variation in ΔHP, like geological variation is on this length scale. Under these circumstances it is probably worth seeking high heat producing areas of basement, if calculations show that the additional heat influx could provide higher temperature geological fluids.

Drops in ΔHP with increasing length scale are observed for the Prydz Bay and Denman Glacier datasets. The reason for this is not fully understood, but could reflect either: (1) an anomalous increase at the length scale immediately preceding the drop. This could reflect short scale variation due to features such as dykes; or (2) a decrease in variation due to repetition of features at the length scale of interest. Explanation (1) seems most likely given the heterogeneity and natural variability of geological datasets.

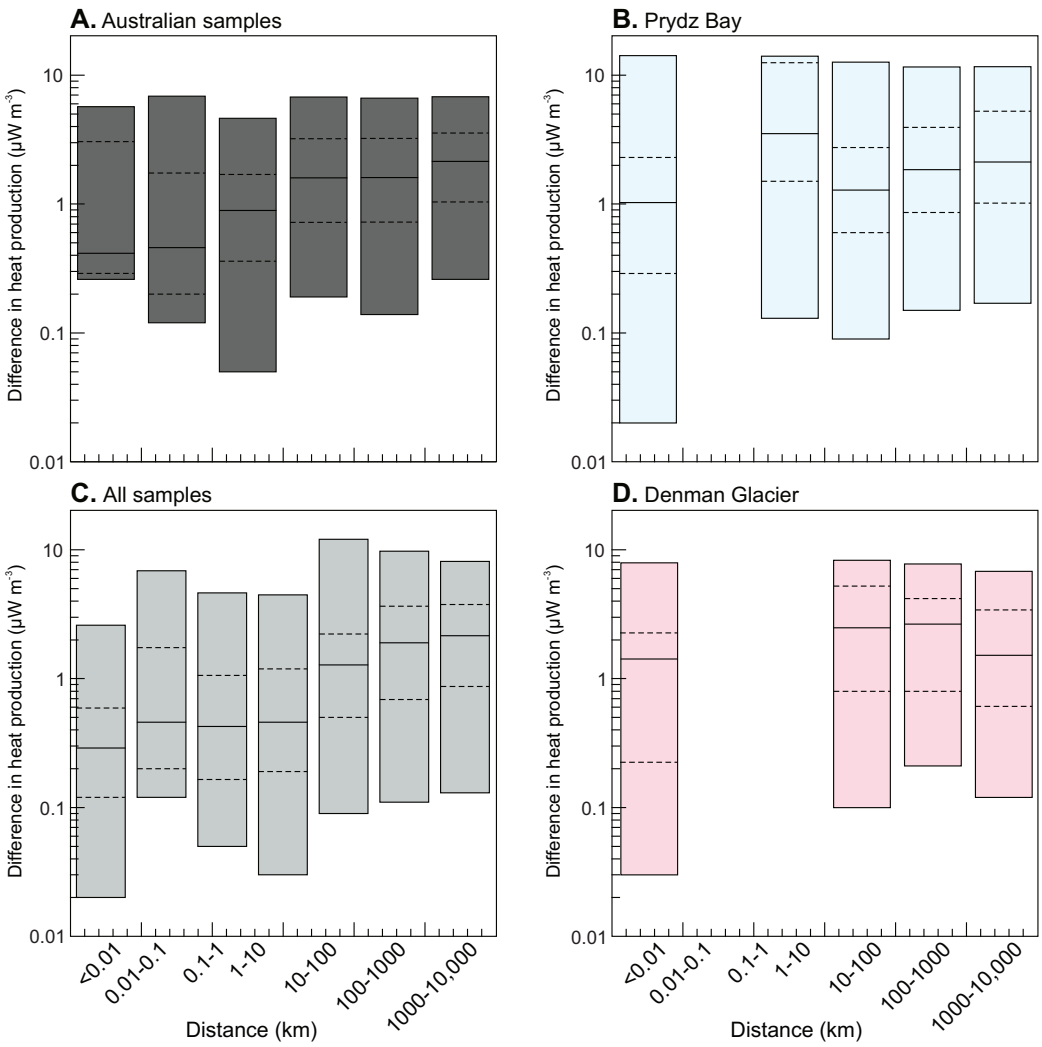

Figure 8.10: Box plots to represent variation in heat producing capacity at the different length scales studied. the thick line in each box is the median value, the dashed lines are the 1st and 3rd quartiles, and the end of the boxes are the 5th and 95th percentiles. (a) Australian samples; (b) Prydz Bay samples; (c) All samples; (d) Denman Glacier samples.

8.5.4 Stochastic models for heat distribution

A preliminary investigation of the predicted heat flow contribution from the Perth Basin basement assuming that the heat production was distributed identically to that at Prydz Bay, and decreased exponentially with depth to 0.8 µW m^{-3}, a plausible value for the lithospheric mantle. The expression for the decrease is

$$HFS = HP_s e^{\frac{1}{30000} Ln\left(\frac{0.8}{HP_s}\right) z} \qquad [1]$$

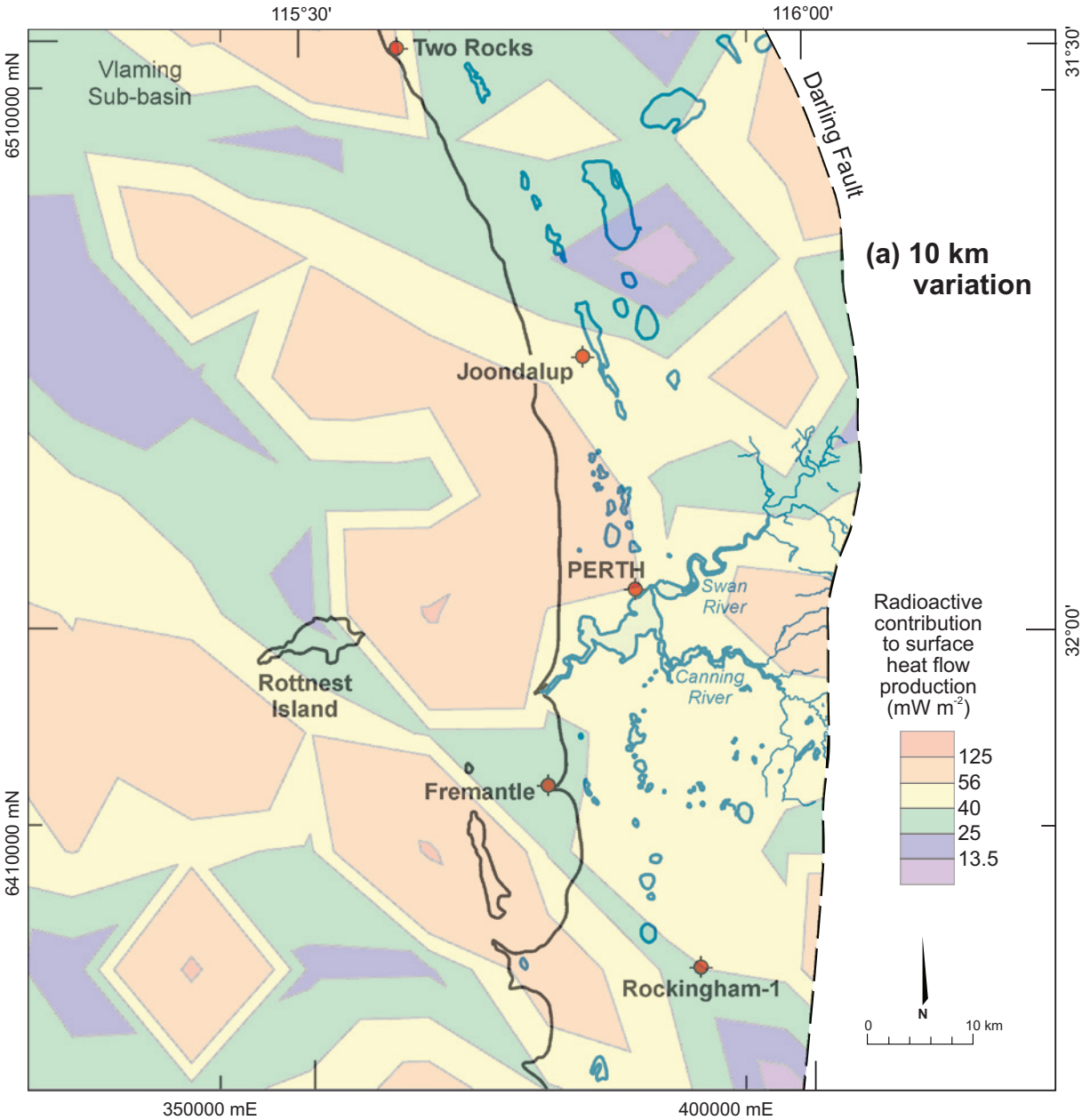

Figure 8.11: Stochastic simulations of the possible heat production from the Perth Basin basement for (a) 10 km characteristic length scale variation and (b) 1 km characteristic length scale variation.

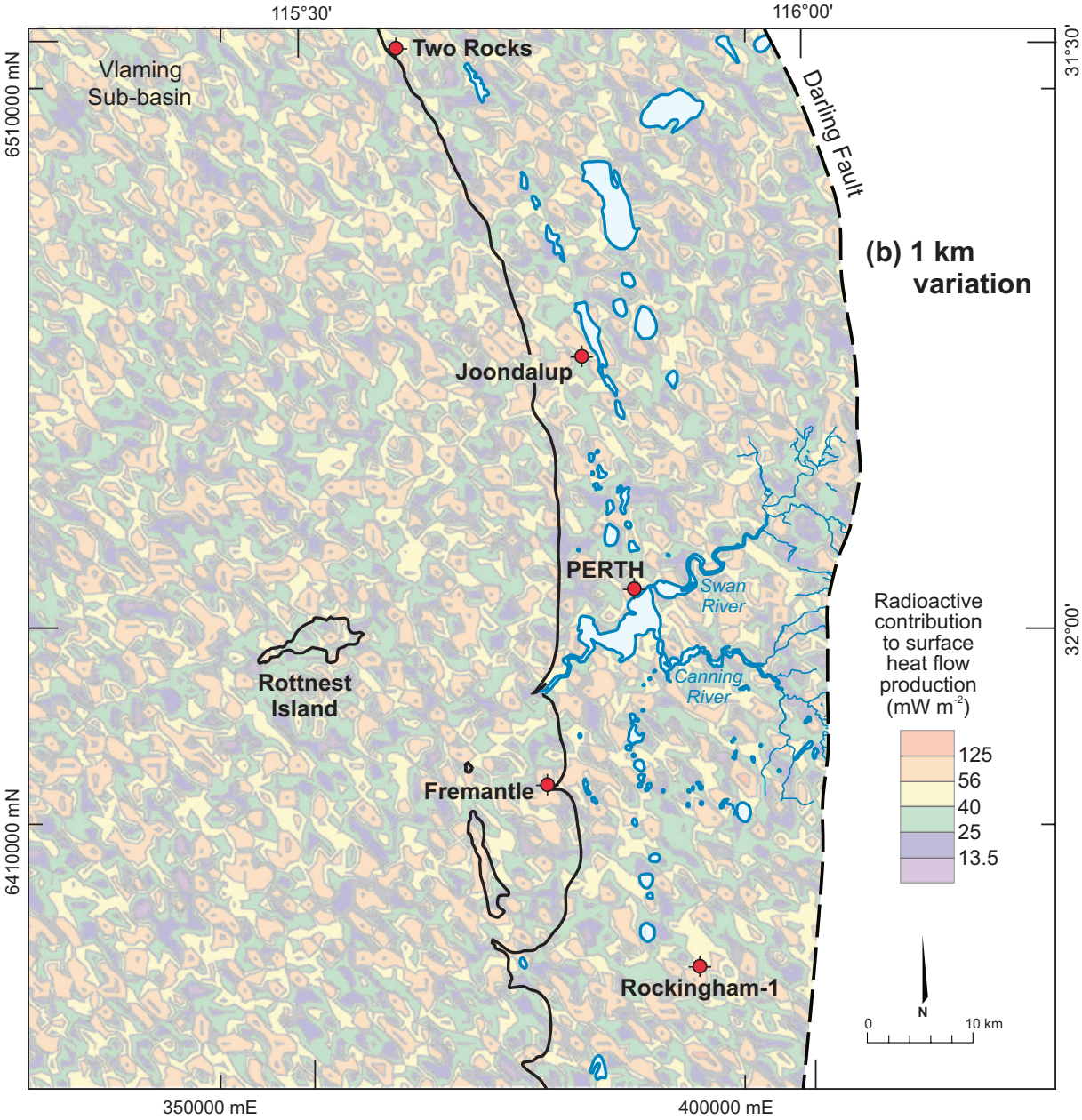

where *HFS* is the heat flow from the basin rocks at the top of the basement and *HPs* is the heat production at the surface. Random values were generated from the Prydz Bay distribution and allocated to grid co-ordinates. Stochastic simulations with grid spacing of 10 km (Fig. 8.11a) and 1 km (Fig. 8.11b) were made. Although these simulations are unconstrained by local data, the spatial correlation scales shown indicate the potential length scales of basal heat flow variation that may persist into the sedimentary cover. For example, it can be seen that heat flow will vary significantly on the 10 km scale if the characteristic length scale of heat production variation is of the order of 10 km, whereas, heat flow might be expected to be averaged by kilometre-scale flow cells if the characteristic length scale of variation is closer to 1 km. Further work is necessary to constrain this length scale of variation and to assess the potential conductive and advective heat signatures in the saturated sedimentary sequences above the basement.

8.5.5 Contribution of basement heat flow to the overall heat flow budget.

The proposed heat flow distribution contribution from the Perth Basin basement is likely to be between 25 and 56 mW m^{-2}, taken from the range between the 1st and 3rd quartiles of the Prydz Bay distribution. These data are consistent with average heat flow for Proterozoic rocks compiled by Jessop (1990). If basal heat flow from the mantle is around 25 mW m^{-2}, as suggested by Sclater et al. (1980) then the total heat flow, neglecting any contribution from overlying sediments, should be 50 to 81 mW m^{-2}. These values are similar to those proposed by Geoscience Australia for the Perth Basin (<87.5 mW m^{-2}; Beardsmore, 2009), and to those proposed by the authors of the Hot Dry Rock report, who used a small number (< 10) data samples in the Perth Basin to obtain estimates of 70 – 80 mW m^{-2} for the Perth Basin area. These values are sufficient to create temperatures gradients of 15 to 35 °C km^{-1} for plausible thermal conductivity values (HDR, 2008). These values are similar to those measured in Perth Basin boreholes.

8.6 Goals for future research

- More direct measurements from exposed regions of crystalline basement in the vicinity of the Perth Basin will help to better define the potential range and variability of basement heat flow in the Perth Basin.
- Better constraints on heat flow from borehole logs in the Perth Basin to account for surface heat flow contribution to better assess the contribution of basement heat flow.
- Test the approach documented in this study on a comparable yet better exposed orogen to develop as an exploration tool for application elsewhere.

8.7 Summary

The Perth Basin holds considerable potential for HSA (Hot Sedimentary Aquifer) geothermal energy. If this potential is to be properly assessed then it is necessary to determine the heat flow, and heat producing capacity, of the basin to the Perth Basin. However, this basement is largely covered by up to 12 km of sedimentary cover, so it is necessary to employ indirect methods for assessment.

Existing data from the Perth Basin basement, data from proposed analogues to the Perth Basin basement, and new data from the Leeuwin complex, SW Australia, has been compiled, and assessed. The small Perth Basin basement dataset shows similarities, in terms of rock types and heat producing capacity, to material from the Prydz Bay region of Antarctica. The Bunger Hills and Vestfold Hills regions have lower heat production than the proposed Perth Basin basement, most likely due to the presence of significant quantities of Archean crust in these areas. The Leeuwin complex has higher heat production than the proposed Perth Basin basement, most likely due to spatially restricted inputs of high heat production A type granites during the Neoproterozoic.

Typical heat production values are estimated to be of the order of 0.9 to 3.6 µW m^{-3}, with a median value of 2.2 µW m^{-3}. This value is greater than the average heat production of the Earth's crust, but less than the average for granites (2.8 µW m^{-3}). Estimates of the total heat flow due to radioactive decay in the basement are of the order of 25 to 56 mW m^{-2}, and are consistent with estimates from

other sources. Geothermal gradients calculated for plausible thermal conductivity values are 17 to 35 °C km^{-1}.

Estimates of the length scales of variation in heat producing capacity were made to support the incorporation of basement-geology considerations into geothermal exploration. Characteristic length scales of variation are of the order of 1 to 10 km for the regions of interest; if variation is of the order of 1 km then heat flow is likely to be homogenized by fluid flow in the overlying sediments. However, if variation is of the order of 10 km then it is possible that there may be basement-induced hot and cold spots within the Perth Basin, which it may be possible to discover via exploration.

9. REFERENCES

Ababou, R., 1996. Random porous media flow on large 3D grids: Numerics, performance and application to homogenization. In: Wheeler, M.F., ed., Environmental studies: Mathematical, computational and statistical analysis: New York, Springer, 1-25.

Abdulagatova, Z., Abdulagatov, I., and Emirov, V., 2009. Effect of temperature and pressure on the thermal conductivity of sandstone. International Journal of Rock Mechanics and Mining Sciences 46(6), 1055-1071.

Adeoti, L., Ayolabi, E.A., and James, P.L., 2009. An integrated approach to volume of shale analysis: Niger Delta example, Orire Field. World Applied Sciences Journal, 7, 448-452.

Allen, A.D., 1981. The hydrogeology of the Swan Valley, Perth Basin, Western Australia, In: Whelan, B.R. (Ed), Groundwater Resources of the Swan Coastal Plain. CSIRO, Proceedings of CSIRO and Water Research Foundation of Australia Symposium, 29-74.

Anderson, E.M., 1942. The Dynamics of Faulting and Dyke Formation with Application to Britain. Oliver and Boyd, Edinburgh, London.

Augustsson, C., and Bahlburg, H., 2003. Cathodoluminescence spectra of detrital quartz as provenance indicators for Paleozoic metasediments in southern Andean Patagonia. Journal of South American Earth Sciences 16(1), 15-26.

Bale, K., 2004, Geophysics Notes: Vlaming Sub-basin Seismic Interpretation Stage. Research Program 1.1- Technologies for Assessing Sites for CO_2 Storage. (Appendix 2 of report no.RPT06-0162). CO2CRC report number RPT06-0150.

Bathurst, R.G.C., 1987. Diagenetically enhanced bedding in argillaceous platform limestones: stratified cementation and selective compaction. Sedimentology 34, 749-778.

Beard, J.S., 1999. Evolution of the river systems of the south-west drainage division, Western Australia. J. R. Soc. West. Aust. 82, 147–164.

Beardsmore, G.R., 2009. Heat Flow Map of Australia. Hot Dry Rocks Pty Ltd.

Beardsmore, G.R., and Cull, J.P., 2001. Crustal heat flow: A guide to measurement and modelling. Cambridge University Press, Cambridge.

Ben-Zion, Y., and Sammis, C.G., 2003. Characterisation of fault zones, Pure & Applied Geophysics, 160, 677-715.

Billi, A., Salvini, F., and Storti, F., 2003. The damage zone-fault core transition in carbonate rocks: implications for fault growth, structure and permeability. Journal of Structural Geology 25(11), 1779-1794.

Blenkinsop, T.G., and Doyle, M.G., 2010. A method for measuring the orientations of planar structures in cut core. Journal of Structural Geology 32(6), 741-745.

Boger, S.D., 2011. Antarctica - Before and after Gondwana. Gondwana Research 19, 335-371.

Bonson, C.G., Childs, C., Walsh, J.J., Schöpfer, M.P.J., and Carboni, V., 2007. Geometric and kinematic controls on the internal structure of a large normal fault in massive limestones: The Maghlaq Fault, Malta. Journal of Structural Geology 29(2), 336-354.

Boschetti, F., Horowitz, F.G., Hornby, P., Holden, D., Archibald, N., and Hill, J., 2000. Improved edge detection in potential field maps and graphical estimation of depth to top. In 70th Annual International Meeting: Society of Exploration Geophysics, 406-409. Calgary, Alberta: Society of Exploration Geophysics.

Boschetti, F., Hornby, P., and Horowitz, F.G., 2001. Wavelet based Inversion of Gravity Data. Exploration Geophysics , 32(1), 48-55.

Bozanic, D., 1969. Gage Roads No. 1 well completion report. West Australian Petroleum Pty Ltd Petroleum Search Subsidy Acts Report (unpublished).

Brownhill, M. H., 1966. Gingin No.2 well completion and evaluation report. West Australian Petroleum Pty Limited.

Calcagno, P., Chilès, J.P., Courrioux, G., and Guillen, A., 2008.Geological modelling from field data and geological knowledge: part I. modelling method coupling 3D potential-field interpolation and geological rules: recent advances in computational geodynamics: theory, numerics and applications, Physics of the Earth and Planetary Interiors, 171(1–4), 147–157.

Canole, P., Odonne, F., and Polve, M., 1997. Heterogeneous strain associated with normal faulting: evidence of mass transfer by pressure solution associated with fault displacement. Tectonophysics 283(1-4), 129-143.

Causebrook, R., Dance, T., Bale, K., 2006. Southern Perth Basin Site Investigation and Geological Model for Storage of Carbon Dioxide. CO2CRC Report Number: RPT06-0162.

Cawood, P. A., and Nemchin, A. A., 2000. Provenance record of a rift basin: U/Pb ages of detrital zircons from the Perth Basin, Western Australia. Sedimentary Geology 134, 209-234.

Cherniak, D.J., Watson, E.B., and Wark, D.A., 2007. Ti diffusion in quartz. Chemical Geology 236(1-2), 65-74.

Clauser, C., 2006. Geothermal energy, in Advances materials and technologies. In: Energy technologies, subvol. C, Renewable Energies (edited by Heinloth, K.) 3. Springer, Heidelberg, Germany, 493-604.

Clauser, C., and Huenges, E., 1995. Thermal conductivity of rocks and minerals. In: Rock Physics and Phase Relations: A Handbook of Physical Constants (edited by Ahrens, T. J.) 3. American Geophysical Union, Washington, D.C., 105-126.

Cockbain, A.E., 1990. Perth Basin, Geology and Mineral Resources of Western Australia, Geological Survey of Western Australia, Memoir 3, 495-524.

Collins, A.S., 2003. Structure and age of the northern Leeuwin Complex, Western Australia: constraints from field mapping and U-Pb isotopic analysis. Australian Journal of Earth Sciences 50, 585-599.

Corbel, S., Griffiths, C., Dyt, C., and Ricard, L.P., 2012. Hot Sedimentary Aquifer Characterization Using Stratigraphic Forward Modelling, Perth Basin, Australia. Proceedings, Thirty-Seventh Workshop on Geothermal Reservoir Engineering, Stanford University, Stanford, California, January 30 - February 1, 2012 SGP-TR-194

Crostella, A., and Backhouse, J., 2000. Geology and Petroleum exploration of the Central and Southern Perth Basin, Western Australia. Geological Survey of Western Australia Report 57.

Davidson, W.A., 1995. Hydrogeology and groundwater resources of the Perth Region, Western Australia: Western Australia. Geological Survey, Bulletin 142, 270 p.

Davidson, W.A., and Yu, X., 2006. Perth regional aquifer modelling system (PRAMS) model development: Hydrogeology and groundwater modelling, Western Australia Department of Water, Hydrogeological record series HG 20, 237 p.

De Marsily, G., Delay, F., Gonçalvès, J., Renard, P., Teles, V., and Violette, S., 2005. Dealing with spatial heterogeneity. Hydrogeology Journal, 161-183.

Deming, D., 1989: Application of bottom-hole temperature corrections in geothermal studies. Geothermics, 18, No. 5/6, 775-786.

Department of Mines and Petroleum, Government of Western Australia, 1995, 1:2 500 000 Depth to Base Phanerozoic, Western Australia.

Dilks, A., and Graham S.C., 1985. Quantitative mineralogical characterisation of sandstones by back-scattered electron image analysis, Journal of Sedimentary Petrology, 55, 347-355.

Dresser Atlas, 1979. Log interpretation charts. Houston, Texas, Dresser Industries Inc., 107 p.

Esteban, L., Delle Piane, C., Israni, S. R., Evans, C., Pimienta, L., Timms, N., and McLaren, S., 2012. Thermal conductivity analysis in the Perth Basin, West Australia. CSIRO Report, Perth.

Fairbridge, R.W., 1953. Australian Stratigraphy. University of Western Australia Text Books Board, Perth.

Faulkner, D.R., Jackson, C.A.L., Lunn, R.J., Schlische, R.W., Shipton, Z.K., Wibberley, C.A.J., and Withjack, M.O., 2010. A review of recent developments concerning the structure, mechanics and fluid flow properties of fault zones. Journal of Structural Geology, 32(11), 1557-1575.

Fisher, Q. J., and Knipe, R. J., 1998. Fault sealing processes in siliciclastic sediments. Geological Society, London, Special Publications 147(1), 117-134.

Fisher, Q. J., and Knipe, R. J., 2001. The permeability of faults within siliciclastic petroleum reservoirs of the North Sea and Norwegian Continental Shelf. Marine and Petroleum Geology 18(10), 1063-1081.

Fisher, Q. J., Knipe, R. J., and Worden, R. H., 2000. Microstructures of deformed and non-deformed sandstones from the North Sea: implications for the origins of quartz cement in sandstones. Quartz cementation in sandstones 29, 129-146.

Fitzsimons, I.C.F., 2000. The Neoproterozoic evolution of Austalia's western margin. Geological Society of Australia Abstracts 65, 39-42.

Fitzsimons, I.C.W., 2000. Grenville-age basement provinces in East Antarctica: Evidence for three separate collisional orogens. Geology 28, 879-882.

Fitzsimons, I.C.W., 2002. Proterozoic basement provinces of southern and southwestern Australia, and their correlation with Antarctica. Proterozoic East Gondwana: Supercontinent Assembly and Breakup 206, 93-130.

Fletcher, I.R., Libby, W.G., 1993. Further isotopic evidence for the existence of two distinct terranes in the sourthern Pinjarra Orogen, Western Australia, Western Australia Geological Survey Reports. Geological Survey of Western Australia, Perth, 81-83.

Fletcher, I.R., Wilde, S.A., and Rosman, K.J.R., 1985. Sm-Nd model ages across the margins of the Archean Yilgarn Block, Western Australia. 3. The Western margin. Australian Journal of Earth Sciences 32, 73-82.

Folk, R.L., 1965. Petrology of Sedimentary Rocks. Hemphill, Austin, Texas.

Frog Tech, 2005, The Oz Seebase project: a new view of Australia's Phanerozoic Basins. PESA News, August/September 2005, 12-13. [http://www.frogtech.com.au/ozseebase-details/]PESA News, August/September 2005, 12-13.

Gardner, G.H.F., Gardner, L.W., and Gregory, A.R., 1974. Formation velocity and density – the diagnostic basics for stratigraphic traps. Geophysics 39, 770 – 780.

Geological Survey of Western Australia, 2011, 3D geological model building, and 3D temperature and heat flow calculation for the northern Perth Basin: Geological Survey of Western Australia, Record 2011/6, 76 p.

Ghori, K.A.R., 2008. Western Australia's Geothermal Resources. In: AAPG Annual Convention, San Antonio, Texas, USA.

Goldie Divko, L.M., O'Brien, G.W., Harrison M.L., Hamilton, P.J., 2010. Evaluation of the regional top seal in the Gippsland Basin: Implications for geological carbon storage and hydrocarbon prospectivity. APPEA Journal, 50, 463-486.

Górniak, K., 1997. The role of diagenesis in the formation of kaolinite raw materials in the Santonian sediments of the North-Sudetic Trough (Lower Silesia, Poland). Applied Clay Science 12(4), 313-328.

Gradstein, F.M., Ogg, J.G., Smith, A.G., Agterberg, F.P., Bleeker, W., Cooper, R.A., Davydov, V., Gibbard, P., Hinnov, L., House, M.R., Lourens, L., Luterbacher, H-P., McArthur, J., Melchin, M.J., Robb, L.J., Shergold, J., Villeneuve, M., Wardlaw, B.R., Ali, J., Brinkhuis, H., Hilgen, F.J., Hooker, J., Howarth, R.J., Knoll, A.H., Laskar, J., Monechi, S., Powell, J., Plumb, K.A., Raffi, I., Röhl, U., Sanfilippo, A., Schmitz, B., Shackleton, N.J., Shields, G.A., Strauss, H., Van Dam, J., Veizer, J., van Kolfschoten, Th., and Wilson D., 2004, A Geologic Time Scale 2004. Cambridge University Press, 589 p.

Gratier, J.P., Muquet, L., Hassani, R., and Renard, F., 2005. Experimental microstylolites in quartz and modeled application to natural stylolitic structures. Journal of Structural Geology 27(1), 89-100.

Gratier, J-P., and Gueydam, F., 2007. Deformation in the presence of fluids and mineral reactions: Effect of fracturing and fluid-rock interaction on seismic cycles. In Tectonic Faults: Agents of change on a dynamic Earth, Edited by Handy, M.R., Hirth, G., and Hovius, N., Report of the 95th Dahlem Workshop on The Dynamics of Fault Zones, Berlin, 2005. MIT Press, Cambridge USA, 446 p.

Gray, N.M., Sofoulis, J., de la Hunty, L., and Low, G., 1952a. Geological Map of Perth and Environs: Sheet 2 Fremantle-Perth-Midland Junction, Geological Survey of Western Australia. 1 mile to an inch map series.

Gray, N.M., Sofoulis, J., de la Hunty, L., and Low, G., 1952b, Geological Map of Perth and Environs: Sheet 3 Rockingham-Serpentine-Armadale, Geological Survey of Western Australia. 1 mile to an inch map series.

Griffiths, C.M., and Dyt, C., 2001. Six Years of Sedsim Exploration Applications (Abstract Only), AAPG Bulletin, 85 , 13.

Griffiths, C.M., and Hadler-Jacobsen, F., 1993. Practical Dynamic Modelling Of Sequence Stratigraphy. In: Steel, R. et al, Eds, Sequence Stratigraphy: Advances and Applications For Exploration and Production In North West Europe, Norwegian Petroleum Society, NPF Special Publication No. 5, 31-49.

Griffiths, C. M., and Paraschivoiu, E., 1998. Three-Dimensional Forward Stratigraphic Modelling Of Early Cretaceous Sedimentation on The Leveque and Yampi Shelves, Browse Basin. APPEA Journal, 38 (1), 147-158.

Griffiths, C., Dyt, C., Paraschivoiu, E., and Liu, K., 2001. Sedsim in hydrocarbon exploration. In: Merriam, D. & Davis, J. (Eds.), Geologic Modelling and Simulation. Kluwer Academic, New York, 71–97.

Gringarten, A.C., 1978. Reservoir lifetime and heat recovery factor in geothermal aquifers used for urban heating, Pure and Applied Geophysics, 117 (1) 297-308.

Hamilton, J., Reddy, S.M., Olierook, H., and Timms, N.E., 2011. Stylolites; Their Origin and Impact on Reservoir Quality. In: AAPG Annual Conference and Exhibition: Making the Next Giant Leap in Geosciences. American Association of Petroleum Geologists, Houston, Texas, U.S.A.

Haq, B.U., and Al-Qahtani, A.M., 2005. Phanerozoic cycles of sea-level change on the Arabian Platform. GeoArabia , 10 (2), 127-160.

Haq, B.U., and Schutter, S.R., 2008. A Chronology of Paleozoic Sea-Level Changes. Science, 322 (5898), 64-68.

Haq, B.U., Hardenbol, J., and Vail, P.R., 1987. Chronology Of Fluctuating Sea-Levels Since The Triassic (250 Million Years Ago To Present). Science 235, 1156-1167.

Haq, B.U., and Schutter, S.R., 2008. Chronology of Paleozoic Sea-Level Changes. Science, 64, 322 p.

Harris, L.B., 1994, Structural and tectonic synthesis for the Perth Basin, Western Australia. Journal of Petroleum Geology, 17(2), 129-156.

Hayon, S., 1999. Deformation and its Implication for fault seal within the Mungaroo Formation. Unpublished Honours Thesis, Curtin University.

Hays, J.D., Imbrie, J., and Shackleton, N.J., 1976. Variations in the Earth's Orbit: Pacemaker of the Ice Ages. Science 194 (4270), 1121–1132.

Heald, M. T., 1955. Stylolites in sandstones. Journal of Geology 63, 101-114.

Holden, D.J., Archibald, N.J., Boschetti, F., and Jessell, M.W., 2000, Inferring geological structures using wavelet-based multiscale edge analysis and forward models. Exploration Geophysics 31, 617-621.

Homewood, P. and Allen, P., 1981. Wave-, tide-, and current-controlled sandbodies of Miocene Molasse, Western Switzerland. AAPG Bulletin-American Association of Petroleum Geologists 65 2534-2545.

Hopkins, J., 2011. Relationships in the Leeuwin Complex; Mineralogy, Lithology and Heat Production, Western Australia, Honours Thesis, Applied Geology. Curtin University, Perth, 79 p.

Hornby, P., Boschetti, F., and Horowitz, F. G., 1999. Analysis of potential field data in the wavelet domain. Geophysical Journal International 137(1), 175-196.

Hornby, P., Horowitz, F.G., and Boschetti, F., 2002. A physical interpretation of the Poisson wavelet transform of potential fields. In Proceedings, EGS XXVII General Assembly. European Geophysical Society , Abstract 5568.

Hot Dry Rocks Pty. Ltd., 2008. Geothermal energy potential in selected areas of Western Australia (Perth Basin): A report prepared for the Department of Industry and Resources, Western Australia. Hot Dry Rocks Pty Ltd, Report DOIR0060108, Melbourne, 75, 270 p.

Iasky, R.P., 1993. A structural study of the Southern Perth Basin, Western Australia. Geological Survey of WA Report 31.

Iasky, R.P., Young, R.A., and Middleton, M.F., 1991. Structural study of the Southern Perth Basin by Geophysical Methods. Exploration Geophysics 22, 199-206.

Iasky, R.P., and Mory, A.J., 1993. Structural and tectonic framework of the Onshore Northern Perth Basin. Exploration Geophysics , 585-592.

Iasky, R.P., and Shevchenko, S., 1995. Onshore Northern Perth basin Gravity Project. GSWA Record 1995/6.

International Commission on Stratigraphy, IUGS, 2009. International Stratigraphic Chart, 2009. [http://www.geomorph.org/sp/arch/ISChart2009.pdf]

Israni, S. R., and Delle Piane, C., 2011. Rock Physics and Petrophysical characterization of units from the Perth Basin. CSIRO Confidential Report Number EP113342, Perth, 43 p.

Jayr, S., Gringarten, E., Tertois, A.L., Mallet J.L., and Dulac, J.C., 2008. The need for a correct geological modelling support: the advent of the UVT Transform, First Break, European Association of Geoscientists & Engineers, 26, 73-79.

Jansen, D.P., Collins, A.S., and Fitzsimons, I.C.W., 2003. Structure and tectonics of the Leeuwin complex and Darling Fault zone, southern Pinjarra orogen Western Australia: a field guide. Geological survey of Western Australia Record 2003/15.

Jessop, A.M., 1990. Thermal Geophysics. In Developments in Solid Earth Geophysics 17. Elsevier, Amsterdam. 316 p.

Johansen, T.E.S., Fossen, H., and Kluge, R., 2005. The impact of syn-faulting porosity reduction on damage zone architecture in porous sandstone: an outcrop example from the Moab Fault, Utah. Journal of Structural Geology 27(8), 1469-1485.

Johnson, L., 2002. Microstructural and diagenetic history of a hydrocarbon reservoir. Unpublished Honours thesis, Curtin University.

Johnson, N.E.A., 1965. Gingin-1 Well Completion Report. West Australian Petroleum Pty Limited.

Jones, D.K., and Nicholls, J., 1966. Pinjarra No.1 Well, Western Australia: Well Completion Report. West Australian Petroleum Pty Limited., Perth.

Kamel, M.H., 2011. An approach for minimizing errors in computing effective porosity in reservoir of shaly nature in view of Wyllie–Raymer–Raiga relationship. Journal of Petroleum Science & Engineering, 77, 386-392.

Kim, Y.-S., Andrews, J.R., and Sanderson, D.J., 2000. Damage zones around strike–slip fault systems and strike–slip fault evolution, Crackington Haven, southwest England. Geoscience Journal 4, 53-72.

Kim, Y.-S., Peacock, D.C.P., and Sanderson, D.J., 2004. Fault damage zones. Journal of Structural Geology 26(3), 503-517.

Kim, Y.-S. and Sanderson, D.J., 2010. Inferred fluid flow through fault damage zones based on the observation of stalactites in carbonate caves. Journal of Structural Geology 32, 1305-1316.

King, R.C., Hillis, R.R., and Reynolds, S.D., 2008. In situ stresses and natural fractures in the Northern Perth Basin, Australia. Australian Journal of Earth Sciences 55(5), 685-701.

Knipe, R. J., 1989. Deformation mechanisms -- recognition from natural tectonites. Journal of Structural Geology 11(1-2), 127-146.

Kohn, B.P., Gleadow, A.J.W., Brown, R.W., Gallagher, K., O'Sullivan, P.B., and Foster, D.A., 2002. Shaping the Australian crust over the last 300 million years: insights from fission track thermotectonic imaging and denudation studies of key terrain. Australian Journal of Earth Sciences 49, 697-717.

Koltermann, C.E,. and Gorelick, S.M., 1992. Palaeoclimatic Signature in Terrestrial Flood Deposits. Science, 256 (5065), 1775-1782.

Kwon, Y.I., and Boggs, S., 2002. Provenance interpretation of Tertiary sandstones from the Cheju Basin (NE East China Sea): a comparison of conventional petrographic and scanning cathodoluminescence techniques. Sedimentary Geology 152(1-2), 29-43.

Labaume, P., Carrio-Schaffhauser, E., Gamond, J.F., and Renard, F., 2004. Deformation mechanisms and fluid-driven mass transfers in the recent fault zones of the Corinth Rift (Greece). Comptes Rendus Geosciences, 336(4-5), 375-383.

Landini, G., 2010. Software: Threshold_Colour. http://www.dentistry.bham.ac.uk/landinig/software/software.html

Le Blanc Smith, G.,1993. Geology and Permian coal resources of the Collie Basin, Western Australia. Geological Survey of Western Australia, Perth.

Lewis, G., Knipe, R. J., Li, A., Andreas, G. K., and Robert, H., 2002. Fault seal analysis in unconsolidated sediments: a field study from Kentucky, USA. In: Norwegian Petroleum Society Special Publications, 11. Elsevier, 243-253.

Li F., Dyt C., and Griffiths C., 2004. 3D modelling of flexural isostatic deformation. Computers and Geosciences, 30 (9-10), 1105-1115.

Li, F., Dyt, C., Griffiths, C.M., Jenkins, C., Rutherford, M., and Chittleborough, J., 2005. Seabed sediment transport and offshore pipeline risks in the Australian Southeast. APPEA Journal 45, 523-534.

Lloyd, G.E., and Knipe, R.J., 1992. Deformation mechanisms accommodating faulting of quartzite under upper crustal conditions. Journal of Structural Geology 14(2), 127-143.

Lockwood, A.M., 2004. Western Australia Isostatic Residual Gravity Anomaly and Depth to Basement Model. Geological Survey of WA Record 2004/14.

Lockwood, A.M., and Iasky, R.P., 2004. Gravity and magnetic interpretation of the Southern Perth Basin. Geological Survey of WA Record 2004/8.

Logan, B., 1966. Report to Empire Oil Company (WA) NL on porosity & permeability in the Cattamarra Coal Formation Gingin Gas Field, WA. Logiden Pty Ltd.

Loutit, T., Pryer, L., Henley, P., and Gardner, P., 2005. The OZ SEEBASETM Project: A New View of Australia's Phanerozoic Basins. PESA News, August/Sept. 2005, 12-13

Macchi, L., 2000. X-Ray diffraction analysis of clay separate from nine sandstone samples from wells Gingin 1, Gingin 2 & Gingin 3: A report prepared by GH Geochemical Services for Dr L. Macchi (Reservoir Associates International). Empire Oil Company (WA) Ltd. EP389, Shocklach, Cheshire, UK, 30 p.

Martinez, P., and Harbaugh, J.W., 1993. Simulating Nearshore Environments. Pergamon Press, New York.

McIlroy, D., Flint, S., Howell, J.A., and Timms, N., 2005. Sedimentology of the tide-dominated Jurassic Lajas Formation, Neuquẽn Basin, Argentina. Geological Society, London, Special Publications 252(1), 83-107.

McKenna, T., Sharp Jr, J., and Lynch, F., 1996. Thermal conductivity of Wilcox and Frio sandstones in south Texas (Gulf of Mexico basin). AAPG Bulletin-American Association of Petroleum Geologists 80(8), 1203.

McKibbin, R., and Tyvand, P.A., 1982. Anisotropic modelling of thermal convection in multilayered porous media. Journal of Fluid Mechanics, 118, 315-339.

McWhae, J.R.H., Playford, P.E., Lindner, A.W., Glenister, B.F., and Balme, B.E., 1958. The stratigraphy of Western Australia. Geological Society of Australia Journal 4(2), 1-161.

Messent, B.E.J., and Farmer, L., 2008. Basker Field, Gippsland Basin: assessing reservoir connectivity with the aid of complementary technologies. In: EABSIII 2008, Development and Application of New Exploration/Production Technologies, Sydney, NSW, 29-44.

Meyer, M., Harff, J., and Dyt, C., 2011. Modelling coastline change of the Darss-Zingst Peninsula with Sedsim. (in J. Harff et al. (eds.)), The Baltic Sea Basin, central and eastern European development studies , (CEEDES) 2011, Part 5, 281-298, DOI: 10.1007/978-3-642-17220-5_14

Miall, A.D., 1992. Alluvial deposits. In: Facies models: response to sea level change (edited by Walker, R. G., & James, N. P.,). Geological Association of Canada, Ontario, 119-142.

Miall, A.D., 1996. The geology of fluvial deposits: sedimentary facies, basin analysis, and petroleum geology. Springer, New York.

Michael, H.A., and Voss, C.I., 2009. Estimation of regional-scale groundwater flow properties in the Bengal Basin of India and Bangladesh. Hydrogeology Journal, 17, 1329-1346.

Mitchell, J., 2004. Apium-1 interpretive well completion report, L1/L2 Western Australia. ARC Energy.

Mooney, W.D., Beroza, G.C., and Kind, R., 2007. Fault zones from top to bottom: A geophysical perspective. In Tectonic Faults: Agents of change on a dynamic Earth, Edited by Handy, M.R., Hirth, G., & Hovius, N., ,Report of the 95th Dahlem Workshop on The Dynamics of Fault Zones, Berlin, 2005. MIT Press, Cambridge USA, 446 p.

Mørk, M.B.E., and Moen, K., 2007. Compaction microstructures in quartz grains and quartz cement in deeply buried reservoir sandstones using combined petrography and EBSD analysis. Journal of Structural Geology 29(11), 1843-1854.

Mory, A.J., and Iasky, R.P., 1996. Stratigraphy and Structure of the onshore Northern Perth Basin Western Australia. Geological Survey of WA Report 46.

Myers, J., 1990. The Pinjarra Orogen, in Geology and Mineral Resources of Western Australia: Western Australia Geological Survey Memoir 3, 77-119.

Myers, J.S., 1990. Albany-Fraser Orogen. Western Australian Geological Survey Memoir. 3, 255-263.

Myers, J.S., and Hocking, R.M., 1998, Geological map of Western Australia, 1:2,500,000 (13th Edition): Western Australia Geological Survey.

Nadri, D., 2011a., Reprocessing of the Vertical Seismic Profiling Data from the Geothermal Borehole SHG-1 at St Hilda School Mosman Park, CSIRO Report EP117563 to GT Power Pty Ltd, 68 p.

Nadri, D., 2011b. Reprocessing of the Vertical Seismic Profiling Data from the Geothermal Borehole AM40 at Kensington, CSIRO Report EP117564 to GT Power Pty Ltd, 73 p.

Nemchin, A.A., and Pidgeon, R.T., 1997. Evolution of the Darling Range Batholith, Yilgarn Craton, Western Australia. Journal of Petrology, 38, 625-649.

Neuzil, C., 1986. Groundwater flow in low-permeability environments. Water Resources Division 22(8), 1163-1195.

Newman, J.K., 1959, Preliminary Report of an aeromagnetic survey of the Perth basin 1957. Geoscience Australia Record 1959/64.

Nordlund, U., 1996. Formalising geological knowledge: with an example of stratigraphic modeling using fuzzy logic. Journal of Sedimentary Research 66, 689-698.

Nordlund, U., 1999. FUZZIM: forward stratigraphic modelling made simple. Computers & Geosciences 25 (1999) 449-456.

Odling, N.E., Harris, S.D., and Knipe, R.J., 2004. Permeability scaling properties of fault damage zones in siliclastic rocks. Journal of Structural Geology 26(9), 1727-1747.

Ogg, J.G., Ogg, G., and Gradstein, F.M., 2008. The Concise Geologic Time Scale. Cambridge: Cambridge University Press, 178 p.

Olierook, H., 2011. Fault-related strain accommodation and diagenesis in the Northern Perth Basin: Implications for fluid pathways. Unpublished Honours thesis, Curtin University.

Olierook, H.K., Stütenbecker, L., Timms, N., Delle Piane, C., Wilson, M., Hamilton, J., and Cope, P., 2012a. Petrography and facies analysis report on Cockburn-1, Perth Metropolitan area, Western Australia. WA Geothermal Centre of Excellence Confidential Report, Perth, 52 p.

Olierook, H.K., Timms, N., Delle Piane, C., Wilson, M., Hamilton, J. and Cope, P., 2012b. Petrography and facies analysis report on Gingin-1, Perth Metropolitan area, Western Australia. WA Geothermal Centre of Excellence Confidential Report, Perth, 56 p.

Olierook, H.K., Timms, N., Delle Piane, C., Wilson, M., Hamilton, J., and Cope, P., 2012c. Petrography and facies analysis report on Pinjarra-1, Perth Metropolitan area, Western Australia. WA Geothermal Centre of Excellence Confidential Report, Perth, 52 p.

Olierook, H.K., Delle Piane, C., and Wilson, M., 2012d. Petrography and facies analysis report on Gingin-2, Perth Metropolitan area, Western Australia. WA Geothermal Centre of Excellence Confidential Report, Perth, 32 p.

Owad-Jones, D., and Ellis, G., 2000. Western Australia atlas of petroleum fields. Volume 1, Onshore Perth Basin Department of Minerals and Energy, Petroleum Division, Perth.

Ozkahraman, H., Selver, R., and Isik, E., 2004. Determination of the thermal conductivity of rock from P-wave velocity. International journal of rock mechanics and mining sciences 41(4), 703-708.

Pagoulatos, A., and Sondergeld, C., 2004. Evaluation of multistage triaxial testing on berea sandstone, University of Oklahoma.

Paraschivoiu, E., Griffiths, C.M., and Dyt, C.P., 2000. The use of three-dimensional nested forward stratigraphic simulations to provide variable-scale heterogeneity models of sedimentary volumes. Presented at upscaling uownunder, Melbourne, February 2000.

Peacock, D.C.P., Fisher, Q.J., Willemse, E.J.M., and Aydin, A., 1998. The relationship between faults and pressure solution seams in carbonate rocks and the implications for fluid flow. Geological Society, London, Special Publications 147(1), 105-115.

Playford, P.E., Cockbain, A.E., and Low, G.H., 1976. Geology of the Perth Basin Western Australia. Geological Survey of Western Australia Bulletin 124.

Popov, Y., 1997. Optical Scanning Technology for non-destructive contactless measurements of thermal conductivity and diffusivity of solid matters. In: Proceedings of the 4th World Conference. Experimental Heat Transfer, Fluid Mechanics and Thermodynamics, Brussels, 109-117.

Popov, Y., Pribnow, D., Sass, J., Williams, C., and Burkhardt, H., 1999. Characterisation of rock thermal conductivity by high resolution optical scanning. Geothermics, 28, 253-276.

Press, W.H., Teukolsky, S.A., Vetterling, W.T., and Flannery, B.P., 1992. Numerical recipes in FORTRAN; The art of scientific computing, 2nd edition, Cambridge University Press, Section 16.2, 708-717.

Prior, D.J., Boyle, A.P., Brenker, F., Cheadle, M.C., Austin, D., Lopez, G., Peruzzo, L., Potts, G. J., Reddy, S.M., Spiess, R., Timms, N.E., Trimby, P., Wheeler, J., and Zetterström, L., 1999. The application of electron backscatter diffraction and orientation contrast imaging in the SEM to textural problems in rocks. American Mineralogist 84(11-12), 1741-1759.

Pujol, M., 2011, Examples of successful hot Sedimentary Aquifer direct-use projects in Perth, Western Australia, in Middleton, M., & Gessner, K., (eds.) Western Australian Geothermal Energy Symposium Abstracts v1, 23.

Quilty, J.H., 1963, Perth Basin Aeromagnetic Survey, Geoscience Australia Record 1963/74.

Raiga-Clemenceau, J., Martin, J.P., and Nicoletis, S., 1988. The concept of acoustic formation factor for more accurate porosity determination from sonic transit time data. The Log Analyst, 29, 54-60.

Rasband, W. S., 2011. ImageJ. (edited by Health, U. S. N. I. o.), National Institutes of Health http://imagej.nih.gov/ij/, Bethesda, Maryland, USA.

Reddy, S.M., Timms, N. E., Pantleon, W., and Trimby, P., 2007. Quantitative characterization of plastic deformation and geological implications. Contributions to Mineralogy and Petrology 153, 625-645.

Reid, A., 1989. Measuring the unmeasurable – recent advances in applied mineralogy. The AusIMM Bulletin and Proceedings 294(2), 20-24.

Reid, L.B., Bloomfield, G., Botman, C., Ricard, L., and Wilkes, P.G., 2011. Temperature regime in the Perth Metropolitan Area: Results of temperature and gamma logging and analysis, June/July 2010, CSIRO report EP111422, Western Australian Geothermal Centre of Excellence, 197 p.

Reid, L.B., Bloomfield, G., Ricard, L.P., Botman, C., and Wilkes, P.G., 2012. Shallow geothermal regime in the Perth metropolitan area. Submitted to Australian Journal of Earth Sciences.

Reid, L.B., Corbel, S., Poulet, T., Ricard, L.P., Schilling, O., Sheldon, H.A., and Wellmann, J.F., 2012. Hydrothermal modelling in the Perth Basin, Western Australia Final Report of Project 3, Perth Basin Assessment.

Renard, P., and de Marsily, G., 1997. Calculating equivalent permeability: A review. Advances in Water Resources, 20, 253-278.

Renard, F., Gratier, J.-P., and Jamtveit, B., 2000. Kinetics of crack-sealing, intergranular pressure solution, and compaction around active faults. Journal of Structural Geology 22(10), 1395-1407.

Rispoli, R., 1981. Stress fields about strike–slip faults inferred from stylolites and tension gashes. Tectonophysics 75, 29-36.

Roduit, N., 2006. JMicroVision: Image analysis toolbox for measuring and quantifying components of high-definition images Version 1.2.2.

Salles T., Marchès, E., Dyt, C., Griffiths, C., Hanquiez, V., and Mulder, T., 2009. Simulation of the interactions between gravity processes and contour currents on the Algarve Margin (South Portugal) using the stratigraphic forward model Sedsim. Sedimentary Geology, 229, 3, 95–109.

Salles, T.B., Griffiths, C. M., Dyt, C.P., and Li, F., 2011. Australian shelf sediment transport responses to climate change-driven ocean perturbations. Marine Geology 282, 268–274.

Salles, T.B., Griffiths, C.M., and Dyt, C.P., 2011. Aeolian sediment transport integration in general stratigraphic forward modelling. JGR/186062, Journal of Geological Research, vol. 2011, Article ID 186062, 12 p.

Sandwell, D. T., and Smith, W.H.F., 2009. Global marine gravity from retracked Geosat and ERS-1 altimetry: Ridge segmentation versus spreading rate, Journal of Geophysical Research, 114, B01411.

Schenau, S., Passier, H.F., Reichart, G.J., and de Lange, G.J., 2002. Sedimentary pyrite formation in the Arabian Sea. Marine Geology 185(3-4), 393-402.

Sclater, J.G., Jaupart, C., and Galson, D., 1980. The heat flow through oceanic and continental crust and the heat loss of the Earth. Reviews of Geophysics 18, 269-311.

Selley, R.C., 1988. Applied Sedimentology. Academic Press, Cambridge.

Sibley, D.F., and Blatt, H., 1976. Intergranular pressure solution and cementation of the Tuscarora orthoquartzite. Journal of Sedimentary Petrology 46, 881-896.

Sircombe, K., and Freeman, M.J., 1999. Provenance of detrital zircons on the Western Australia coastline - Implications for the geologic history of the Perth basin and denudation of the Yilgarn. Geology 27, 879-882.

Schlumberger, 1989. Log interpretation principles/applications. Sugar Land, Texas, Schlumberger.

Smith, D. N., 1967. Cockburn No.1 Well, Western Australia: Well Completion Report. West Australian Petroleum Pty. Ltd., 60 p.

Song, T., and Cawood, P.A., 2000. Structural styles in the Perth Basin associated with the Mesozoic break-up of Greater India and Australia, Tectonophysics 317, 55-72.

Stütenbecker, L., 2011. Internship Report. West Australian Geothermal Centre of Excellence, Perth, 26 p.

Stütenbecker, L., and Timms, N., 2011. Petrography of samples of Cockburn-1 well. Perth Basin, Western Australia. WA Geothermal Centre of Excellence Confidential Report EP113151, Perth, 207 p.

Tada, R., and Siever, R., 1989. Pressure solution during diagenesis. Annual Reviews of Earth and Planetary Sciences 17, 89-118.

Tanikawa, W., and Shimamoto, T., 2006. Klinkenberg effect for gas permeability and its comparison to water permeability for porous sedimentary rocks. Hydrology and Earth System Sciences Discussions. 3, 1315-1328.

Taylor, A. M., and Goldring, R., 1993. Description and analysis of bioturbation and ichnofabric. Journal of the Geological Society, London 150, 141-148.

Tetzlaff, D.M., and Harbaugh, J.W., 1989. Simulating Clastic Sedimentation; Computer Methods In The Geosciences, Van Nostrand Reinhold, New York, 202 p (??).

Tong, F., Jing, L., and Zimmerman, R., 2009. An effective thermal conductivity model of geological porous media for coupled thermo-hydro-mechanical systems with multiphase flow. International Journal of Rock Mechanics & Mining Sciences 46(8), 1358-1369.

Veevers, J.J., Saeed, E. A., Belousova, E.A., and Griffin, W.L., 2005. U–Pb ages and source composition by Hf-isotope and trace element analysis of detrital zircons in Permian sandstone and modern sands from southwestern Australia and a review of the paleogeographical and denudation history of the Yilgarn Craton. Earth Science Reviews 68, 245-279.

Volk, H., Kempton, R.H., Ahmed, M., Gong, S., George, S.C., and Boreham, C.J., 2009. Tracking petroleum systems in the Perth Basin by integrating microscopic, molecular and isotopic information on petroleum fluid inclusions. Journal of Geochemical Exploration 101(1), 109-109.

Walker, R.G., and James, N.P., 1992. Facies models: Response to sea level change. Geological Association of Canada, Ontario.

Wang ,X., Bierwirth, A., Christ, A., Whittaker, P., Regenauer-Lieb, K., and Chua, H.T., (submitted), Application of geothermal absorption air-conditioning system: a case study. Submitted to Applied Thermal Engineering.

Weber, U.D., Kohn, B.P., Gleadow, A.J.W., and Nelson, D.R., 2005. Low temperature Phanerozoic history of the Northern Yilgarn Craton, Western Australia. Tectonophysics 400, 127-151.

Wellmann, J.F., and Regenauer-Lieb, K., 2011, Uncertainties have a meaning: Information entropy as a quality measure for 3-D geological models. Tectonophysics, 526-529, 207-216.

Wellmann, J.F., Horowitz, F.G., Schill, E., and Regenauer-Lieb, K., 2010. Towards incorporating uncertainty of structural data in 3D geological inversion, Tectonophysics, 490 (3–4), 141–151.

Wentworth, C. K., 1922. A scale of grade and class terms for clastic sediments. Journal of Geology 30, 377-392.

Wilde, S. A., 1999. Evolution of the Western Margin of Australia during the Rodinian and Gondwanan Supercontinent Cycles. Gondwana Research 2(3), 481-499.

Wilde, S.A., Middleton, M.F., and Evans, B.J., 1996. Terrane accretion in the southwestern Yilgarn Craton: evidence from a deep seismic crustal profile. Precambrian Research, 78, 179-396.

Wilde, S.A., and Murphy, D.M.K., 1990. The nature and origin of late Proterozoic high-grade gneisses of the Leeuwin Block, Western Australia. Precambrian Research 47, 251-270.

Wilde, S.A., and Nelson, D.R., 2001, Geology of the western Yilgarn Craton and Leeuwin Complex, Western Australia — a field guide: Western Australia Geological Survey Record 2001/15, 41 p.

Wilde, S.A., 1999, Evolution of the Western Margin of Australia during the Rodinian and Gondwanan supercontinent cycles, Gondwana Research, 2(3), 481-499.

Wilkes, P.G., Timms, N.E., Horowitz, F.G., and Corbel, S., 2011 A new structural interpretation of the Perth Basin and the Perth metropolitan area using gravity and aeromagnetic data, geomorphology and geology. WA Geothermal Centre of Excellence Report EP117411, Perth, 60 p.

Willmott, S. P., 1964. Revisions to the Mesozoic stratigraphy of the Perth Basin. In: Australia Bureau of Mineral Resources Petroleum Search Subsidy Acts Publication 54, App. 1, 11.

Wilson, M.D., and Pittman, E.D., 1977. Authigenic clays in sandstones; recognition and influence on reservoir properties and paleoenvironmental analysis. Journal of Sedimentary Petrology 47, 3-31.

Wingate, M.T.D., and Giddings, J.W., 2000. Age and palaeomagnetism of the Mundine Well dyke swarm, Western Australia: implications for an Australia–Laurentia connection at 755 Ma. Precambrian Research, 100, 335–357.

Wooding, R.A., 1978. Large-scale geothermal field parameters and convection theory. New Zealand Journal of Science, 21, 219-228.

Worden, R.H., and Morad, S., 2003. Clay minerals in sandstones: controls on formation, distribution and evolution. International Association of Sedimentology Special Publication, 34, 3-41.

Wyllie, M.R.J., Gregory, A.R., and Gardner, L.W., 1956. Elastic wave velocities in heterogeneous and porous media. Geophysics, 21, 41-70.

Wynn, P., and Bachin, M., 2009. Index of gravity surveys (second edition) Geoscience Australia Record 2009/07.

Xiao, S., Schiffbauer, J.D., McFadden, K.A.,and Hunter, J., 2010. Petrographic and SIMS pyrite sulfur isotope analyses of Ediacaran chert nodules: Implications for microbial processes in pyrite rim formation, silicification, and exceptional fossil preservation. Earth and Planetary Science Letters 297(3-4), 481-495.

APPENDIX A LISTING OF STUDENTS

APPENDIX B CONFERENCE AND WORKSHOP CONTRIBUTIONS

The research presented in this report has been presented in local and international conferences. In addition to publicising work performed by WAGCoE or affiliated students, conference participation provides an important forum for attendees to be exposed to related research and develop professional networks in the geothermal field. Notable conferences attended include:

WAGCoE Workshop, ARRC Building, Perth, 16 February 2011.

First International Workshop on Rock Physics, 7-12 August, 2011, Colorado School of Mines, USA.

9th Euroconference on Rock Physics and Geomechanics, 17-21 October, 2011, Trondheim, Norway.

Gas Petrophysics from Formation Evaluation Society of Australia (FESAus), 13-15 September, 2011, Perth, Australia.

Australian Geothermal Energy Conference, 2011. Melbourne, Australia.

American Association of Petroleum Geologists, 2011, Houston, Texas, USA.

Western Australian Geothermal Energy Symposium, 2011. Perth. This conference was organised in large part by members of WAGCoE.

Stanford Geothermal Reservoir Engineering Workshop, 2011 and 2012. Palo Alto, California, USA.

Structural Geology and Tectonics Specialist Group Meeting, Waratah Bay. Jan 2012.

22nd International Geophysical Conference and Exhibition, Australian Society of Exploration Geophysicists, Brisbane, February 2012.

53rd Society of Petrophysicists and Well Log Analysts Symposium, 16-20 June 2012, Cartagena, Colombia.

Presentations given at these conferences are listed in Appendix C.

APPENDIX C SCIENTIFIC PUBLICATIONS

Publications with WAGCoE authors related to geothermal characterisation and hydrothermal modelling are listed in this section, even if they have been included in the References section above. Some of these publications may also appear in reports relating to other projects with WAGCoE's Program 1.

Alix, R. June 2011. Reservoir characterisation of the Yarragadee Formation for geothermal exploration in the Perth Metropolitan Area, Perth Basin, Western Australia. MS, Montpellier University, France.

Corbel, S., Schilling, O., Horowitz, F.G., Reid, L.B., Sheldon, H.A., Timms, N.E., Wilkes, P., 2012, Identification and geothermal influence of faults in the Perth Metropolitan Area, Australia. PROCEEDINGS, Thirty-Seventh Workshop on Geothermal Reservoir Engineering, Stanford University, Stanford, California, January 30 - February 1, 2012, SGP-TR-194.

Esteban, L., Pimienta, L., Sarout, J. and Delle Piane, C., Haffen, S. and Geraud, Y., June 2012. Predicted and measured thermal conductivities in two potential geothermal fields: Soultz-sous-forets (France) and Perth Basin (Australia). 53rd Society of Petrophysicists and Well Log Analysts Symposium, 16-20 June 2012, Cartagena, Colombia.

Esteban, L., Delle Piane, C., Israni, S.R., Evans, C., Pimienta, L., Timms, N., and McLaren, S., 2012, Thermal conductivity analysis in the Perth Basin, Western Australia. CSIRO Report, February 2012.

Hamilton, J., Reddy, S.M., Olierook, H., and Timms, N.E., 2011. Stylolites; Their Origin and Impact on Reservoir Quality. In: AAPG Annual Conference and Exhibition: Making the Next Giant Leap in Geosciences. American Association of Petroleum Geologists, Houston, Texas, U.S.A.

Hopkins, J., 2011. Relationships in the Leeuwin Complex; Mineralogy, Lithology and Heat Production, Western Australia, Applied Geology. Honours Thesis (unpublished), Curtin University, Perth, pp. 79.

Horowitz, F., Wilkes, P., Corbel, S. and Timms, N. 2011, Metropolitan Perth Geological Fault Locations Using Gravity and Magnetic "Worms" for Geothermal Projects, in Middleton, M and Gessner, K. (eds.) Western Australian Geothermal Energy Symposium Abstracts v. 1: p11.

Israni, S.R., Delle Piane, C., 2011, Rock Physics and Petrophysical characterization of units from the Perth Basin. CSIRO Confidential Report Number EP113342, May 2011, 43 pp.

Jenner, C., 2011 Determining the geothermal properties of the Perth Basin lithology to aid geothermal energy projects. Exploration Geophysics Honours Thesis (unpublished), Curtin University, Perth.

Nadri, D., Urosevic, M, Wilkes, P.G., Asgharzadeh, M , 2012. Tube wave removal from vertical seismic profiling (VSP) surveys. 22nd International Geophysical Conference and Exhibition , Australian Society of Exploration Geophysicists, Brisbane, February 2012.

Nadri, D., 2011a, Reprocessing of the Vertical Seismic Profiling Data from the Geothermal Borehole SHG-1 at St Hilda School Mosman Park, CSIRO Report EP117563 to GT Power Pty Ltd, 68pp.

Nadri, D., 2011b, Reprocessing of the Vertical Seismic Profiling Data from the Geothermal Borehole AM40 at Kensington, CSIRO Report EP117564 to GT Power Pty Ltd, 73pp.

Olierook, H., 2011, Fault-related strain accommodation and diagenesis in the Northern Perth Basin: Implications for fluid pathways, Applied Geology Honours Thesis (unpublished), Curtin University, Perth.

Olierook, H., Stütenbecker, L., Timms, N.E., Delle Piane, C., Wilson, M., Hamilton, J., and Cope, P., 2012a, Petrography and facies analysis report on Cockburn-1, Perth Metropolitan area, Western Australia. WA Geothermal Centre of Excellence Confidential Report, Perth, 52pp.

Olierook, H., Timms, N.E., Delle Piane, C., Wilson, M., Hamilton, J., and Cope, P., 2012b, Petrography and facies analysis report on Pinjarra-1, Perth Metropolitan area, Western Australia. WA Geothermal Centre of Excellence Confidential Report, Perth, 52pp.

Olierook, H., Timms, N.E., Delle Piane, C., Wilson, M., Hamilton, J., and Cope, P., 2012c, Petrography and facies analysis report on Gingin-1, Perth Metropolitan area, Western Australia. WA Geothermal Centre of Excellence Confidential Report, Perth, 56pp.

Olierook, H., Timms, N.E., Delle Piane, C., and Wilson, M., 2012d, Petrography and facies analysis report on Gingin-2, Perth Metropolitan area, Western Australia. WA Geothermal Centre of Excellence Confidential Report, Perth, 32pp.

Olierook, H., Timms, N.E., Hamilton, P.J., Reddy, S.M., 2011, Characterisation of fault damage zones in the north Perth Basin, West Australian Geothermal Energy Symposium, Perth, 21-22 March 2011.

Olierook, H., 2011, Fault-related strain accommodation and diagenesis in the Northern Perth Basin: Implications for fluid pathways, CSIRO Australian Resources Research Centre seminar series, Perth, 11 November 2011.

Pimienta, L., Sarout, J., Esteban, L. and Ricard, L., 2011. Microstructure-based modelling of the thermal conductivity of natural and synthetic aggregates. First International Workshop on Rock Physics, 7-12 August, Colorado School of Mines, USA.

Pimienta, L., Sarout, J., Esteban, L., and Delle Piane, C., 2011. Prediction of rock thermal conductivity from mineral composition, elastic wave velocities and microstructure. 9th Euroconference on Rock Physics and Geomechanics, 17-21 October, Trondheim, Norway.

Pimienta, L., Sarout, J., Esteban, L., Delle Piane, C. and Ricard, L., 2011. Thermal conductivity prediction from elastic wave velocity. Gas Petrophysics from Formation Evaluation Society of Australia (FESAus), 13-15 September, Perth, Australia.

Ricard, L.P., Esteban, L., Pimienta, L., Delle Piane, C., Evans, C., Chanu, J.B. and Sarout J., 2011. Temperature estimates for geothermal application: Cockburn-1, Perth Basin, Australia. Australian Geothermal Energy Conference 2011, Melbourne.

Stütenbecker, L., 2011. Internship Report. West Australian Geothermal Centre of Excellence, Perth, pp. 26.

Stütenbecker, L., Timms, N., 2011, Petrography of samples of Cockburn-1 well. Perth Basin, Western Australia. WA Geothermal Centre of Excellence Confidential Report EP113151, Perth, 207pp.

Timms, N.E., Wilkes, P.G., Healy, D., Corbel, S. and Horowitz, F.G., 2012, Revealing faults in the Perth Metropolitan Area, Western Australia: Implications for groundwater systematics. Structural Geology and Tectonics Specialist Group Meeting, Waratah Bay. Jan 2012.

Timms, N.E., Wilson, M., Israni, S., Delle Piane, C., Clennell, B., 2011, Sedimentary facies and permeability analysis of Cockburn-1 core: Implications for Geothermal exploration in the Perth metropolitan area, West Australian Geothermal Energy Symposium, Perth, 21-22 March 2011.

Timms, N., Wilson, M., Israni, S., Clennell, B., Delle Piane, C., Esteban, L., 2011, Cores, sediments and chemistry. WAGCoE Workshop, ARRC Building, 16 February 2011.

Tressler, S., 2011 Temperature and gamma logging, Perth metropolitan area. Exploration Geophysics Honours Thesis (unpublished), Curtin University, Perth.

Wilkes, P.G and WAGCoE team, 2011 Vertical seismic profiling surveys to investigate the top 4 km of subsurface in the Perth Metropolitan Area. Presentation at WA Geothermal Energy Symposium, Perth, May 2011

Wilkes, P.G, Timms, N, Corbel, S and Horowitz, F.G, 2011, Using gravity and magnetic methods with geomorphology and geology for basement and structural studies to assist geothermal applications in the Perth Basin. Australian Geothermal Energy Conference. Melbourne, Nov 2011.

Wilkes, P., Timms, N., Horowitz, F., and Corbel, S., 2011, A new structural interpretation of the Perth Basin and the Perth metropolitan area using gravity and aeromagnetic data, geomorphology and geology. WA Geothermal Centre of Excellence Confidential Report EP 117411, Perth, 60pp.